Damage assessment of structures against blast load based on mode approximation method

Huang, Xin

2011

Huang, X. (2011). Damage assessment of structures against blast load based on mode approximation method. Doctoral thesis, Nanyang Technological University, Singapore.

https://hdl.handle.net/10356/45499

https://doi.org/10.32657/10356/45499

DAMAGE ASSESSMENT OF STRUCTURES AGIANST BLAST LOAD BASED ON MODE APPROXIMATION METHOD

NANYANG TECHNOLOGICAL UNIVERSITY

DAMAGE ASSESSMENT OF STRUCTURES AGAINST BLAST LOAD BASED ON MODE APPROXIMATION METHOD

HUANG XIN

HUANG XIN

SCHOOL OF CIVIL AND ENVIRONMENTAL ENGINEERING

2011

2011

DAMAGE ASSESSMENT OF STRUCTURES AGAINST BLAST LOAD BASED ON MODE APPROXIMATION METHOD

HUANG XIN

SCHOOL OF CIVIL AND ENVIRONMENTAL

ENGINEERING

NANYANG TECHNOLOGICAL UNIVERSITY

2011

Damage Assessment of Structures against Blast Load Based on Mode Approximation Method

Huang Xin

School of Civil & Environmental Engineering

A thesis submitted to

Nanyang Technological University

in fulfillment of the requirement for the degree of

Doctor of Philosophy

2011

ACKNOWLEDGEMENT

Foremost, I would like to express my sincere gratitude to my supervisor Dr. Ma Guowei for the continuous support of my Ph.D study and research, for his patience, motivation, enthusiasm, and immense knowledge. His guidance helped me in all the time of research and writing of this thesis. I could not have imagined having a better supervisor and mentor for my Ph.D study.

Besides my supervisor, I would like to thank professors who bring me to this research field and give me guidance. Dr. Lu Yong, Dr. Zhao Zhiye, and Dr. Yang Yaowen, thank you for your strictness during class and patience when I asked questions. I also would like to show my gratitude to Dr. Hao Hong, Dr. Li Qingming, and Dr. Wu Chengqing, I could not finish my research work without the ideas and help from you.

I am very grateful to Dr. Yu Jianxing and Dr. Tan Soon Keat, referees of my Ph.D application. I will never forget that you gave me this opportunity studying abroad. I am thankful to Dr. Gho Wie Min as well for the project experience he gave me. I believe such experience will be helpful in the future.

Thanks are also due to Bao Huirong, He Lei, and other classmates and staff from the office I have stayed and the group we used to work together. I would like to thank technical staff in the P.E. lab, Construction lab, and CADD lab in NTU who support my research and work.

The financial support from Nanyang Technological University and DSTA in the form of research scholarship is gratefully acknowledged.

Lastly, and most importantly, I wish to thank my parents, Huang Weiguo and Chang Xiaoyun. They always support me and love me. Special thanks are given to my wife, Han Linlin, for her love and everything she does for me.

ABSTRACT

Damage assessment plays an important role in the evaluation of the stability and strength of structures, which is significant for both the existing structures and those under construction. An effective damage assessment method based on the deformation behavior of a structure is essential in order to apply protective measures when there exists potential blast load risks. For a reinforced concrete structural element, the analysis becomes more complicated because the reinforced concrete always deforms in a nonlinear way, especially in the post-failure stage.

Although it is straightforward to use the single-degree-of-freedom (SDOF) approach to derive the structural response, the SDOF model usually oversimplifies the structural deformation due to the limitation of its mathematical form and ignores the influence of the shear deformation in bending failure. In the present study, the mode approximation method (MAM) is adopted to generate pressure-impulse (P-I) equations and diagrams. According to this method, the shear and bending responses can be considered simultaneously, and the combined failure modes for structural elements are included.

Damage assessment for underground structures is also studied. The soil-structure interactions (SSI) due to external or internal explosion are simplified as damping or stiffness effect and theoretical solutions are derived based on the MAM. To obtain a more accurate theoretical solution and consider the complexities of the material strength and the SSI effect, the MAM has been subsequently extended to use a generalized integration procedure on scenarios of both surface and underground structures. Therefore, the pulse-shape effect and the nonlinearities of material strength and the complicated SSI effect could be considered.

Numerical simulation of a reinforced concrete (RC) wall is carried out to verify the analytical study and extend the analysis into three dimensional problems. The blast loads used in the simulation are calibrated by TM5-1300 and some available experimental data. The simulation results are compared with the results obtained from theoretical solution.

TABLE OF CONTENTS

LIST OF TABLES

LIST OF FIGURES

LIST OF SYMBOLS

Δt	iterative time step
β	constant in stress wave attenuation equation
β_0	ratio of centerline deflection to half span
γ_v	average shear strain
δ	material parameter
θ	support rotation
$\xi_0, \dot{\xi}, \xi$	half length of plastic zone, velocity of the moving plastic hinge, half length of plastic zone as a function of time
ρc	acoustic impedance of soil
σ_f, σ_i	free-field and interface pressure respectively
ν	dimensionless strength ratio
a	depth of equivalent rectangular stress block
b	width of compression face
c	P- wave velocity
d, d'	distance from extreme compression fiber to centroid of tension/compression reinforcement respectively
f	coupling factor of explosive energy
f'_{dc}	dynamic ultimate compressive strength of concrete
f_{ds}	dynamic design stress for reinforcement
h	depth of element
m, m_e	mass per unit length, effective unit mass
n	attenuation coefficient
p	function of blast pressure
p_0	constant pressure in blast load duration
p_b	strength ratio which produces balanced conditions at ultimate strength

t_1	final time of plastic hinges moving
t_d	blast load duration
t_{mean}	mean time of the pulse
t_{me}, t_{se}	end time of elastic bending and shear stage respectively
t_f, t_s, t_y	final time of total and shear deformation, the time when material begins to yield respectively
$\dot{u}, v$	structural velocity and soil velocity respectively
x	abscissa on the element
$\dot{y}, \ddot{y}$	velocity and acceleration of unit mass respectively
$y_m, y_{me}, \dot{y}_m, \ddot{y}_m$	maximum displacement, elastic displacement, velocity and acceleration of bending deformation respectively
$y_s, y_{se}, \dot{y}_s, \ddot{y}_s$	maximum displacement, elastic displacement, velocity and acceleration of shear deformation respectively
A_s, A'_s	area of tension and compression reinforcement within the width b respectively
C	equivalent damping coefficient
D^*, M^*, Q^*	normalized displacement, normalized bending resistance, and normalized shear resistance respectively
I	impulse per unit area
I^*, P^*	dimensionless impulse and pressure respectively
K	equivalent damping coefficient
K_1, K_2, K_3	dimensionless rates of slope in multi-linear deformation model respectively
L	half length of element
M, Q	transverse bending moment and shear force respectively
M_0, Q_0	bending and shear strength respectively
$M_0(y), Q_0(y)$	bending and shear resistance in multi-linear R-D relationship
M_e, Q_e	maximum elastic bending and shear resistance respectively

M_u	ultimate unit resisting moment
P_e, P_i, P_0, P	effective pressure, reflected pressure, peak pressure, external pressure respectively
R^*	normalized general resistance
S, B	unified forms for shear and bending failure criterion respectively
T	general time variable
T_n	temporary variable of time, n=1,2,3,4,5,6,7
V_d	ultimate direct shear force

CHAPTER 1

INTRODUCTION

1.1. Background

Damage assessment plays an important role in the evaluation of the stability and strength of structures, which is significant for both the existing structures and those under construction. In an extreme condition, such as a blast load scenario that is normally not considered in the original structural design of civilian structures, structural elements may experience damage in different degrees. An effective damage assessment method based on the deformation behavior of a structure is essential in order to apply protective measures when there are potential blast load risks. For a reinforced concrete (RC) structural element, the analysis becomes more complicated because the reinforced concrete always deforms in a nonlinear way, especially in the post-failure stage.

Early in the World War II, the pressure-impulse (P-I) diagram method was first used to assess the damage of structural elements and buildings against blast load. For a certain blast load, the P-I diagram indicates the safety status of the structural element. Researchers used to simplify a structural element by adopting an equivalent single-degree-of-freedom (SDOF) model or a rigid-plastic beam model to analyze the structural response against blast load, and most of the structural blast designs are based on the SDOF approach. Based on the SDOF model, the shear deformation effect was either neglected in the analysis or considered separately by another SDOF model. For a mixed failure mode, the SDOF model becomes invalid.

Although it is straightforward to use the SDOF approach to derive the structural response, the SDOF model has its limitations. It usually oversimplifies the structural deformation due to the limitation of its mathematical form and ignores the influence of the shear deformation in bending failure and vice versa, which may yield unreasonable estimation of the structural failure. The localized transverse shear, which is known as a shear hinge, is an important feature of structural

deformation when a structural element is under blast load (Jones 1989, Jones 1997). Through experimental and analytical studies (Yu and Jones 1991, Krauthammer 1998), it has been realized that, when the span-to-height ratio of a structural element is relatively small or when a detonation is at a close-in distance from the structure, the shear failure likely occurs. If the duration of blast load is very short, the shear failure becomes dominant and cannot be ignored. Although both the shear and bending response of a structural element have been analyzed by an SDOF model (Krauthammer *et al*. 1986), the two failure mechanisms have to be considered separately due to the SDOF simplifications. Sometimes shear failure is the main cause of successive collapse of a structure. Bending failure often occurs near the middle of a structural element which is simply supported or fixed at both ends, while shear failure occurs close to the supports where the shear force is always to be the maximum under a blast load.

The classical mode approximation method (MAM) for a rigid-plastic structural element has also been widely used for decades (Martin and Symonds 1966, Jones and Song 1986, Li and Jones 1999). The estimated deflections caused by the MAM in most cases agree well with the final deflections observed in tests (Symonds and Chon 1979). Lellep and Torn (2005) developed a method for the investigation of rigid-plastic beams subjected to impulsive load. Theoretical solutions are derived for beams made of perfectly plastic material obeying the square yield condition. According to this method, the shear and bending responses can be considered simultaneously, and the combined failure modes for structural elements are involved. Ma *et al*. (2007) plotted the P-I diagrams for beam structures based on the rigid-plastic structural model. The MAM has the advantages in characterizing the combined failure modes. The P-I diagrams derived from such model agreed reasonably well with those from an elastic-perfectly-plastic SDOF model, especially for a severe damage case.

In the classical MAM, the rigid-plastic model is not effective for analysis of RC structures. It is because in practical structural engineering RC structures deform in a nonlinear way and the softening behavior significantly affects the blast resistance of a structural element. In most of the previous analytical derivations, the structural

deformation was simplified as linear (rigid-plastic) or bi-linear (elastic, perfectly plastic or plastic hardening) models. For more accurate analysis of RC structures, the softening behavior cannot be neglected even in the light and moderate damage cases. Besides, nearly all of the existing research works were for surface structures. Seldom studies have been done on the damage analysis of underground structures, and the nonlinearity of the material and the non-constancy of soil-structure interaction (SSI) were rarely considered.

With the development of underground technology, a lot of underground structures are constructed or under construction, including tunnels, underground storage, underground protective structures, etc. Different from design of surface structures, there is no commonly used standard or a reliable design reference available for underground structures. Many underground structures were designed and constructed based on code for surface structures. The propagation of blast wave in soil is different from that in air, and the response of underground structures against blast loads with SSI.

The present study aims to find out a convenient and unified way to carry out damage assessment of different structures. The MAM is further developed to generate P-I diagrams for different surface and underground structures.

1.2. Research objectives

The primary objective of the present research is to extend the conventional MAM to the damage assessment of structural element in various blast loading and structural/material conditions. Starting from the conventional MAM for inelastic structural response analysis, more parameters will be considered when deriving the P-I equations for surface or underground structures against blast load, for example, the SSI effect in structural response, the pulse shape effect on final displacement of structural element, the nonlinearities of material strength, the effect of elastic deformation, and the effect of simplified SSI.

The specific targets are outlined as follows:

- to generate P-I diagrams based on the MAM and rigid-plastic material model for damage assessment of underground structures against blast load. In the external and internal blast load scenarios, the SSI will be simplified as damping and spring effect respectively.
- to work out a generalized integration method based on the MAM so that different pulse shapes of the blast load can be analyzed.
- to extend the generalized integration method to be applied to damage assessment of underground structures. Besides the pulse shape effect, more simplified SSI will also be taken into account.
- to further extend the analytical solution to consider the effects of the elastic phase and nonlinearities of material strength based on the MAM simplifications.
- to verify the analytical solutions by using numerical simulations.

1.3. Thesis organization

This thesis is organized into 9 chapters. Chapter 1 introduces the background and the objectives of this thesis. Chapter 2 reviews the P-I diagram method based on SDOF system and mode approximation method. The calculation of shear and bending strengths for structural element in TM5-1300 is reviewed as well. Chapter 3 analyzes the underground structure against external blast load with consideration of SSI. It extends the P-I analysis based on the MAM from surface structure to underground structure. Chapter 4 studies the underground structure against internal blast load with consideration of the SSI. Chapter 5 uses a semi-analytical integration method in derivation of P-I equations so that the pulse shape effect on P-I diagrams based on the MAM for surface structure under blast load is studied. Chapter 6 extends the research work in Chapter 5 to underground structures and studies more complicated SSI effect. The pulse shaped effect is analyzed as well. Chapter 7 further extends the P-I diagram method based on the MAM and considers the nonlinearity of material strength and the effect of the elastic phase. Chapter 8 performs numerical simulation of an RC wall which verifies the analytical study in

earlier chapters, and also extends the analysis into three dimensional problems. Chapter 9 summarizes the conclusions and gives recommendations for future study.

1.4. Originality and contributions

All the research work done in this thesis is original. The MAM is used in the damage assessment for underground structures against blast load. The SSI is simplified as constant damping and spring coefficients for external and internal explosion scenarios respectively. When the general integration method is adopted in the procedure of solving the governing equations, it is feasible and easy to involve non-constant parameters in P-I equations. Therefore, pulse shape effect, non-constant SSI and piece-wise strengths of structural element are considered in damage assessments of both surface and underground structures against blast load. All results are shown in the form of P-I diagrams and discussions are performed. Numerical simulations are attached to validate those P-I results.

Findings from the present research work would help engineers to optimize their design of structures against blast load.

CHAPTER 2

LITERATURE REVIEW

Damage assessment is a critical issue in protective structure design against blast load. In each assessment, the structural response is the most important factor among others that designers and engineers care about. Based on the SDOF system and MAM, the structural acceleration, velocity and displacement of a structural element can be calculated. Consequently by plotting the P-I diagrams, the structural damage can be assessed.

2.1. P-I diagram method

P-I diagram was first used to assess the damage extent of structural elements and buildings in the World War II (Smith and Hetherington 1995). Different damage extents, such as complete demolition, severe damage, relatively minor structural damage, were quantified by a series of curves.

Stanford Research Institute contributed to the development of P-I diagram from 1959 to 1966 (Abrahamson and Lindberg, 1976). They used P-I diagram to evaluate the effects of blast on aircraft structures in 1950s and 1960s. Kornhauser (1954) used velocity and acceleration as the coordinates, which are equivalent to the peak load and impulse system, to derive the curves for different structures. Coombs and Thornhill (1960) identified that the peak load is very important for impulsive loads. Researchers in Lovelace Foundation (Richmond *et al*. 1966) studied the influences of the duration and the peak load on animal injuries. Mortion (1966) computed the critical load curves for simple rigid-plastic system. Abrahamson and Lindberg (1976) brought up the closed-form formula for rigid-plastic system. Smith and Hetherington (1994) analyzed the human body response to blast loads with P-I diagram and categorized the damage with critical curves. Li and Meng (2002a) used the least-square method to constitute universal formula to fit the critical P-I diagram curves.

It has been widely admitted that the P-I diagram has three regions: an impulsive controlled region, a peak pressure controlled region, and a peak pressure and impulse combination controlled region (Abrahamson and Lindberg 1976, Smith and Hetherington 1994, Li and Meng 2002a). The division of the three regions is shown in Table 2-1.

Table 2 - 1 Three regions of the P-I diagram

	Abrahamson, 1971	Smith, 1994
Impulse controlled	$t_d \le 0.05T$	$0.4 > \omega t_d$
Peak pressure and impulse combination controlled	$0.05T \le t_d \le 1.25T$	$0.4 \le \omega t_d \le 40$
Peak pressure controlled	$t_d \ge 1.25T$	$40 < \omega t_d$

where: T is the natural period, ω is the natural vibration frequency and t_d is the blast load duration.

The P-I diagram categorizes into part I, II, and III as illustrated in Fig. 2-1 (idealized P-I diagram in (Li and Meng 2002a)). Although there is small difference about the specific value for the dividing, they are similar in principle because they are all based on the comparison with the natural period of structure or structural members.

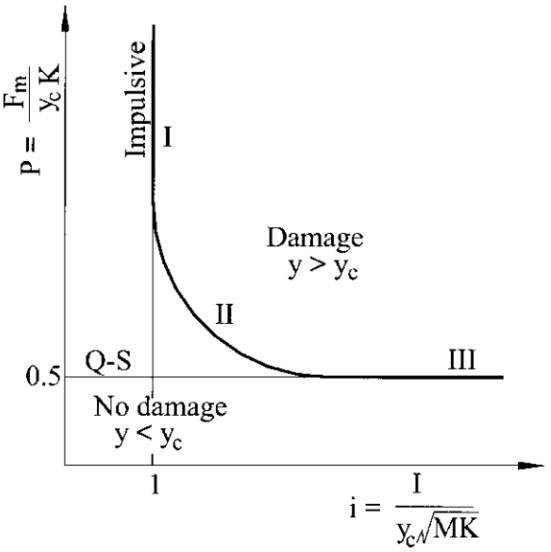

Fig. 2 - 1 Idealized P-I diagram

There are three representative load types as shown in Fig. 2-2, i.e., (1) rectangular load with step rise, constant value, and step down, (2) triangular load with step rise and linear depreciation, (3) exponential load with step rise and exponential depreciation. For the same structural element, the rectangular load gives the lower bound of the threshold curve, while the exponential load results in the upper bound. For the triangular load, the corresponding curve is between the two boundary curves. The maximum difference between the lower bound and the upper bound could be up to 40% (Abrahamson and Lindberg 1976). Li and Meng (2002b) also discussed the difference due to pulse shape effect (Fig. 2-3).

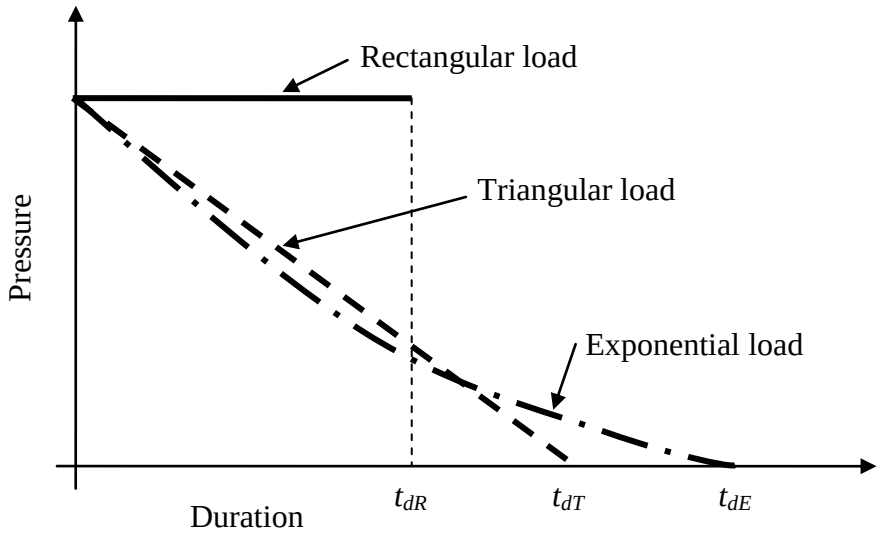

Fig. 2 - 2 Simplified blast load types

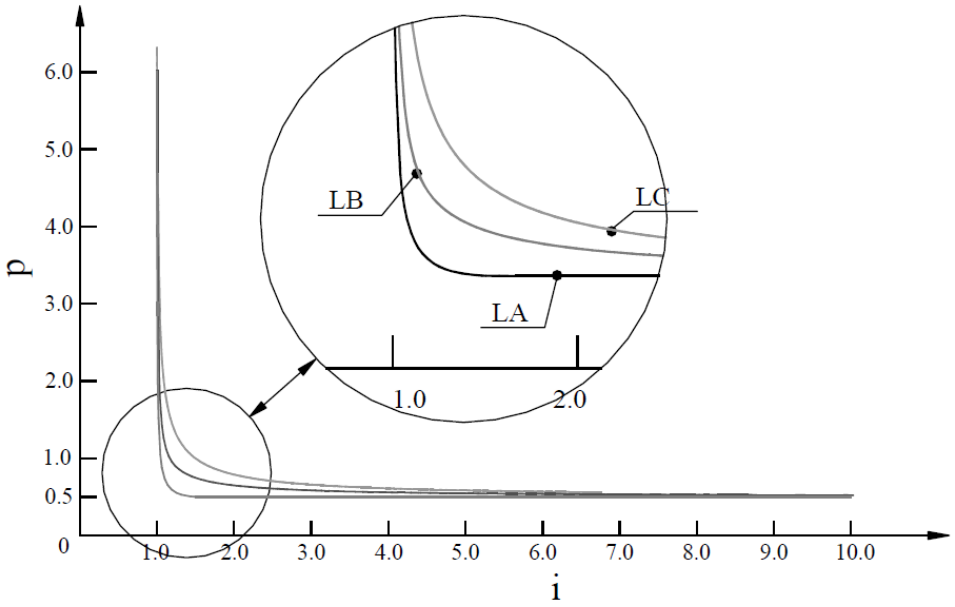

LA: rectangular load; LB: triangle load; LC: Exponential load.

Fig. 2 - 3 Difference of loading shapes

The advantage of the P-I diagram is to simplify the judgment for the damage of structural members or structures. According to the P-I diagram, a certain load with the peak pressure and impulse above the critical curve will result in damage of the structures, while the structure is safe if the peak pressure and impulse combination locates below the curve.

The critical or threshold curve of the P-I diagram is plotted by the peak load and impulse combinations which produces the maximum displacement that the structure can undertake. Though there is small difference among the shapes of the critical curves of the P-I diagram, the similarity suggests a uniform approximate expression for all load cases. There have been such endeavors and the results are summarized in Table 2-2.

Table 2 - 2 Comparison of simplified equations of P-I diagram

Denotation to symbols	Applicable situations	Formula	
P_0: the magnitude of ideal load that produces the critical displacement; I_0: the ideal impulse that produces the critical displacement.	Rigid-plastic system, linear spring-mass system, all three kinds of impulse	$\left(\frac{P}{P_0}-1\right)\cdot\left(\frac{I}{I_0}-1\right)=1$	Abrahamson (1971)
$I_e=\int_{t_y}^{t_f}P(t)dt,\ P_e=\frac{I_e}{2t_{mean}}$, $t_{mean}=\frac{1}{I_e}\int_{t_y}^{t_f}(t-t_y)P(t)dt\cdot P_y$ P_y means static yield load; I_e means ideal impulse, t_y and t_f are the times when structural element yield and stops moving respectively, *P(t)* is the loading function of time, P_e is the effective pressure, t_{mean} is the mean loading duration.	Plastic structural members such as simply supported beam, simply supported circular plate and circular cylindrical shell under various impulse	$\frac{6}{5}(\frac{I_e}{I_0})^2\cdot\left(1-\frac{P_y}{P_e}\right)=1$ for $\frac{P_y}{P_e}\le 2$ $(\frac{I_e}{I_0})^2\cdot\left(1-\frac{4P_y}{5P_e}\right)=1$ for $\frac{P_y}{P_e}\ge 2$	Zhu (1986)
x_{max}: the maximum displacement; K: the stiffness; M: the mass.	Almost all the possible cases	$\frac{2F}{Kx_{max}}=1$ $\frac{I}{x_{max}\sqrt{KM}}=1$	Smith (1994)
$n_{1,2}=\beta_0+\beta_1 d+\beta_2 d^2$ $d=\sqrt{x_0^2+y_0^2}$ Where β_0, β_1, β_2, x_0, and y_0 are coefficients got by curve-fitting.	Elastic structures and dynamic loading such as descending impulse load	$p=\frac{n_1}{(i-1)^{n_2}}+0.5$	Li (2002)

2.2. P-I diagrams based on SDOF system

Among the existing damage assessment methods, the simplified Single-Degree-Of-Freedom (SDOF) system has been widely used to analyze the structural response under blast load for a variety of structures or structural elements. A structural member can be simplified as a SDOF model and described by the following equilibrium equation (Biggs, 1964):

$$M\ddot{y} + Ky = F \cdot f(t) \tag{2.1}$$

where M is the equivalent lumped mass, $\ddot{y}$ is the structural acceleration, K is the equivalent structural stiffness, $F \cdot f(t)$ is the equivalent applied force and y is the structural deformation.

The solution of Eq. (2.1) is:

$$y(t) = y_0 \cdot \cos(\omega t) + \frac{\dot{y}_0}{\omega} \cdot \sin(\omega t) + \frac{F}{\omega M} \int_0^t f(\tau) \cdot \sin\left[\omega(t-\tau)\right] d\tau \tag{2.2}$$

where y_0 is the initial displacement, $\dot{y}_0$ is the initial velocity, and ω is the natural vibration circular frequency.

Usually the initial conditions are:

$$\begin{cases} y \,|\, (t=0) = y_0 = 0 \\ \dot{y} \,|\, (t=0) = \dot{y}_0 = 0 \end{cases} \tag{2.3}$$

For simplification, the impulsive load is normally assumed to start at its maximum value and then descend to zero when $t=t_d$, where t_d is the duration of the blast load. The negative pressure phase is neglected.

Most of the structural blast designs were based on the SDOF approach (TM5-1300, 1990). Although various extensions and applications of the SDOF approach have been carried out, in many cases it oversimplifies a structure or a structural element due to the limitation of its mathematical form. Based on the SDOF model, the shear deformation effect was either neglected in the analysis (Li and Meng 2002a; Campidelli and Viola 2007; Fallah and Louca 2007) or considered separately by

another SDOF model (Krauthammer *et al*. 1986). For a mixed failure mode, the SDOF model becomes invalid. The SDOF system has its advantages in deriving analytically the structural response. In many cases of practical engineering, it has been used to give a preliminary assessment of structural damage induced by a blast load. However, due to its inherent limitation, the SDOF model oversimplifies the structural elements and neglects the influence of shear deformation, or it can only analyze the shear and bending response separately.

In a blast event, structures at close-in distance may experience localized transverse shear failure which deforms as a shear hinge (Symonds 1968, Jones 1989, Jones 1997). Depending on different loading rates, intensities, and material properties, the localized shear deformation can be isothermal rupture (Menkes and Opat 1973) or adiabatic shear bending failure (Kalthoff and Winkler 1987, Kalthoff 1990). The analytical solutions for the dynamic plastic shear/bending response of beams with general boundary conditions were studied (Li and Jones 1991) including both fully-clamped and simply-supported beams when subjected to blast loading. Based on experimental and analytical results (Yu and Jones 1991, Krauthammer 1998), it has been realized that, when the span-to-height ratio of a structural element is relatively small or when a detonation is at close-in distance from the structure, the shear failure probably occurs. If duration of blast load is sufficiently short, shear failure becomes dominant and cannot be ignored and sometimes shear failure is the main cause of successive collapse of a structure. Bending failure often occurs near the middle of a structural element which is simply supported or fixed at both ends, while shear failure occurs close to the supports where the shear force is often to be the maximum under a blast load.

2.3. P-I diagrams based on mode approximation method

The problem of estimating permanent deformations of structures subjected to high intensity dynamic loading started to receive increasing attention in the early 1950s. At that time, above the complexity of the problem of elastic structures subjected to transient loading, additional complicating factors which are of importance included the dissipation of energy in plastic work, elastic unloading from plastic states, strength hardening, the dependence of yield stress upon rate of strain, geometry

change, and other non-linear effects. Very few solutions of dynamic loading problem had recognized all these factors. More commonly, one or more of the factors were assumed to dominate the behavior of the structure, and all others are neglected or approximated.

The widely used approximation was the replacement of distributed mass of structure by one or more point masses. Such approximation had been used in conjunction with a variety of idealizations of the material behavior. In fairly simple structures, the actual distribution of mass, elastic stiffness and yield stress can be considered. Solutions for an elastic, perfect plastic material had been found by some researchers, e.g. Bleich and Salvadori (1955) and Seiler *et al*. (1956), but were difficult if the load magnitudes were much larger than those causing the yield stress to be reached.

Martin and Symonds (1966) suggested the MAM to provide a rational method of constructing an SDOF approximations for impulsively loaded metal structures which are analyzed according to an elementary rigid-plastic theory. The approximation follows automatically from a chosen mode shape. Such method was based on the elementary rigid-plastic theory which involved in two idealizations: 1) for the purpose of the dynamic loading problem under consideration, a ductile material is represented by a rigid perfectly plastic constitutive equation. All elastic effects are in consequence excluded. 2) geometry changes are assumed to be small, and the yield stress is assumed to be independent of the rate of strain.

There were two examples to show the difference of solutions between SDOF approximation and mode approximation method. One example of the clamped beam indicated that, the final central displacement can be obtained as a function of *b/l* (width of the load along the beam over total length of the beam as shown in Fig. 2-4, and velocity for different phases can be referred to Fig. 2-5). The final central displacement parameter versus the ratio *b/l* in Fig. 2-6 shows the accuracy of MAM. The displacements in the mode solution overestimate the actual displacements in some regions and underestimate them in others. Another example of the cantilever with an attached tip mass showed that, the final tip displacement was a function of the parameter γ, and hence the accuracy of the approximation depended on γ.

Based on the analysis and discussion, Martin and Symonds (1966) tried to rationalize the setting up of an SDOF approximation in elementary rigid-plastic theory for impulse loading. The method required a mode shape be chosen, thereafter the equivalent spring force, mass, and the initial mode velocity followed without further assumptions. A good approximation solution was from small initial difference, i.e. small compared to the initial energy in any other solutions. It could be concluded that the mode approximation can be reasonably good.

The work done by Martin and Symonds in 1966 showed that, by using the mode approximation method, good result for beam element can be obtained in the analysis of impulse load and the error of mode shape assumption is acceptable.

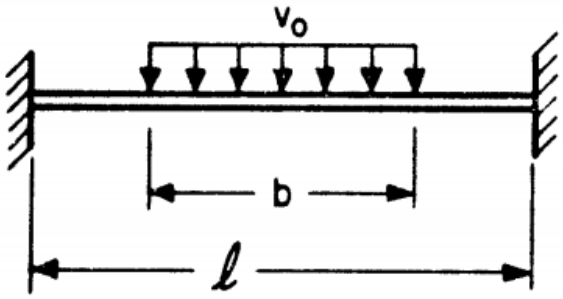

Fig. 2 - 4 Clamped beam model

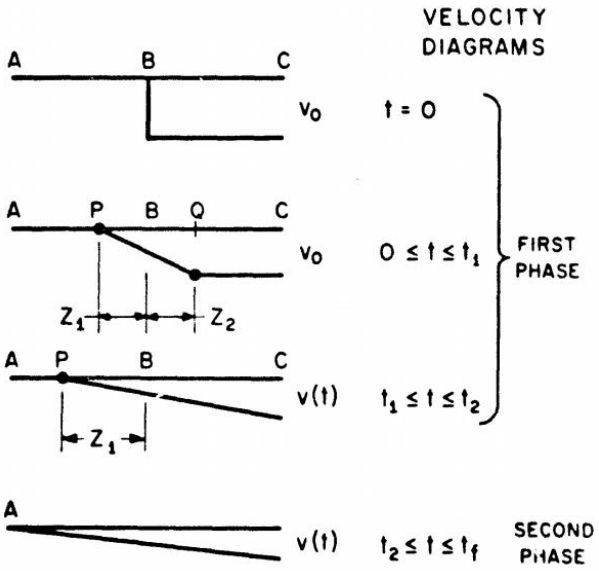

Fig. 2 - 5 Velocity profile for clamped beam model

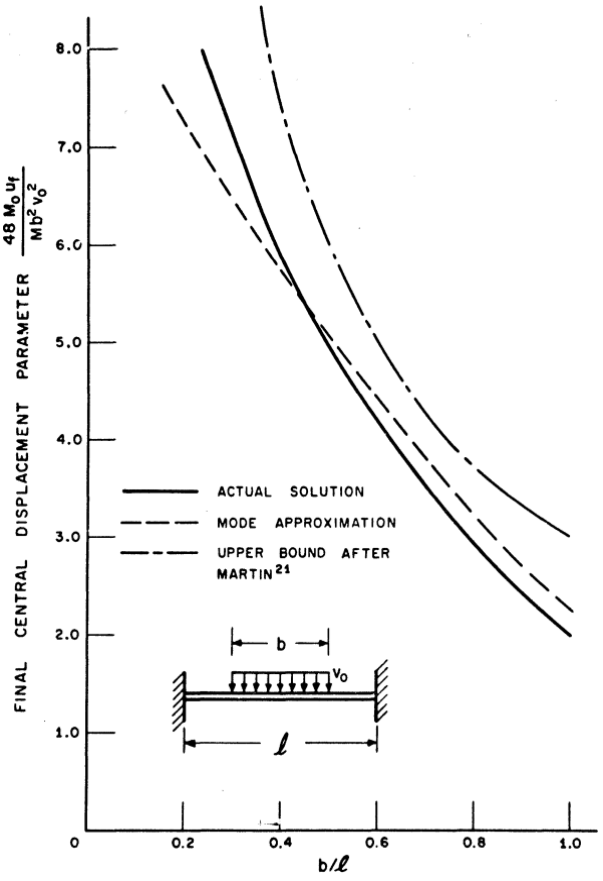

Fig. 2 - 6 Final central displacement parameter versus *b/L*

The classical mode approximation method for rigid-plastic structural elements analysis is already well known. Research work has been done on different constraints and load distributions (Martin and Symonds 1966; Symonds and Chon 1979; Jones and Song 1986; Liu and Jones 1988; Li and Jones 1999; Alves and Jones 2002; Jones and Jones 2002; Lellep and Torn 2005; Li and Jones 2005a). By comparison with the SDOF results, it shows that, although the rigid-plastic model neglects the elastic deformation, the estimated deflections by the mode approximation method in most cases agree well with the final deflections observed in tests (Symonds and Chon 1979). The pressure-impulse (P-I) diagrams derived from a rigid-plastic model are very close to those from elastic, perfectly plastic SDOF model, especially when severe damage occurs to the structure element. Lellep and Torn (2005) analyzed rigid-plastic beam damage subjected to an impulsive load by assuming the perfectly plastic material obeying the square yield criterion. According to this method, shear and bending responses can be analyzed

together and thus combined failure modes for beams can be considered. Ma *et al*. (2007) further developed a P-I diagram method for damage assessment of surface structures subjected to blast load in consideration of both bending and shear damage. An explicit analytical solution for the P-I diagrams were obtained which could be conveniently used for assessing structural damage.

2.3.1. P-I diagrams for beam element

The MAM was widely used for different element models and material models. Some research works based on the MAM are summarized below:

Nonaka (1977) analyzed the shear and bending response of a rigid-plastic beam element under blast-type loading. He used a simply supported uniform beam with limit moment M_0 and limit shear Q_0 to analyze the structural response under blast-type load. The blast-type load was simplified as pressure $P(t)$ uniformly distributed over the whole span. Five failure modes were assumed including rotation with single hinge, rotation with plastic zone, sliding, sliding and rotation with single hinge, and sliding and rotation with plastic zone. Such five failure modes indicated the shear failure, bending failure, and combined failure modes. Results of the analysis showed that, the maximum shear magnitude was always attained at the beam ends where the bending moment was zero, while the bending moment was the maximum at the middle portion of the beam where the shear force was zero. For a yield curve smaller than the assumed polygon, there may be a possibility of reaching the yield limit under the *M*-*Q* interaction. It was important to state that any yield curves in the analysis of Nonaka was valid only when $(|M/M_o|-1)(|Q/Q_0|-1)=0$. Some of the important conclusions were generated such as that, the shear deformation reduced the bending part of the kinetic energy being absorbed in shearing, and for impulsive loading with the ratio $\mu_0=p_0L/4M_0$ high enough, shearing always took place and this effect became maximum among blast-type loads with the same total impulse as shown in Fig. 2-7.

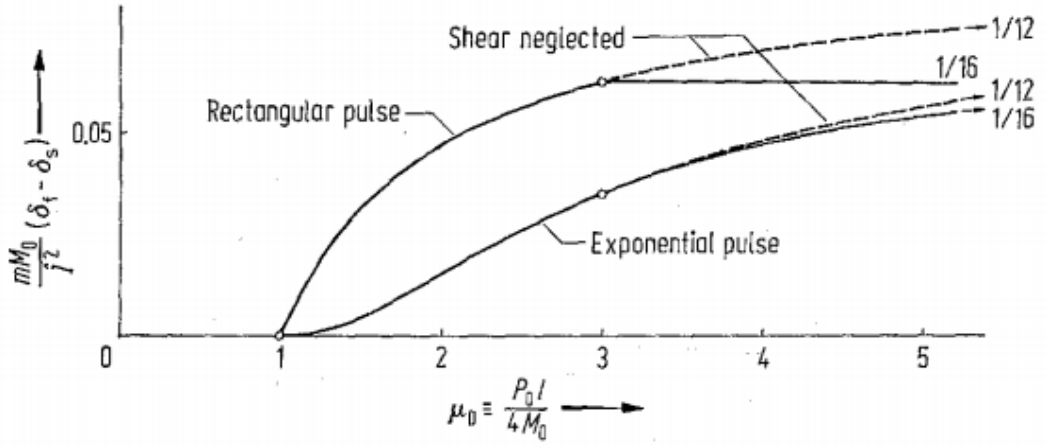

Fig. 2 - 7 Differences among pulse shapes and shear effect

It was also concluded that, in the case of an ordinary load pulse with μ_0 of the order greater than ten, the permanent deformation was well approximated by treating the loading as impulsive, which gave the largest plastic deformation for the same total impulse; when μ_0 was of the order of ten or less, the finiteness of the load magnitude should be taken into account, and if μ_0 was not much larger than unity, the exact load-time relation had to be considered.

Jones and Song (1986) did the similar analysis of shear and bending response of a rigid-plastic beam, but under partly distributed blast-type loading. The blast-type loading was assumed as a pressure distributed along the beam symmetrically about the beam center but in the region with half length of L_1. There were also five possibilities of motion which represented the shear failure mode, bending failure modes, and combined failure modes but slight different from work of Nonaka (1977) since the loading was different. The results showed that, dynamic response was governed by nine different patterns of initial motion, when the influence of transverse shear force was retained in the yield condition as well as bending moment. The initial velocity fields in the analysis were controlled by parameters that related to shear strength, loading magnitude, and loading distribution. The influence of transverse shear on the maximum transverse displacement were negligible when v is bigger than 1.5 and the loading distribution η was in the range of 0.5 and 1, but became more important as η decreased. It was also confirmed that based on other researcher's work, rotational inertia effects turned out to be

unimportant for most practical problems and ignoring such effect only cause less than 10% of the error in the maximum transverse displacement. The pulse shape effect was also briefly discussed that the triangular and exponential pressure pulse loadings produced less transverse shear sliding and smaller bending deformations than a rectangular pressure pulse loading did.

Youngdahl (1997) used the MAM for strain-hardening cantilever beams where it was hypothesized that deflection shape satisfies smoothness and continuity requirements. Arbitrary load distributions and pulse shapes were considered and the differential equations were solved numerically. Li and Jones (1999) discussed the shear and adiabatic shear failures in an impulsively loaded fully clamped beam. The results showed that, with an increasing impulsive pressure load there was a direct transition between a transverse shear failure mode and an adiabatic shear failure mode. Yu and Chen (2000) did a further study of plastic shear failure of impulsively loaded clamped beams. The interaction between the shear force and bending moment, and the weakening of the sliding sections during the failing process were emphatically considered. Lellep and Torn (2005) used the MAM on different boundary condition, one side clamped and another side simply supported. The results differed from those obtained from beams with both ends simply supported or clamped, and calculations showed that the shear sliding was more essential for shorter beams.

Ma *et al*. (2007) used the MAM on P-I diagram method for combined failure modes of rigid-plastic beams, thus the damage assessment of real structures can be carried out straightforwardly. In the paper of Ma *et al*. (2007) the results were compared with SDOF approach to show the difference of those two models in Fig. 2-8. The difference between boundary conditions (simply supported and fully clamped) was discussed that, if the parameter v is replaced by $2v$, the P–I equations for the fully clamped beam are exactly the same as that for the simply supported beam as shown in Fig. 2-9. The works done in Chapter 3 to 7 of this thesis are based on the basic idea of Ma *et al*. (2007), and it is extended to underground structures and a generalized integration procedure is proposed. Derivation of P-I equations for surface structure against blast load (Ma *et al*. 2007) is shown in Section Appendix.

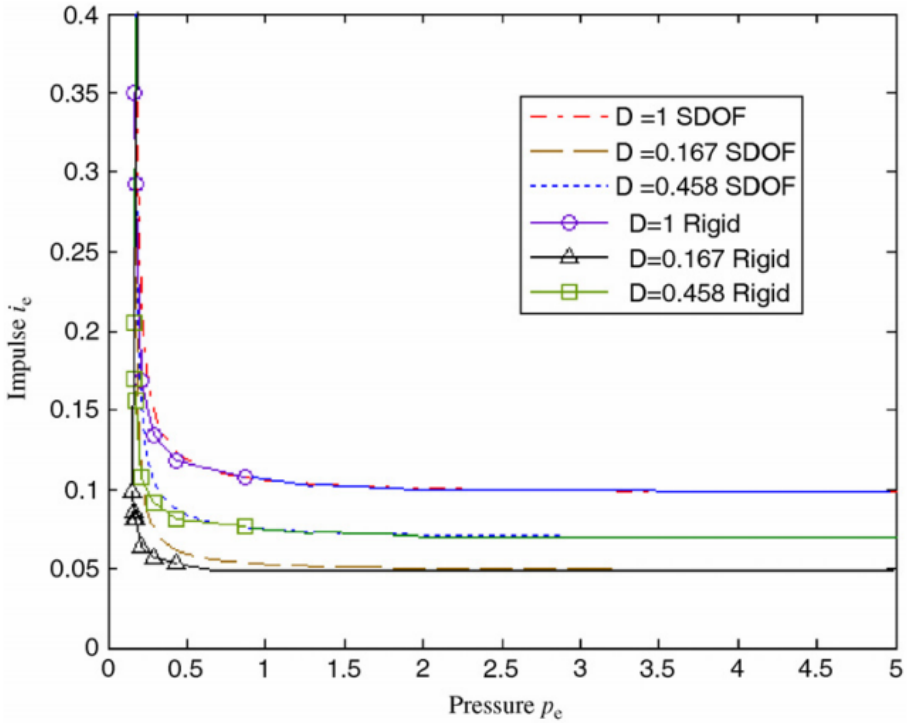

Fig. 2 - 8 Difference between SDOF model and rigid-plastic beam model

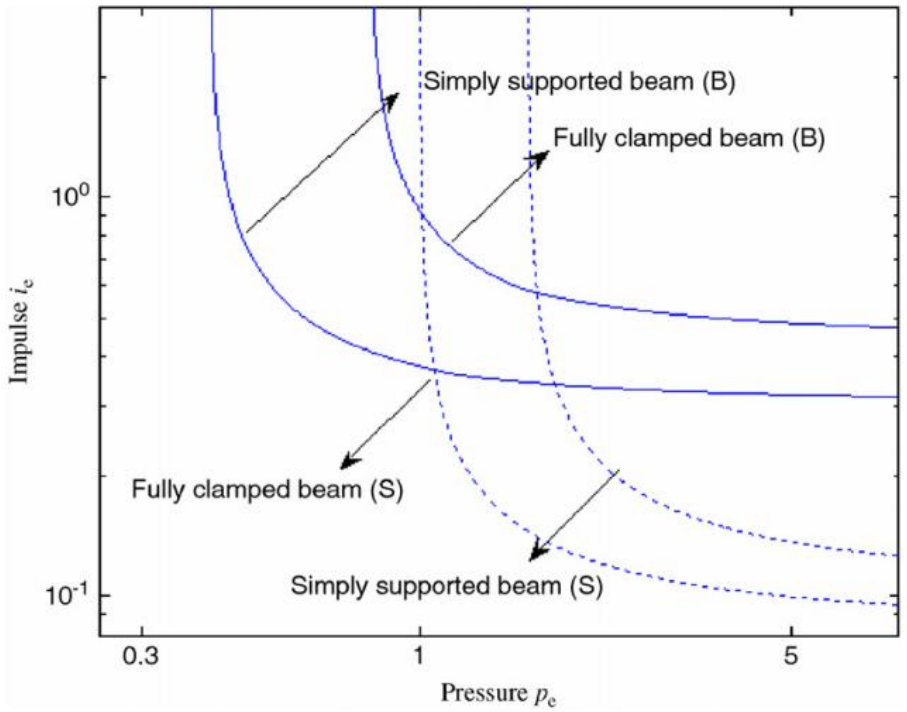

Fig. 2 - 9 Difference between boundary conditions

2.3.2. P-I diagrams for plate element

Early in 1960s, Jones (1968) studied the finite deflections of a simply supported rigid-plastic annular plate under a rectangular pressure pulse. It was founded that the deformation predicted by his analysis was smaller than those given by the bending only theory even for maximum deflections of the order of the plate thickness. Then Shen and Jones (1993) used the MAM to analyze the dynamic response and failure of fully clamped circular plates under a rectangular pressure pulse. Good agreement was obtained between the theoretical predictions for the permanent transverse deflections and the corresponding experimental results of Bodner and Symonds (1979), and Teeling-Smith and Nurick (1991) recorded on strain rate sensitive plates.

Li and Jones published their results in 1994 of fully clamped circular plates with transverse shear effects under blast loading. Similar to the analysis of beam element, the five failure modes were studied and P-I curves were generated to discuss the effect of strength ratio *v*. It was also realized that the relationships existed between the theoretical solutions for simply supported and fully clamped circular plates, which were similar to the observations made for beams in Li and Jones (1994) as shown in Fig. 2-10.

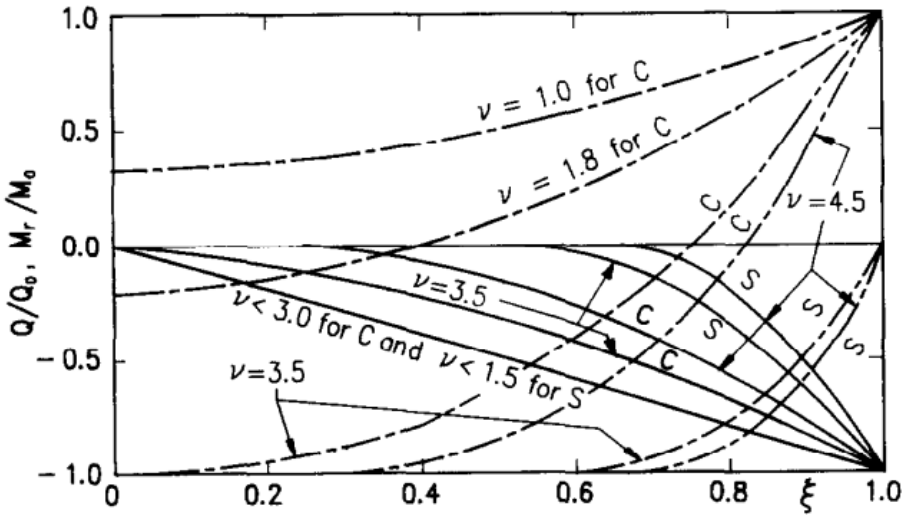

Fig. 2 - 10 Variations of the dimensionless transverse shear force and the dimensionless radial bending moment with ξ during the transverse shear sliding phase: C: fully clamped circular pate; S: simply supported circular plate

Chen and Li (2003) presented a shear plugging model to predict the ballistic limit and residual velocity of a metallic circular plate impacted by a blunt rigid projectile. Besides shear effect, plate bending, membrane stretching and local indentation/penetration were included in the model. Simple formulae and good predictions were given. Chen *et al*. (2005) extended their research works and the critical condition for the initiation of an adiabatic shear failure in the plate was determined according to the maximum shear stress criterion.

The plastic response of a circular cylindrical shell to dynamic loadings was studied by Lellep and Torn (2004) that, similar results to the beam model (Lellep and Torn, 2005) were obtained. It was interesting to note that, the solutions differed from those corresponding to shells with simply supported or clamped ends respectively. It was noted by Lellep and Torn (2004) that in the case of tubes with identical supports at both ends the solution (except for the longitudinal bending moment) was not sensitive to the support conditions. That was similar for beams and circular plates.

2.4. Design parameters of RC element against blast load

The material properties of RC and design procedure of RC structural element against blast load are reviewed as follows. The calculated bending and shear capacities of structural element will be used in the analytical studies in following chapters.

2.4.1. Material properties of reinforced concrete

Concrete is a mixture of cement paste and aggregate, each of which has an essentially linear and brittle stress-strain relationship in compression. Brittle materials tend to develop tensile fractures perpendicular to the direction of the largest tensile strain. Thus, when concrete is subjected to uniaxial compressive loading, cracks tend to develop parallel to the maximum compressive stress. Although concrete is made up of essentially elastic, brittle materials, its stress-strain curve is nonlinear and appears to be somewhat ductile (MacGregor and Wight, 2005).

Generally, the concrete strength is taken to refer to the uniaxial compressive strength as measured by a compression test of a standard test cylinder, because this test is used to monitor the concrete strength for quality control of acceptance purposes. Factors affecting concrete compressive strength include water/cement ratio, type of cement, age of concrete, rate of loading, and so on. The tensile strength of concrete falls between 8 and 15 percent of the compressive strength, however the actual value is strongly affected by the type of test carried out to determine the tensile strength, the type of aggregate, the compressive strength of the concrete, and the presence of a compressive stress transverse to the tensile stress (Raphael 1984, McNeely and Lash 1963).

Because concrete is weak in tension, it is reinforced with steel bars or wires that resist the tensile stresses. The most common types of reinforcement for non-prestressed members are hot-rolled deformed bars and wire fabric.

When a structural element is subjected to blast load, it exhibits a higher strength than a similar element subjected to a static loading. This increase in strength for both the concrete and reinforcement is attributed to the rapid rates of strain that occur in dynamically loaded members. The higher the strain rate, the higher the compressive strength of concrete and the higher the yield and ultimate strength of the reinforcement. Therefore in the design of protective RC structure, the Dynamic Increase Factor (DIF) should be considered for material strength. The design values of DIF presented in Table 2-3 vary not only for the design ranges and type of material but also with the state of stress (bending, diagonal tension, direct shear, bond, and compression) in the material (TM5-1300, 1990).

Table 2 - 3 DIF for design of RC elements

Type of stress	Far design range			Close-in design range		
	Reinforcing bars		Concrete	Reinforcing bars		Concrete
	f_{dy}/f_y	f_{du}/f_u	f'_{dc}/f'_c	f_{dy}/f_y	f_{du}/f_u	f'_{dc}/f'_c
Bending	1.17	1.05	1.19	1.23	1.05	1.25
Diagonal tension	1.00	-	1.00	1.10	1.00	1.00
Direct shear	1.10	1.00	1.10	1.10	1.00	1.10
Bond	1.17	1.05	1.00	1.23	1.05	1.00
Compression	1.10	-	1.12	1.13	-	1.16

2.4.2. Design of RC structural element

The bending and shear capacities of RC structural element would follow the following calculation. Considering the possible structural damage involved in the present study, only ultimate moment capacity and direct shear capacity in TM5-1300 are shown.

2.4.2.1. Ultimate moment capacity

The ultimate unit resisting moment M_u of a rectangular section of width b with tension reinforcement is given by:

$$M_u = \left(A_s f_{ds} / b\right) \cdot \left[d - \left(a/2\right)\right] \tag{2.4}$$

in which:

$$a = A_s f_{ds} / \left(0.85 b f'_{dc}\right) \tag{2.5}$$

where A_s is the area of tension reinforcement within the width b, f_{ds} is the dynamic design stress for reinforcement, d is the distance from extreme compression fiber to the centroid of tension reinforcement, a is the depth of equivalent rectangular stress block, b is the width of compression face, f'_{dc} is the dynamic ultimate compressive strength of concrete.

The reinforcement ratio p is defined as:

$$p = A_s / bd \tag{2.6}$$

To prevent sudden compression failures, the reinforcement ratio p must not exceed 0.75 of the ratio p_b which produces balanced conditions at ultimate strength and is given by:

$$p_b = \left(0.85 K_1 f'_{dc} / f_{ds}\right)\left[87000 / \left(87000 + f_{ds}\right)\right] \tag{2.7}$$

where K_1 equals to 0.85 for f'_{dc} up to 27.58 MPa and is reduced 0.05 for each 6.895 MPa in excess of 27.58 MPa.

For a rectangular section of width b with compression reinforcement, the ultimate unit resisting moment is:

$$M_u = \left[\left(A_s - A'_s\right) f_{ds} / b\right] \cdot \left[d - \left(a/2\right)\right] + \left(A'_s\, f_{ds} / b\right)\left(d - d'\right) \tag{2.8}$$

in which:

$$a = \left(A_s - A'_s\right) f_{ds} / \left(0.85 b f'_{dc}\right) \tag{2.9}$$

where A'_s is the area of compression reinforcement within the width b, d' is the distance from extreme compression fiber to the centroid of compression reinforcement, a is the depth of equivalent rectangular stress block.

The reinforcement ratio p' is:

$$p' = A'_s / bd' \tag{2.10}$$

2.4.2.2. Direct shear capacity

Direct shear failure of a member is characterized by the rapid propagation of a vertical crack through the depth of the member. This crack is usually located at the supports where the maximum shear stresses occur. Failure of this type is possible even in members reinforced for diagonal tension.

If the support rotation θ is greater than 2 °, or if a section with any support rotation is in net tension, then the ultimate direct shear capacity of the concrete V_d is zero and diagonal bars are required to take all direct shear.

If the design support rotation θ is less than or equal to 2 °, or if the section with any rotation θ is simply supported (total moment capacity of adjoining elements at the support must be significantly less than the moment capacity of the section being checked for direct shear), then the ultimate direct shear force V_d that can be resisted by the concrete in a slab is:

$$V_d = 0.16 f'_{dc} bd \tag{2.11}$$

The above design procedure is based on the SDOF system analysis. Dimensions of concrete structural element and reinforcement can be calculated effectively, but it is insufficient to carry out damage assessment of RC structural element since only one failure mode (shear or bending) can be considered at one time and such analysis cannot be used to the combined failure mode. Therefore, the mode approximation method is highly recommended to be used in damage assessment of RC structural element.

The shear and bending capacity calculated from above procedure will be used in the derivation of P-I equations in the following chapters. In the rigid-plastic material model, M_u and V_d will be the constant bending and shear strength respectively. In the consideration of nonlinear material model, M_u and V_d will be the maximum bending and shear strength respectively.

2.5. Summary

From the above review on P-I diagram method and design or RC element against blast load, it can be summarized as follows:

- The SDOF system could give out P-I results quickly and P-I diagrams based on such model can be used as a preliminary assessment of structural damage induced by a blast load. However, the SDOF model oversimplifies the structural elements and cannot analyze shear and bending response at the same time.
- The MAM is suitable for analyzing the structural response against blast loading, especially for beam element. It can analyze combined mode so that shear and bending failure can be studied simultaneously. Result of damage

assessment from such method can be generated simply by reading points from P-I diagrams, and it agrees well with that from SDOF system.

- Parameters in the design procedure of RC element can be used in P-I diagrams based on MAM. The procedure can be further simplified by adopting results of the present research work, and can be extended to non-constant parameters easily.

CHAPTER 3

DAMAGE ASSESSMENT FOR UNDERGROUND STRUCTURES AGAINST EXTERNAL BLAST LOAD

3.1. Introduction

The present study extended the damage assessment method, P-I diagrams based on MAM for surface structures by Ma *et al*. (2007) to underground structures by considering soil-structure interactions (SSI) which was proposed by Weidlinger and Hinman (1988). Comparison between the present study and the results of surface structures has been carried out and the simplified SSI effect has been discussed. To verify the continuity of the results for different failure modes, verifications are carried out on some special conditions. Effect of the blast load pressure and duration on the damage of an underground structural element is discussed. A case study is also given to demonstrate the applicability of the proposed method.

3.2. Simplification of soil-structure interaction

Considering a reinforced concrete box-type structure which is buried in soil, the explosion occurs at a certain distance from the structure as schematically shown in Fig. 3-1(a). Taking out one unit strip from the structural wall, the structure can be simplified into a simply supported beam model which is subjected to external blast load as shown in Fig. 3-1(b). The present analysis assumes a rigid-plastic deformation to the beam model and the interaction between soil and structure is considered. The bending strength of the beam model is denoted as M_0, and the transverse shear strength is Q_0, the mass per unit length of the beam model is m. A blast pressure P_i is uniformly distributed over the span of beam. The SSI is simplified as a damping effect as shown in Fig. 3-1(b), which will be derived in detail below. Half of the beam is analyzed because of symmetry. For simplicity, the square yield criterion presented in Fig. 3-2 is used for the bending and shear failure

analysis in the present study. The detailed discussion on the accuracy of the square yield criterion has been given by de Oliveira and Jones (1978).

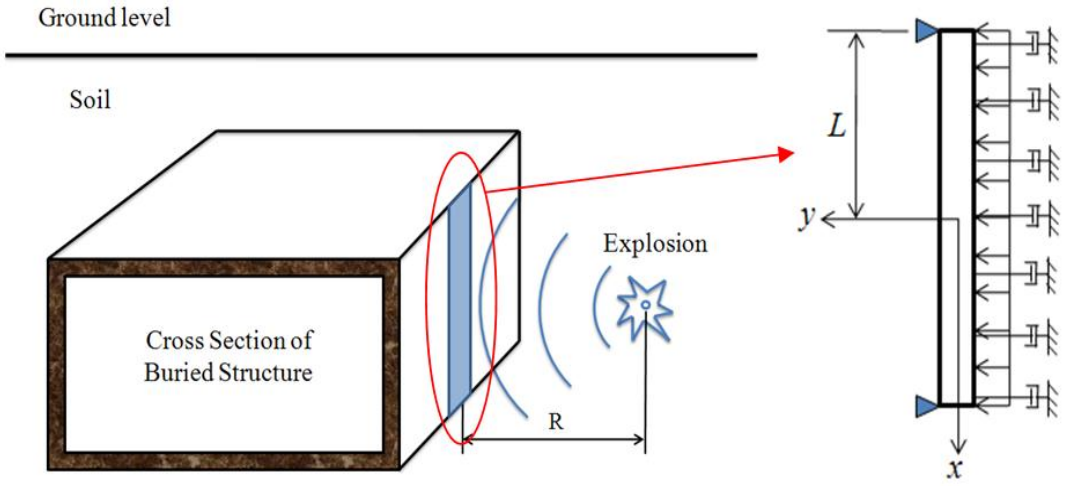

(a) Box-type underground structure (b) A unit strip beam model under external blast load

Fig. 3 - 1 Underground structure and beam model

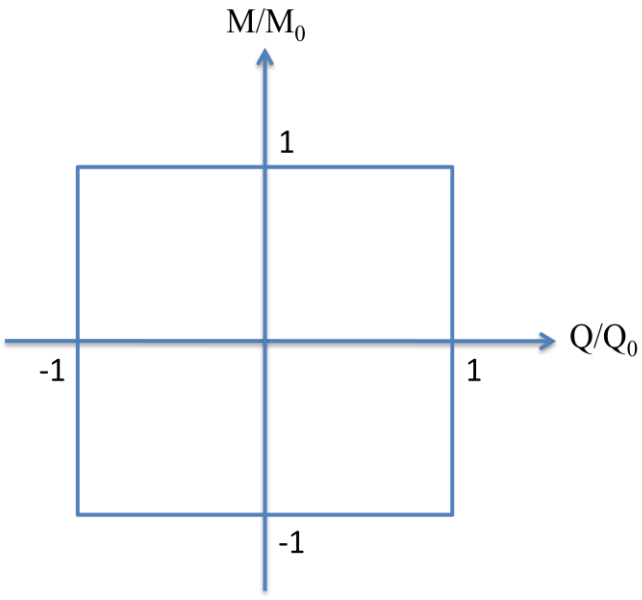

Fig. 3 - 2 Square yield surface

The rotational inertia effect on the beam dynamic failure has been investigated by other researchers (de Oliveira and Jones 1979, Jones and de Oliveira 1979, de Oliveira 1982). It has been verified that the rotational inertia was less important for most practical cases. Considering this effect would make the mathematical derivations much more complex while the reductions in maximum transverse

displacements was less than 10% even in extreme cases as examined by de Oliveira and Jones (1979). The continuity requirements at a discontinuous interface have also been discussed by Symonds (1968) and Jones (1989).

In the analysis of underground structures, SSI may have significant effects on the structural response. Simplification of SSI was discussed by many researchers (Wolf 1985, Krauthammer *et al.* 1986, Weidlinger and Hinman 1988). In the present study, the method by Weidlinger and Hinman (1988) is adopted, and it is briefly introduced below.

The simplest formulation of the free-field stress wave generated by conventional weapons is the semi-empirical formula from TM5-855-1 (1986). It gives the peak amplitude of the stress wave at the arrival time as:

$$P_0 = \beta f\left(\rho c\right)\left(\frac{R}{W^{1/3}}\right)^{-n} \tag{3.1}$$

where P_0 is the peak pressure, β=0.47 for P_0 in MPa, ρc in MPa-s/m, W in N, R in m, f is the coupling factor of the explosive, ρc is the acoustic impedance of soil, R is the distance measured from the center of an explosion to the structure, W is the equivalent TNT weight, and n is an attenuation coefficient. The value of n differs from different soil types which were discussed by Smith and Hetherington (1994). For example, n=3.0 for loose dry sand, n=2.75 for dense sand, and n=1.5 for saturated sandy clay. The decay of the stress wave in time is given by:

$$P\left(R,t\right) = P_0 e^{-t/t_a} \tag{3.2}$$

where t_a=R/c is the arrival time of stress wave and c is the P-wave velocity.

When neglecting the curvature of the wave front, the particle velocity in the free field is approximated by the linear plane wave relation:

$$v\left(R,t\right) = \frac{P\left(R,t\right)}{\rho c} \tag{3.3}$$

Further simplifying the free-field stress by neglecting difference of the distances from the center of explosion to different part of a structure element, the free field pressure at the interface between the soil and structure can be expressed as:

$$\sigma_f = P(R,t) \tag{3.4}$$

The loading experienced by the structural element can be divided into two parts, i.e. σ_f, the free-field pressure at the interface, and σ_i, the interface pressure due to difference between the structural velocity $\dot{u}(t)$, and the soil velocity $v(t)$.

The interface pressure is defined as:

$$\sigma_i = \rho c(v - \dot{u}) \tag{3.5}$$

Thus the total interaction load is:

$$P_i = \sigma_f + \sigma_i = \sigma_f + \rho c(v - \dot{u}) \tag{3.6}$$

By considering Eqs. (3.3) and (3.4) and eliminating the velocity term *v(t)* in Eq. (3.6), Eq. (3.6) transforms into:

$$P_i = 2\sigma_f - (\rho c)\dot{u} \tag{3.7}$$

In the current analysis, Eq. (3.7) is transformed to:

$$P_i = p_0 - (\rho c)\dot{u} = p_0 - C\dot{y} \tag{3.8}$$

where p_0 is the constant pressure in blast load duration acting on beam element, C is the damping coefficient, and $\dot{y}$ is the structural velocity.

Therefore the SSI is simplified as a damping coefficient. Because the soil at interface can only transmit compression, the damping coefficient will equal to zero when $2\sigma_f < (\rho c)\dot{u}$ in Eq. (3.7). Under the case of a real blast load, the SSI becomes zero before the blast duration t_d, since the blast pressure decrease with time. While in the present study, the pressure on structural element p_0 is assumed as a constant within the blast duration, therefore $C=0$ only at $t=t_d$.

The simplification of SSI is based on the elastic wave propagation theory which limits the application of current results within moderate and far-range underground explosion cases, and the close-in range cases with low charge weight. The reflected pressure is obtained from TM5-1300 (1990) directly, and the SSI is considered only when structural element starts to response. The actual load on element in a real case should be further studied considering non-elastic wave propagation theories and a complicated soil material model, and it is not in the scope of current analysis.

3.3. Failure criteria and structural failure assessment

According to the previous results done by other researchers (Yu and Jones 1991, Krauthammer 1998) for simply supported or clamped beams, the ratio of centerline-deflection to half-span is used as the criterion of the bending failure, since the largest ductile plastic deformation usually appears at the mid-span due to bending effects. The maximum transverse displacement due to bending, and the direct shear failure at the element supports can be expressed as follow:

$$\begin{cases} y_m = L\beta_0 \\ y_s = \gamma_v \delta h \end{cases} \tag{3.9}$$

where y_m is the maximum transverse displacement due to bending, L is the half length of the beam model, β_0 is the ratio of centerline deflection to the half span, y_s is the maximum transverse displacement due to direct shear, γ_v is the average shear strain, δ is the material parameter obtained from experimental results, h is the depth of the structural element. Normally δ varies in 0.6-0.866 for different materials. In the present study, δ is defined as 0.8 which is the same as that used by Ma *et al*. (2007) for surface structures.

Table 3-1 shows different damage level under empirical bending and shear failure criteria (Krauthammer 1998). The criteria are applied to reinforced concrete structure element.

Table 3 - 1 Different damage level under empirical bending and shear failure criteria

Type of failure	Criteria	Light Damage (%)	Moderate Damage (%)	Severe Damage (%)
Shear	Average shear strain γ_v	1	2	3
Bending	Ratio of centerline deflection to half span β_0	2.5	6	12.5

For convenience in performing analytical failure analysis of underground structures, a rectangular pulse load with equivalent pressure and impulse as given in the semi-empirical Eq. (3.1) is used to represent blast load, where the pulse shape effect is neglected. The rectangular pulse load can be expressed by a side-on blast load p_0, and blast load duration t_d. The pulse shape effect has been discussed by Youngdahl (1970, 1971), Li and Meng (2002b), and Li and Jones (2005b) which can be eliminated by using the Youngdahl's (1971) correlation parameter method. It has been validated that the pulse shape effect to the P-I diagrams is minor especially in the quasi-static load region and the impulsive load region.

The damping effect of SSI is assumed to exist only when $t<t_d$. This assumption is discussed in the following section. The governing equation of the element is expressed as:

$$\frac{\partial Q}{\partial x} = -P_i + m\ddot{y} \tag{3.10}$$

When substitute Eq. (3.8) into Eq. (3.10), Eq. (3.10) can be rewritten as:

$$\frac{\partial Q}{\partial x} = -p_0 + m\ddot{y} + C\dot{y} \tag{3.11}$$

where Q is the transverse shear force, x is the abscissa on the element, m is the mass per unit length of the element, $\ddot{y}$ is the acceleration of structural element.

Similar to the analysis for surface structures, there are totally five possible transverse velocity profiles which include one shear failure mode, two bending failure modes, and two combined failure modes, as illustrated in Fig. 3-3. A dimensionless strength ratio is introduced as below:

$$\nu = \frac{Q_0 L}{2M_0} \tag{3.12}$$

where Q_0 and M_0 are respectively the shear and bending strength of the element.

Table 3-2 shows the velocity profile of different phases under different modes. Mode 1 contains shear failure only. Mode 2 is for simple bending failure which has a plastic hinge at the center of the element. Mode 3 can be considered as a combination of mode 1 and mode 2. Mode 4 is the complex bending failure mode which has a plastic zone at the middle of the element. And mode 5 is the combination of mode 1 and mode 4. Differentiation of the five failure modes is the same as that for surface structures. However, the SSI has been incorporated in the derivations. The x-axis starts at the mid of the beam and only half of the beam is considered due to symmetry of the structure and load as seen in Fig. 3-1(b).

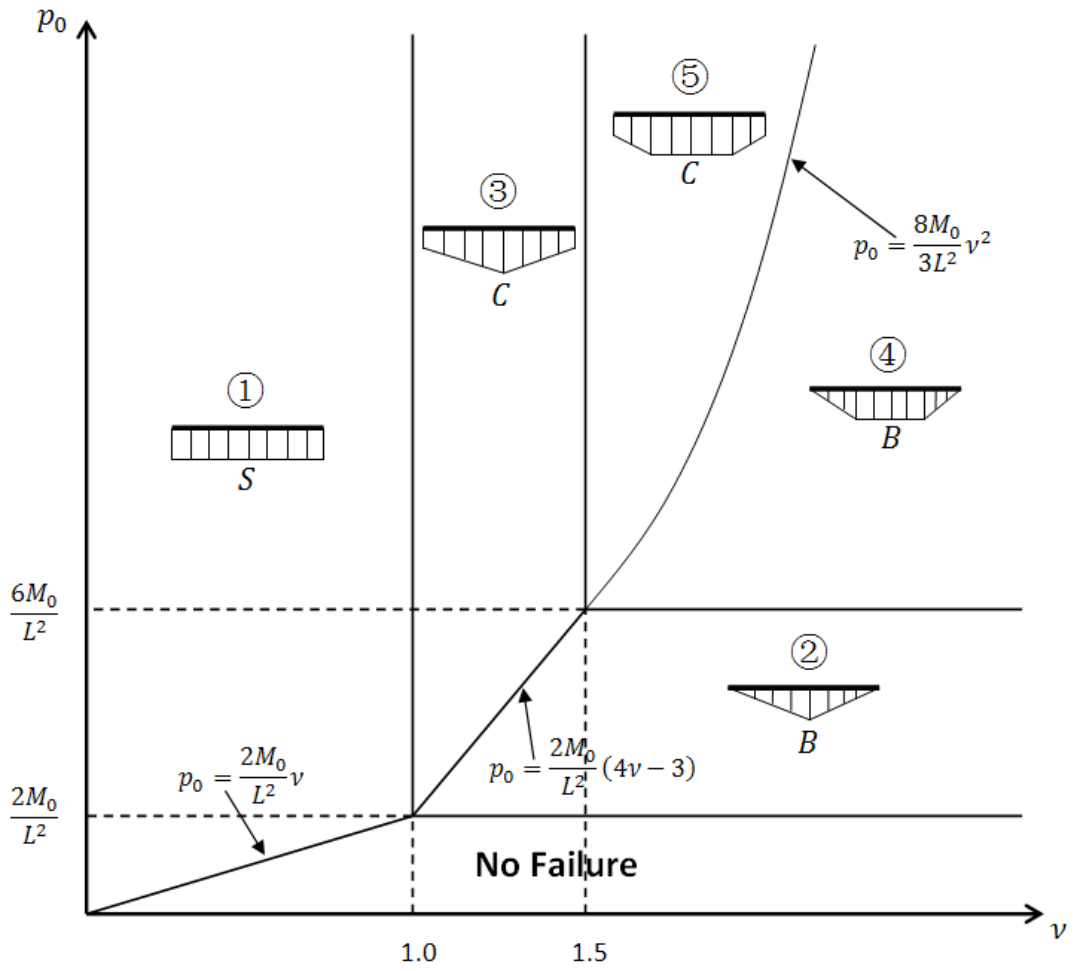

S: Shear failure; B: Bending failure; C: Combined failure

Fig. 3 - 3 Distribution of failure modes

Table 3 - 2 Velocity profile

	Mode 1	Mode 2	Mode 3	Mode 4	Mode 5
Phase 1			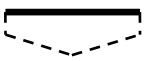	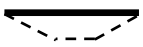	
Phase 2		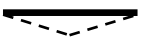	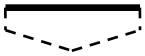	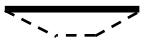	
Phase 3	N.A.	N.A.			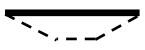
Phase 4	N.A.	N.A.	N.A.	N.A.	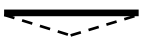

Mode 1. $0 < \nu \le 1$ and $p_0 \ge \frac{2M_0}{L^2}\nu$, shear failure mode.

The shear failure mode provides that direct shear failure occurs at the two supports where carries the maximum shear force. Bending deformation will not occur in this case. The shear failure occurs only when the parameter υ is smaller than one which indicates a very low shear-to-bending strength ratio.

There are totally two phases in this mode including a loading phase (phase 1) and a post-loading phase (phase 2) which are assumed to end at t_d and t_f respectively.

In phase 1, the governing equation is:

$$\frac{\partial Q}{\partial x} = -p_0 + m\ddot{y}_s + C\dot{y}_s \tag{3.13}$$

The boundary and initial conditions are:

$$Q(x=0)=0, \quad Q(x=L)=-Q_0 \tag{3.14}$$

$$\dot{y}_s(t=0)=0, \quad y_s(t=0)=0 \tag{3.15}$$

By integrating Eq. (3.13) with respect to x and substituting Eq. (3.14), Q can be solved. Then integrates the equation of Q with respect to time twice, the expressions of structural displacement, velocity, and acceleration can be obtained. At the end of phase 1 when $t=t_d$, the maximum displacement $y_s(t_d)$ and the velocity of the element $\dot{y}_s(t_d)$ are solved.

In phase 2, the governing equation becomes:

$$\frac{\partial Q}{\partial x} = m\ddot{y}_s \tag{3.16}$$

By using Eq. (3.14) as the boundary condition, $y_s(t_d)$ and $\dot{y}_s(t_d)$ as the initial conditions for phase 2 motion, Eq. (3.16) can be solved under the same procedure when solve Eq. (3.13) in phase 1. When the structural velocity equals to zero, the motion termination time t_f of phase 2 is determined as:

$$t_f = \frac{m\left(1-e^{\frac{-Ct_d}{m}}\right)\left(p_0 L - Q_0\right)}{Q_0 C} + t_d \tag{3.17}$$

The final transverse displacement due to shear is derived as:

$$y_s\left(t_f\right) = -\frac{Q_0\left(t_f - t_d\right)^2}{2mL} + \dot{y}_s\left(t_d\right)\cdot\left(t_f - t_d\right) + y_s\left(t_d\right) \tag{3.18}$$

Mode 2. $1 < \nu \le 1.5$ and $\frac{2M_0}{L^2} < p_0 \le \frac{2M_0}{L^2}\left(4\nu - 3\right)$, or $\nu \ge 1.5$ and $\frac{2M_0}{L^2} < p_0 \le \frac{6M_0}{L^2}$, bending failure mode.

There are also two phases in this mode including a loading phase (phase 1) and a post-loading phase (phase 2) which end at t_d and t_f respectively, as given in Table 3-2.

In phase 1, the governing equation is:

$$\frac{\partial Q}{\partial x} = -p_0 + m\ddot{y}_m\left(1-\frac{x}{L}\right) + C\dot{y}_m\left(1-\frac{x}{L}\right) \tag{3.19}$$

The boundary and initial conditions are:

$$Q\left(x=0\right)=0, \quad Q\left(x=L\right)=-Q_0, \quad M\left(x=0\right)=M_0, \quad M\left(x=L\right)=0 \tag{3.20}$$

$$\ddot{y}_m\left(t=0\right)=0, \quad y_m\left(t=0\right)=0 \tag{3.21}$$

By integrating Eq. (3.19) with respect to time, at the end of phase 1 when $t=t_d$, the maximum displacement $y_m\left(t_d\right)$ and the velocity of the element due to bending deformation $\dot{y}_m\left(t_d\right)$ are solved.

In phase 2, the governing equation changes to:

$$\frac{\partial Q}{\partial x} = m\ddot{y}_m\left(1-\frac{x}{L}\right) \tag{3.22}$$

By using Eq. (3.20) as the boundary condition and $y_m(t_d)$ and $\dot{y}_m(t_d)$ as the initial conditions, the termination time t_f of phase 2 can be solved as:

$$t_f = \frac{m\left(1-e^{\frac{-Ct_d}{m}}\right)\left(p_0 L - M_0\right)}{2M_0 C} + t_d \tag{3.23}$$

The final bending displacement is then derived as:

$$y_m\left(t_f\right) = -\frac{3M_0\left(t_f - t_d\right)^2}{2mL^2} + \dot{y}_m\left(t_d\right)\cdot\left(t_f - t_d\right) + y_m\left(t_d\right) \tag{3.24}$$

When $t=t_f$, the velocity of the beam motion becomes zero.

Mode 3. $1<\nu\le 1.5$ and $p_0 > \frac{2M_0}{L^2}(4\nu-3)$, combined failure mode.

Mode 3 is the combination of mode 1 and mode 2. Both shear failure and bending failure occur to the element. The shear failure occurs at the two supports while the bending failure induces plastic hinge at the mid-span of the element. Deformation of the element includes one loading phase (phase 1) and two post-loading phases (phase 2 and phase 3) which are assumed to end at t_d, t_s, and t_f respectively.

In phase 1, the governing equation is given by:

$$\frac{\partial Q}{\partial x} = -p_0 + m\ddot{y}_s + m\left(\ddot{y}_m - \ddot{y}_s\right)\left(1-\frac{x}{L}\right) + C\dot{y}_s + C\left(\dot{y}_m - \dot{y}_s\right)\left(1-\frac{x}{L}\right) \tag{3.25}$$

with the same boundary and initial conditions given in Eqs. (3.20), (3.15) and (3.21).

Similar to mode 1 and mode 2, at the end of phase 1 when $t=t_d$, the maximum displacement and velocity of the element due to shear and bending deformation can be determined.

In phase 2, the governing equation is:

$$\frac{\partial Q}{\partial x} = m\ddot{y}_s + m\left(\ddot{y}_m - \ddot{y}_s\right)\left(1-\frac{x}{L}\right) \tag{3.26}$$

The boundary conditions are still the same as the first phase, while the final velocities and displacements in phase 1 are used as the initial condition of phase 2 motion. Solving Eq. (3.26), at the end of phase 2 when $t=t_s$, the displacement due to shear stops, while the bending displacement remains to the next phase motion. The ending time and maximum displacement of shear is derived as below, and the maximum displacement and velocity due to bending motion can then be solved.

$$t_s = \frac{-6t_d M_0 + 4t_d Q_0 L + mL^2 \cdot \dot{y}_s(t_d)}{2(2Q_0 L - 3M_0)} \tag{3.27}$$

$$y_s(t_s) = \frac{(3M_0 - 2Q_0 L)(t_s - t_d)^2}{mL^2} + \dot{y}_s(t_d)\cdot(t_s - t_d) + y_s(t_d) \tag{3.28}$$

where t_s is determined when the shear velocity becomes zero when the shear deformation stops.

In phase 3, only the bending failure induced motion remains, and the governing equation is the same as Eq. (3.22). Similarly, the motion termination time t_f and the final displacement $y_m(t_f)$ are determined as:

$$t_f = \frac{\dot{y}_m(t_s)\cdot mL^2}{3M_0} \tag{3.29}$$

$$y_m(t_f) = -\frac{3M_0(t_f - t_s)^2}{2mL^2} + \dot{y}_m(t_s)\cdot(t_f - t_s) + y_m(t_s) \tag{3.30}$$

Mode 4. $1.5 \le \nu$ and $\frac{6M_0}{L^2} < p_0 \le \frac{8M_0}{3L^2}\nu^2$, bending failure mode.

The bending failure with a plateau deformation at the central portion of the element may occur when the blast load is sufficiently intensive. Different from mode 2, two plastic hinges are generated offset from the mid-span of the element. Three phases including one loading phase (phase 1) and two post-loading phases (phase 2 and phase 3) which end at t_d, t_1, and t_f respectively are considered.

In phase 1, the governing equation is expressed as:

$$\frac{\partial Q}{\partial x} = -p_0 + m\ddot{y}_m\left(\frac{L-x}{L-\xi_0}\right) + C\dot{y}_m\left(\frac{L-x}{L-\xi_0}\right) \tag{3.31}$$

where ξ_0 is the distance of the plastic hinge from the mid-span.

The boundary conditions are as follows:

$$Q(x=\xi_0)=0, Q(x=L)=-Q_0, M(x=\xi_0)=M_0, M(x=L)=0 \tag{3.32}$$

And the initial conditions are the same as Eq. (3.21). Thus Eqs. (3.32) and (3.21) are used to determine the integral constants when Eq. (3.31) is integrated.

At the end of the loading period, when $t=t_d$, the plastic hinge location indicated by ξ_0 is derived as:

$$\xi_0 = L - \frac{\sqrt{6p_0M_0}}{p_0} \tag{3.33}$$

And the displacement and velocity of the beam model due to bending at the end of phase 1 are then obtained.

In phase 2, the blast load has been released, and the velocity profile is the same as that in phase 1. However, the two plastic hinges start to move toward the mid-span of the element. At the end of phase 2, the two plastic hinges meet at the mid-span and phase 3 motion then starts. The governing equation of the phase 2 motion is:

$$\frac{\partial Q}{\partial x} = m\ddot{y}_m\left(\frac{L-x}{L-\xi}\right) \tag{3.34}$$

where ξ is the half length of plastic zone which is a function of time.

By considering the boundary condition given as:

$$Q(x=\xi)=0, Q(x=L)=-Q_0, M(x=\xi)=M_0, M(x=L)=0 \tag{3.35}$$

The final displacement and velocity of the first phase as the initial conditions, Eq. (3.34) of phase 2 motion can be solved. The termination time t_1 of phase 2 is given by:

$$t_1 = \frac{\left(1 - e^{\frac{-Ct_d}{m}}\right) m p_0 L^2}{6CM_0} + \frac{m}{C}\left(e^{\frac{-Ct_d}{m}} - 1\right) + t_d \tag{3.36}$$

In phase 3, the governing equation is the same as Eq. (3.22) and it can be solved in a similar way as it has been done for mode 2 and mode 3.

At the end of phase 3, when $t=t_f$, the motion stops and the final time t_f is determined as:

$$t_f = \frac{p_0\left(1 - e^{\frac{-Ct_d}{m}}\right) mL^2}{3M_0} + t_1 \tag{3.37}$$

The final bending displacement y_m at the mid-span when $t= t_f$ is given by:

$$y_m\left(t_f\right) = \frac{-3M_0\left(t_f - t_1\right)}{2mL^2} + \dot{y}_m\left(t_1\right)\cdot\left(t_f - t_1\right) + y_m\left(t_1\right) \tag{3.38}$$

Mode 5. $1.5 \le \nu$ and $p_0 > \frac{8M_0}{3L^2}\nu^2$, combined failure mode.

Mode 5 is the most complicated mode which combined mode 1 and mode 4. There are altogether four phases including one loading phase (phase 1) and three post-loading phases (phase 2, phase 3, and phase 4). They are assumed to end at t_d, t_s, t_1, and t_f respectively.

In phase 1, both shear and bending deformation occur. The governing equation is:

$$\frac{\partial Q}{\partial x} = -p_0 + m\ddot{y}_s + m\left(\ddot{y}_m - \ddot{y}_s\right)\left(\frac{L-x}{L-\xi_0}\right) + C\dot{y}_s + C\left(\dot{y}_m - \dot{y}_s\right)\left(\frac{L-x}{L-\xi_0}\right) \tag{3.39}$$

The boundary conditions are the same as Eq. (3.32), and the initial conditions of mode 1 and mode 4 are also combined as:

$$\dot{y}_s\left(t=0\right)=0, \quad y_s\left(t=0\right)=0, \quad \dot{y}_m\left(t=0\right)=0, \quad y_m\left(t=0\right)=0 \tag{3.40}$$

At the end of phase 1 when $t=t_d$, the plastic hinge location ξ_0 is shown in Eq. (3.41) below, and the final displacement and velocity of phase 1 due to shear and bending deformation can then be derived.

$$\xi_0 = L - \frac{3M_0}{Q_0} \tag{3.41}$$

In phase 2, the velocity profile is the same as that in phase 1, while the shear deformation tends to stop. The governing equation becomes:

$$\frac{\partial Q}{\partial x} = m\ddot{y}_s + m\left(\ddot{y}_m - \ddot{y}_s\right)\left(\frac{L-x}{L-\xi}\right) \tag{3.42}$$

Based on the same boundary condition given in Eq. (3.32) and the final displacement and velocity of phase 1, Eq. (3.42) can then be solved. At the end of phase 2 when $t=t_s$, the shear deformation stops. The termination time and the final shear displacement of phase 2 are given by:

$$t_s = \frac{m\left(1-e^{\frac{-Ct_d}{m}}\right)\left(3p_0M_0 - 2Q_0^2\right) + 2Ct_dQ_0^2}{2CQ_0^2} \tag{3.43}$$

$$y_s\left(t_s\right) = \frac{-Q_0^2\left(t_s - t_d\right)^2}{3mM_0} + \dot{y}_s\left(t_d\right)\cdot\left(t_s - t_d\right) + y_s\left(t_d\right) \tag{3.44}$$

In phase 3, the bending deformation remains the same velocity profile as that in phase 2 of mode 4, and the two plastic hinges start to move toward the mid-span of the element. The governing equation is the same as Eq. (3.34). Similarly, at the end of phase 3, when $t=t_1$, the two plastic hinges coincides at the mid-span, and:

$$t_1 = \left(L^2 - \frac{6M_0}{p_0}\right)\cdot\frac{mp_0\left(1-e^{\frac{-Ct_d}{m}}\right)}{6CM_0} + t_s \tag{3.45}$$

Similarly, in phase 4 of mode 5, the governing equation is the same as Eq. (3.22). At the end of phase 4 when $t=t_f$ the motion stops and:

$$t_f = \frac{mp_0L^2\left(1-e^{\frac{-Ct_d}{m}}\right)}{3CM_0} + t_1 \tag{3.46}$$

The final bending displacement is:

$$y_m\left(t_f\right) = \frac{-3M_0\left(t_f - t_1\right)^2}{2mL^2} + \dot{y}_m\left(t_1\right)\cdot\left(t_f - t_1\right) + y_m\left(t_1\right) \tag{3.47}$$

3.4. P-I diagrams and discussions

In each of the five modes discussed previously, the final shear displacement y_s for the direct shear failure and the final bending displacement y_m for bending failure, or both for combined failure can be derived. Given a certain failure criterion in terms of the maximum shear and bending displacements, P-I diagrams for different modes can then be obtained. Although the five failure modes and the analysis of the structural response are very similar to that done for the surface structures (Ma *et al*. 2007), the present study focuses on the damage assessment for underground structures against external blast load.

Define dimensionless variables P^* and I^* of the pressure and impulse of a blast load as:

$$\begin{cases} P^* = \dfrac{p_0L^2}{M_0} \\ I^* = \dfrac{Ct_dP^*}{m} \end{cases} \tag{3.48}$$

From the equations for final displacements induced by shear and bending failure, the P-I equations can be represented in unified forms as follows:

$$\begin{cases} S\left(P^*, I^*\right) = \gamma_v\delta h \\ B\left(P^*, I^*\right) = L\beta_0 \end{cases} \tag{3.49}$$

where the shear and bending failure criteria given respectively in Eq. (3.9) are used.

S(P,I*)* and *B(P*,I*)* are implicit expressions with respect to the normalized pressure and impulse for shear and bending failure mode respectively. *S(P*,I*)* equals to the right part of Eqs. (3.18), (3.28), or (3.44) as the shear failure P-I equation, and *B(P*,I*)* equals to the right part of Eqs. (3.24), (3.30), (3.38), or (3.47) to represent the bending failure P-I equation.

3.4.1. Boundaries between different failure modes

By determining relevant parameters, the P-I diagrams can be plotted for all five failure modes. Differentiation between different modes given in Fig. 3-3 is determined by the requirement of the motion initiation. For example, for mode 1, the acceleration induced by the shear force at the supports should be larger than zero, and the maximum bending moment should be smaller than the bending strength of the element. Therefore $p_0 \geq \frac{2M_0}{L^2}\nu$ and $0<\nu<1$ are derived, respectively. For mode 2, the initial acceleration due to bending should be larger than zero, while the maximum shear force should be less than the shear strength. So $1\leq\nu\leq1.5$ and $\frac{2M_0}{L^2}\leq p_0\leq\frac{2M_0}{L^2}(4\nu-3)$, or $\nu\geq1.5$ and $\frac{2M_0}{L^2}\leq p_0\leq\frac{6M_0}{L^2}$ are required. Similarly, all the boundaries between different failure modes can be determined.

Three typical P-I diagrams of shear and bending failures are plotted in Fig. 3-4.

1) When *υ=0.8*, which is in the range of *υ<1*, only shear failure exists as shown in Fig. 3-4(a) (mode 1). Region A and region B indicate shear failure and no failure respectively.
2) As shown in Fig. 3-4(b) when *υ=1.2*, which satisfies $1\leq\nu\leq1.5$ and $p_0>\frac{2M_0}{L^2}(4\nu-3)$, the element fails with mode 3, which is a combination of mode 1 and mode 2. Two P-I diagrams, for shear failure and bending failure respectively, are plotted based on the failure criteria given in Eqs. (3.9). There are four regions in this case which indicate four different failure types of the element. In region A, which corresponds to larger pressure and impulse, combined failure occurs since both the maximum shear displacement and the

maximum bending displacement exceed the failure threshold given by the shear and failure criteria. In region D, the pair of pressure and impulse locates above the shear failure diagram but below the bending failure diagram, which indicates only shear failure occurred to the element. Similarly, in region B, the pair of pressure and impulse exceeds the bending failure diagram while it is below the shear failure diagram, which defines bending failure for the element. In region C, the element remains safe due to the pressure and impulse pair is below both diagrams.

3) When $\upsilon=1.8$, which is in the range of $\upsilon>1.5$, mode 4 and mode 5 may occur. Fig. 3-4(c) shows the P-I diagrams of mode 5 which is similar to mode 2 with 4 different regions. It is seen that shear failure occurs when the pressure reaches a certain level. The P-I diagram for shear failure is zoomed up in Fig. 3-4(d).

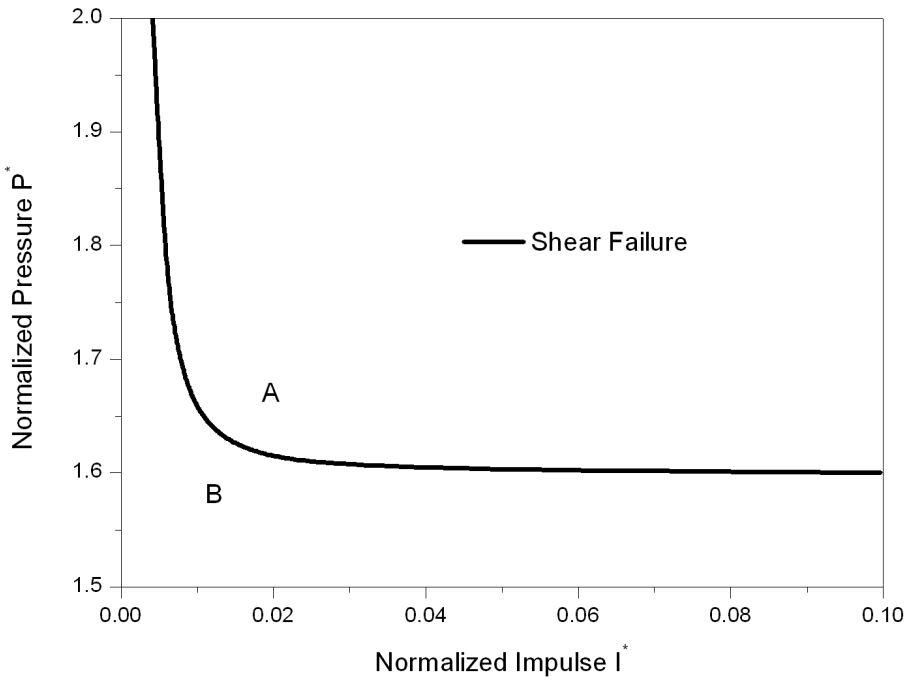

(a) Typical failure mode $\upsilon < 1.0$ (mode 1)

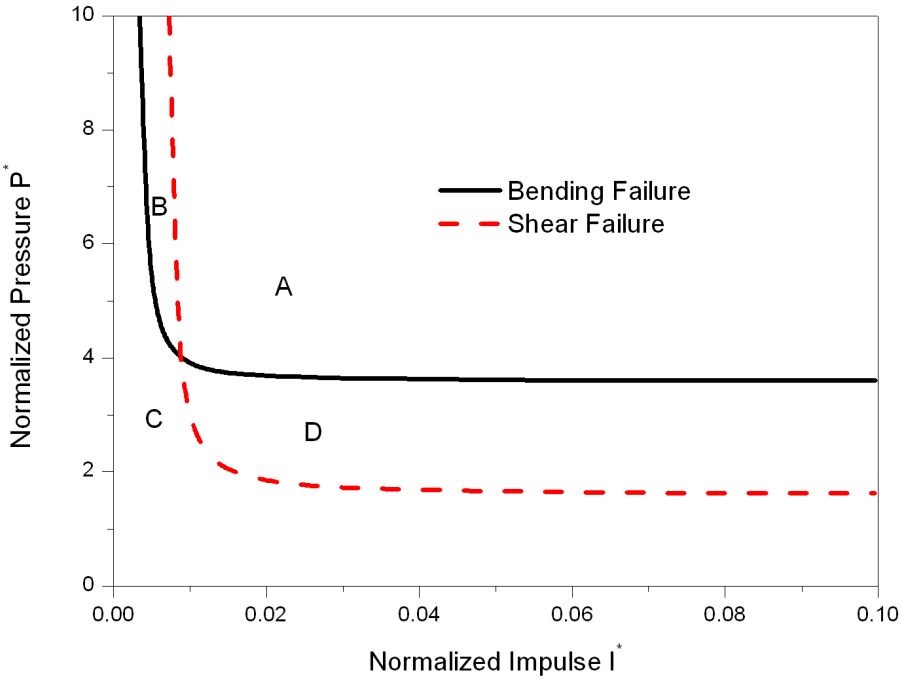

(b) Typical failure mode $1 \leq \upsilon \leq 1.5$ (mode 3)

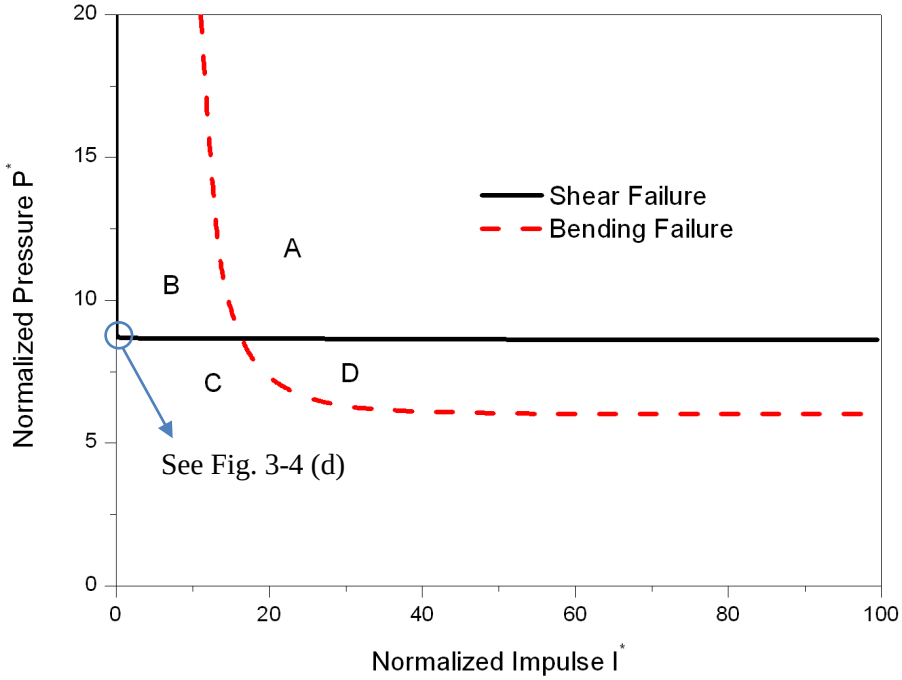

(c) Typical failure mode $1.5 < \upsilon$ (mode 5)

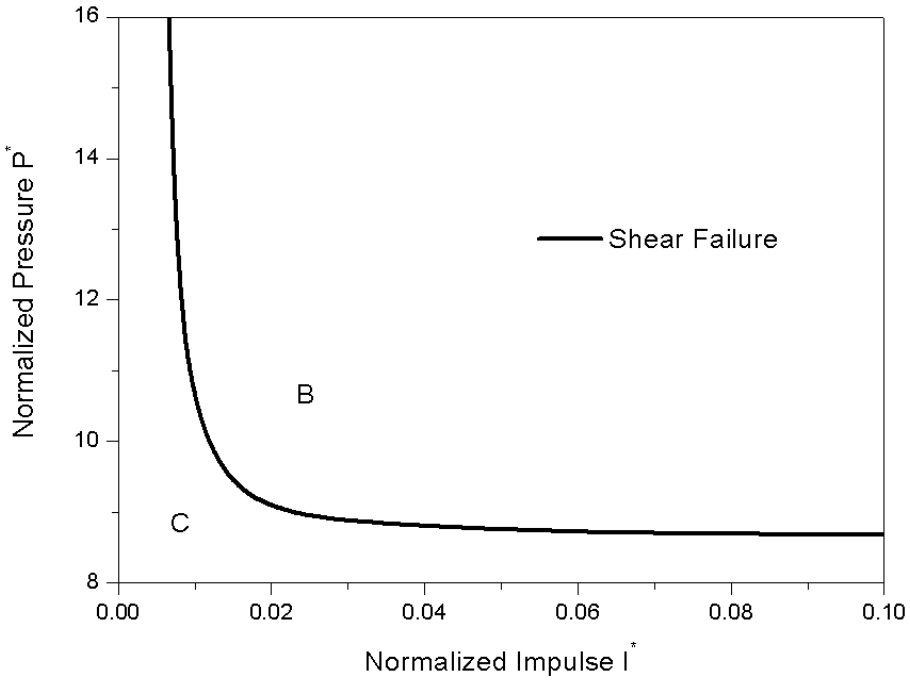

(d) Typical failure mode $1.5 < \upsilon$ (mode 5 shear failure)

Fig. 3 - 4 Typical failure modes for different value of υ

3.4.2. Damping effect due to soil-structural interaction

Different soil has different acoustic impendence, and the damping effect due to SSI is investigated as below. Considering three different cases with dry sand and backfills (ρc=*0.497* MPa s/m), dense sands (ρc=*0.995* MPa s/m), and saturated sandy clay (ρc=*2.941* MPa s/m) respectively, the P-I diagrams for shear and bending failure modes are plotted and compared in Fig. 3-5. It shows that the saturated sandy clay gives higher P-I diagrams for both shear and bending failure, which indicates that the acoustic impendence has significant effect on the structural failure.

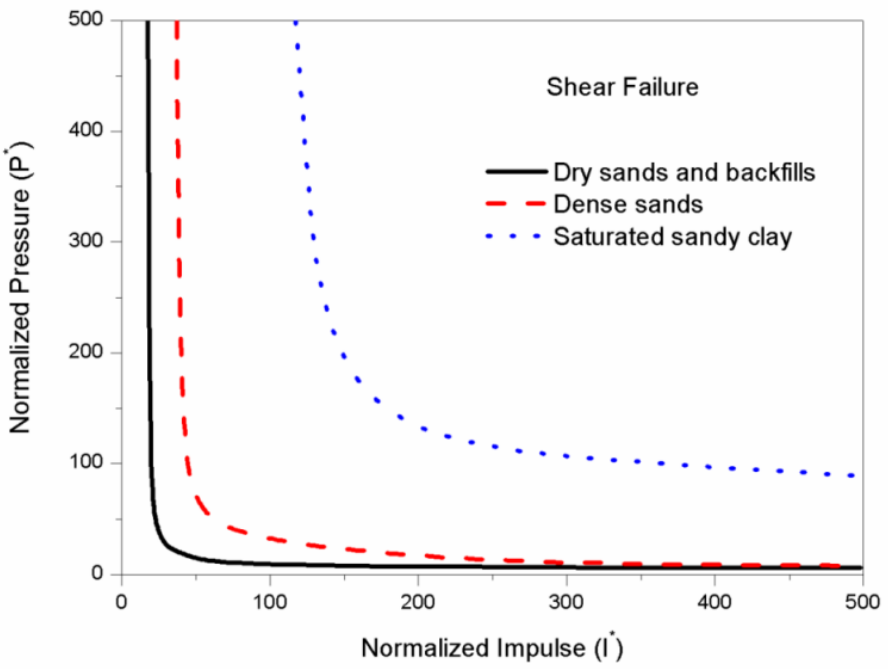

(a) Shear failure in different soils

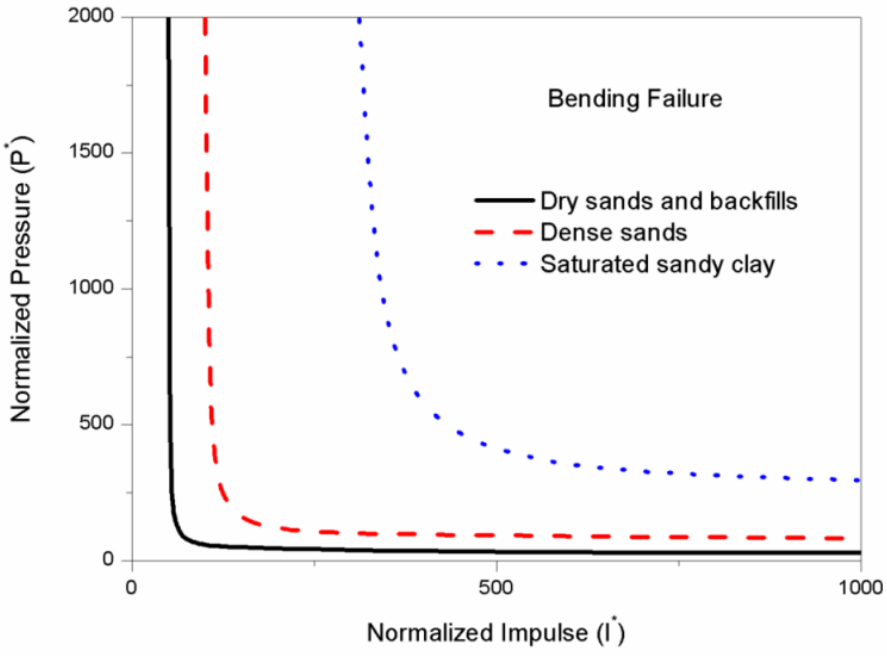

(b) Bending failure in different soils

Fig. 3 - 5 Shear and bending failures in different soils

Comparison is also done to the damage assessment results for surface structures when the damping coefficient is set sufficient small (for example, ρc=10 Pa s/m). The comparison is done for all the five failure modes, and here mode 3 is chosen as an example, as shown in Fig. 3-6. It can be seen that both shear failure and bending

failure diagrams match well with those for surface structures. It verifies that the present P-I diagrams are valid and the P-I diagram method suggested by Ma *et al*. (2007) has been successfully extended to damage assessment for underground structures when the decoupling of SSI is considered. It should be noted that a zero damping coefficient is not allowed in the P-I equations in the present study, however, the present results can be applied to damage assessment for surface structures by assigning a sufficient small damping coefficient in the equations.

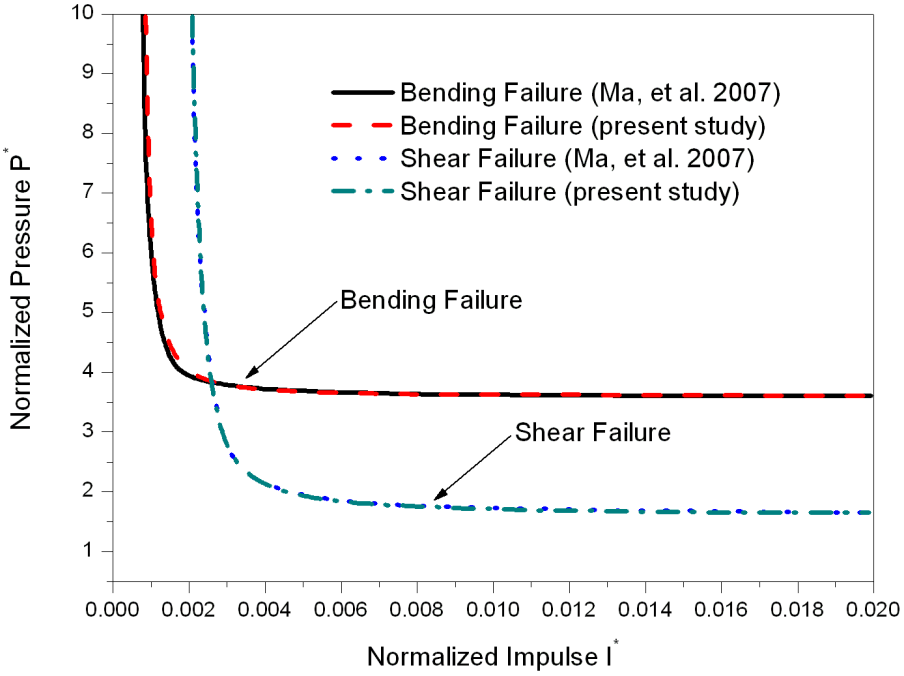

Fig. 3 - 6 Comparison with blast result of surface structure

3.4.3. Verification of continuity

Since different failure modes give different final shear and/or bending displacement, the solutions at the boundaries between different modes in Fig. 3-3 should be continuous. It means that two modes should give the same P-I diagram at their sharing boundary line. To verify the continuity of the equations, three checking points as shown in Fig. 3-3 have been examined. CP1 ($p_0 = \frac{3.60M_0}{L^2}$ and $\nu = 1.2$) is shared by mode 2 and mode 3, CP2 ($p_0 = \frac{6.00M_0}{L^2}$ and $\nu = 1.5$) is shared by mode 2, mode 3, mode 4 and mode 5, and CP3 ($p_0 = \frac{8.64M_0}{L^2}$ and $\nu = 1.8$) is shared by

mode 4 and mode 5. The verification results are given in Table 3-3 which indicate that the results of mode 2, 3, 4, and 5 match very well at the three checking points.

Table 3 - 3 Continuity verification

	$\nu = 1.2$		$\nu = 1.5$		$\nu = 1.8$	
Mode	P^*	I^*	P^*	I^*	P^*	I^*
2	3.6	50606	6.0	20241	N.A.	N.A.
3	N.A.	N.A.	6.0	20241	8.4	77
4	3.6	50606	6.0	20241	N.A.	N.A.
5	N.A.	N.A.	6.0	20241	8.4	77

3.4.4. Pressure and impulse effects

When the mechanical parameters of the element are given, the pressure and impulse will have different effects on the maximum displacement due to shear or bending deformation. Fig. 3-7 takes mode 3 as an example and the surrounding soil is dry sand and backfills. It shows that the tendency of the shear and bending displacements vary with the normalized pressure and impulse. The maximum displacement due to shear failure is much more sensitive to the pressure than the maximum bending displacement as shown in Fig. 3-7(a). However, the influence of the normalized impulse on both of the maximum shear and bending displacements is very similar. The maximum shear and bending displacements increase almost linearly with the increase of the normalized impulse as shown in Fig. 3-7(b).

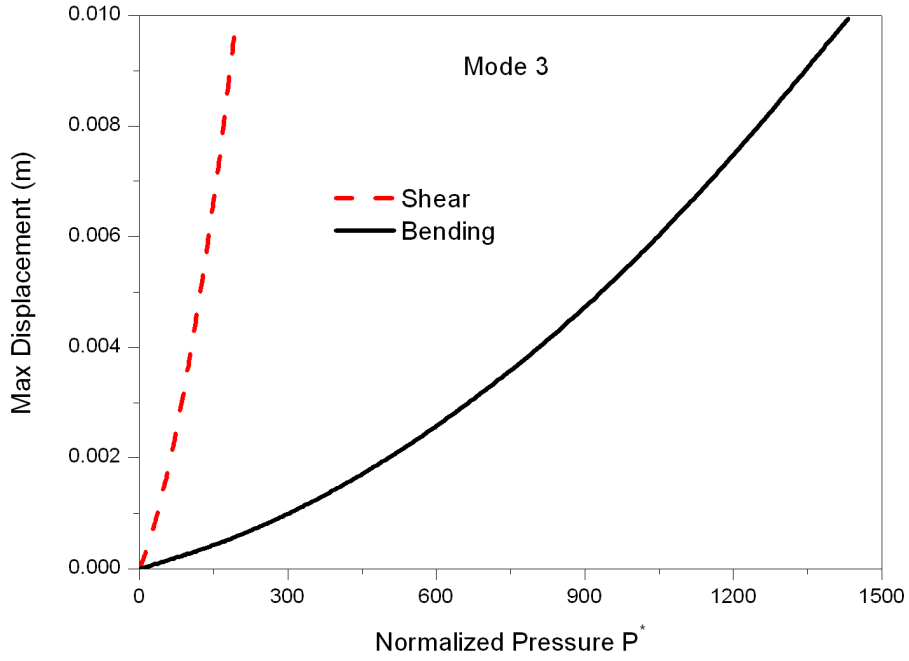

(a) Maximum displacement versus normalized pressure

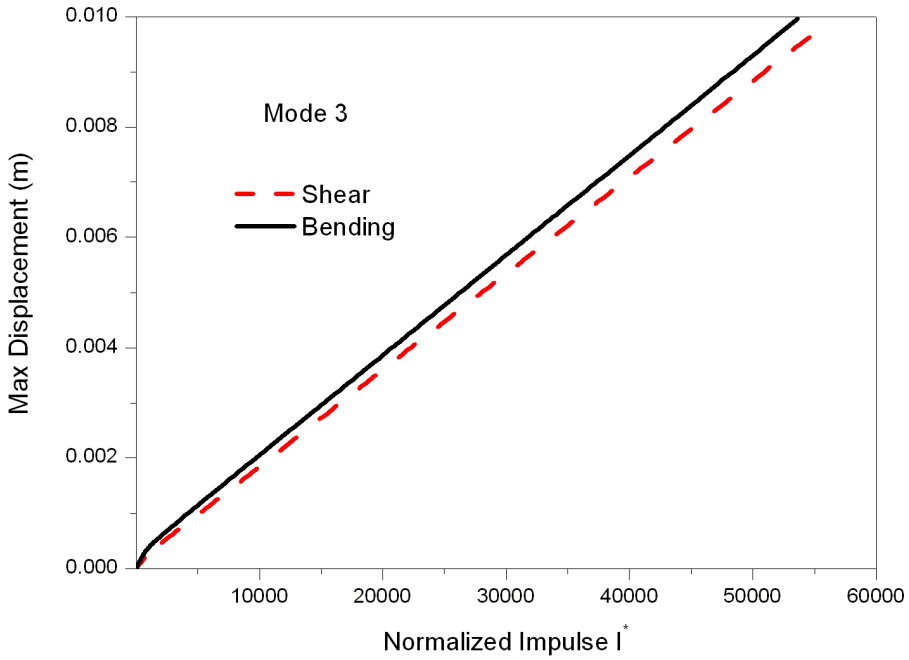

(b) Maximum displacement versus normalized impulse

Fig. 3 - 7 Pressure and impulse effects

3.4.5. Further discussions

Researchers sometimes use a clamped beam model for underground structure analysis. The difference of the P-I diagrams between a simple supported beam and a fixed beam has been discussed for surface structures by Ma *et al*. (2007). Damage

assessment for underground structures by simplifying the structure to be simply supported gives a conservative analysis and it will lead to a safer design of the underground structures. By using similar derivations as given in the present study, the results of a fixed beam model can also be obtained correspondingly.

When the underground structures are in a middle or far range from the explosion, the blast wave acting on the structures is very close to a plane wave. In a close-in range, the load acting on the beam model can be simplified as a cycloidally, exponentially, sine-shapely, or linearly descending pressure from the beam center to the two ends. Again, using a uniformly distributed load with a consistent peak pressure will give more conservative analysis results which ensure a safer design of underground structures. Furthermore, the pulse shape effect produces error less than 10% (Oliveira and Jones 1979).

In the present study, the damping effect is assumed to exist in phase 1 of all the five modes, but it disappears in the following phases. This is reasonable because as soon as the blast load is released, the interaction between the surrounding soil and the structure becomes minor. Such assumption also leads to conservative predictions of beam shear and bending failures.

In a real case of underground explosion, especially when an explosion occurs near a structure, the stress wave is very unlikely to remain as elastic. While based on assumptions of the present study, only elastic wave propagation can be considered as shown in Eqs. (3.5) to (3.8). This leads to that, results of the present study are more accurate in cases of moderate and far explosions, but the pressure in close-in explosion should be checked carefully before plotting P-I diagrams.

3.5. Case study

To verify the applicability of the developed P-I diagrams, a case study is carried out for a box-shape underground structure. R is the distance from the explosion center to the side wall as shown in Fig. 3-1(a). Damage assessment for the side wall is carried out and one unit strip of the side wall is considered for simplicity. In a typical underground structure, the side wall is made up of laced reinforced concrete with stirrups to increase its shear and bending strength. The transverse

reinforcement ratio is between 0.4 and 0.6 percent. Details of such blast design can be referred to the TM5-1300 manual, and are omitted here. The soil layer is dry sand and relevant parameters are given below.

Half span: L = 2 m

Thickness of the side wall: h = 0.2 m

Unit length mass of the side wall: m = 500 kg

Shear strength of the side wall: Q_0 = 175.5 kN

Bending strength of the side wall: M_0 = 127.7 kN·m

Soil acoustic impedance: ρc = 0.497 MPa·s/m

Charge weight: W = 125 kg

Once the distance R is determined, by using the above parameters, the constant pressure p_0 and the blast duration t_d can be approximated by using the semi-empirical Eqs. (3.1) and (3.2). Subsequently, the normalized pressure and impulse are calculated. In the present case study, we took three different standoff distances, i.e., R=6.4 m, 7.3 m and 10 m, respectively (see Table 3-4).

Table 3 - 4 Case study

Point	Distance (R)	Duration (t_d)	Scaled Distance Z	Normalized Impulse I^*	Pressure (p_0)	Normalized Pressure P^*
Z1	6.4 m	2.038 ms	1.283	152.6	2.406 MPa	75.3
Z2	7.3 m	2.314 ms	1.465	116.4	1.615 MPa	50.6
Z3	10.0 m	2.756 ms	1.978	57.27	0.667 MPa	20.9

The strength ratio υ is calculated as 1.374, and the failure criteria of Eq. (3.9) in which β_0=2.5% and γ_υ=1% are used. Judging from Fig. 3-3, the failure mode is mode 3, which is a combination of shear and bending failures. As shown in Fig. 3-8, point Z1 is in region A, point Z2 is in region B, and point Z3 is in region C. That means, when the scaled distance is 1.283, the structure will endure both shear and bending failure; when the scaled distance is 1.465, the structure will endure bending failure only; when the scaled distance is 1.978, the structure is safe.

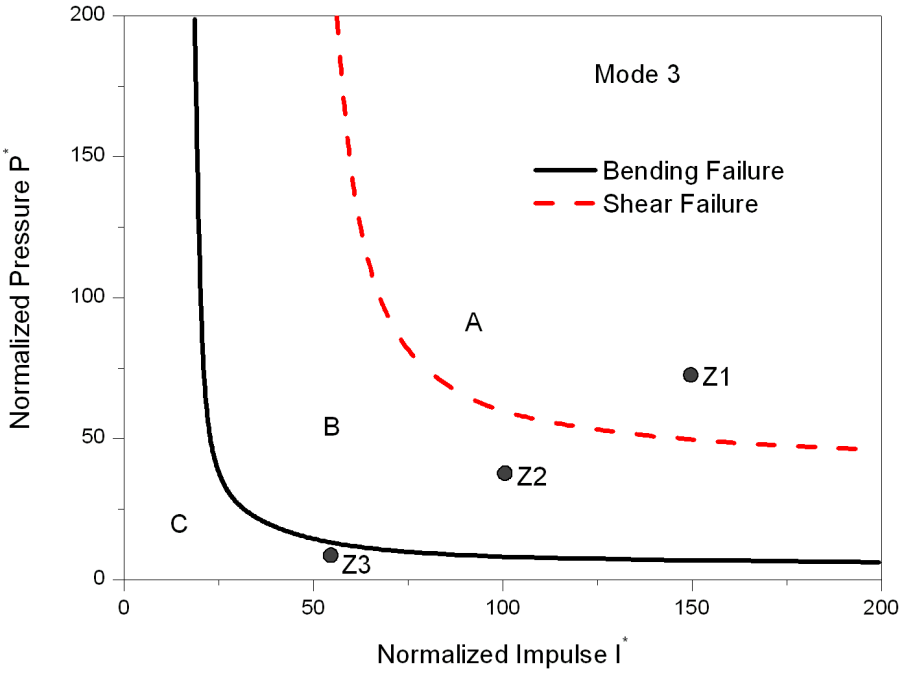

Fig. 3 - 8 Case study

3.6. Conclusions

The present analysis is based on a rigid-plastic element model and the MAM to assess damage of underground structures against external blast load. The developed P-I diagrams consider simplified SSI and they can be applied conveniently to damage assessment of the underground structures in the form of different failure modes. For a given strength ratio of υ, different regions for shear, bending, and combined failure modes according to the P-I diagrams can be determined. Comparison has been done to the results of surface structures which verifies the validity of the developed P-I diagrams.

The effect of soil cannot be ignored in estimating the blast load applied to structure. With the increase of acoustic impendence, interaction between structure and surrounding soil becomes more significant.

The maximum shear displacement is more sensitive to the pressure applied than the maximum bending displacement, while the effect of impulse to the maximum shear and bending displacements is similar.

The case study shows that, the proposed method can be effectively applied to damage assessment of underground structures against blast load.

CHAPTER 4

DAMAGE ASSESSMENT FOR UNDERGROUND STRUCTURES AGAINST INTERNAL BLAST LOAD

4.1. Introduction

Most existing works focused on damage assessment of surface structures. Very few involved in failure of underground structures. In fact, the complexity of soil property makes it difficult to perform structure response analysis when the SSI is considered. From the result of previous chapter, it is understood that the surrounding soil interacts with the underground structure and such effect cannot be ignored. When an underground structure is under internal blast load, the soil acts as an elastic support which absorbs part of the blast energy during an internal blast event occurred to an underground structure.

In the present study, the SSI is simplified as an equivalent spring coefficient. The rigid plastic model with the mode approximation method is adopted. P-I diagrams are subsequently developed for structural element by considering the SSI. The results of the present study can also be applied to the scenario when an explosion occurs near a retaining wall, over a foundation slab, or basement, etc. Comparison between the present study and damage assessment for surface structures is carried out to evaluate the SSI effect. P-I diagrams of different damage levels are also plotted. To verify the continuity of different failure modes, verifications are done by checking a few sharing points of different failure modes. A case study for an underground RC structure has also been conducted to show the applicability of the proposed damage assessment method.

4.2. Simplification of soil effect

During the physical process when a blast wave interacts with underground structure, as shown in Fig. 4-1, the soil medium is considered as a macroscopic homogeneous material which can be simplified to an elastic foundation to support the structure.

Therefore the SSI effect is simplified to a spring support which distributes over the structural element. Such simplification ignores the change of soil stiffness during response of structural element, and would under-estimate structural damage especially in a close-in explosion. But it is still suitable for cases of moderate and far-range explosions, and cases of close-in explosion with low charge weight.

Previous research works showed that, soil stiffness is frequency-dependent, but those were based on seismic wave and cyclic loading. Some of the conclusions also showed that: R-waves are predominant when away from vibration center (Athanasopoulos et al. 2000); When bulk modulus of soil is high, error in static and dynamic SSI is low (ülker-Kaustell et al. 2010); Soil stiffness degrades in soft clay due to cyclic loading (Li and Assimaki, 2010); SSI is significant in stiff soil (Stehmeyer and Rizos, 2008), etc. In the present study, only the first half circle is adopted to calculate the maximum structural response, therefore the degradation and dynamic effects of SSI are not so evident and are ignored. For the same reason, any kind of soil damping is ignored, although there are viscous damping, hysteretic damping and radiation damping of soil in a real underground explosion case.

The SSI effect exists in the deformation phase till the motion of element vanishes. Change of soil density during deformation is not considered; therefore the average stiffness of soil is adopted according to the analytical and laboratorial results (Sawangsuriya *et al*. 1974, Dutta *et al*. 2004). Such simplification aims on getting result efficiently in the analysis of the structure response by considering the SSI effect.

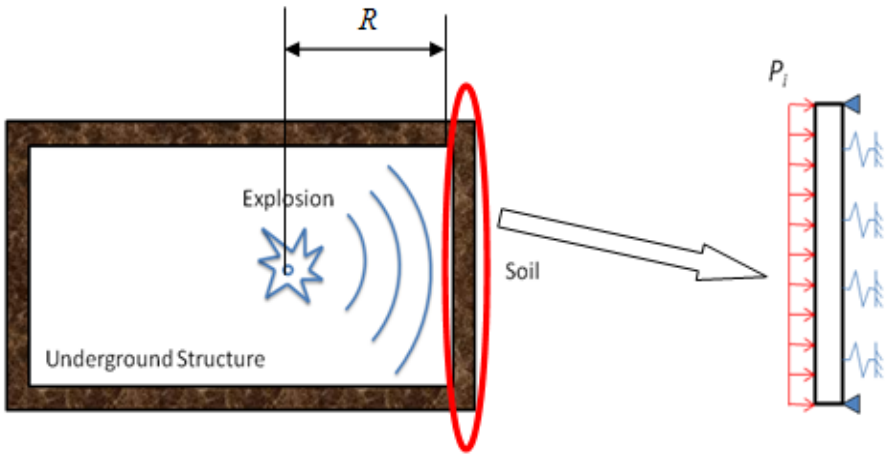

Fig. 4 - 1 Soil-structure interaction in internal blast load scenario

4.3. Failure criteria

A typical resistance-deflection curve for laterally restrained elements is shown in Fig. 4-2 (TM5-1300, 1990). The initial portion of the curve is primarily due to the flexural action. The ultimate flexural resistance is maintained until 2 degrees of support rotation is produced. At this support rotation, the concrete begins to crush and the element loses flexural capacity. If adequate single leg stirrups were provided, the flexural action would be extended to 4 degrees. However, due to the presence of the continuous reinforcement and adequate lateral restraint, a tensile membrane action is developed. The resistance due to this action increases with increasing deflection up to incipient failure at approximately 12 degrees support rotation. In order to simplify the analysis, the resistance is assumed to be due to plastic action throughout the entire range of behavior. To approximate the energy absorbed under the actual resistance-deflection curve, the deflection of the idealized curve is limited to 8 degrees support rotation. Design for this maximum deflection would produce incipient failure conditions. Existing studies (Yu and Jones 1991, Krauthammer 1998) also suggested use the ratio of centerline-deflection to half-span as the criterion of bending failure, since the largest ductile plastic deformation usually appeared at the mid-span due to bending effects.

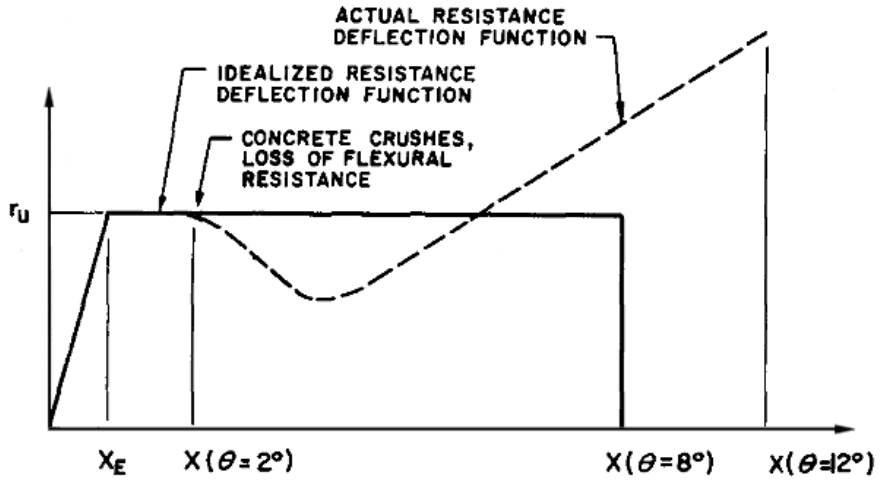

Fig. 4 - 2 Idealized resistance-deflection curve for large deflections

The maximum bending and shear deformations of the element are defined the same as Eqs. (3.9).

For a reinforced concrete structure member, the dynamic bending strength M_0 varies for different cross section designs. According to TM5-1300, for type I design, there is no crushing or spalling in concrete; only cracking appears on the tension side and the M_0 can be expressed as:

$$M_0 = \frac{A_s f_{ds}}{b}\left(d - \frac{a}{2}\right) \tag{4.1}$$

in which:

$$a = \frac{A_s f_{ds}}{0.85 b f'_{dc}} \tag{4.2}$$

where A_s is the area of tension reinforcement within the width, f_{ds} is the dynamic design stress for reinforcement, b is the width of compression face, d is the distance from extreme compression fiber to centroid of tension reinforcement, a is the depth of equivalent rectangular stress block, f'_{dc} is the dynamic ultimate compressive strength of concrete.

In the cross section type II, cracking appears on the tension side of member while crushing appears on the compression side. The M_0 can be shown as:

$$M_0 = \frac{A_s f_{ds} d_c}{b} \tag{4.3}$$

where A_s shows the area of tension or compression reinforcement within the width b, d_c is the distance between the centroids of the compression and the tension reinforcement.

In the cross section type III, disengagement of concrete appears on both tension and compression sides of the member. The bending strength M_0 is expressed the same as in Eq. (4.3).

The dynamic shear strength of a rectangular section reinforced concrete structure member Q_0 can be expressed as:

$$Q_0 = 0.16 f'_{dc} bd \tag{4.4}$$

The same damage level under empirical bending and shear failure criteria from results of Yu and Jones (1991) and Krauthammer (1998) are used as those in Table 3-1. There are three levels of damage, including light damage, moderate damage, and severe damage. For shear design, average shear strain γ_v indicates different damage levels, while the support rotation β_0 is for bending.

4.4. Failure modes and response analysis

The internal blast load is simplified as a rectangular pulse load with magnitude of p_0 and duration of t_d, while the pulse shape effect is eliminated. The pulse shape effect has been discussed by Youngdahl (1970, 1971), Li and Meng (2002b), and Li and Jones (2005b) that the loading shape effects on the P-I diagrams of a rigid, perfectly plastic SDOF model can be eliminated by using the Yougdahl's correlation parameter method. For convenience of P-I equations derivation while not losing the generality of the solution, the rectangular pulse load with equivalent pressure and impulse is adopted in the present study. The pulse shape effect on the P–I diagrams of a rigid, perfectly plastic SDOF model can be eliminated by using the Youngdahl's (1971) correlation parameter method as follows.

$$\begin{cases} I = \int_{t_y}^{t_f} P(t)\,dt \\ t_{mean} = \dfrac{1}{I}\int_{t_y}^{t_f} (t - t_y) P(t)\,dt \\ P_e = \dfrac{I}{2t_{mean}} \end{cases} \tag{4.5}$$

where I is the impulse, t_y is the time when material begins to yield, t_f is the end time of total deformation, $P(t)$ is the external pressure, t_{mean} is the mean time, P_e is the effective pressure.

As discussed in section 4.2, the governing equation is Eq. (3.10). Since the spring effect exists in all the phases, the governing equation is expressed as:

$$\frac{\partial Q}{\partial x} = -p_0 + m\ddot{y} + Ky \tag{4.6}$$

where Q is the transverse shear force, x is the abscissa on the element, m is the mass per unit length, $\ddot{y}$ is the acceleration of unit mass, K is the equivalent spring coefficient to represent the SSI effect, and y is the displacement of unit mass.

The same as the analysis of surface structure, there are totally five possible transverse velocity profiles including one pure shear failure mode, two pure bending failure modes, and two combined failure modes as shown in Fig. 3-3. A dimensionless strength ratio v is introduced the same as that in Eq. (3.12).

The velocity profile of different phases under different modes is the same as Table 3-2. Mode 1 contains shear failure only. Mode 2 is for simple bending failure which has a plastic hinge at the center of the element. Mode 3 can be considered as a combination of mode 1 and mode 2. Mode 4 is the complex bending failure mode which has a plastic zone at the middle of the element. And mode 5 is the combination of mode 1 and mode 4. Differentiation of the five failure modes is the same as that for surface structures. Derivation of the displacement time history for the five failure modes is summarized as follows. The x-axis starts at the mid of the beam and only half of a strip beam is considered due to symmetry as seen in Fig. 4-1.

Mode 1. $0 < \nu \le 1$ and $p_0 \ge \frac{2M_0}{L^2}\nu$, shear failure mode.

This shear failure mode provides direct shear failure occurs at the two supports where carries the maximum shear force, while bending failure does not occur. In this mode, the dimensionless parameter *v* is less than one which indicates a very low shear-to-bending strength ratio.

There are totally two phases in this mode including a loading phase (phase 1) and a post-loading phase (phase 2) which end at t_d and t_f respectively.

In phase 1, the governing equation is:

$$\frac{\partial Q}{\partial x} = -p_0 + m\ddot{y}_s + Ky_s \tag{4.7}$$

where $\ddot{y}_s$ and y_s are the acceleration and displacement due to shear force respectively.

The boundary and initial conditions are:

$$Q(x=0) = 0, Q(x=L) = -Q_0 \tag{4.8}$$

$$\dot{y}_s(t=0) = 0, y_s(t=0) = 0 \tag{4.9}$$

where $\dot{y}_s$ is the velocity due to shear force.

Integrating Eq. (4.7) with respect to time, at the end of phase 1 when $t=t_d$, the maximum displacement and velocity of the element are shown as follows:

$$y_s(t_d) = \frac{(p_0 L - Q_0)}{KL}\left[\cos\left(\frac{\sqrt{K}t_d}{\sqrt{m}}\right) - 1\right] \tag{4.10}$$

$$\dot{y}_s(t_d) = \frac{(p_0 L - Q_0)}{\sqrt{mK}L}\sin\left(\frac{\sqrt{K}t_d}{\sqrt{m}}\right) \tag{4.11}$$

In phase 2, the governing equation transfers to:

$$\frac{\partial Q}{\partial x} = m\ddot{y}_s + Ky \tag{4.12}$$

Using Eq. (4.8) as the boundary condition and Eqs. (4.10)-(4.11) as the initial conditions to solve Eq. (4.12), at the end of phase 2, the termination time t_f will be:

$$t_f = \arctan\left[\frac{\sin\frac{\sqrt{K}t_d}{\sqrt{m}}\left(p_0 L - Q_0\right)}{p_0 L + \cos\frac{\sqrt{K}t_d}{\sqrt{m}}\cdot Q_0 - \cos\frac{\sqrt{K}t_d}{\sqrt{m}}\cdot p_0 L}\right] + t_d \tag{4.13}$$

The element's final transverse displacement due to shear is:

$$y_s\left(t_f\right) = \frac{\sqrt{m}}{\sqrt{K}}\sin\left(T_1\right)\cdot \dot{y}_s\left(t_d\right) + \cos\left(T_1\right)\cdot\frac{y_s\left(t_d\right)\cdot KL + Q_0}{KL} - \frac{Q_0}{KL} \tag{4.14}$$

where $T_1 = \sqrt{K}\left(t_f - t_d\right)\Big/\sqrt{m}$.

Mode 2. $1 < \nu \le 1.5$ and $2M_0/L^2 < p_0 \le 2M_0\left(4\nu - 3\right)/L^2$, or $\nu \ge 1.5$ and $2M_0/L^2 < p_0 \le 6M_0/L^2$, bending failure mode.

A bending failure mode will occur when the above conditions are satisfied. A plastic hinge is generated at the mid-span of the element. There are totally two phases in this mode including a loading phase (phase 1) and a post-loading phase (phase 2) which end at t_d and t_f respectively.

In phase 1, the governing equation is:

$$\frac{\partial Q}{\partial x} = -p_0 + m\ddot{y}_m\left(1 - \frac{x}{L}\right) + Ky_m\left(1 - \frac{x}{L}\right) \tag{4.15}$$

where $\ddot{y}_m$ and y_m are the acceleration and displacement due to bending force respectively.

The boundary and the initial conditions are:

$$Q\left(x = 0\right) = 0, Q\left(x = L\right) = -Q_0, M\left(x = 0\right) = M_0, M\left(x = L\right) = 0 \tag{4.16}$$

$$\dot{y}_m\left(t=0\right)=0, y_m\left(t=0\right)=0 \tag{4.17}$$

where $\dot{y}_m$ is the velocity due to bending force.

Integrating Eq. (4.15), at the end of phase 1 when $t=t_d$, the maximum displacement and velocity of the element due to bending are shown respectively as follows:

$$y_m\left(t_d\right)=\frac{3\left(p_0L^2-2M_0\right)}{2KL^2}\left[1-\cos\left(\frac{\sqrt{K}t_d}{\sqrt{m}}\right)\right] \tag{4.18}$$

$$\dot{y}_m\left(t_d\right)=\frac{3\left(p_0L^2-2M_0\right)}{2KL^2}\sin\left(\frac{\sqrt{K}t_d}{\sqrt{m}}\right) \tag{4.19}$$

In phase 2, the governing equation changes to:

$$\frac{\partial Q}{\partial x}=m\ddot{y}_m\left(1-\frac{x}{L}\right)+Ky_m\left(1-\frac{x}{L}\right) \tag{4.20}$$

Using Eq. (4.16) as the boundary conditions and Eqs. (4.18)-(4.19) as the initial conditions, the final time t_f will be:

$$t_f=\frac{\sqrt{m}}{\sqrt{K}}\cdot\arctan\left[\frac{\sqrt{mK}L^2\cdot\dot{y}_m\left(t_d\right)}{KL^2\cdot y_m\left(t_d\right)+3M_0}\right]+t_d \tag{4.21}$$

The final bending displacement of the element is solved as:

$$y_m\left(t_f\right)=\frac{\sqrt{m}\cdot\sin\left(T_1\right)\cdot\dot{y}_m\left(t_d\right)}{\sqrt{K}}+\frac{\cos\left(T_1\right)\left[KL^2\cdot y_m\left(t_d\right)+3M_0\right]}{KL^2}-\frac{3M_0}{KL^2} \tag{4.22}$$

Mode 3. $1<\nu\le1.5$ and $p_0\ge\frac{2M_0}{L^2}\left(4\nu-3\right)$, combined failure mode.

Mode 3 is the combination of mode 1 and mode 2. Both shear failure and bending failure occur to the element. The shear failure occurs at the two supports, while the bending failure induces plastic hinge at the mid-span of the element. There are three phases including one loading phase (phase 1) and two post-loading phases (phase 2 and phase 3) which end at t_d, t_s, and t_f respectively.

In phase 1, the governing equation is:

$$\frac{\partial Q}{\partial x} = -p_0 + m\ddot{y}_s + m\left(\ddot{y}_m - \ddot{y}_s\right)\left(1-\frac{x}{L}\right) + Ky_s + K\left(y_m - y_s\right)\left(1-\frac{x}{L}\right) \quad (4.23)$$

with the same boundary and initial conditions given in Eqs. (4.16), (4.9), and (4.17).

Similar to mode 1 and mode 2, after integrating Eq. (4.23), at the end of phase 1 when $t=t_d$, the maximum displacement and velocity of the element due to shear and bending are given respectively as follows:

$$y_s\left(t_d\right) = \frac{\left[1-\cos\left(\frac{\sqrt{K}t_d}{\sqrt{m}}\right)\right]\left(p_0L^2 - 4Q_0L + 6M_0\right)}{KL^2} \quad (4.24)$$

$$\dot{y}_s\left(t_d\right) = \frac{\sin\left(\frac{\sqrt{K}t_d}{\sqrt{m}}\right)\cdot\left(p_0L^2 - 4Q_0L + 6M_0\right)}{\sqrt{mK}L^2} \quad (4.25)$$

$$y_m\left(t_d\right) = \frac{\left[1-\cos\left(\frac{\sqrt{K}t_d}{\sqrt{m}}\right)\right]\left(p_0L^2 + 2Q_0L - 6M_0\right)}{KL^2} \quad (4.26)$$

$$\dot{y}_m\left(t_d\right) = \frac{\sin\left(\frac{\sqrt{K}t_d}{\sqrt{m}}\right)\cdot\left(p_0L^2 + 2Q_0L - 6M_0\right)}{\sqrt{mK}L^2} \quad (4.27)$$

In phase 2, the governing equation is:

$$\frac{\partial Q}{\partial x} = m\ddot{y}_s + m\left(\ddot{y}_m - \ddot{y}_s\right)\left(1-\frac{x}{L}\right) + Ky_s + K\left(y_m - y_s\right)\left(1-\frac{x}{L}\right) \quad (4.28)$$

The boundary conditions are still the same as in the first phase, while the velocities and displacements given in Eqs. (4.24)-(4.27) are used as the initial conditions. Solving Eq. (4.28), at the end of phase 2 when $t=t_s$, the displacement due to shear stops first, while the bending displacement remains to the next phase. The ending time t_s and the maximum displacement and velocity due to shear and bending are shown respectively as follows:

$$t_s = \frac{\sqrt{m}}{\sqrt{K}} \cdot \arctan\left[\frac{\sqrt{mK} L^2 \cdot \dot{y}_s(t_d)}{y_s(t_d) \cdot KL^2 + 4Q_0 L - 6M_0} \right] + t_d \tag{4.29}$$

$$y_s(t_s) = \frac{\sqrt{mK} L^2 \dot{y}_s(t_d) \sin(T_2) + \left[KL^2 y_s(t_d) + 4Q_0 L - 6M_0 \right] \cos(T_2) - 4Q_0 L + 6M_0}{KL^2} \tag{4.30}$$

$$y_m(t_s) = \frac{\sqrt{mK} L^2 \dot{y}_s(t_d) \sin(T_2) + \left[KL^2 y_s(t_d) - 2Q_0 L + 6M_0 \right] \cos(T_2) + 2Q_0 L}{KL^2} \tag{4.31}$$

$$\dot{y}_m(t_s) = \frac{\sqrt{mK} L^2 \dot{y}_m(t_d) \sin(T_2) + \left[KL^2 y_m(t_d) - 2Q_0 L + 6M_0 \right] \sin(T_2)}{\sqrt{m} KL^2} \tag{4.32}$$

where $T_2 = \sqrt{K}(t_s - t_d)/\sqrt{m}$.

In phase 3, only the bending failure induced motion remains, and the governing equation is the same as Eq. (4.20). Similarly, the motion termination time t_f and the final displacement $y_m(t_f)$ are determined as:

$$t_f = \frac{\sqrt{m}}{\sqrt{K}} \cdot \arctan\left[\frac{\sqrt{mK} L^2 \cdot \dot{y}_m(t_s)}{KL^2 \cdot t_m(t_s) + 3M_0} \right] + t_s \tag{4.33}$$

$$y_m(t_f) = \frac{\sqrt{m}}{\sqrt{K}} \cdot \sin(T_3) \cdot \dot{y}_m(t_s) + \frac{\left[KL^2 \cdot y_m(t_s) + 3M_0 \right] \cdot \cos(T_3)}{KL^2} - \frac{3M_0}{KL^2} \tag{4.34}$$

where $T_3 = \sqrt{K}(t_f - t_s)/\sqrt{m}$.

Mode 4. $1.5 \le \nu$ and $6M_0\nu^2/L^2 < p_0 \le 8M_0\nu^2/3L^2$, bending failure mode.

In this mode, the bending failure with a plateau deformation at the central portion of the element occurs when the blast load is sufficiently intensive. Different from mode 2, two plastic hinges are generated offset from the mid-span of the element. There are totally three phases including one loading phase (phase 1) and two post-loading phases (phase 2 and phase 3) which end at t_d, t_1, and t_f respectively.

In phase 1, the governing equation is expressed as:

$$\frac{\partial Q}{\partial x} = -p_0 + m\ddot{y}_m\left(\frac{L-x}{L-\xi_0}\right) + Ky_m\left(\frac{L-x}{L-\xi_0}\right) \tag{4.35}$$

where ξ_0 is the distance of the plastic hinge from the mid-span.

The boundary conditions are as follows:

$$Q\left(x=\xi_0\right)=0, Q\left(x=L\right)=-Q_0, M\left(x=\xi_0\right)=M_0, M\left(x=L\right)=0 \tag{4.36}$$

And the initial conditions are the same as Eqs. (4.9)and (4.17). Thus Eqs. (4.36), (4.9), and (4.17) are used to determine the integral constants when Eq. (4.35) is integrated.

At the end of the loading period, when $t=t_d$, the plastic hinge location which is indicated by ξ_0 and the ending displacement and velocity of phase 1 are derived respectively as follows:

$$\xi_0 = L - \frac{\sqrt{6p_0M_0}}{p_0} \tag{4.37}$$

$$y_m\left(t_d\right) = \frac{p_0\left[1-\cos\left(\frac{\sqrt{K}t_d}{\sqrt{m}}\right)\right]}{K} \tag{4.38}$$

$$\dot{y}_m\left(t_d\right) = \frac{p_0\cdot\sin\left(\frac{\sqrt{K}t_d}{\sqrt{m}}\right)}{\sqrt{mK}} \tag{4.39}$$

In phase 2, the blast load has been released, and the velocity profile is the same as that given in phase 1. However, the two plastic hinges move toward the mid-span of the element. At the end of phase 2, the two plastic hinges meet at the mid-span and phase 3 motion starts then. The governing equation of phase 2 is:

$$\frac{\partial Q}{\partial x} = m\ddot{y}_m\left(\frac{L-x}{L-\xi}\right) + Ky_m\left(\frac{L-x}{L-\xi}\right) \tag{4.40}$$

where ξ is the distance between the plastic hinge and the mid-span of the element.

The boundary conditions are:

$$Q(x=\xi)=0, Q(x=L)=-Q_0, M(x=\xi)=M_0, M(x=L)=0 \quad (4.41)$$

Eqs. (4.38) and (4.39) are used as the initial condition to solve Eq. (4.40). At the end of phase 2 when $t=t_1$, the two plastic hinges stops moving. The ending time of phase 2 and the maximum displacement and velocity due to bending are shown respectively as follows:

$$t_1 = \frac{\ln\left(\frac{p_0 \cdot C + 6BM_0}{p_0}\right)\cdot A - \ln\left(C + BL^2\right)\cdot A}{2B} + t_d \quad (4.42)$$

where $A = 4Q_0\left(L-\xi_0\right) - 6M_0$, $B = y_s\left(t_d\right)\cdot K\cdot\left(L-\xi^2\right)^2$, $C = 6M_0 - 2Q_0\left(L-\xi_0\right)$.

$$y_m\left(t_1\right) = \dot{y}_m\left(t_d\right)\cdot\left(t_1 - t_d\right) + y_m\left(t_d\right) \quad (4.43)$$

$$\dot{y}_m\left(t_1\right) = \frac{p_0 \cdot \sin\left(\frac{\sqrt{K}t_d}{\sqrt{m}}\right)}{\sqrt{mK}} \quad (4.44)$$

In phase 3, the governing equation is the same as Eq. (4.20), and it can be solved in a similar way as it was done for mode 2 and mode 3.

At the end of phase 3, when $t=t_f$, the motion stops and the final time t_f is determined as:

$$t_f = \frac{\sqrt{m}}{\sqrt{K}}\cdot\arctan\left[\frac{p_0 L^2 \cdot \sin\left(\sqrt{K}t_d/\sqrt{m}\right)}{KL^2\cdot y_m\left(t_1\right) + 3M_0}\right] + t_1 \quad (4.45)$$

The final bending displacement $y_m(t_f)$ is:

$$y_m\left(t_f\right) = \frac{\sqrt{m}}{\sqrt{K}}\cdot\dot{y}_m\left(t_1\right)\cdot\sin\left(T_4\right) + \frac{\left[KL^2\cdot y_m\left(t_1\right) + 3M_0\right]}{KL^2}\cdot\cos\left(T_4\right) - \frac{3M_0}{KL^2} \quad (4.46)$$

where $T_4 = \sqrt{K}\left(t_f - t_1\right)/\sqrt{m}$.

Mode 5, $1.5 < \nu$ and $p_0 > 8M_0\nu^2/3L^2$, combined failure mode.

Mode 5 is the most complicated mode as mode 1 and mode 4 are combined. There are four phases including one loading phase (phase 1) and three post-loading phases (phase 2, phase 3, and phase 4) which end at t_d, t_s, t_1, and t_f respectively.

In phase 1, both shear and bending deformation occur. The governing equation is:

$$\frac{\partial Q}{\partial x} = -p_0 + \ddot{m}y_s + m\left(\ddot{y}_m - \ddot{y}_s\right)\left(\frac{L-x}{L-\xi_0}\right) + Ky_s + K\left(y_m - y_s\right)\left(\frac{L-x}{L-\xi_0}\right) \quad (4.47)$$

The boundary conditions are the same as those in Eq. (4.16), and initial conditions are the same as Eqs. (4.9) and (4.17). After integrating Eq. (4.47), at the end of phase 1 when $t=t_d$, the plastic hinge location, the maximum displacement and velocity of this phase are shown respectively as follows:

$$\xi_0 = L - \frac{3M_0}{Q_0} \quad (4.48)$$

$$y_s\left(t_d\right) = \frac{\left[1-\cos\left(\frac{\sqrt{K}t_d}{\sqrt{m}}\right)\right]\left(3p_0M_0 + 2Q_0{}^2\right)}{3KM_0} \quad (4.49)$$

$$\dot{y}_s\left(t_d\right) = \frac{\left(3p_0M_0 - 2Q_0{}^2\right)\cdot\sin\left(\frac{\sqrt{K}t_d}{\sqrt{m}}\right)}{3\sqrt{mK}M_0} \quad (4.50)$$

$$y_m\left(t_d\right) = \frac{p_0\left[1-\cos\left(\frac{\sqrt{K}t_d}{\sqrt{m}}\right)\right]}{K} \quad (4.51)$$

$$\dot{y}_m\left(t_d\right) = \frac{p_0\cdot\sin\left(\frac{\sqrt{K}t_d}{\sqrt{m}}\right)}{\sqrt{mK}} \quad (4.52)$$

In phase 2, the velocity profile is the same as that of the previous phase, while the shear deformation tends to vanish. The governing equation is:

$$\frac{\partial Q}{\partial x} = \ddot{m} y_s + m\left(\ddot{y}_m - \ddot{y}_s\right)\left(\frac{L-x}{L-\xi}\right) + K y_s + K\left(y_m - y_s\right)\left(\frac{L-x}{L-\xi}\right) \tag{4.53}$$

Based on the same boundary conditions given in Eq. (4.15), and the initial conditions of Eqs. (4.49)-(4.52), Eq. (4.53) can be integrated with respect to time. At the end of phase 2 when $t=t_s$, the shear deformation stops. The displacement and velocity at the ending time of phase 2 due to shear and bending are shown respectively as follows:

$$t_s = \frac{\sqrt{m}}{\sqrt{K}} \cdot \arctan \frac{\dot{y}_s\left(t_d\right) \cdot \sqrt{mK}\left(L-\xi_0\right)^2}{4Q_0\left(L-\xi_0\right) - 6M_0 + y_s\left(t_d\right) \cdot K \cdot \left(L-\xi_0\right)^2} \tag{4.54}$$

$$y_s\left(t_s\right) = \frac{\sqrt{m}}{\sqrt{K}} \dot{y}_s\left(t_d\right) \cdot \sin\left(T_2\right) + \frac{\cos\left(T_2\right) \cdot \left(A+B\right)}{K\left(L-\xi_0\right)^2} - \frac{A}{K\left(L-\xi_0\right)^2} \tag{4.55}$$

$$y_s\left(t_s\right) = \frac{\sqrt{m}}{\sqrt{K}} \dot{y}_s\left(t_d\right) \cdot \sin\left(T_2\right) + \frac{\cos\left(T_2\right) \cdot \left(A+B\right)}{K\left(L-\xi_0\right)^2} - \frac{A}{K\left(L-\xi_0\right)^2} \tag{4.56}$$

$$\dot{y}_m\left(t_s\right) = \dot{y}_m\left(t_d\right) \tag{4.57}$$

In phase 3, the bending deformation remains the same velocity profile as that in phase 2 of mode 4, and the two plastic hinges start to move toward the mid-span of the element. The governing equation is the same as given in Eq. (4.40). Similarly, at the end of phase 3, when $t=t_1$, the two plastic hinges coincides at the mid-span, and the ending displacement and velocity of phase 3 are deduced as follows:

$$t_1 = \frac{\ln\left(\frac{p_0 F + 6EM_0}{p_0}\right) \cdot D - \ln\left(F + EL^2\right) \cdot D}{2E} + t_d \tag{4.58}$$

where $D = p_0\sqrt{m} \cdot \sin\left(\sqrt{K}t_d / \sqrt{m}\right) \Big/ \sqrt{K}$, $E = p_0\left[\cos\left(\sqrt{K}t_d / \sqrt{m}\right) - 1\right]$, $F = -3M_0$.

$$y_m\left(t_1\right) = \dot{y}_m\left(t_1\right) \cdot \left(t_1 - t_s\right) + y_m\left(t_s\right) \tag{4.59}$$

$$\dot{y}_m\left(t_1\right) = \dot{y}_m\left(t_s\right) \tag{4.60}$$

Similarly, in phase 4 of mode 5, the governing equation is the same as Eq. (4.20). At the end of phase 4 when $t=t_f$, the motion stops.

$$t_f = \frac{\sqrt{m}}{\sqrt{K}} \cdot \arctan\left[\frac{p_0 L^2 \cdot \sin\left(\sqrt{K} t_d / \sqrt{m}\right)}{KL^2 \cdot y_m(t_1) + 3M_0} \right] + t_1 \tag{4.61}$$

The final bending displacement is:

$$y_m(t_f) = \frac{\sqrt{m}}{\sqrt{K}} \cdot \dot{y}_n(t_1) \cdot \sin(T_4) + \frac{\left[KL^2 \cdot y_m(t_1) + 3M_0 \right]}{KL^2} \cdot \cos(T_4) - \frac{3M_0}{KL^2} \tag{4.62}$$

4.5. P-I diagrams and discussions

In each of the five modes that discussed in section 4.4, the final shear displacement y_s for direct shear failure and the final bending displacement y_m for bending failure, or both for combined failure can be derived. Based on the failure criteria discussed in section 4.3, P-I diagrams for different modes can then be derived.

Define dimensionless variables P^* and I^* of the pressure and impulse of a blast load as:

$$P^* = \frac{p_0 L^2}{M_0} \tag{4.63}$$

$$I^* = \frac{\sqrt{K} t_d P^*}{\sqrt{mL}} \tag{4.64}$$

From the equations for final displacements induced by shear and bending failure, the P-I diagrams can be represented in unified forms as follows:

$$S(P^*, I^*) = \delta \cdot h \cdot \gamma_v = y_s \tag{4.65}$$

$$B(P^*, I^*) = L \cdot \beta_0 = y_m \tag{4.66}$$

where y_s is the maximum displacement due to shear which equals to $y_s(t_f)$ in a shear failure mode, and $y_s(t_s)$ in a combined failure mode; y_m is the maximum displacement due to bending which equals to $y_m(t_f)$; $S(P^*,I^*)$ and $B(P^*,I^*)$ are

implicit expressions with respect to the normalized pressure and impulse for shear and bending according to failure criteria respectively. *S(P*,I*)* equals to the right part of Eqs. (4.14), (4.30), or (4.55) which gave the maximum shear deformation, and *B(P*,I*)* equals to the right part of Eqs. (4.22), (4.34), (4.46), or (4.62) which represent the maximum bending deformation.

Based on Eqs. (4.65) and (4.66), the P-I diagrams corresponding to shear and bending failures can be drawn.

4.5.1. Differentiation of failure modes

By determining relative parameters, the P-I diagrams can be plotted for all five failure modes. Differentiation of the failure modes given in Fig. 3-3 is determined by the requirement of the motion initiation. For example, for mode 1, the acceleration induced by the shear force at the supports should be larger than zero, and the maximum bending moment should be smaller than the bending strength of the element. Therefore $p_0 \geq 2M_0\nu/L^2$ and $0<\nu<1$ are derived, respectively. For mode 2, the initial acceleration due to bending should be larger than zero, while the maximum shear force should be less than the shear strength. Therefore $1\leq\nu\leq 1.5$ and $2M_0/L^2 \leq p_0 \leq 2M_0(4\nu-3)/L^2$, or $\nu\geq 1.5$ and $2M_0/L^2 \leq p_0 \leq 6M_0/L^2$ are required. For mode 3, by combining the two requirements that accelerations due to both shear and bending are larger than zero, the equations of boundaries are derived as $1\leq\nu\leq 1.5$ and $p_0 > 2M_0(4\nu-3)/L^2$. The mode 4 has the same requirements as mode 2 and the boundaries are $1.5<\nu$ and $p_0 > 8M_0\nu^2/3L^2$. On the other hand, the mode 5 has the same requirements as mode 3, and the boundaries are $1.5<\nu$ and $6M_0/L^2 \leq p_0 \leq 8M_0\nu^2/3L^2$.

Three typical P-I diagrams of shear and bending failures are plotted in Fig. 4-3.

1) When $\nu=0.8$ and $p_0 > 2M_0\nu/L^2$, only shear failure exists as shown in Fig. 4-3(a) (mode 1). Region A and region B indicate shear failure and no failure respectively.

2) As shown in Fig. 4-3(b) when $\nu = 1.2$ and $p_0 > 2M_0\left(4\nu - 3\right)/L^2$, the element fails in the mode 3, which is the combination of mode 1 and mode 2. Two P-I diagrams, for shear failure and bending failure respectively, are plotted based on Eqs. (4.65)-(4.66). There are four regions in this case which indicate four different failure types of the element. In region A, which corresponds to larger pressure and impulse, combined failure occurs since both the maximum shear displacement and the maximum bending displacement exceed the failure threshold given by the shear and bending failure criteria. In region D, the pair of pressure and impulse locates above the shear failure diagram but below the bending failure diagram, which indicates only shear failure occurred to the element. Similarly, in region B, the pair of pressure and impulse exceeds the bending failure diagram while it is below the shear failure diagram, which defines bending failure for the element. In region C, the element remains safe due to the pressure and impulse pair is below both diagrams.
3) When $\nu = 1.8$ and $p_0 > 6M_0\nu^2/L^2$, mode 4 and mode 5 may occur. Fig. 4-3(c) shows the P-I diagrams of mode 5 which is similar to mode 2 with 4 different regions.

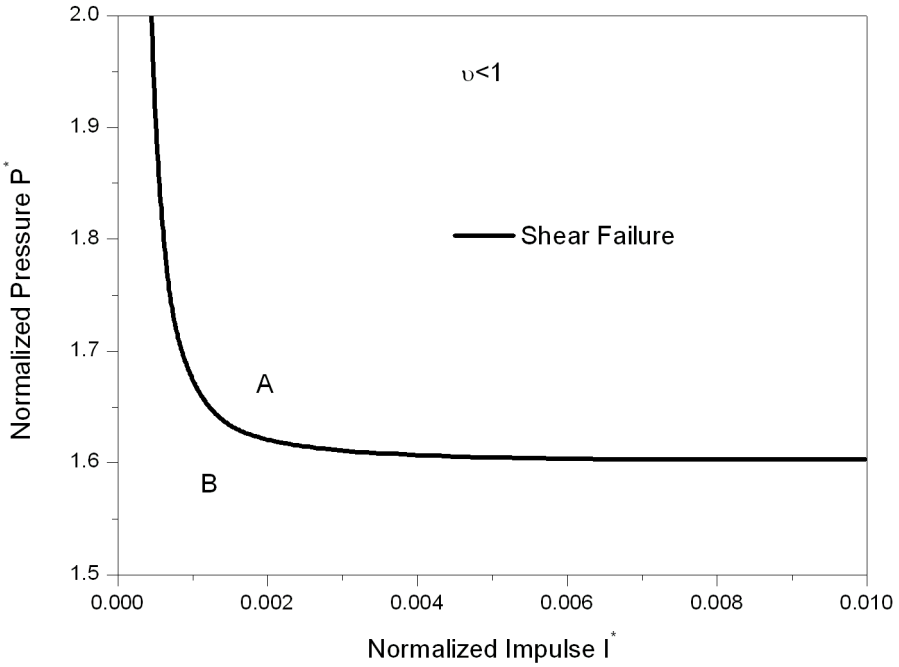

(a) Typical failure mode $\upsilon \leq 1.0$ (Mode 1)

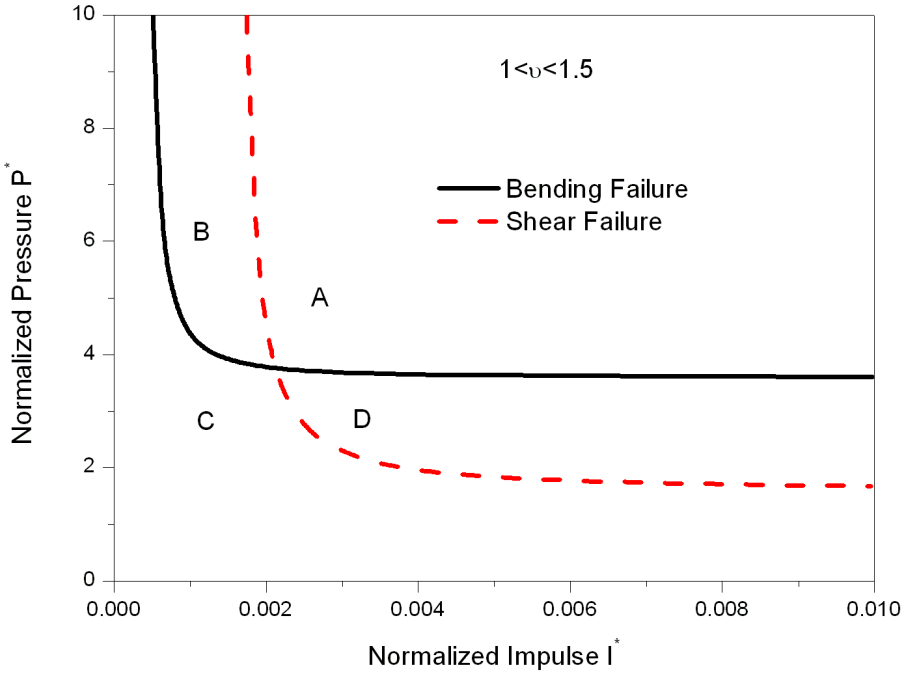

(b) Typical failure mode $1 \leq \upsilon \leq 1.5$ (Mode 3)

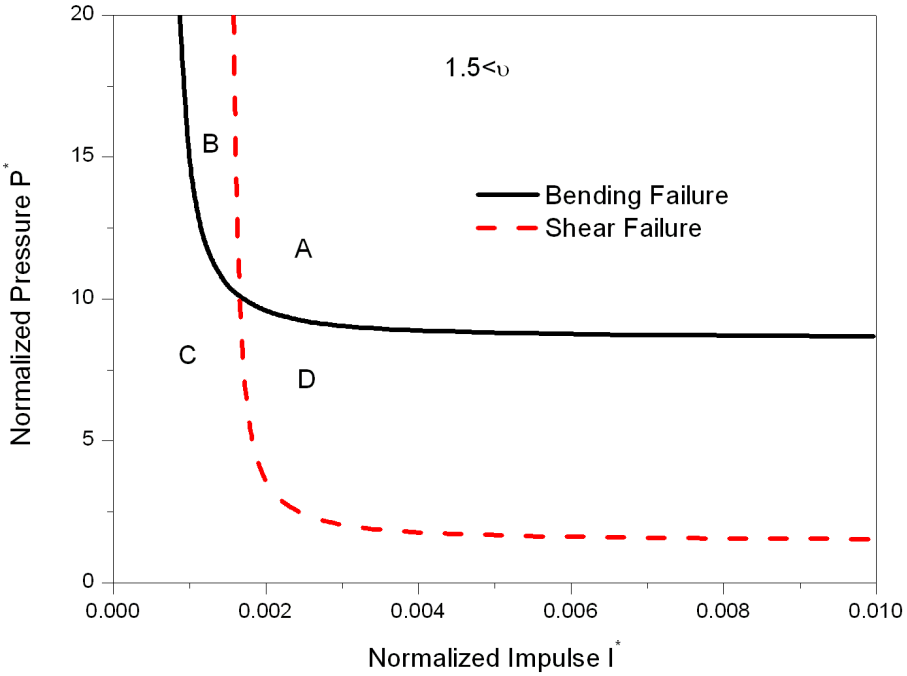

(c) Typical failure mode $1.5 \leq \upsilon$ (Mode 5)

Fig. 4 - 3 Typical failure modes

4.5.2. Soil-structure interaction effect

The boundary conditions of different failure modes are exactly the same as those of surface structures. This is because that, whether the spring effect acts on the beam or not, the initial conditions for all the failure modes remain the same.

Different soil has different density and compressibility, therefore the spring effect varies in all kinds of soil types. Considering a comparison with plastic beads-sand mixture (K=2.39 MN/m), medium sands (K=3.83 MN/m), and crushed rock (K=4.83 MN/m) (Sawangsuriya *et al*. 1974), P-I diagrams for shear and bending failure are plotted and compared in Fig. 4-4. It shows that, these three types of soil are characterized as low stiffness, intermediate stiffness, and high stiffness. The low stiffness material is a mixture of 50% by volume of sand and 50% by volume of plastic beads. The intermediate stiffness material is a medium of uniformly-graded quartz sand. The high stiffness material is 19-mm crushed lime rock. It can be seen from Fig. 4-4 that, the crushed rock has the highest stiffness and has significant effect on the structural failure.

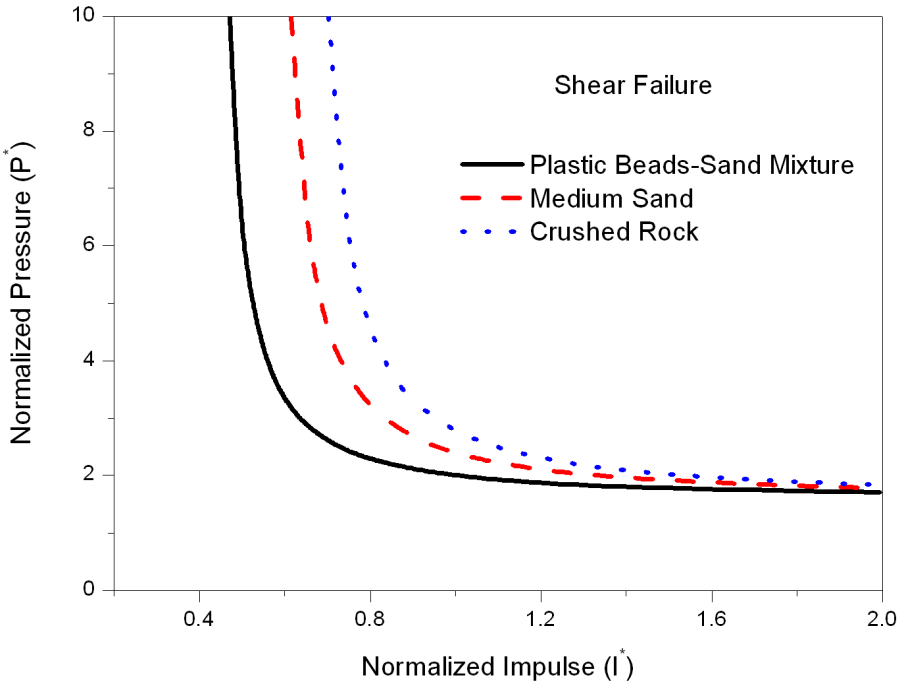

(a) Shear failure in different soils

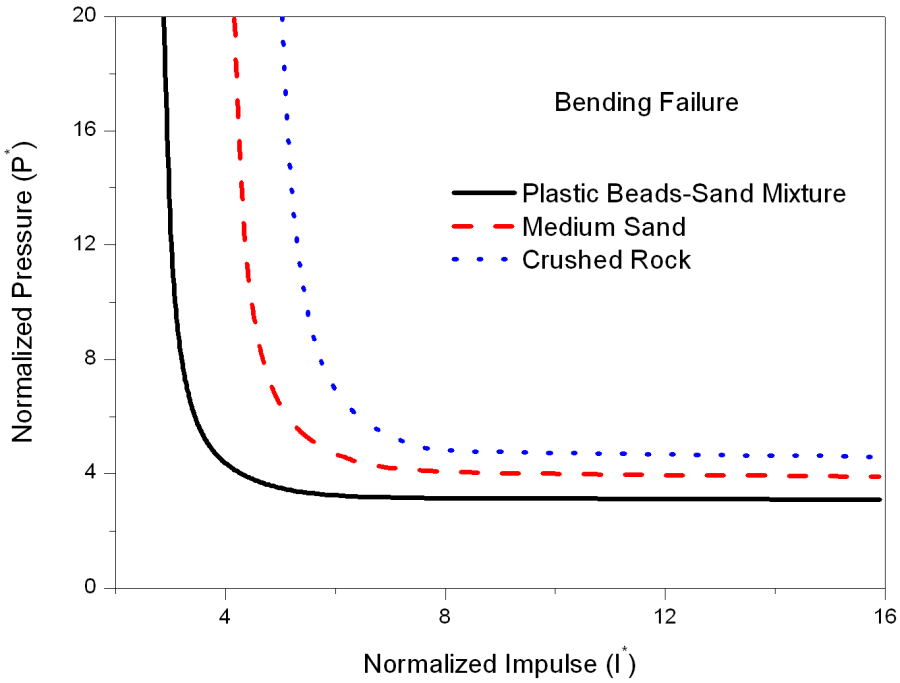

(b) Bending failure in different soils

Fig. 4 - 4 Failures in different soils

Comparison is also done to the damage assessment results for surface structures when the spring coefficient is set sufficient small (for example, K=10 N/m) as shown in Fig. 4-5. It can be seen that both the shear failure and bending failure diagrams match well with those for surface structures. It verifies the present P-I diagrams and the P-I diagram method suggested by Ma *et al*. (2007) has been successfully extended to damage assessment for underground structures when the decoupling of SSI is considered. Furthermore, the present results can be applied to damage assessment for surface structures by assigning a sufficient small spring coefficient in the equations.

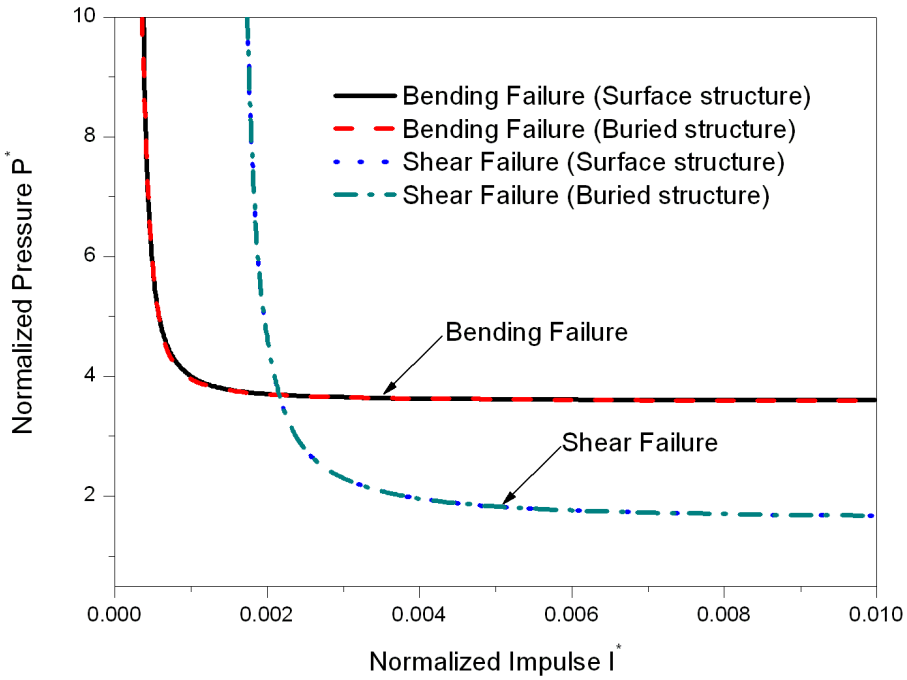

Fig. 4 - 5 Comparison with surface structures against blast load

4.5.3. Verification of continuity

Since different failure modes give different final shear and/or bending displacement, the solutions at the boundaries of different modes in Fig. 3-3 should be continuous. It means that two modes should give the same P-I diagram at their sharing boundary line. To verify the continuity of the equations, three checking points as shown in Fig. 3-3 are examined. CP1 ($p_0 = 3.60M_0/L^2$ and $\nu = 1.2$) is shared by mode 2 and mode 3, CP2 ($p_0 = 6.00M_0/L^2$ and $\nu = 1.5$) is shared by mode 2, mode 3, mode 4 and mode 5, and CP3 ($p_0 = 8.64M_0/L^2$ and $\nu = 1.8$) is shared by mode 4 and mode 5. CP1 and CP3 are chosen randomly from the boundary lines.

The verification is shown in Table 4-1 which indicates the diagrams of Mode 2, 3, 4, and 5 match very well at the check points.

Table 4 - 1 Continuity verification

	$\nu = 1.2$		$\nu = 1.5$		$\nu = 1.8$	
Mode	P^*	I^*	P^*	I^*	P^*	I^*
2	3.6	0.3883	6.0	0.3169	N.A.	N.A.
3	3.6	0.3883	6.0	0.3169	N.A.	N.A.
4	N.A.	N.A.	6.0	0.3169	8.4	0.3032
5	N.A.	N.A.	6.0	0.3169	8.4	0.3032

4.6. Case study

To verify the applicability of the developed P-I diagrams, a case study is carried out by considering a box-shape underground structure. An explosion occurred inside the underground structure as schematically shown in Fig. 4-1. Damage assessment for the side wall is carried out and one unit strip of side wall is considered for simplicity. The soil layer is medium sands and relative parameters are given below.

Half element length: L=2 m

Element height: h=0.2 m

Unit mass of element: m=500 kg/m^2

Shear resistance of element: Q_0=252.8 kN

Bending resistance of element: M_0=153.3 kN·m

Soil spring coefficient: K=3.83 MN/m

Charge weight: W=125 kg

Once the distance R is confirmed, using the above parameters, the constant pressure p_0 and blast duration t_d can be approximated by using relative equations or read from charts in TM5-1300. Subsequently, the normalized pressure and impulse are

calculated. In the present case study, three different distances R=12.7 m, 14.0 m and 15.6 m, are considered respectively (see Table 4-2).

Table 4 - 2 Case study

Point	Distance (R)	Duration (t_d)	Scaled Distance (Z)	Normalized Impulse (I^*)	Pressure (p_0)	Normalized Pressure (P^*)
Z1	12.7 m	2.535 ms	1.674 m/kg$^{1/3}$	5.271	1.086 MPa	33.95
Z2	14.0 m	2.797 ms	2.045 m/kg$^{1/3}$	3.246	0.606 MPa	18.95
Z3	15.6 m	3.117 ms	2.760 m/kg$^{1/3}$	1.591	0.276 MPa	8.338

v is calculated as 1.374, the failure criteria of Eqs. (4.65) and (4.66) in which $\beta = 3.492\%$ and $\gamma_v = 1\%$ are used for light damage criteria. Judging from Fig. 3-3, the failure mode is Mode 5, which is the most complex combination of shear and bending failures. As shown in Fig. 4-6, point Z1 is in region A, point Z2 is in region B, and point Z3 is in region C. That means, when the scaled distance is 1.674, the structure will endure both light shear and light bending damage; when the scaled distance is 2.045, the structure will endure light bending damage only; when the scaled distance is 2.760, the structure is safe.

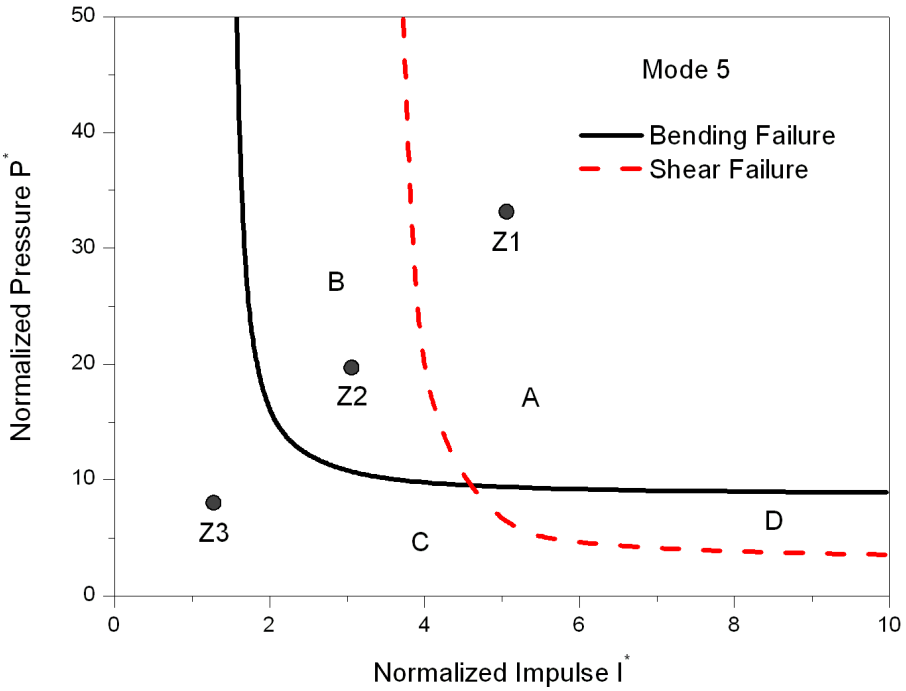

Fig. 4 - 6 Case study

4.7. Concluding remarks

The present study derives P-I diagrams for underground structure subjected to internal blast load. The SSI is considered and a rigid-plastic beam model is applied in order to consider the combined effect of both shear and bending failure. Verification shows that the present analysis is a successful extension of damage assessment of surface structures to underground structures. Results show that with increase of the soil stiffness, the SSI and its effect to the structural damage becomes very significant.

An internal detonation generates very complicated blast load to the underground structure walls, ceiling and floor, which is affected by many factors, such as venting, geometry of the underground structure, charge weight and the way of charge placement, etc. In the present study, the distance from the centroid of the charge to the beam element changes along the beam. For example, when the charge is placed at the floor of the underground structure, the maximum distance will be $\sqrt{4L^2+R^2}$, where R is the perpendicular distance from the centroid of the charge to the beam element. Therefore the scaled distance is sensitive to the ratio of L/R. To ensure the

difference of the peak pressure along the beam within 10%, *L/R* should be less than 0.229. Under the above considerations, the present study assumed that the blast load is uniformly acted to the structural element which gives a conservative assessment of structural damage and leads to a safer design for underground protective structures. And the localized damage due to unevenly distributed blast load is not in the scope of the present study.

The structural element in analysis is simplified to a simply supported beam model which ignores the rigidity at the supports. This results in conservative assessment of structural damage and gives a safe design of the structure although adjustment of the P-I diagrams can be done for a fixed beam as it has been done for surface structures (Ma *et al*. 2007).

The rigid-plastic model ignores the elastic deformation stage which may cause discrepancies at the minor damage case, however it can well represent the structural deformation behavior when the structure undergoes mediate and large deformations.

In the present analysis, a rectangular pulse shape is adopted. The pulse shape effect to the P-I diagrams is minor especially in the two extreme impulsive and quasi-static cases.

Besides, the rate dependence of the soil stiffness is also not considered in the analysis which is mainly due to that experimental data on the soil stiffness rate dependence is not available.

Discussion of the P-I diagrams shows that, the effect of soil cannot be ignored in estimating the dynamic response of underground structures against internal blast load. With the increase of soil stiffness, interaction between structure and surrounding soil becomes more significant, and more blast energy is absorbed by the soil. Comparison between the present result and the result of Ma *et al*. (2007) shows that, result of present study can be easily applied to surface structure by setting a small enough spring coefficient *K*. The case study shows that, damage assessment can be carried out by using the P-I diagram based on the mode approximation method.

CHAPTER 5

PULSE SHAPE EFFECT ON STRUCTURAL DAMAGE INDUCED BY BLAST LOAD

5.1. Introduction

In the early research work of Youngdahl's (1971), the pulse shape effect was eliminated by using a correlation parameter method as shown in Eq. (4.5). Li and Meng (2002b), and Li and Jones (2005b) also gave out some useful results. It has been claimed that the pulse shape effect to the P-I diagrams is minor especially in the quasi-static load region and the impulsive load region. However, such conclusions were drawn based on the analysis of the SDOF system. Since the analysis using the MAM always simplifies the blast load to be a rectangular pulse, the pulse shape effect based on the MAM is still not clear, and the error caused by such difference is unknown.

In the damage assessment using P-I diagrams, the MAM used by Ma *et al*. (2007) can be extended by using a generalized integration procedure so that rectangular, triangular, exponential or any other pulse-shaped pressure can be analyzed. Therefore the pulse shape effect can be considered in the analysis.

In another aspect, the blast loads used by Li and Meng (2002b) were based on the same load magnitude and duration. Their result contains the difference in pulse shapes and the difference in impulse of each load type.

In the present study, the blast load is simplified in three types with the same impulse and maximum pressure magnitude. Details of applying a generalized integration procedure to analyze the pulse shape effect for surface structure against blast load will be given. Both shear and bending failure modes will be adopted to show the difference.

5.2. General assumptions and failure criteria

To simplify the calculation, the shear and bending resistances of the beam element are assumed to be constants. That is to say the rigid-plastic material model is adopted. This assumption leads to the lower bound solution of the problem since the independent maximum bending and shear strength criteria used in analysis circumscribe an interactive shear-bending yield surface.

The maximum displacement of the beam element is again adopted as the criterion when generating the P-I diagrams. To ensure the MAM is applicable in each failure mode, small displacement assumption should be used as Martin and Symonds (1966) did, and the yield stress is assumed to be independent of the rate of strain.

The failure modes include shear failure mode, bending failure mode, combined failure mode, bending failure mode with a plastic zone, and combined failure mode with a plastic zone, which are the same as those in Ma *et al*. (2007) as shown in Fig. 3-3.

The failure criteria of the structural element under bending and shear are the same as used in Chapter 3 and 4.

5.3. Integration procedure

In the present study, a simply supported beam element under uniformly distributed blast pressure is adopted as the model to illustrate the surface structure under blast load. The derivation procedure of P-I equations remains the same as previous chapters, therefore the governing equations, boundary conditions, initial conditions, and results of structural response are the same in each phase of each mode as those in Ma *et al*.'s work (2007). Since a general shape of the pulse loading is assumed and to simplify the derivation of P-I equations, a generalized integration procedure for different cases have to be adopted.

In the work of Ma *et al*. (2007) and Chapters 3 and 4, the blast load is a function of time in the governing equations which couples with other parameters such as structural velocity or displacement. It becomes difficult and even impossible to solve the governing equation without decoupling this "redundant" time-dependent

parameter. By using the integration procedure, the differential equations can be solved easily without losing accuracy. Therefore, the general integration procedure is adopted.

In the cases of surface structure under blast load, the pressure changes with time. The material properties (shear strength Q_0 and bending strength M_0) and the blast pressure p_0 should be obtained first, so that the failure mode can be determined. Starting from the first phase (loading phase), the blast duration t_d is divided into plenty of time steps. In each time step, the pressure will be calculated according to the blast load shape equation and the structural responses obtained will be used as the initial conditions for the next time step till the end of current phase. In the post-loading phase(s), the similar procedure will be used and the final structural displacement can be calculated. The flowchart in Fig. 5-1 shows the generalized integration procedure.

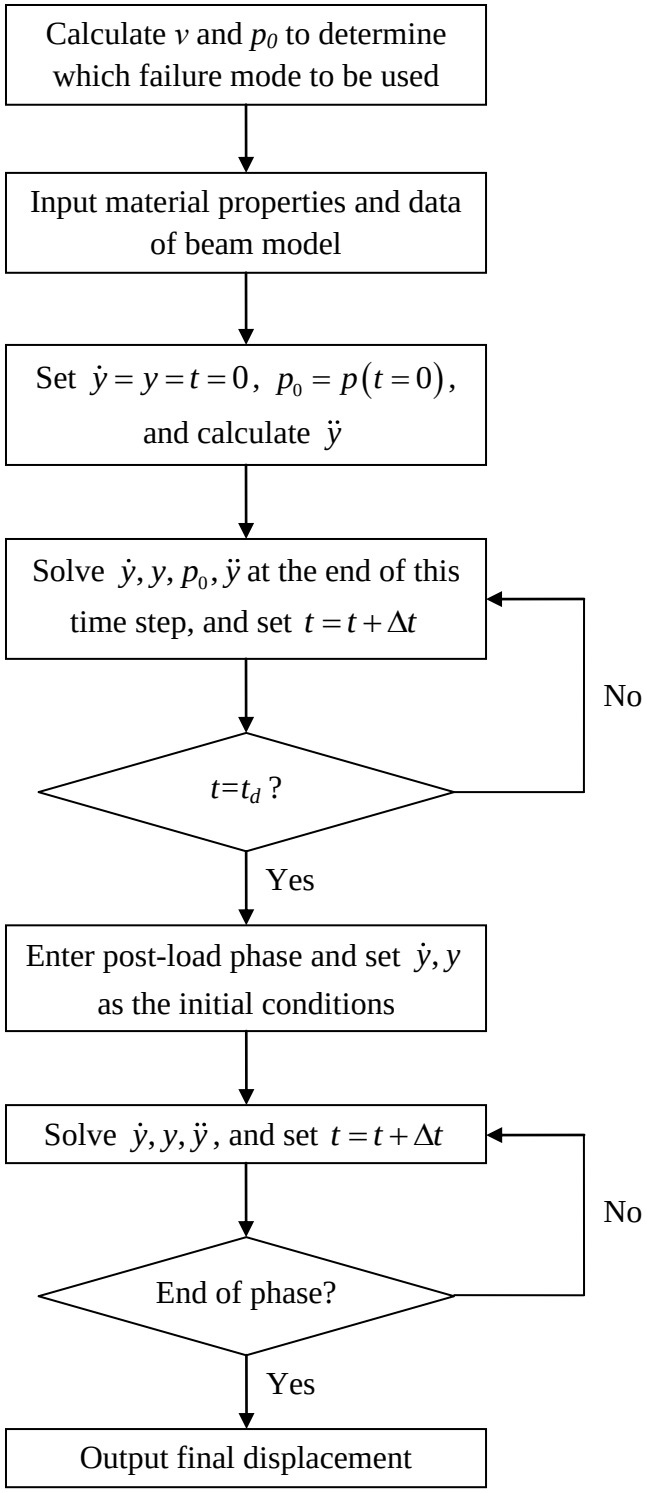

Fig. 5 - 1 Flow chart for surface structural element against blast load

5.4. Derivation of P-I equations

Before carrying out the numerical calculation, the blast pressure p and the strength ratio v ($\nu = 0.5Q_0L/M_0$) should be given, and consequently the failure mode can be decided. Three different load cases are used in the present study, i.e.,

1) Rectangular load,

$$\begin{cases} p = p_0 & when \quad t \le t_d \\ p = 0 & when \quad t > t_d \end{cases} \tag{5.1}$$

2) Triangular load,

$$\begin{cases} p = p_0\left(1 - t/t_d\right) & when \quad t \le t_d \\ p = 0 & when \quad t > t_d \end{cases} \tag{5.2}$$

3) Exponential load,

$$\begin{cases} p = p_0\left(1 - t/t_d\right)\cdot e^{-2.725t/t_d} & when \quad t \le t_d \\ p = 0 & when \quad t > t_d \end{cases} \tag{5.3}$$

Then the material properties (shear resistance Q_0, bending resistance M_0), geometrical properties of the beam (unit mass m, half length L) should be inputted to the integration procedure. For comparison reason, the present study uses the three pulse shapes only. More general pulse shapes with an arbitrary pressure-time history can also be applied.

In this section, the iterative time step is set as $\Delta t = t_d / n$, where n is a pre-defined constant which satisfies the precision requirement of the integration.

5.4.1. Mode 1 (Shear failure mode)

For mode 1 failure, the governing equations in phase 1 and phase 2 are the same as given in Eq. (5.4) and (5.5) respectively. The only difference is that the pressure-time history of the blast load becomes arbitrary and it can be represented by *p=p(t)* in the above equations.

$$\frac{\partial Q}{\partial x} = -p + m\ddot{y}_s \tag{5.4}$$

$$\frac{\partial Q}{\partial x} = m\ddot{y}_s \tag{5.5}$$

In phase 1, the boundary conditions and the initial conditions are the same as in Eq. (3.14) and (3.15). Then Eq. (5.4) is integrated with respect to time *t*. In every integration step, the value of *p* needs be updated according to the load function.

The equations for integration are derived as:

$$\ddot{y}_s\left(t_i\right) = \frac{p\left(t_i\right)\cdot L - Q_0}{mL} \tag{5.6}$$

$$\dot{y}_s\left(t_{i+1}\right) = \dot{y}_s\left(t_i\right) + \ddot{y}_s\left(t_i\right)\cdot \Delta t \tag{5.7}$$

$$y_s\left(t_{i+1}\right) = y_s\left(t_i\right) + \dot{y}_s\left(t_i\right)\cdot \Delta t \tag{5.8}$$

After each time step, set $t_{i+1} = t_i + \Delta t$. At the end of this phase when $t = t_d$, the maximum velocity and displacement of the beam are $\dot{y}_s\left(t_d\right)$ and $y_s\left(t_d\right)$ respectively.

In phase 2, the boundary conditions remain the same as in the previous phase, while the initial conditions change to:

$$\dot{y}_s\left(t = t_d\right) = \dot{y}_s\left(t_d\right), y_s\left(t = t_d\right) = y_s\left(t_d\right) \tag{5.9}$$

The integration equations for structural maximum velocity and displacement remain the same as Eqs. (5.7) and (5.8), while the maximum shear acceleration is as follow:

$$\ddot{y}_s\left(t_i\right) = \frac{-Q_0}{mL} \tag{5.10}$$

The integration stops when $\dot{y}_s = 0$ ($t = t_f$), and the final displacement is $y_s\left(t_f\right)$.

5.4.2. Mode 2 (Bending failure mode)

In phase 1, the pulse pressure acts on the beam and the governing equation for each time step is:

$$\frac{\partial Q}{\partial x} = -p + m\ddot{y}_m\left(1-\frac{x}{L}\right) \tag{5.11}$$

The boundary conditions and the initial conditions are the same as Eq. (3.20) and (3.21).

In every integration step, the value of *p* needs to be updated according to the load function.

The equations for integration are derived as:

$$\ddot{y}_m\left(t_i\right) = \frac{3\left[\, p\left(t_i\right)\cdot L^2 - 2M_0 \,\right]}{2mL^2} \tag{5.12}$$

$$\dot{y}_m\left(t_{i+1}\right) = \dot{y}_m\left(t_i\right) + \ddot{y}_m\left(t_i\right)\cdot\Delta t \tag{5.13}$$

$$y_m\left(t_{i+1}\right) = y_m\left(t_i\right) + \dot{y}_m\left(t_i\right)\cdot\Delta t \tag{5.14}$$

After each time step, set $t_{i+1} = t_i + \Delta t$. At the end of this phase when $t = t_d$, the maximum velocity and displacement of the beam are $\dot{y}_m\left(t_d\right)$ and $y_m\left(t_d\right)$ respectively.

Phase 2 is the only post-loading phase and the governing equation is:

$$\frac{\partial Q}{\partial x} = m\ddot{y}_m\left(1-\frac{x}{L}\right) \tag{5.15}$$

The boundary conditions remain the same as Eq. (3.20), while the initial conditions change to:

$$\dot{y}_m\left(t = t_d\right) = \dot{y}_m\left(t_d\right), y_m\left(t = t_d\right) = y_m\left(t_d\right) \tag{5.16}$$

The integration equations for structural maximum velocity and displacement remain the same as Eqs. (5.13) and (5.14), while the maximum bending acceleration is as follow:

$$\ddot{y}_m = \frac{-3M_0}{mL^2} \tag{5.17}$$

The integration stops when $\dot{y}_m = 0$ ($t = t_f$), and the final displacement is $y_m\left(t_f\right)$.

5.4.3. Mode 3 (Combined failure mode)

During phase 1, the governing equation is:

$$\frac{\partial Q}{\partial x} = -p + m\ddot{y}_s + m\left(\ddot{y}_m - \ddot{y}_s\right)\left(1 - \frac{x}{L}\right) \tag{5.18}$$

The initial conditions are as Eqs. (3.15) and (3.21), and the boundary conditions are the same as Eq. (3.20).

The equations for the shear and bending responses integration are the same as in Eqs. (5.7), (5.8), (5.13), and (5.14), while the maximum shear and bending acceleration are as follows:

$$\ddot{y}_s\left(t_i\right) = \frac{p\left(t_i\right) + 6M_0 - 4Q_0}{mL^2} \tag{5.19}$$

$$\ddot{y}_m\left(t_i\right) = \frac{p\left(t_i\right) - 6M_0 + 2Q_0}{mL^2} \tag{5.20}$$

After each time step, set $t_{i+1} = t_i + \Delta t$. At the end of this phase when $t = t_d$, the maximum velocity and displacement of the beam for shear and bending are $\dot{y}_s\left(t_d\right)$, $y_s\left(t_d\right)$, $\dot{y}_m\left(t_d\right)$ and $y_m\left(t_d\right)$ respectively.

In phase 2, shear deformation will terminate at the end, and the bending deformation will continue. The governing equation is:

$$\frac{\partial Q}{\partial x} = m\ddot{y}_s + m\left(\ddot{y}_m - \ddot{y}_s\right)\left(1 - \frac{x}{L}\right) \tag{5.21}$$

The boundary conditions remain the same as Eq. (3.20), while the initial conditions change to Eqs. (5.9) and (5.16) for shear and bending respectively.

The integration equations for structural maximum velocity and displacement remain the same as Eqs. (5.7), (5.8), (5.13), and (5.14), while the maximum shear and bending acceleration are as follows:

$$\ddot{y}_s(t_i) = \frac{6M_0 - 4Q_0L}{mL^2} \tag{5.22}$$

$$\ddot{y}_m(t_i) = \frac{2Q_0L - 6M_0}{mL^2} \tag{5.23}$$

The integration of this phase stops when $\dot{y}_s = 0$ ($t = t_s$), and the final shear displacement is $y_s(t_s)$. At the end of this phase, the maximum bending velocity and displacement are $\dot{y}_m(t_s)$ and $y_m(t_s)$.

In the following phase 3, the integration procedure is similar to phase 2 of mode 2. Only the difference is that the initial conditions changes to:

$$\dot{y}_m(t = t_s) = \dot{y}_m(t_s), y_m(t = t_s) = y_m(t_s) \tag{5.24}$$

The integration of this phase stops when $\dot{y}_m = 0$ ($t = t_f$), and the final bending displacement is $y_m(t_f)$.

5.4.4. Mode 4 (Bending failure mode with a plastic zone)

Mode 4 is the bending failure with a plateau deformation at the central portion of the element which may occur when the blast load is sufficiently intensive. Different from mode 2, two plastic hinges are generated offset from the mid-span of the element.

In the range of $\xi_0 < x < L$, the governing equation is:

$$\frac{\partial Q}{\partial x} = -p + m\ddot{y}_m\left(\frac{L - x}{L - \xi_0}\right) \tag{5.25}$$

where ξ_0 is the distance of the plastic hinge from the mid-span and $\xi_0 = L - \sqrt{6M_0 / p_0}$.

The initial conditions are the same as those in Eq. (3.21) and the boundary conditions are as those in Eq. (3.32).

The equations for the bending responses integration are the same as in Eqs. (5.13) and (5.14), while the maximum bending acceleration is:

$$\ddot{y}_m\left(t_i\right)=\frac{p\left(t_i\right)}{m} \tag{5.26}$$

After each time step, set $t_{i+1}=t_i+\Delta t$. At the end of this phase when $t=t_d$, the maximum velocity and displacement of the beam are $\dot{y}_m\left(t_d\right)$ and $y_m\left(t_d\right)$ respectively.

In phase 2 which is the first post-loading phase the two plastic hinges move toward the mid-span of the beam and meet at the mid-span. The governing equation is:

$$\frac{\partial Q}{\partial x}=m\ddot{y}_m\frac{\left(L-x\right)\cdot\dot{\xi}}{\left(L-\xi\right)} \tag{5.27}$$

The initial conditions are as Eq. (5.16) and the boundary conditions are as Eq. (3.35).

The integration equations for structural maximum velocity and displacement remain the same as Eqs. (5.13) and (5.14), while the maximum bending acceleration equals to zero.

The integration of this phase stops when $\xi\left(t\right)=0$ ($t=t_1$), and the bending displacement at the end of this phase is $y_m\left(t_1\right)$.

In phase 3, i.e., the second post-loading phase, bending deformation will terminate at the end. The iterative procedure is similar to phase 2 of mode 2 and the only difference is that, the initial condition changes to:

$$\dot{y}_m\left(t=t_1\right)=\dot{y}_m\left(t_1\right),y_m\left(t=t_1\right)=y_m\left(t_1\right) \tag{5.28}$$

The integration of this phase stops when $\dot{y}_m=0$ ($t=t_f$), and the final bending displacement is $y_m\left(t_f\right)$.

5.4.5. Mode 5 (Combined failure mode with a plastic zone)

Mode 5 is the most complicated mode which combined mode 1 and mode 4.

The governing equation for each time step in the range of $\xi_0 < x < L$ for phase 1 is:

$$\frac{\partial Q}{\partial x} = -p + m\ddot{y}_s + m\left(\ddot{y}_m - \ddot{y}_s\right)\left(\frac{L-x}{L-\xi_0}\right) \tag{5.29}$$

The initial conditions are as Eqs. (3.14) and (3.20), and the boundary conditions are as Eq. (3.32).

The equations for the shear and bending responses integration are the same as in Eqs. (5.7), (5.8), (5.13), and (5.14), while the maximum shear and bending acceleration are as follows:

$$\ddot{y}_s\left(t_i\right) = \frac{p\cdot\left(L-\xi_0\right)^2 - 4Q_0\left(L-\xi_0\right) + 6M_0}{\left(L-\xi_0\right)^2} \tag{5.30}$$

$$\ddot{y}_m\left(t_i\right) = \frac{p\cdot\left(L-\xi_0\right)^2 + 2Q_0\left(L-\xi_0\right) - 6M_0}{m\left(L-\xi_0\right)^2} \tag{5.31}$$

After each time step, set $t_{i+1} = t_i + \Delta t$. At the end of this phase when $t = t_d$, the maximum velocity and displacement of the beam for shear and bending are $\dot{y}_s\left(t_d\right)$, $y_s\left(t_d\right)$, $\dot{y}_m\left(t_d\right)$ and $y_m\left(t_d\right)$ respectively.

In phase 2, which is the first post-loading phase, the shear deformation will terminate at the end, and the bending deformation will continue. The governing equation is:

$$\frac{\partial Q}{\partial x} = m\ddot{y}_s + m\left(\ddot{y}_m - \ddot{y}_s\right)\left(\frac{L-x}{L-\xi_0}\right) \tag{5.32}$$

The boundary conditions remain the same as Eq. (3.32), while the initial conditions change to Eqs. (5.9) and (5.16) for shear and bending respectively.

The integration equations for structural maximum velocity and displacement remain the same as Eqs. (5.7), (5.8), (5.13), and (5.14), while the maximum shear and bending acceleration are as follows:

$$\ddot{y}_s\left(t_i\right)=\frac{-2Q_0}{m\left(L-\xi_0\right)} \tag{5.33}$$

$$\ddot{y}_m\left(t_i\right)=0 \tag{5.34}$$

The integration of this phase stops when $\dot{y}_s=0$ ($t=t_s$), and the final shear displacement is $y_s\left(t_s\right)$. At the end of this phase, the maximum bending velocity and displacement are $\dot{y}_m\left(t_s\right)$ and $y_m\left(t_s\right)$.

The integration for phase 3 is similar to phase 2 of mode 4. The integration of this phase stops when $\xi\left(t\right)=0$ ($t=t_1$), and the bending displacement at the end of this phase is $y_m\left(t_1\right)$.

In phase 4, bending deformation will terminate at the end. The integration procedure is similar to phase 3 of mode 4, and it stops when $\dot{y}_m=0$ ($t=t_f$), and the final bending displacement is $y_m\left(t_f\right)$.

5.5. Result discussions

Based on the integration method, the final displacements induced by shear or bending can be derived numerically, and the P-I diagrams can be represented in a similar way. It should be mentioned that the present integration analysis uses a constant load in each time step in spite of the pulse shape of the blast load. Analytical results can thus be derived for each time step. The integration method adopted here is semi-analytical which has the advantage to consider arbitrary pulse shapes and thus the effect of the pulse shape to the P-I diagrams can be analyzed.

Damages to the structure are categorized into three levels as shown in Table 5-1. It lists different damage levels of an RC beam element according to empirical shear failure criteria of Yu and Jones (1991) and Krauthammer (1998) which are for the

structures without protective design. The bending damage levels are derived from the damage of RC members in TM5-1300 (1990). There are three levels of damage: light damage, moderate damage, and severe damage. For shear design, average shear strain γ_v indicates different damage levels, while support rotation β_0 is applied for bending. By using the failure criteria and damage level in table 5-1, the P-I equations can be represented in unified forms as Eq. (3.49). The dimensionless variables P^* and I^* of the pressure and impulse of a blast load are defined as:

$$P^* = \frac{p_0 L}{Q_0} = \frac{p_0 L^2}{2\nu M_0} \tag{5.35}$$

$$I^* = \frac{p_0 t_d}{\sqrt{2mQ_0}} = \frac{p_0 t_d}{\sqrt{4mM_0 \cdot \nu / L}} \tag{5.36}$$

Table 5 - 1 Different damage level under empirical bending and shear failure criteria

Failure	Criteria	Light Damage	Moderate Damage	Severe Damage
Shear	Average shear strain γ_v	1%	2%	3%
Bending	Ratio of centerline deflection to half span β_0	6.993%	14.054%	21.256%

The pulse shape effect on P–I diagrams has been early discussed by Youngdahl's (1971) for a rigid, perfectly plastic SDOF model. The correlation parameter method is shown in Eq. (4.5). Such method was widely used, but it is not verified for the application in MAM.

Based on the semi-analytical results, the pulse shape effect can be presented. The three kind of load shapes are shown in Fig. 2-2. The pressure magnitude remains the same among each type of loads but the blast duration differs.

The t_{dR}, t_{dT}, and t_{dE}, in Fig. 2-2 are blast durations for rectangular load, triangular load, and exponential load respectively. In normal procedure of plotting P-I

diagrams, the blast pressure and duration are input and the structural displacements are output. But in Fig. 5-2 and 5-3, the blast pressure and the structural displacements are input and the blast durations are calculated reversely. In Fig. 5-4, the blast durations are calculated according to Eq. (4.5).

In the following figures, T load means the triangular load, E load denotes the exponential load, and R load denotes the rectangular load.

When a damage level of the structural element is determined, the P-I diagrams for the pulse shape effect of surface structure under blast load at different shear and bending damage levels are shown in Fig. 5-2 and 5-3. It indicates that to reach the same damage level, higher pressure and impulse are required for the exponential pulse load and the result from the rectangular load can be considered as the upper bound solution which is relatively conservative. The pulse effect in shear failure is minor in all regions of P-I diagrams, but it is significant in bending failure, especially in the dynamic region and some part of the impulse region.

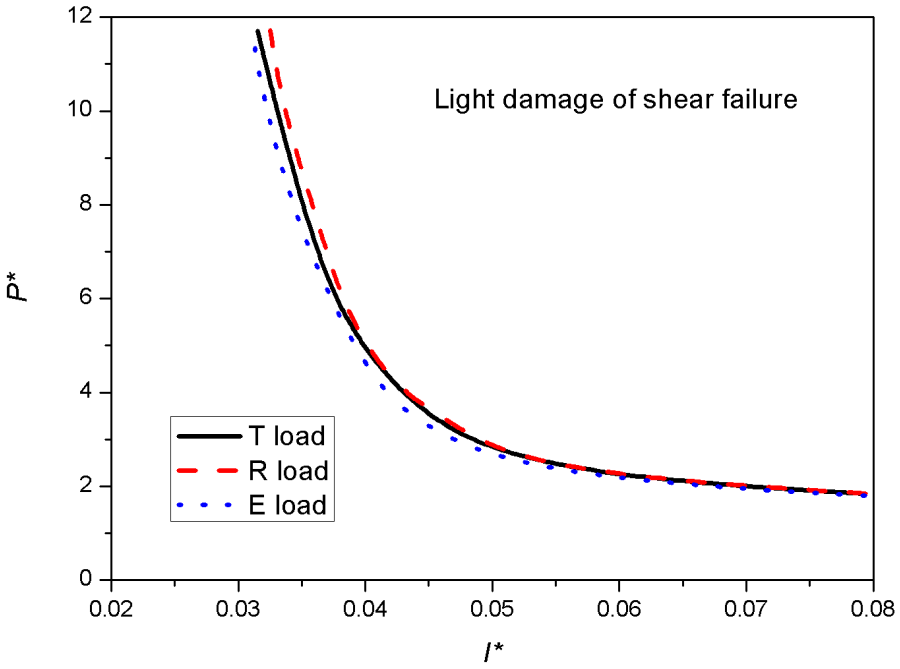

(a) Light damage

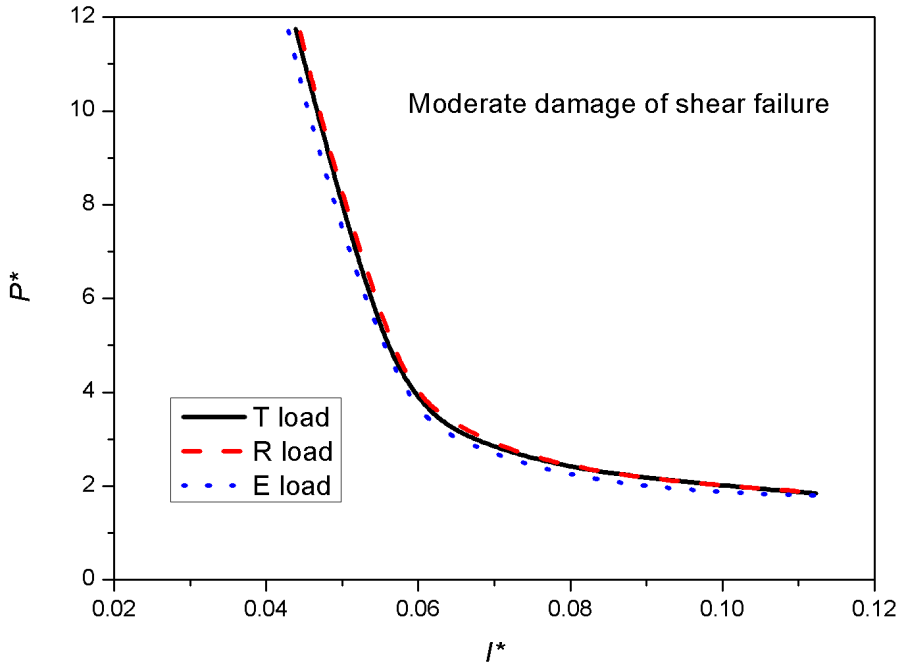

(b) Moderate damage

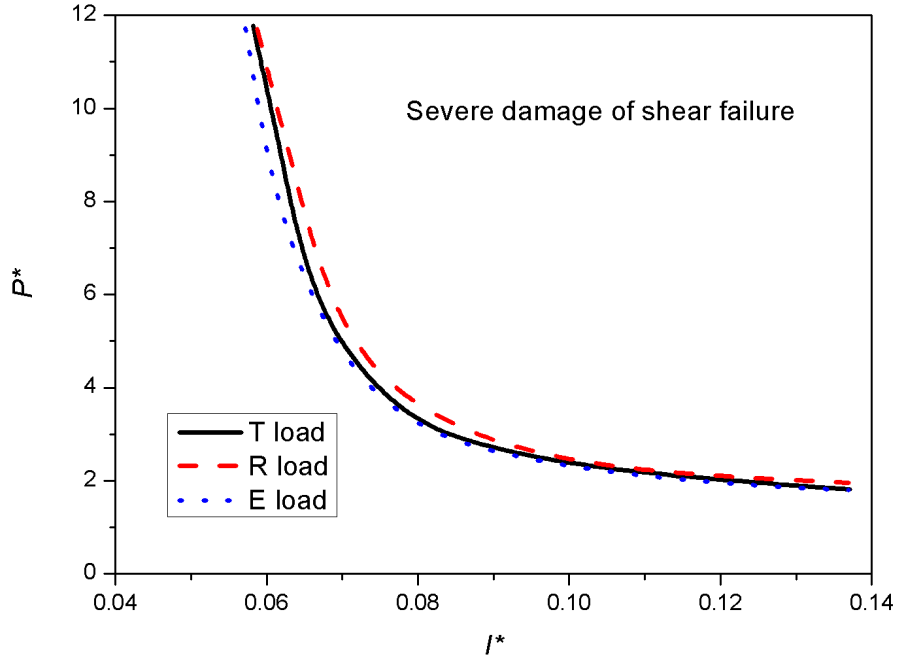

(c) Severe damage

Fig. 5 - 2 Pulse shape effect on shear failure for surface structure against blast load (fixed damage level)

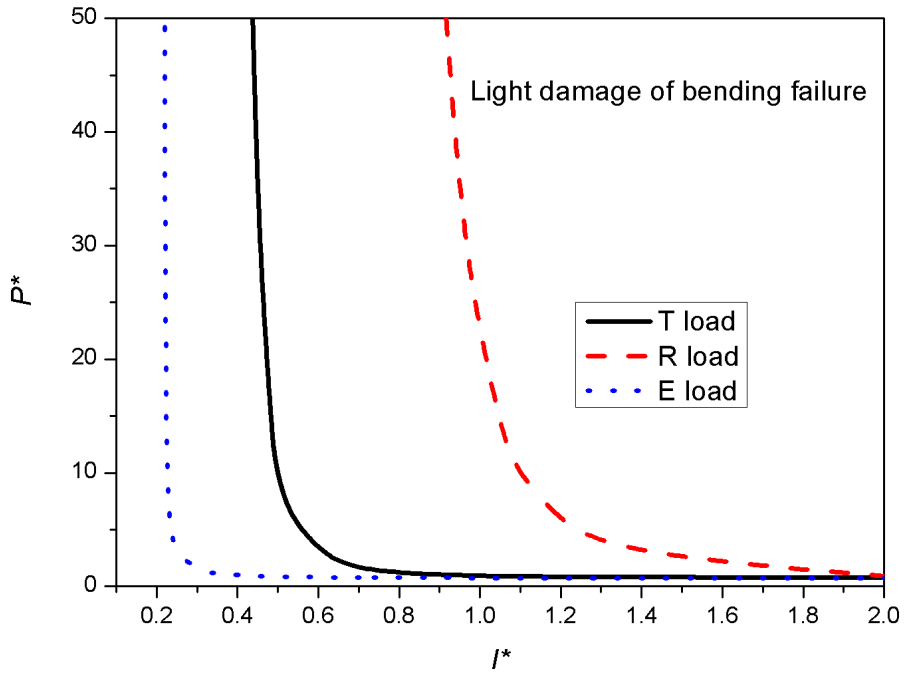

(a) Light damage

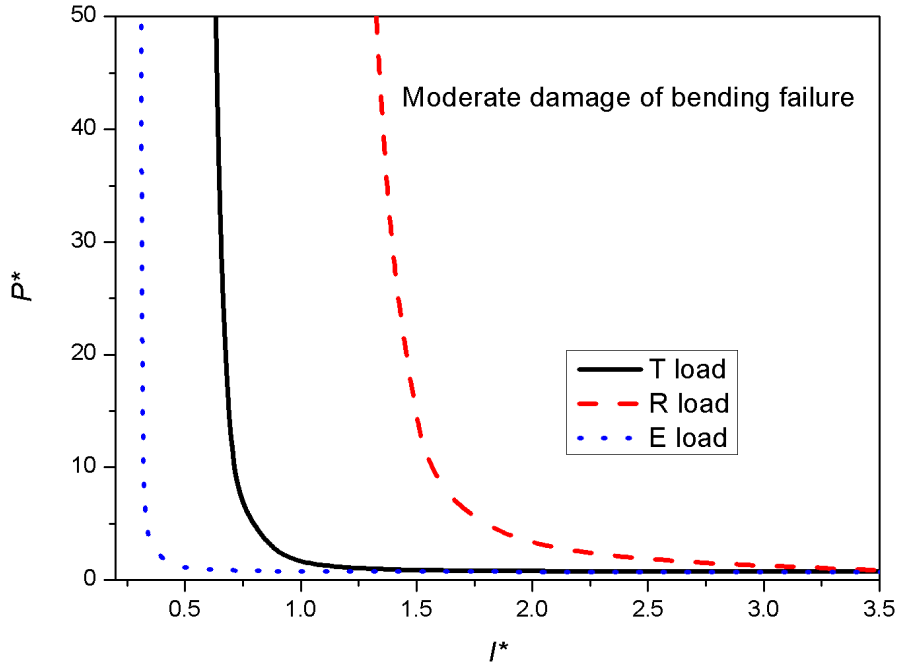

(b) Moderate damage

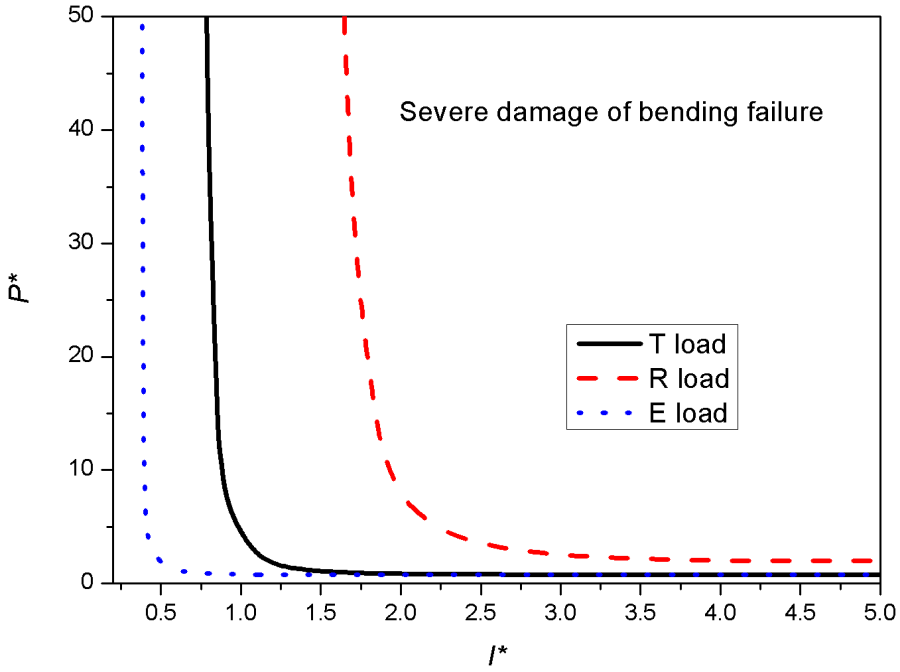

(c) Severe damage

Fig. 5 - 3 Pulse shape effect on bending failure for surface structure against blast load (fixed damage level)

Taking moderate shear and bending damage level as an example, when using results of Youngdahl (1971) to eliminate the pulse shape effect, the relationship among P-I diagrams under the same impulse and pressure magnitude for different load shapes is shown in Fig. 5-4. In this example, although the load durations $t_{dR}<t_{dT}<t_{dE}$, the final displacement of structural element under the exponential load is the smallest, meanwhile that under the rectangular load is the largest. Such result coincides with that of Jones and Song (1986). It also indicates that the shear failure is sensitive to the pulse shape in the dynamic region of P-I diagrams and the bending failure is sensitive in both the dynamic and impulse regions. Moreover, the error caused by pulse shape effect in shear failure is relatively small, and the error in bending failure cannot be ignored. Generally speaking, the shear failure is not sensitive to the pulse shape effect as the bending failure does. It is reasonable since: a) shear displacement stops before structural element reaches its final bending displacement, and is much smaller than the bending displacement; b) structural element has less time to response on shear displacement than bending, therefore shear displacement is mainly decided by magnitude of blast load, while bending displacement is controlled by load magnitude and pulse shape as well.

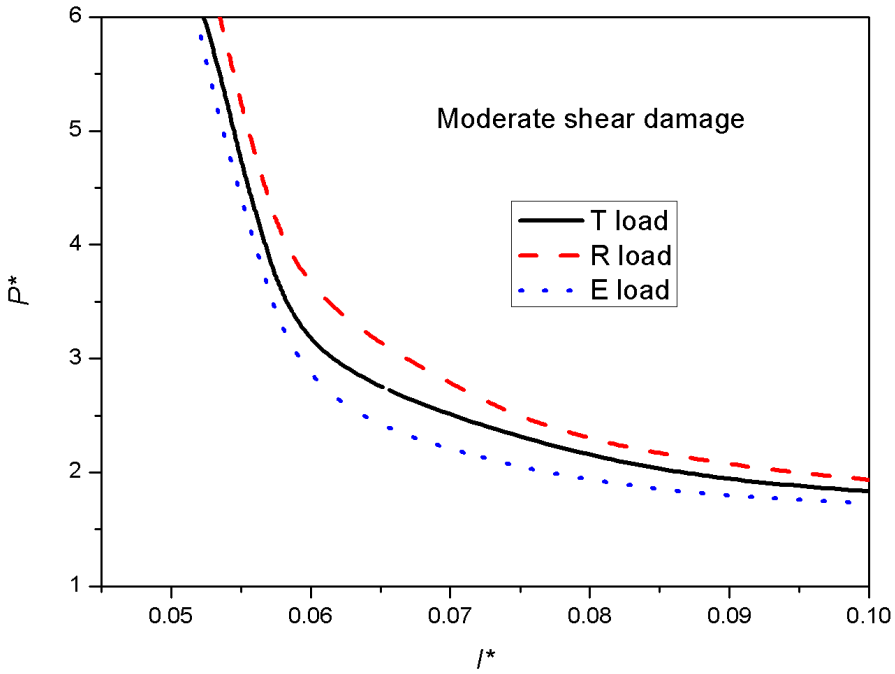

(a) Moderate shear damage

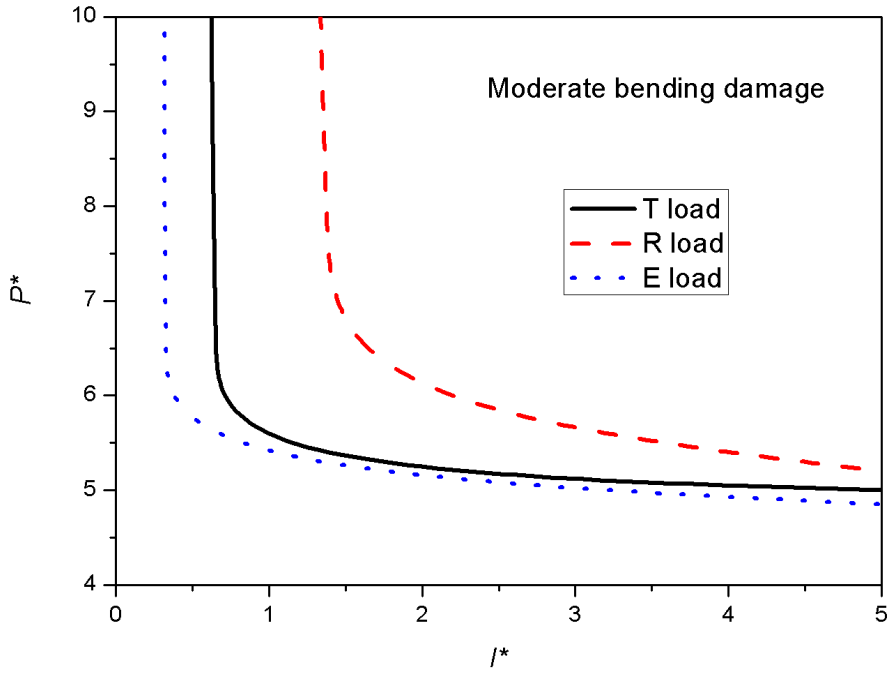

(b) Moderate bending damage

Fig. 5 - 4 Pulse shape effect on surface structure against blast (fixed impulse)

Fig. 5-5 and 5-6 show the relative errors of final time and displacement for the shear and bending failures at different damage levels. At the light damage level, the errors of t_s, t_f, y_s, and y_f are 10%, 9%, 10% and 11% respectively. At the moderate damage level, the errors change to 15%, 22%, 14%, and 22%. The errors at the severe

damage level are the smallest which are 5%, 5%, 5%, and 6% respectively. The largest errors exist in moderate damage level, and the error at light or severe damage level is relatively small. The reason of such phenomenon exists in the pulse shape effect on P-I diagrams as explained previously. At light and severe damage levels it is closer to the quasi-static and impulse region of P-I diagrams respectively, and the pressure and impulse resulted in the moderate level are more likely to fall in the dynamic region. Such phenomenon is only valid for structural element under blast load.

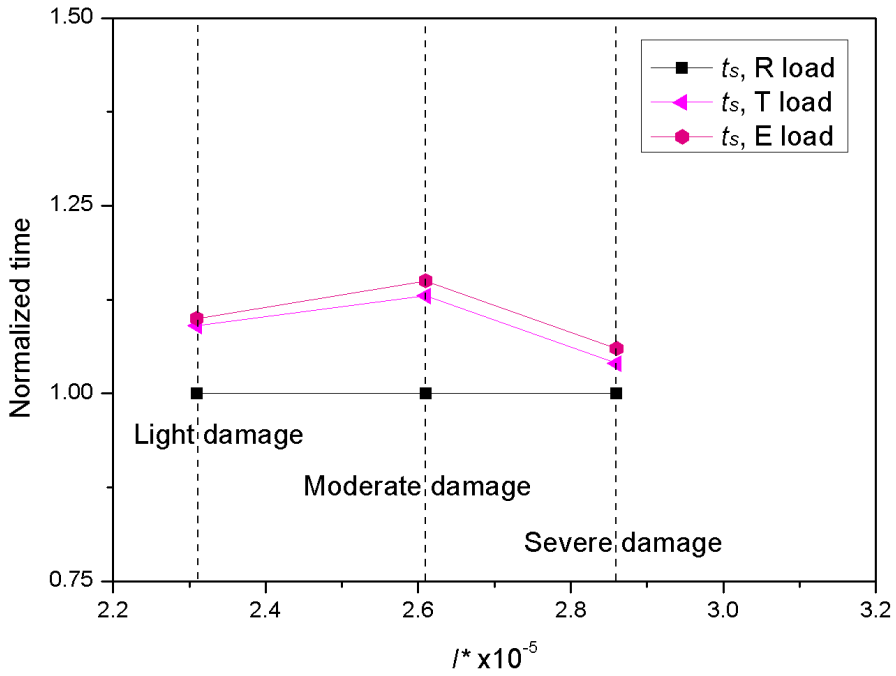

(a) Final time of shear displacement

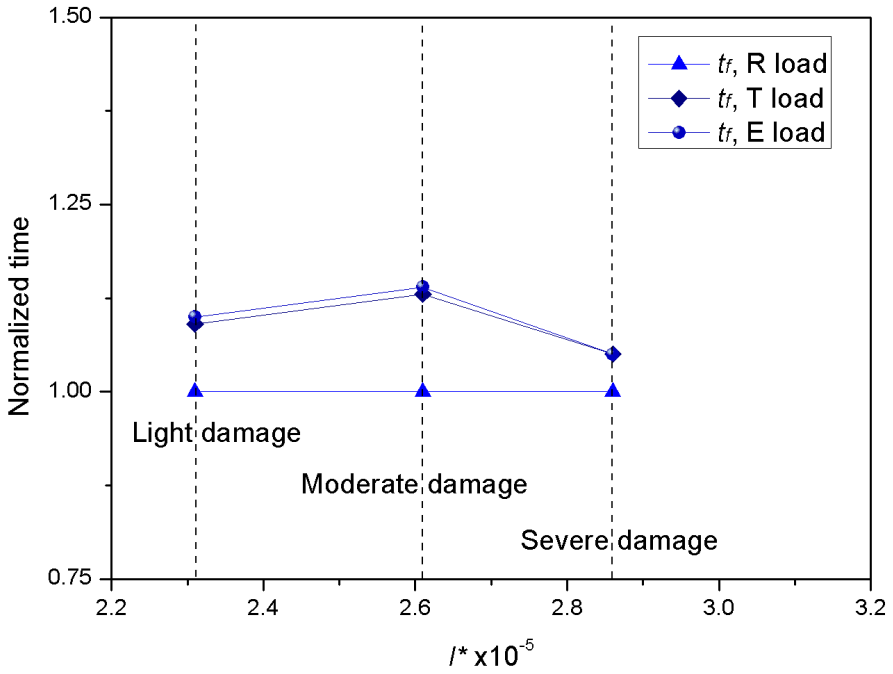

(b) Final time of bending failure

Fig. 5 - 5 Error in the final time of structural response

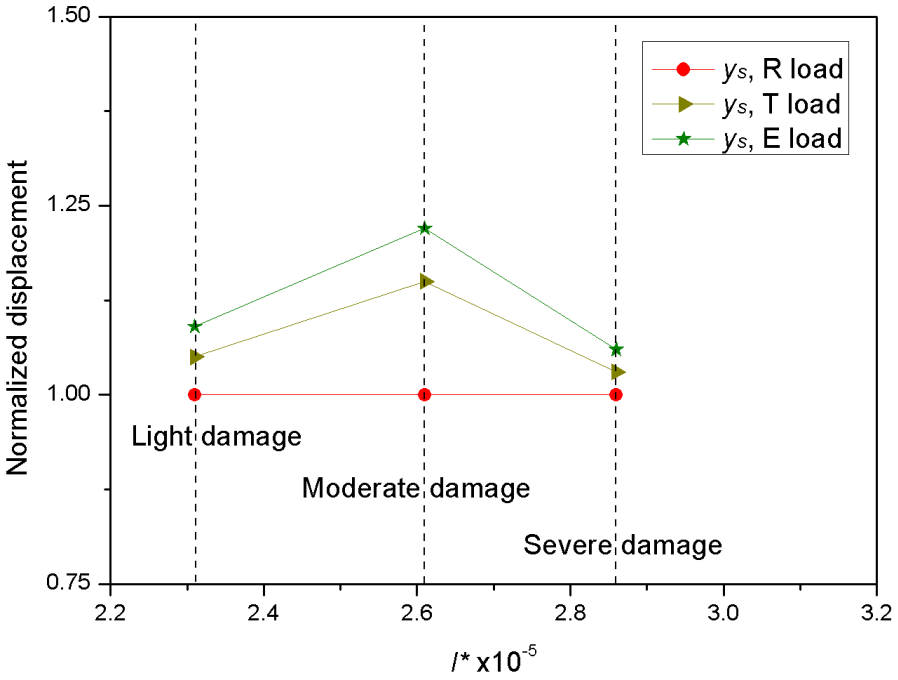

(a) Final displacement of shear failure

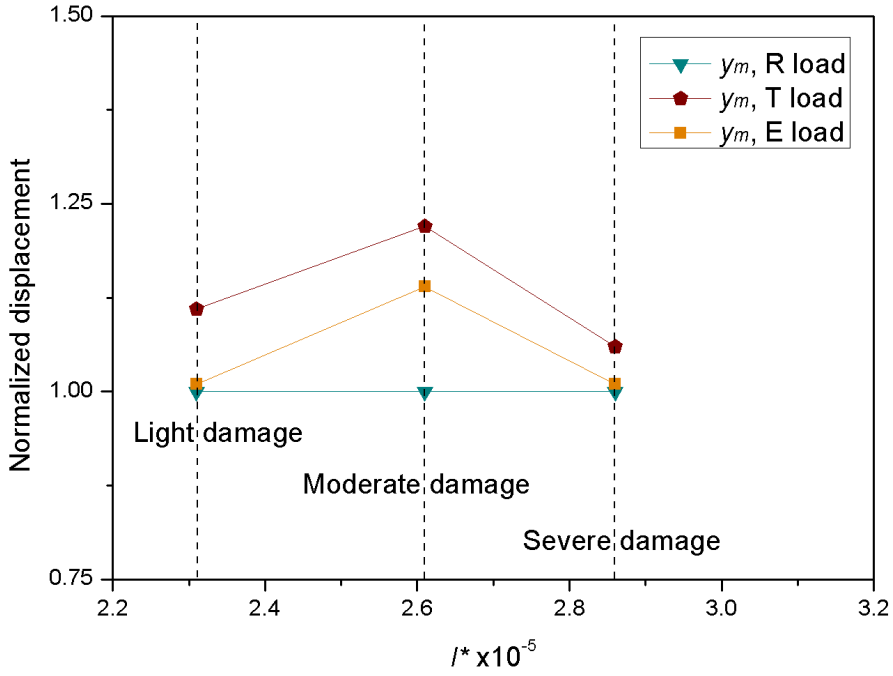

(b) Final displacement of bending failure

Fig. 5 - 6 Error in the final structural displacement

5.6. Conclusions

In the analysis of surface structure, the error caused by the pulse shape difference is very limited in shear displacement, while the effect is distinct in bending displacement. The pulse effect in shear failure is minor in all regions of P-I diagrams, but it is significant in the dynamic region and the impulse region in bending failure. The reason of such phenomenon could be explained by the properties of combined failure modes. In the two combined failure modes (modes 3 and 5), the shear displacement always stops before the bending displacement, and is smaller than the final bending displacement. The pulse shape effect on shear displacement is not as significant as that on bending displacement.

Results from the present study verify that, under the same impulse, the final displacement of structural element under exponential load is the smallest meanwhile that under rectangular load is the largest. The largest errors exist in moderate damage level, and the error in light or severe damage level is relatively small. In

another aspect, errors in quasi-static and impulse regions in P-I diagrams are minor, but the error in dynamic region is significant in all damage levels.

Youngdahl (1971) stated that the pulse shape effect to the P-I diagrams of bending displacement is minor especially in the quasi-static load region and the impulsive load region. But the result from the present study shows that P-I diagrams may also be sensitive to pulse shape effect in the impulsive region for both shear and bending displacements. That is to say the correlation parameter method may not be applied to P-I diagrams based on the MAM.

Generally speaking, results under triangular load and rectangular load overestimate the final displacements of both shear and bending, and the pulse shape effect cannot be ignored.

In the following chapter, the generalized integration method will be applied to the P-I equations for underground structure against blast external and internal blast load. Further extension will be carried out.

CHAPTER 6

NON-CONSTANT SOIL-STRUCTURE INTERACTION EFFECT ON UNDERGROUND STRUCTURE DAMAGE TO BLAST LOAD

6.1. Introduction

In Chapters 3 and 4, the P-I diagrams based on the MAM are extended from surface structures to underground structures. The SSI is simplified to be a damping or stiffness coefficient for underground structure against external or internal blast load respectively. Research result shows that, soil is a complex material which cannot be easily simplified as a homogenous and linear material. Therefore, the assumption of constant SSI coefficient may lead to unavoidable error when calculating the maximum structural deformation, and such error will affect the accuracy of the evaluated structural damage.

This chapter extends the MAM introduced in Chapter 3 and 4. Non-constant SSI is considered for underground structures subjected to external or internal explosions. Based on a similar integration procedure as introduced in Chapter 5, the P-I diagrams of the underground structures are derived semi-analytically and the non-constant SSI effect is therefore included. Both scenarios of underground structures against external and internal blast loads are adopted and the results are compared to those given in Chapter 3 and 4, and the pulse shape effect will also be discussed as done in Chapter 5.

6.2. Assumptions and failure criteria

The assumptions and failure criteria used in the present study remain the same as those in chapters 3 to 5. The rigid-plastic material model is again adopted which leads to the lower bound solution of the problem since the independent maximum bending and shear strength criteria used in analysis circumscribe an interactive shear-bending yield surface.

The maximum deformation occurred in the beam element is again adopted as the failure criterion.

As the major advantage of the MAM, the failure modes still include shear failure, bending failure, combined failure, bending failure with a plastic zone, and combined failure with a plastic zone, which are the same as those in Ma *et al*. (2007) as shown in Fig. 3-3.

These analytical solutions kinematically admissible only.

6.3. Derivation of P-I equations

In the present study, a simply supported beam under uniformly distributed blast pressure is adopted. The derivation of P-I equations remains the same as previous chapters, therefore the governing equations, boundary conditions, initial conditions, and results of structural response are the same in each phase of each mode, except that the damping coefficient and the soil stiffness varies over the response time. The integration procedures for different cases are discussed as follows.

In the cases of underground structure under external blast load, the pressure and damping coefficient changes with time. Again, the material properties (shear strength Q_0 and bending strength M_0) and the maximum blast pressure p_0 should be obtained first, so that the corresponding failure mode from the five possible modes can be determined. In the loading phase, the whole duration is divided into sufficiently small time steps. In each time step, the pressure will be calculated according to the blast load shape equation, the damping coefficient C will be calculated based on the structural response time, and the structural responses obtained will be used as the initial conditions for the next time step till the end of this phase. In the post-loading phase(s), the similar procedure of integration will be used and the final structural displacement can be calculated. In the post-loading phase(s), the damping effect is ignored, and the reason was discussed in section 3.4.5. The flowchart in Fig. 6-1 shows the general procedure of such generalized integration procedure.

In the cases of underground structure under internal blast load, the pressure and soil stiffness effect changes with time. Again, the failure mode can be determined by the material properties (shear strength Q_0 and bending strength M_0) and the maximum blast pressure p_0. In the loading phase, the whole duration is divided into sufficient small time steps. In each time step, the pressure p and soil stiffness K will be updated according to the structural displacement, and the structural responses will be used as the initial conditions for the next time step till the end of this phase. In the post-loading phase(s), the similar procedure of integration will be used and the final structural displacement can be calculated. In the post-loading phase(s), the stiffness effect exists throughout the phases since the beam model always contacts with the soil. The flowchart in Fig. 6-2 shows the flow of such generalized integration procedure.

It should be mentioned that the integration procedures give semi-analytical solutions of underground structural response to arbitrary loading and non-constant soil property. The current analysis is applicable to a more general case for the assessment of structural damage against blast loading. With numerical integrations being involved, P-I curves with respect to different case can be conveniently generated and the MAM becomes more effective in structural damage assessment. Again in each time step, since a constant load, a constant damping coefficient or a soil stiffness are considered, an analytical solution is obtained similar to Chapter 3 and 4. The result of the current step becomes the initial condition of the next step, and thus the explicit integration solves the inelastic dynamic response of the structure element efficiently.

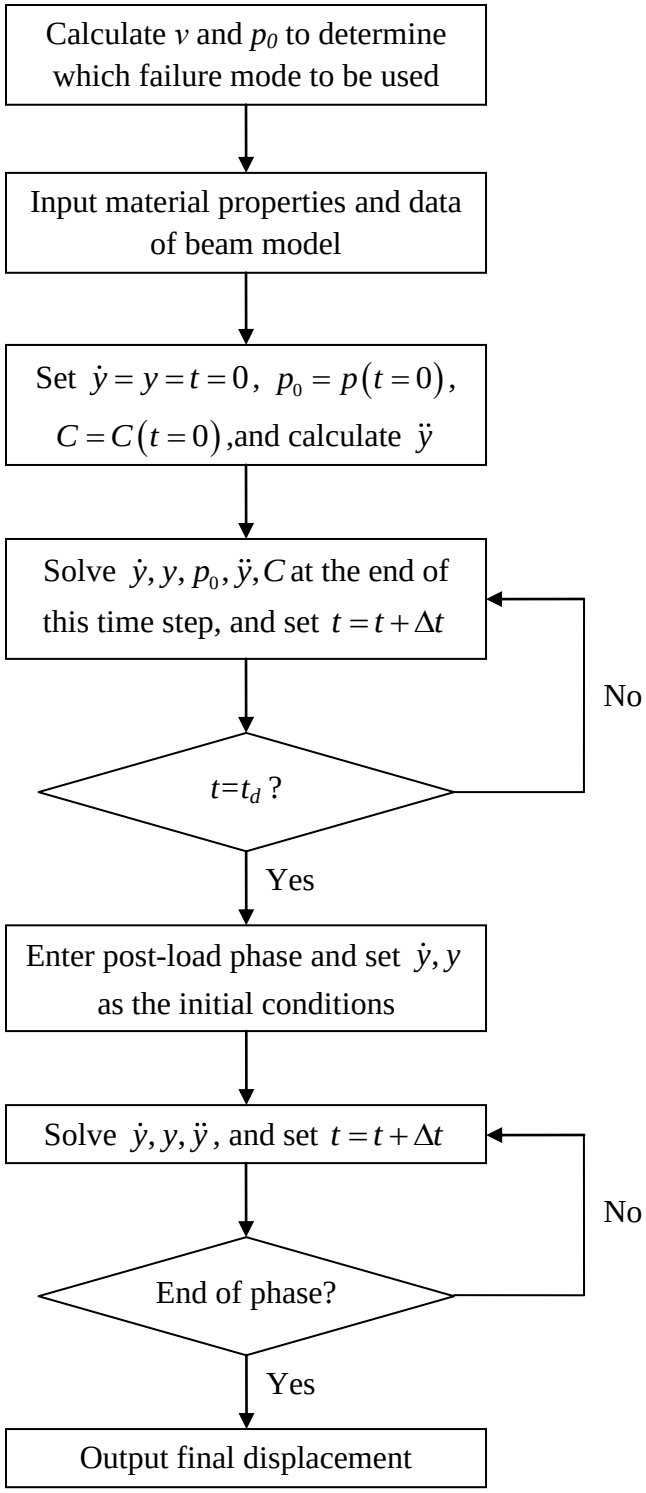

Fig. 6 - 1 Flow chart for underground structure against external blast load

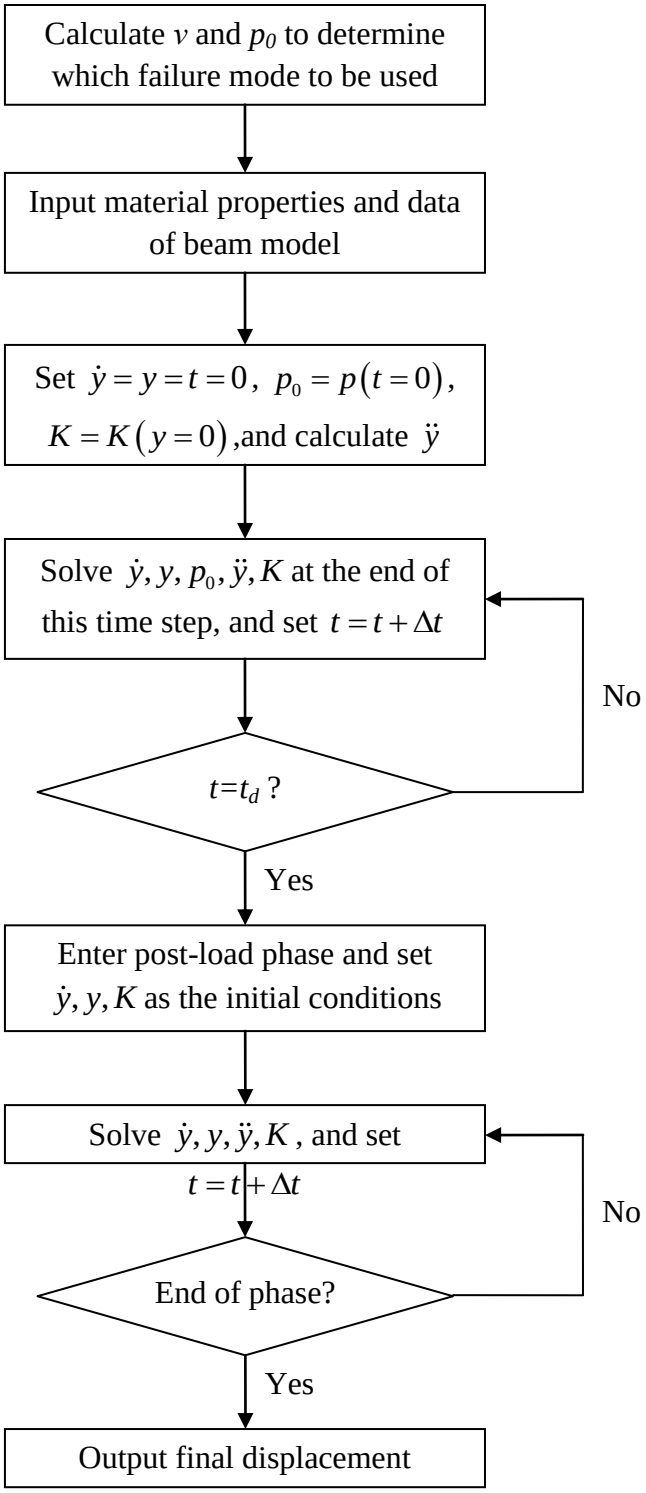

Fig. 6 - 2 Flow chart for underground structure against internal blast load

6.3.1. Underground structure against external blast load

The procedure and most of the equations for generalized integration procedure of underground structure under external blast load are the same as those for surface structure under blast load in Chapter 5. Only the differences are stated below.

The SSI is simplified as a damping coefficient *C* which is a function of time. The governing equation cannot be solved by iteration method used in previous chapters since it couples with $\dot{y}$. Therefore, *C* is treated as a constant in every time step when using the general integration method and the time step is smaller enough to make sure the error caused by such dealing method of *C* does not affect result of structural displacement so much.

Mode 1 (Shear failure mode)

Phase 1: Due to the non-constant damping coefficient effect, the governing equation becomes:

$$\frac{\partial Q}{\partial x} = -p + m\ddot{y}_s + C\dot{y}_s \tag{6.1}$$

where *C(t)* is the damping effect, which is a function of time.

And the maximum shear acceleration for integration is:

$$\ddot{y}_s\left(t_i\right) = \frac{e^{\frac{-C\cdot t_i}{m}}\left[\,p\left(t_i\right)L - Q_0\,\right]}{mL} \tag{6.2}$$

Phase 2: All equations are the same as those for surface structure since the damping coefficient vanishes in the post-loading phase.

Mode 2 (Bending failure mode)

Phase 1: The governing equation changes to:

$$\frac{\partial Q}{\partial x} = -p + m\ddot{y}_m\left(1-\frac{x}{L}\right) + C\dot{y}_m\left(1-\frac{x}{L}\right) \tag{6.3}$$

The maximum bending acceleration for integration is:

$$\ddot{y}_m(t_i) = \frac{3e^{\frac{-C\cdot t_i}{m}}\left[p(t_i)L^2 - 2M_0\right]}{mL^2} \tag{6.4}$$

Phase 2: All equations are the same as those for surface structure.

Mode 3 (Combined failure mode)

Phase 1: The governing equation is:

$$\frac{\partial Q}{\partial x} = -p + m\ddot{y}_s + m(\ddot{y}_m - \ddot{y}_s)\left(1 - \frac{x}{L}\right) + C\dot{y}_s + C(\dot{y}_m - \dot{y}_s)\left(1 - \frac{x}{L}\right) \tag{6.5}$$

For integration, the maximum shear and bending acceleration are as follows:

$$\ddot{y}_s(t_i) = \frac{e^{\frac{-C\cdot t_i}{m}}\left[p(t_i)L^2 + 6M_0 - 4Q_0L\right]}{mL^2} \tag{6.6}$$

$$\ddot{y}_m(t_i) = \frac{e^{\frac{-C\cdot t_i}{m}}\left[p(t_i)L^2 - 6M_0 + 2Q_0L\right]}{mL^2} \tag{6.7}$$

Phase 2: All equations are the same as those for surface structure.

Phase 3: All equations are the same as those for surface structure.

Mode 4 (Bending failure mode with a plastic zone)

Phase 1: The governing equation changes to:

$$\frac{\partial Q}{\partial x} = -p + m\ddot{y}_m\frac{(L-x)}{(L-\xi_0)} + C\dot{y}_m\frac{(L-x)}{(L-\xi_0)} \tag{6.8}$$

The maximum bending acceleration for integration are as follows:

$$\ddot{y}_m(t_i) = \frac{e^{\frac{-C\cdot t_i}{m}}p(t_i)}{m} \tag{6.9}$$

Phase 2: All equations are the same as those for surface structure.

Phase 3: All equations are the same as those for surface structure.

Mode 5 (Combined failure mode with a plastic zone)

Phase 1: The governing equation is:

$$\frac{\partial Q}{\partial x} = -p + m\ddot{y}_s + m\left(\ddot{y}_m - \ddot{y}_s\right)\frac{\left(L-x\right)}{\left(L-\xi_0\right)} + C\dot{y}_s + C\left(\dot{y}_m - \dot{y}_s\right)\frac{\left(L-x\right)}{\left(L-\xi_0\right)} \quad (6.10)$$

The maximum shear and bending acceleration for integration are as follows:

$$\ddot{y}_s\left(t_i\right) = \frac{e^{\frac{-C\cdot t_i}{m}}}{m\left(L-\xi_0\right)^2}\left[\, p\left(t_i\right)\cdot\left(L-\xi_0\right)^2 - 4Q_0\left(L-\xi_0\right) + 6M_0 \,\right] \quad (6.11)$$

$$\ddot{y}_m\left(t_i\right) = \frac{e^{\frac{-C\cdot t_i}{m}}}{m\left(L-\xi_0\right)^2}\left[\, p\left(t_i\right)\cdot\left(L-\xi_0\right)^2 - 2Q_0\left(L-\xi_0\right) - 6M_0 \,\right] \quad (6.12)$$

Phase 2: All equations are the same as those for surface structure.

Phase 3: All equations are the same as those for surface structure.

Phase 4: All equations are the same as those for surface structure.

6.3.2. Underground structure against internal blast load

The procedure and most of the equations for generalized integration procedure of underground structure under internal blast load are the same as those for surface structure under blast load. The soil stiffness *K* is a function of the structural displacement but it is treated as a constant in every time step of integration. The governing equations cannot be solved by the iteration method used in previous chapters since it couples with structural displacement. Therefore, *K* is treated as a constant in every time step when using the general integration method and the time step is smaller enough to make sure the error caused by such dealing method of *K* does not affect result of structural displacement so much. Only the differences are stated below.

Mode 1 (Shear failure mode)

Phase 1: The governing equation changes to:

$$\frac{\partial Q}{\partial x} = -p + m\ddot{y}_s + Ky_s \tag{6.13}$$

The maximum shear acceleration for integration is:

$$\ddot{y}_s(t_i) = \frac{\sin\left[\frac{\sqrt{K}t_i}{\sqrt{m}}\right]\left[p(t_i)L - Q_0\right]}{\sqrt{mK}L} \tag{6.14}$$

Phase 2: The governing equation is:

$$\frac{\partial Q}{\partial x} = m\ddot{y}_s + K\dot{y}_s \tag{6.15}$$

The maximum shear acceleration in this phase for integration changes to:

$$\ddot{y}_s(t_i) = -\frac{\sin\left(\frac{\sqrt{K}t_i}{\sqrt{m}}\right)\sqrt{K}\cdot\dot{y}_s(t_d)}{\sqrt{m}} - \frac{\cos\left(\frac{\sqrt{K}t_i}{\sqrt{m}}\right)\left[y_s(t_d)LK + Q_0\right]}{mL} \tag{6.16}$$

Mode 2 (Bending failure mode)

Phase 1: The governing equation is:

$$\frac{\partial Q}{\partial x} = -p + m\ddot{y}_m\left(1 - \frac{x}{L}\right) + Ky_m\left(1 - \frac{x}{L}\right) \tag{6.17}$$

The maximum bending acceleration for integration changes to:

$$\ddot{y}_m(t_i) = \frac{3\cos\left(\frac{\sqrt{K}t_i}{\sqrt{m}}\right)\left[p(t_i)L^2 - 2M_0\right]}{2mL^2} \tag{6.18}$$

Phase 2: The governing equation is:

$$\frac{\partial Q}{\partial x} = m\ddot{y}_m\left(1 - \frac{x}{L}\right) + Ky_m\left(1 - \frac{x}{L}\right) \tag{6.19}$$

Here the maximum bending acceleration for integration changes to:

$$\ddot{y}_m(t_i)=\frac{\cos\left(\frac{\sqrt{K}t_i}{\sqrt{m}}\right)\left[-y_m(t_d)\cdot KL^2-3M_0\right]}{mL^2}-\frac{\sin\left(\frac{\sqrt{K}t_i}{\sqrt{m}}\right)\sqrt{K}\cdot\dot{y}_m(t_d)}{\sqrt{m}} \quad (6.20)$$

Mode 3 (Combined failure mode)

Phase 1: The governing equation is:

$$\frac{\partial Q}{\partial x}=-p+m\ddot{y}_s+m(\ddot{y}_m-\ddot{y}_s)\left(1-\frac{x}{L}\right)+Ky_s+K(y_m-y_s)\left(1-\frac{x}{L}\right) \quad (6.21)$$

The maximum shear and bending acceleration changes to:

$$\ddot{y}_s(t_i)=\frac{\cos\left(\frac{\sqrt{K}t_i}{\sqrt{m}}\right)\left[p(t_i)L^2-4Q_0L+6M_0\right]}{mL^2} \quad (6.22)$$

$$\ddot{y}_m(t_i)=\frac{\cos\left(\frac{\sqrt{K}t_i}{\sqrt{m}}\right)\left[p(t_i)L^2+2Q_0L-6M_0\right]}{mL^2} \quad (6.23)$$

Phase 2: The governing equation is:

$$\frac{\partial Q}{\partial x}=m\ddot{y}_s+m(\ddot{y}_m-\ddot{y}_s)\left(1-\frac{x}{L}\right)+Ky_s+K(y_m-y_s)\left(1-\frac{x}{L}\right) \quad (6.24)$$

The maximum shear and bending acceleration changes to:

$$\ddot{y}_s(t_i)=\frac{\cos\left(\frac{\sqrt{K}t_i}{\sqrt{m}}\right)K\left[6M_0-4Q_0L-y_s(t_d)\cdot KL^2\right]}{mKL^2}-\frac{\sin\left(\frac{\sqrt{K}t_i}{\sqrt{m}}\right)K^{\frac{3}{2}}L^2\dot{y}_s(t_d)}{\sqrt{m}KL^2} \quad (6.25)$$

$$\ddot{y}_m(t_i)=\frac{\cos\left(\frac{\sqrt{K}t_i}{\sqrt{m}}\right)K\left[2Q_0L-6M_0-y_m(t_d)\cdot KL^2\right]}{mKL^2}-\frac{\sin\left(\frac{\sqrt{K}t_i}{\sqrt{m}}\right)K^{\frac{3}{2}}L^2\dot{y}_m(t_d)}{\sqrt{m}KL^2} \quad (6.26)$$

Phase 3: The governing equation is the same as Eq. (6.19).

The maximum bending acceleration is as Eq. (6.20).

Mode 4 (Bending failure mode with a plastic zone)

Phase 1: The governing equation changes to:

$$\frac{\partial Q}{\partial x} = -p + m\ddot{y}_m \frac{(L-x)}{(L-\xi_0)} + Ky_m \frac{(L-x)}{(L-\xi_0)} \tag{6.27}$$

The maximum bending acceleration for integration is:

$$\ddot{y}_m(t_i) = \frac{3\cos\left(\frac{\sqrt{K}t_i}{\sqrt{m}}\right)\left[p(t_i)\cdot(L-\xi_0)^2 - 2M_0\right]}{2m(L-\xi_0)^2} \tag{6.28}$$

Phase 2: The governing equation is:

$$\frac{\partial Q}{\partial x} = m\ddot{y}_m \frac{(L-x)}{(L-\xi)} + Ky_m \frac{(L-x)}{(L-\xi)} \tag{6.29}$$

The maximum bending acceleration for integration is zero.

Phase 3: The governing equation is the same as Eq. (6.19), and the maximum bending acceleration for integration is:

$$\ddot{y}_m(t_i) = -\frac{\sin\left(\frac{\sqrt{K}t_i}{\sqrt{m}}\right)\sqrt{K}\cdot\dot{y}_m(t_1)}{\sqrt{m}} - \frac{\cos\left(\frac{\sqrt{K}t_i}{\sqrt{m}}\right)\left[y_m(t_1)\cdot KL^2 + 3M_0\right]}{mL^2} \tag{6.30}$$

Mode 5 (Combined failure with a plastic zone)

Phase 1: The governing equation changes to:

$$\frac{\partial Q}{\partial x} = -p + m\ddot{y}_s + m(\ddot{y}_m - \ddot{y}_s)\frac{(L-x)}{(L-\xi_0)} + Ky_s + K(y_m - y_s)\frac{(L-x)}{(L-\xi_0)} \tag{6.31}$$

The maximum shear and bending acceleration are:

$$\ddot{y}_s(t_i) = \frac{\cos\left(\frac{\sqrt{K}t_i}{\sqrt{m}}\right)\left[p(t_i)\cdot(L-\xi_0)^2 - 4Q_0(L-\xi_0) + 6M_0\right]}{m(L-\xi_0)^2} \tag{6.32}$$

$$\ddot{y}_m(t_i)=\frac{\cos\left(\frac{\sqrt{K}t_i}{\sqrt{m}}\right)\left[p(t_i)\cdot(L-\xi_0)^2+2Q_0(L-\xi_0)-6M_0\right]}{m(L-\xi_0)^2} \tag{6.33}$$

Phase 2: The governing equation is:

$$\frac{\partial Q}{\partial x}=m\ddot{y}_s+m(\ddot{y}_m-\ddot{y}_s)\frac{(L-x)}{(L-\xi)}+Ky_s+K(y_m-y_s)\frac{(L-x)}{(L-\xi)} \tag{6.34}$$

The maximum shear and bending acceleration change to:

$$\ddot{y}_s(t_i)=\frac{-\sin\left(\frac{\sqrt{K}t_i}{\sqrt{m}}\right)K^{\frac{3}{2}}\dot{y}_s(t_d)M_0}{mKM_0}-\frac{\cos\left(\frac{\sqrt{K}t_i}{\sqrt{m}}\right)K\left[2Q_0^2+3y_s(t_i)KM_0\right]}{3mKM_0} \tag{6.35}$$

$$\ddot{y}_m(t_i)=-\frac{\sin\left(\frac{\sqrt{K}t_i}{\sqrt{m}}\right)\sqrt{K}\dot{y}_m(t_d)}{\sqrt{m}}-\frac{\cos\left(\frac{\sqrt{K}t_i}{\sqrt{m}}\right)Ky_m(t_d)}{m} \tag{6.36}$$

Phase 3: The governing equation is:

$$\frac{\partial Q}{\partial x}=m\ddot{y}_m\frac{(L-x)}{(L-\xi)}\dot{\xi}+Ky_m\frac{(L-x)}{(L-\xi)} \tag{6.37}$$

The maximum bending acceleration equals to zero.

Phase 4: The governing equation remains the same as Eq. (6.19), and the maximum bending acceleration is:

$$\ddot{y}_m(t_i)=\frac{\cos\left(\frac{\sqrt{K}t_i}{\sqrt{m}}\right)\left[-y_m(t_1)\cdot KL^2-3M_0\right]}{mL^2}-\frac{\sin\left(\frac{\sqrt{K}t_i}{\sqrt{m}}\right)\sqrt{K}\cdot\dot{y}_m(t_1)}{\sqrt{m}} \tag{6.38}$$

6.4. P-I diagrams and result discussion

The normalized pressure (P^*) and normalized impulse (I^*) used for P-I diagrams in the following remain the same as defined in Eq. (3.48).

6.4.1. Underground structure (external blast load)

The SSI in underground structure against external blast load scenario is simplified as a damping coefficient. Such assumption is based on the physical basis of SSI in the external explosion cases. The damping effect will definitely become smaller during the duration of blast load since the contact area between soil and structure changes from full contact to non-contact when the blast wave is reflected on the surface RC wall. The soil layer will completely be separated from RC wall when the velocity of soil layer is smaller than that of structure according to Eq. (3.5); and the time may be at the end of loading or even earlier, which depends on soil properties and intense of load.

The damping coefficient, which represents the simplification of soil-structure interaction, can be expressed as Eq. (6.39). The damping factor in the present study is assumed attenuating with time and vanishing when the blast load stops. Such simplification is based on the fact that the SSI starts when the blast load acting on the structure and attenuates to zero when the blast load stops. The change of SSI magnitude may be different in real case, while it is not in the scope of current study.

$$C(t) = C_0\left(1 - \frac{t}{t_d}\right) \tag{6.39}$$

where C_0 is the maximum damping effect during blast load.

Fig. 6-3 and 6-4 show the effect of the non-constant damping for underground structure under external blast load. Like the surface structure under blast load, the pulse shape effect on bending deformation at different damage levels is more significant than that on shear deformation. The P-I diagrams of shear and bending deformations are sensitive to the pulse shape effect in the impulse and dynamic regions. Comparing with Fig. 5-3, it indicates that the pulse shape effect on the impulse and dynamic region in P-I diagrams of shear deformation cannot be ignored for underground structures under external blast load. The only reason should be the simplified SSI used in the derivation of P-I equations. The pulse shape effect on bending deformation is not as significant as that on surface structures but still cannot be neglected.

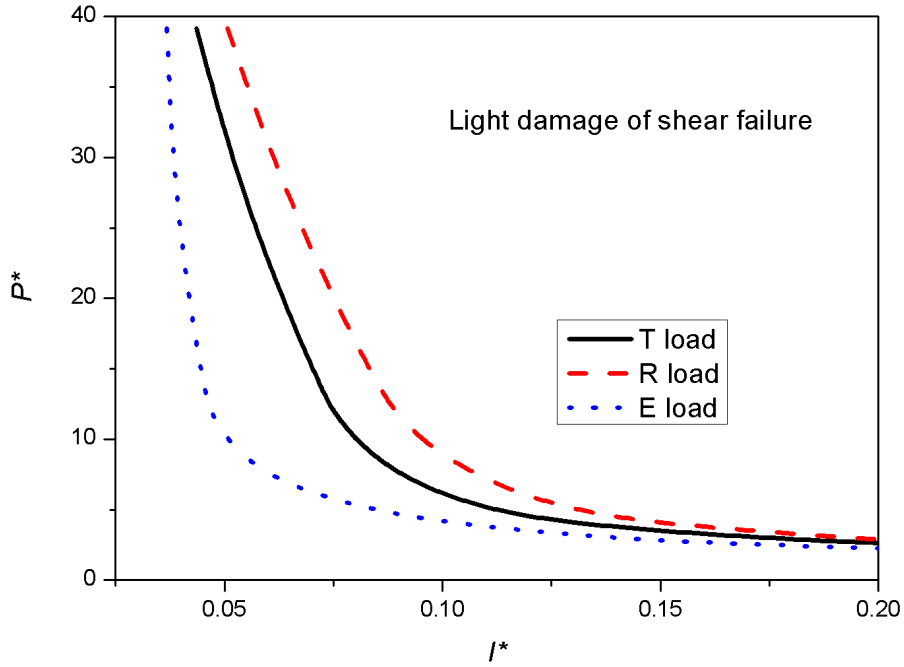

(a) Light damage

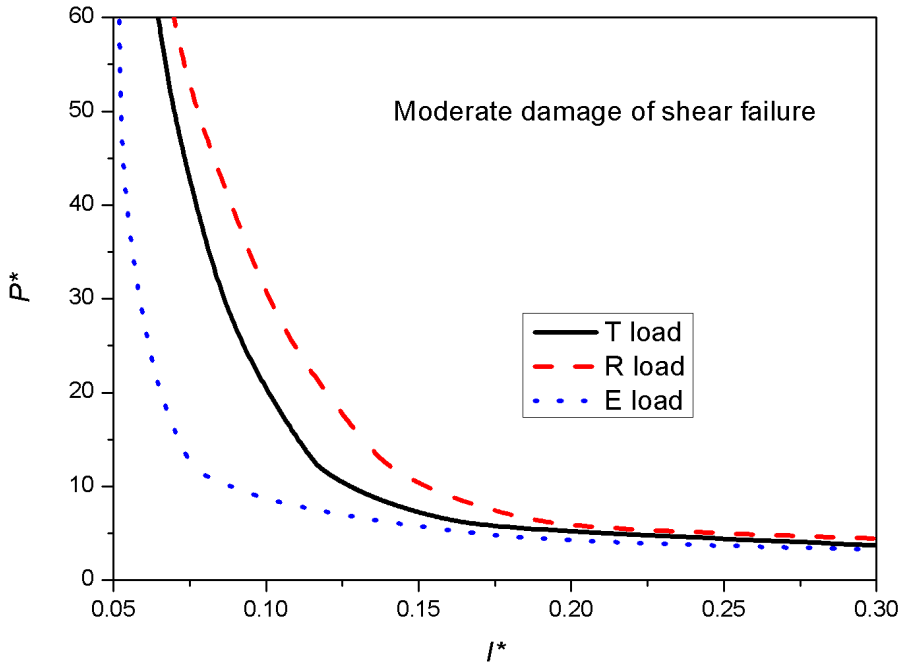

(b) Moderate damage

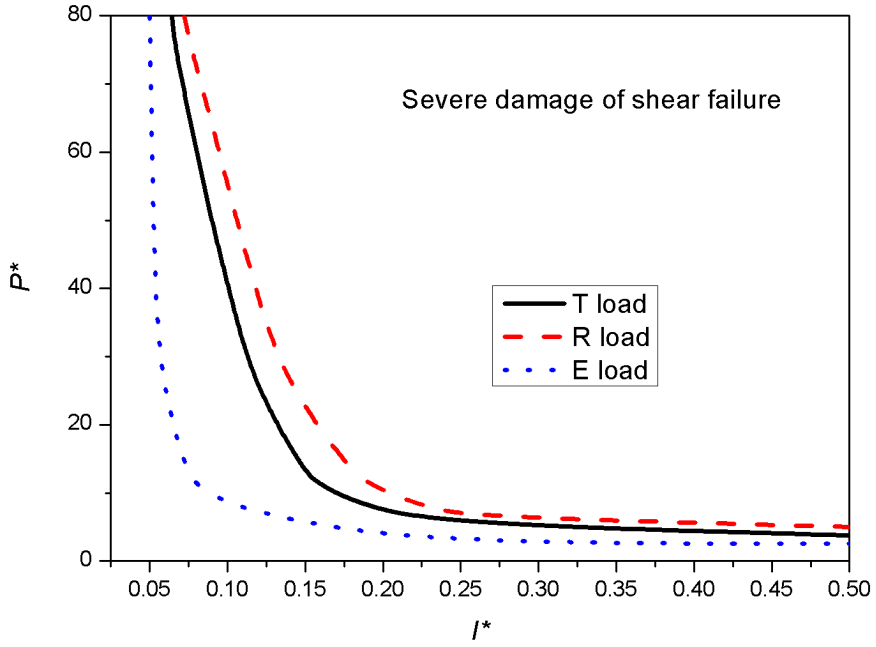

(c) Severe damage

Fig. 6 - 3 Pulse shape difference of shear failure for underground structure against external blast load

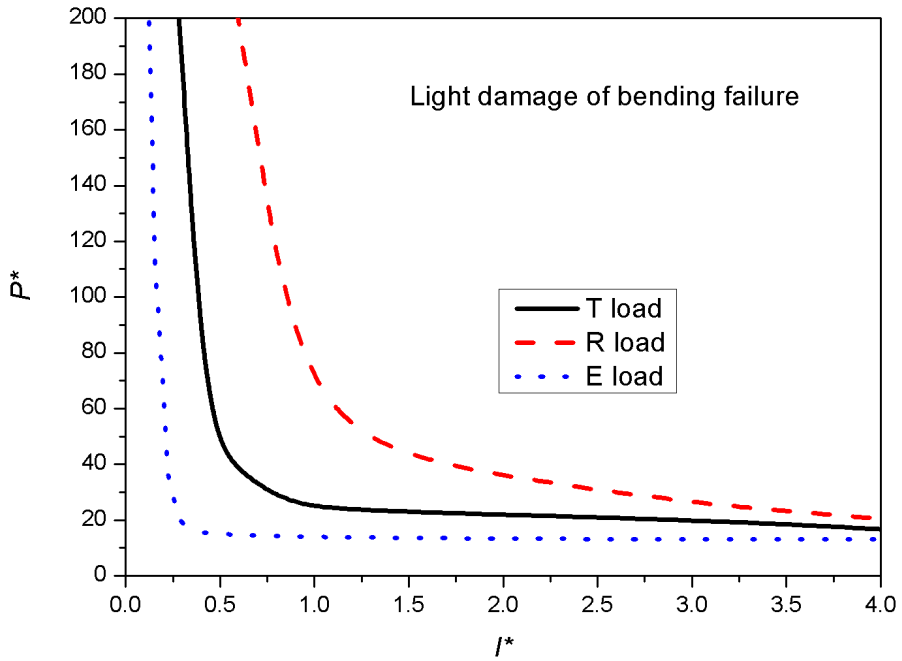

(a) Light damage

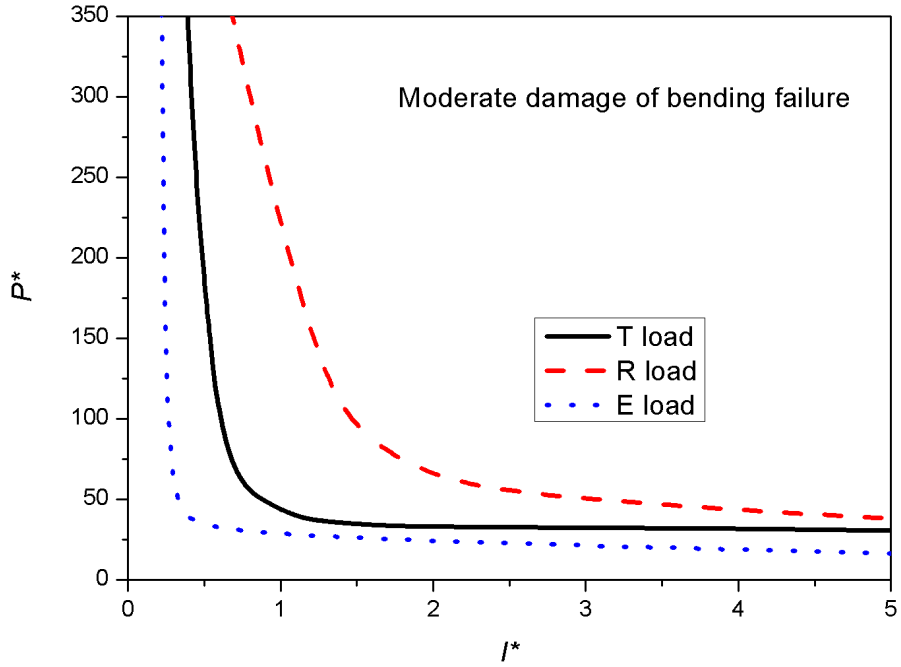

(b) Moderate damage

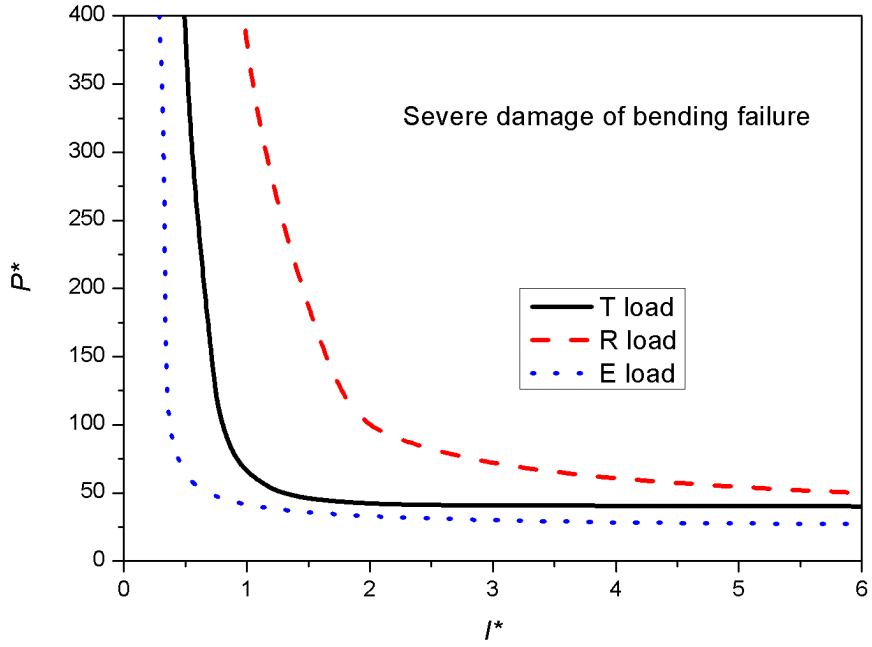

(c) Severe damage

Fig. 6 - 4 Pulse shape difference of bending failure for underground structure against external blast load

The difference of constant and non-constant damping effect for shear and bending failure mode is shown in Fig. 6-5. The moderate damage level is adopted as an example. It can be seen from Fig. 6-5 a) that, the non-constancy of damping effect

on shear deformation is sensitive in the impulsive and dynamic regions of P-I diagrams, and these two P-I curves intersect in the quasi-static region. It is because that, under the same pressure and impulse, the non-constancy of damping affects the final structural displacement especially when the blast pressure is low. Fig. 6-5 b) shows that the pulse shape effect on bending deformation is similar to that on shear deformation, but no intersection of P-I curves.

Generally, Fig. 6-5 shows that the P-I diagrams are sensitive to the non-constancy of SSI in the dynamic and impulsive region. The reason lies in the fact that the effect of damping on the final displacement of structural element is based on the structural velocity. In the quasi-static region of P-I diagrams, the structural velocity is relatively low therefore the damping effect is limited. But in the dynamic and impulsive region, the effect of damping increase with the maximum structural velocity. The constant damping effect will absorb more energy than the non-constant damping effect so that under the same pressure and impulse the structural displacements for shear and bending with non-constant damping coefficient are smaller than that with a constant damping coefficient. It can be seen as well from Fig. 11 that, the result of non-constant damping effect is close to the result of without considering the soil damping effect. This phenomenon somehow verifies that neglecting damping effect in blast effect analysis is reasonable, but the accuracy of result in dynamic region of P-I diagram should be further discussed.

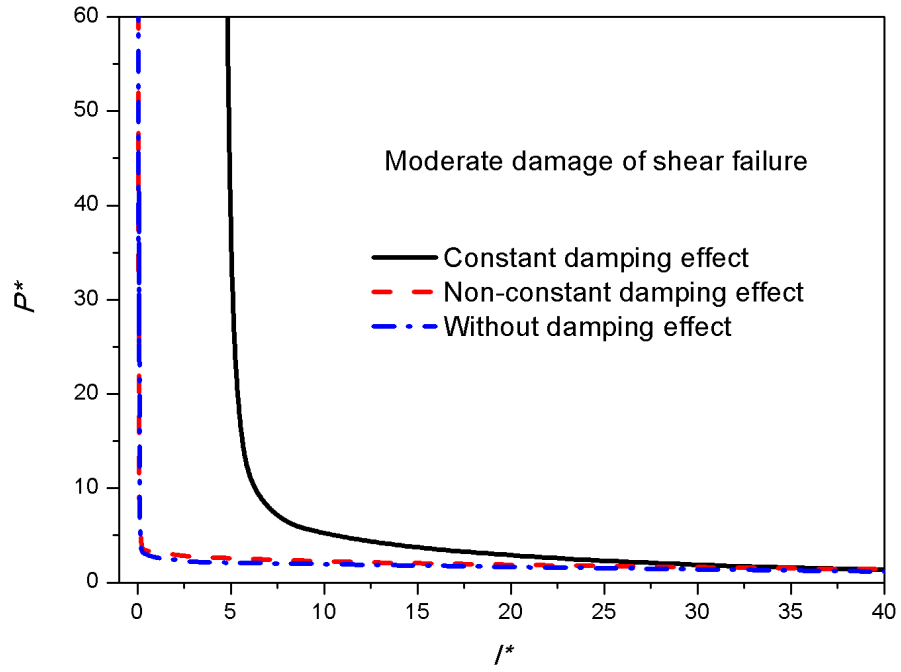

a) Shear failure

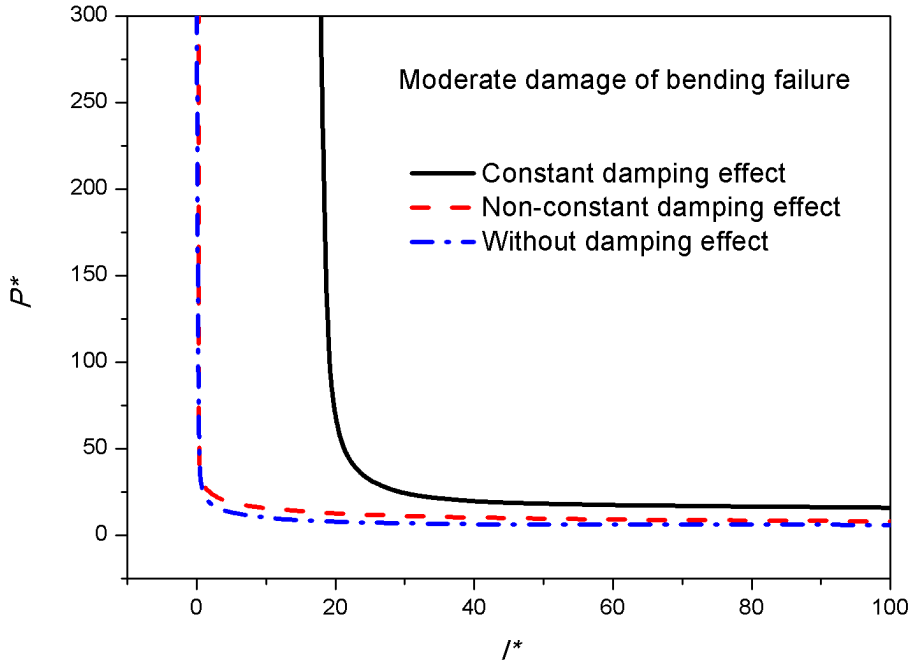

b) Bending failure

Fig. 6 - 5 Difference of constant and non-constant damping effect

6.4.2. Underground structure (internal blast load)

The soil-structure interaction is simplified as the soil stiffness effect, and the K is expressed as a piecewise function as below:

$$K(y)=\begin{cases} K_0+(K_c-K_0)\dfrac{y}{y_c} & y<y_c \\ K_c & y\geq y_c \end{cases} \tag{6.40}$$

where K_0 is the soil stiffness before compression, K_c is the soil stiffness after full compression, y_c is the displacement when the soil is assumed as fully compressed.

The simplification of SSI in underground structure against internal blast load scenario is to adopt a piece-wise stiffness coefficient which is a function of structural displacement. Such assumption is based on the physical properties of soil before and after compression, which presents the hardening of soil material under compression in macro physical scope. Before compression, the soil is assumed as elastic base with stiffness K_0, and its stiffness increases to K_c when the soil is fully compressed and the change of stiffness is assumed as linear.

Fig. 6-6 and 6-7 show the non-constant soil stiffness effect with pulse shape difference of underground structure under internal blast load. Different from the pulse shape effect on underground structure against external blast load, the effect in present study is significant in the quasi-static region in P-I diagrams for shear deformation as well. It is because the soil stiffness effect exists throughout the process of structural deformation. In the quasi-static region and under the same impulse, the effective pressure of rectangular load is higher than that of triangular or exponential load, therefore the displacement of structural element under rectangular load is the largest. Such fact exists in the bending deformation, but the pulse shape effect is not so significant in the quasi-static region because the bending deformation is normally much larger than the shear deformation.

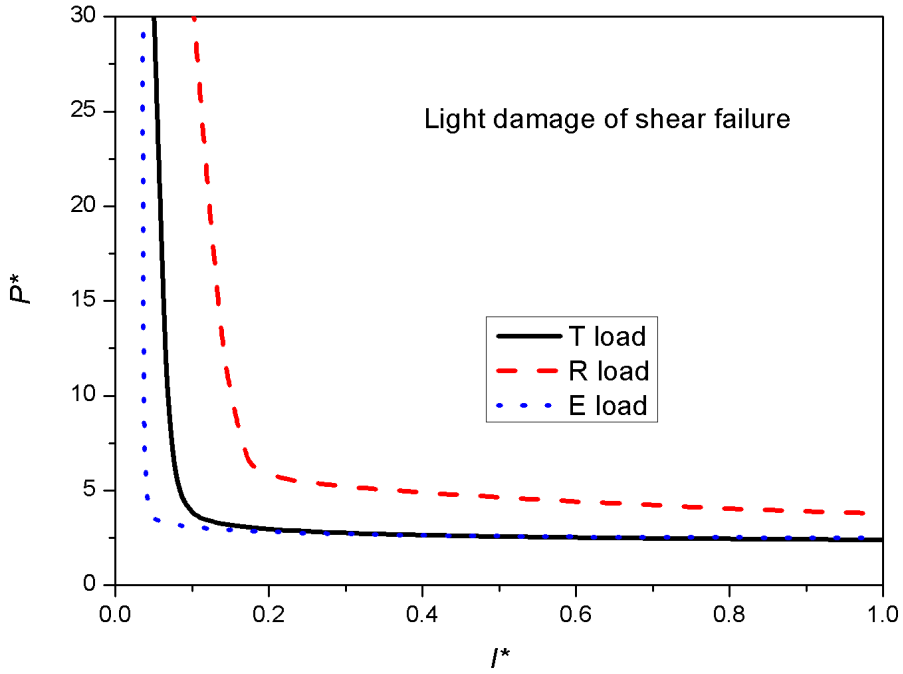

(a) Light damage

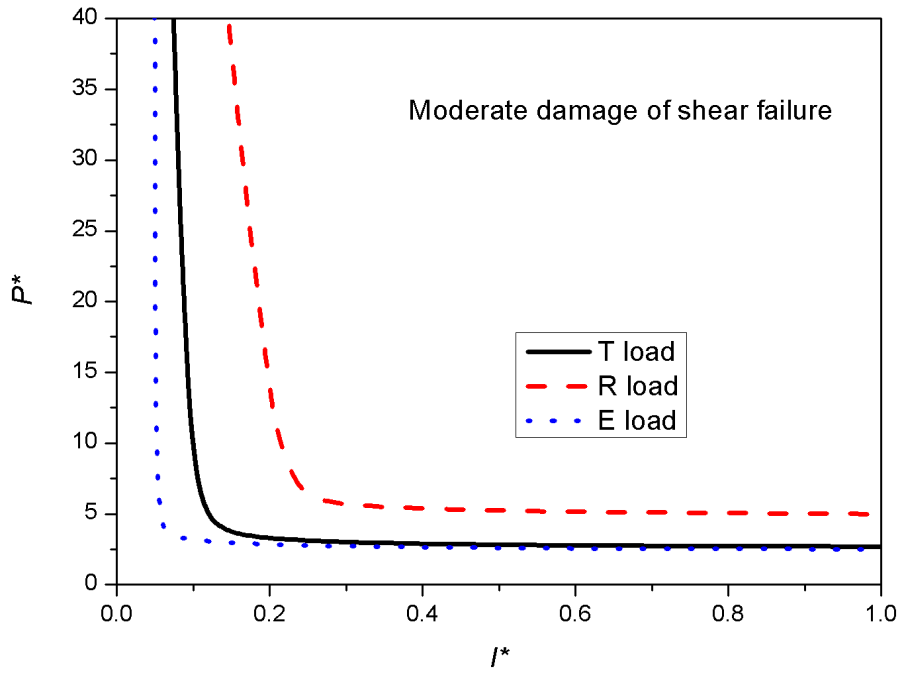

(b) Moderate damage

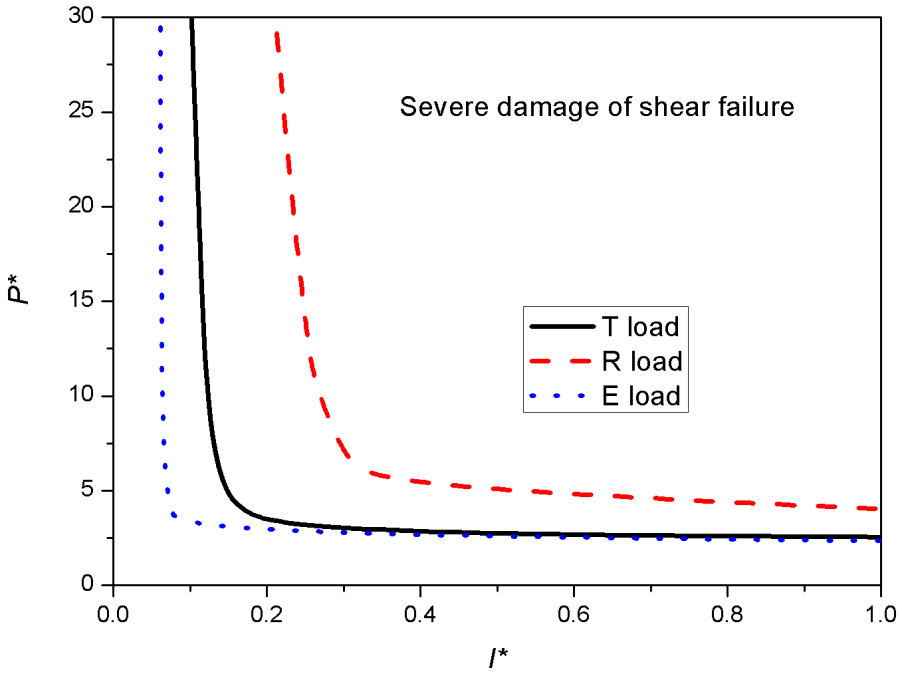

(c) Severe damage

Fig. 6 - 6 Pulse shape difference of shear failure for underground structure against internal blast load

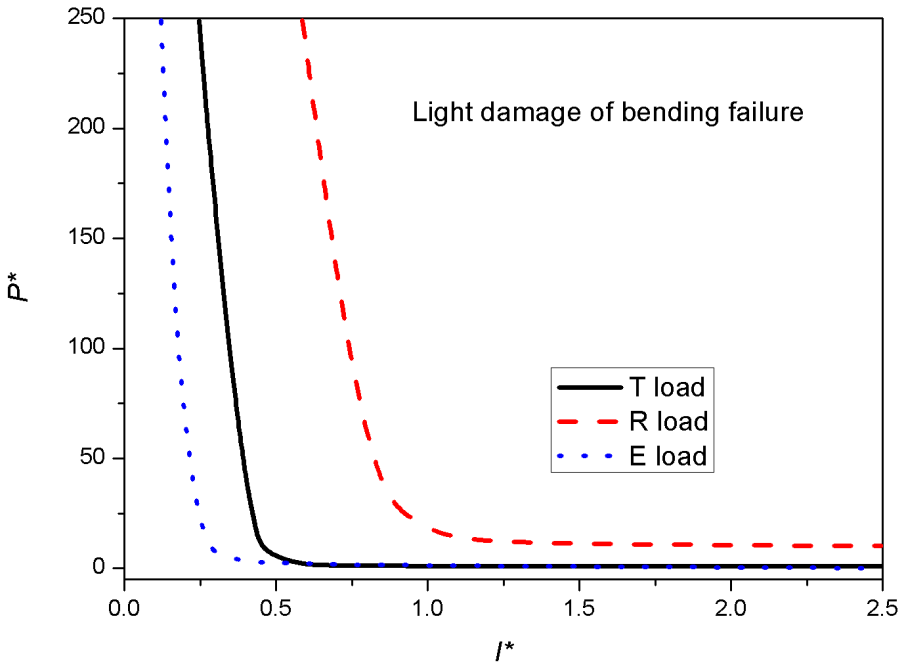

(a) Light damage

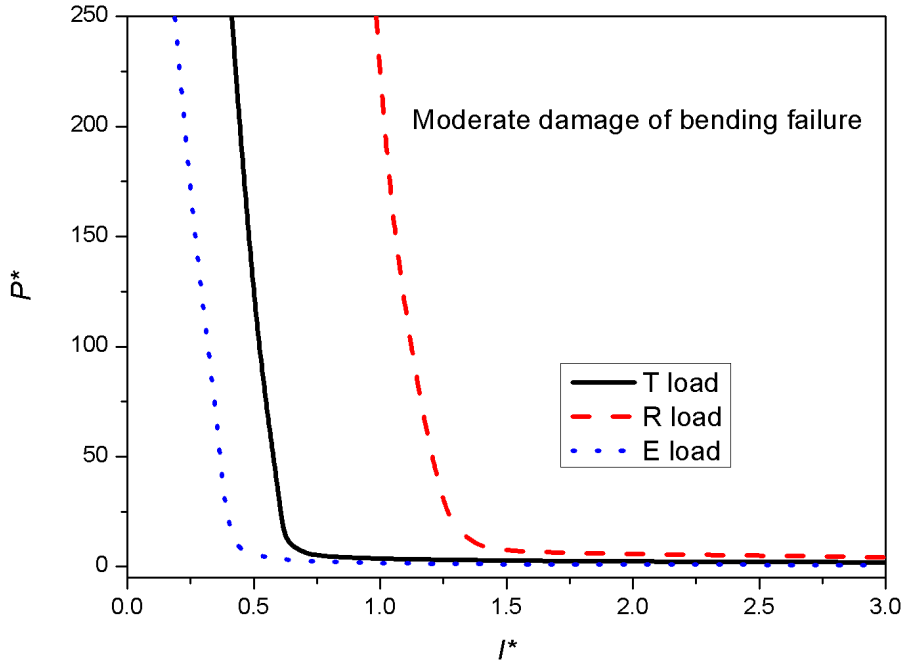

(b) Moderate damage

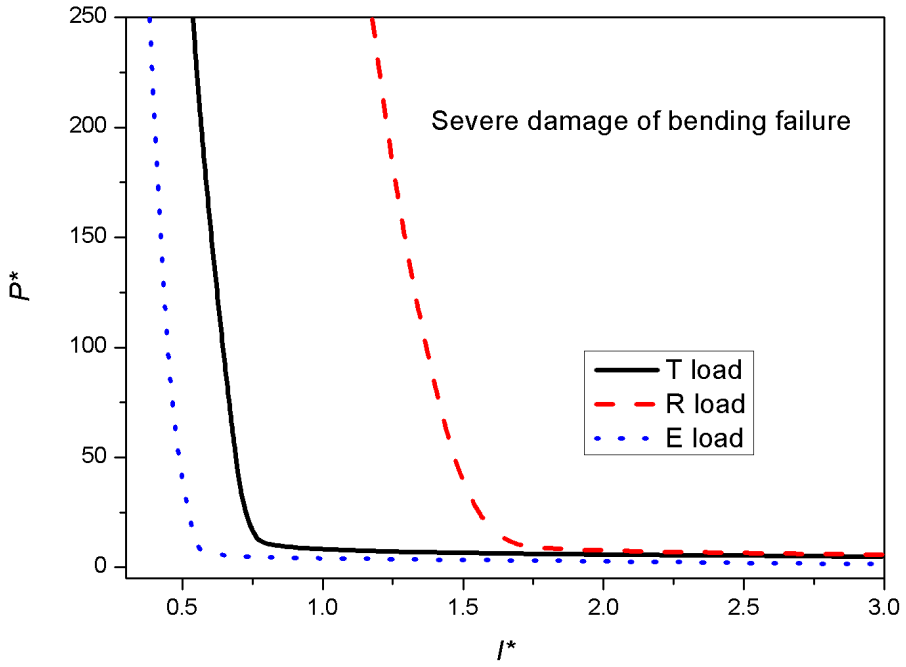

(c) Severe damage

Fig. 6 - 7 Pulse shape difference of shear failure for underground structure against internal blast load

The difference of constant and non-constant soil stiffness effect on shear and bending failure mode is shown in Fig. 6-8. The non-constancy of SSI affects the P-I diagrams in the same way as in Fig. 6-5. It once more indicates that the P-I

diagrams are sensitive to the non-constancy of SSI in the dynamic and impulsive regions. Again, the constant soil stiffness will absorb more energy than the non-constant soil stiffness so that under the same pressure and impulse the structural displacements for shear and bending failure with non-constant soil stiffness are smaller than that with constant one. This explains the reason why the result of non-constant soil stiffness is close to that without considering SSI.

Results in Figs. 6-5 and 6-8 show that, the structural displacement given by constant SSI used in previous study leads to a risky design of underground RC protective structure. The non-constant SSI is more reasonable and highly recommended.

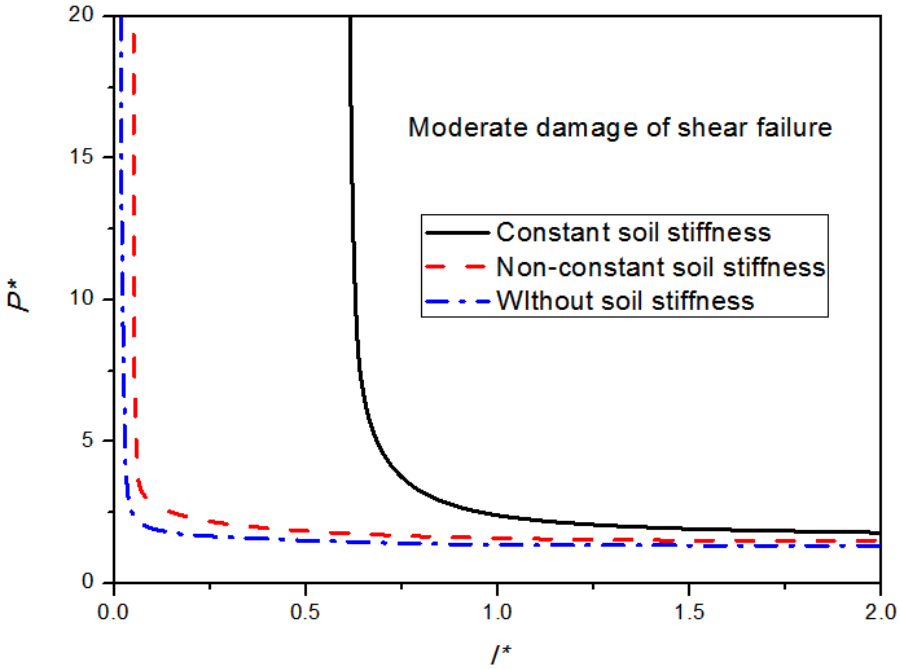

a) Shear failure

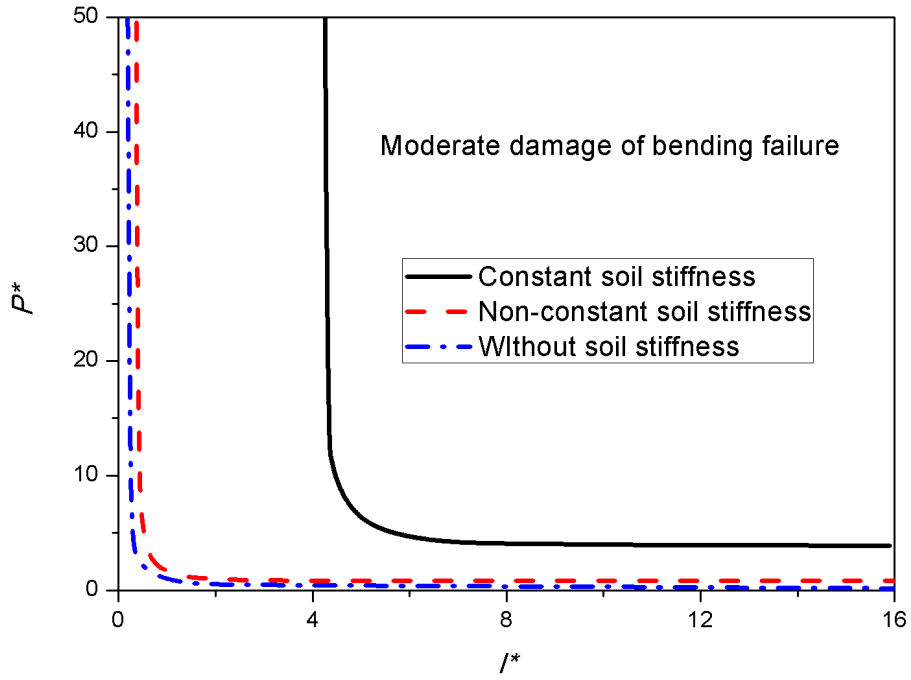

b) Bending failure

Fig. 6 - 8 Difference of constant and non-constant soil stiffness effect

6.5. Concluding remarks

The P-I diagram result is affected by different factors such as pulse shapes, damage levels, non-constancy of damping or spring effect, and so on.

In the analysis of underground structure against external blast load, the pulse shape effect and the non-constancy of damping effect are considered. From the P-I diagrams, it can be concluded that the pulse shape effect still exists in such analysis. The result in shear failure shows that, the error between triangular load and exponential load is relative small, and the over-estimation from rectangular load cannot be ignored. In the analysis of bending failure, results from triangular load and exponential load are closer. Both triangular load and rectangular load overestimate the structural response. The P-I diagrams of shear and bending deformations are sensitive to the pulse shape effect in the impulse and dynamic regions. The pulse shape effect on bending deformation is not as significant as that on surface structures but still cannot be neglected. The P-I diagrams are sensitive to the non-constancy of SSI in the dynamic and impulse region. That means P-I

diagrams for underground structures against external blast load is more sensitive to non-constancy of SSI when the blast duration is short.

The analysis of underground structure against internal blast load shows that, the result of triangular load is closer to the exponential load. Again, both triangular and rectangular loads overestimate the final displacements due to shear and bending. The result also shows that the P-I diagrams for underground structures against internal blast load are more sensitive to non-constancy of SSI when the structural displacement is under control of impulse and dynamic load. Similar conclusions can be drawn as to those for underground structure under external blast load.

Technically, the generalized integration procedure can be easily applied to a more complicated calculation, for example a combined failure with the consideration of more accurate blast load time history, nonlinear material properties, pulse shape effect, and non-constant soil-structure interaction, by combining the results from Chapter 3 into the present chapter. Such idea is realized in the following chapter.

CHAPTER 7

NONLINEAR STRUCTURAL DEFORMATION EFFECT ON THE BLAST INDUCED STRUCTURAL DAMAGE

7.1. Introduction

An effective damage assessment method based on realistic deformation behavior of a structure is essential in order to apply protective measures when there exist potential blast load risks. For an RC structural element, the analysis becomes more complicated because the RC always deforms in a nonlinear way, especially in the post-failure stage.

This chapter extends the work done in Chapters 3 to 6 to derive the P-I diagrams for an RC element by using a multi-linear resistance-deformation model. The three failure modes, i.e. the pure shear failure mode, the pure bending failure mode, and the combined shear and bending failure mode, which are denoted as modes 1, 2, and 3, respectively in the previous chapters are considered in the present analysis. A multi-linear resistance-deformation model including a complex softening regime which is more appropriate to represent the deformation behavior of RC structures is employed, and the non-constant SSI is also considered for underground structure scenarios. The effect of the elastic stage is demonstrated. The simplification of the multi-linear deformation behavior is combined with the MAM. The results from the present analysis are compared to show the effect of the softening behavior of RC structural element on different failure modes. The present method can be applied to various RC structures with different elastic and post-elastic behaviors.

7.2. Phase division

A simply supported beam element is analyzed and both the elastic and post-elastic stages are considered. The difference of the boundary conditions was discussed by Ma *et al*. (2007). The simply supported beam element is again adopted in the

present analysis since such boundary condition will give out larger deformation for both shear and bending failure and lead to a safer design.

In traditional analysis, the resistance-deformation (R-D) relationship of a structural element was usually expressed as an elastic-plastic model, including elastic, perfectly plastic and elastic-hardening models. To simplify the analysis, the elastic portion are normally ignored and thus a rigid-plastic as shown in Fig. 7-1 (a) or an elastic-plastic hardening model as given in Fig. 7-1 (b) are often used. Such simplification is valid only for relatively ductile structures which are able to sustain blast and/or impact loads to a certain degree. For RC columns and beams, the structures always behave with an apparent softening portion and the R-D relationship is similar to that in Fig. 7-1 (c) or (d). To account for such post-elastic behavior, in the present study, a multi-linear model shown in Fig. 7-2, is used in the dynamic response analysis for shear, bending, and combined failure of RC beam structures. R^* in Fig. 7-2 denotes the normalized general resistance of an RC element which can be replaced by normalized shear resistance Q^* or normalized bending resistance M^* respectively. D^* is the corresponding normalized deformation.

The MAM and P-I diagrams in Ma *et al*. (2007) included five failure modes; while in the present study only the first three modes were adopted. It is because the mode 4 and mode 5 are based on the moving plastic hinges phenomenon which requires relative low shear resistance, low depth-to-span ratio, and high intensity loading acting on the element. In consideration that the RC element is relatively brittle and the softening behavior in the post-failure stages is obvious, those two modes with plastic zones are not considered. The pulse load with a pressure p_0 is suggested to be lower than $6M_0/L^2$, and the dimensionless strength ratio υ for mode 3 is suggested to be in the range from 1.0 to 1.5. Although the failure modes 4 and 5 in Ma *et al*. (2007) do exist, for example, beam element made of steel material under blast load in a certain distance, they are not in the scope of the present study for RC elements.

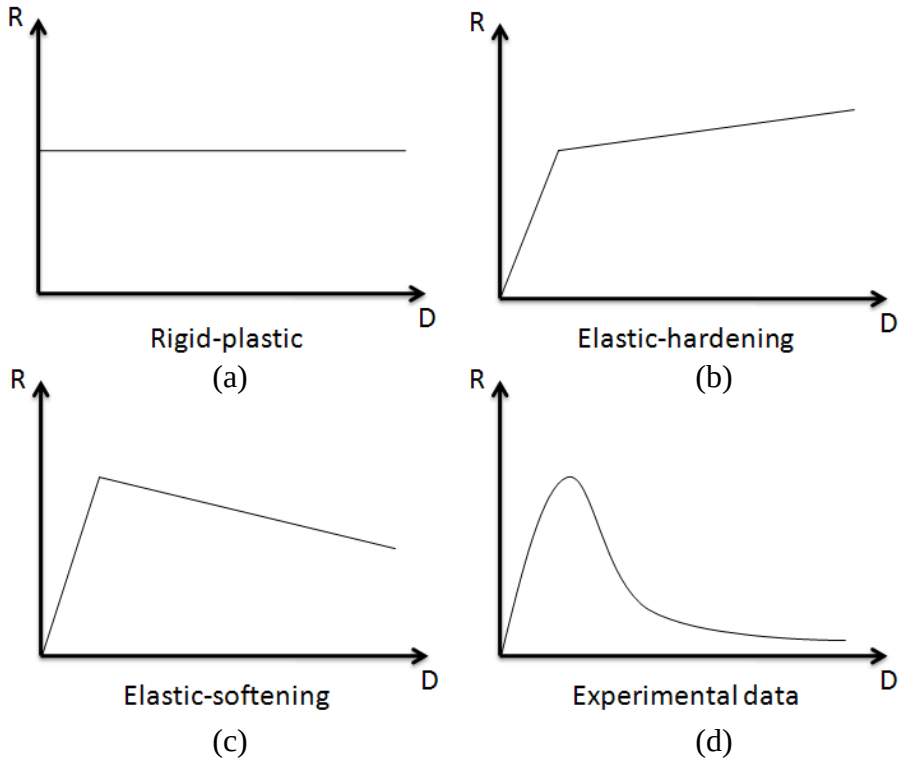

Fig. 7 - 1 R-D relationships for reinforced concrete structural element: (a) Rigid-plastic model; (b) Elastic-plastic hardening model; (c) elastic-plastic soften model; (d) More realistic RC structural deformation model

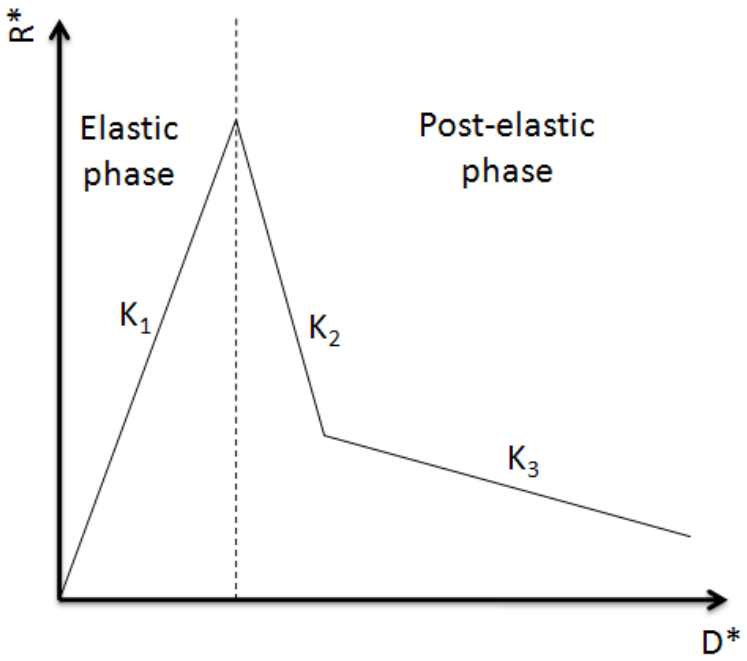

Fig. 7 - 2 Idealized resistance-deformation relationship for RC elements

The structural response can be divided into several stages based on the multi-linear R-D relationship. The element deforms linearly in the elastic stage. A few post-elastic stages subsequently follow in the form of shear, bending, or a combined failure mode.

In the shear failure mode (mode 1), there are two basic phases which are the loading phase (phase 1) and the post loading phase (phase 2). Phase 1 is in the period that the blast loads acts on the beam element and t_d denotes its ending time. During this phase, the acceleration is positive; the velocity and displacement of the beam keep increasing. In phase 2, the structural element is free of the blast load and the beam element reaches the maximum deformation at the end of this phase. Within this phase, the velocity decreases monotonically, while the displacement continues to increase. The phase 2 ends when the velocity equals zero, and the displacement reaches its maximum value. The final response time is denoted as t_f. The above two phases are differentiated according to the action of the blast load; while the structural response can also be divided into an elastic stage (ends at t_{se}) and a few post-elastic stages according to the deformation of the structural element. There are three possibilities when considering different response stages. If the elastic stage ends in phase 1 ($0<t_{se}<t_d$), the entire process is categorized into a loading-elastic phase (phase 1a, $0<t\leq t_{se}$), a loading-post-elastic phase (phase 1b, $t_{se}<t\leq t_d$), and a post-loading-post-elastic phase (phase 2, $t_d<t\leq t_f$), where t is the time variable of the structural response. If the elastic stage ends in phase 2, the entire process includes a loading-elastic phase (phase 1, $0<t<t_d$), a post-loading-elastic phase (phase 2a, $t_d<t\leq t_{se}$), and a post-loading-post-elastic phase (phase 2b, $t_{se}<t\leq t_f$). If $t_{se}=t_d$, as a special case, the process degrades to two phases, i.e., a loading-elastic phase (phase 1) and a post-loading-post-elastic phase (phase 2).

Similar to the shear failure mode, in the bending failure mode (mode 2), there are also three possibilities of combination, i.e., 1) phase 1a => phase 1b => phase 2; 2) phase 1 => phase 2a => phase2b; and 3) phase 1 => phase 2. The end time of the elastic stage for the bending mode is denoted as t_{me}.

In the combined shear and bending failure mode (mode 3), the division of the response phases becomes more complex. Except the loading phase, i.e., phase 1,

there are two post-loading phases with respect to the terminations of shear and bending deformations, respectively. The first post-loading phase (phase 2) ends when the shear deformation terminates, and the second post-loading phase (phase 3) then starts and ends when the bending deformation stops. During phase 1, the acceleration of the beam model is positive, the velocity and displacement increase monotonically. In phase 2, the accelerations of both shear and bending forces become negative so that the corresponding velocities start to decrease, while the displacements keep increasing. When the velocity induced by the shear deformation vanishes, the shear displacement stops, and the ending time is denoted as t_s. On the other hand, the displacement due to bending still increases. In phase 3, the velocity of bending deformation reduces to zero and the beam model reaches its final displacement. By combining the three phases with the elastic and post-elastic deformation stages, there are many possibilities. For brief, only two possibilities are explained as examples in the following context.

If the elastic stages of both shear and bending end in phase 1 ($0<t_{se}<t_{me}<t_d$) for an example, the entire response process can be put into a loading-elastic phase (phase 1a, $0<t\leq t_{se}$), a loading-bending-elastic phase (phase 1b, $t_{se}<t\leq t_{me}$), a loading-post-elastic phase (phase 1c, $t_{me}<t\leq t_d$), a shear-terminating-post-elastic phase (phase 2, $t_d<t\leq t_s$), and a bending-terminating-post-elastic phase (phase 3, $t_s<t\leq t_f$). In this example, phase 1 is divided into phase 1a, phase 1b, and phase 1c. In phase 1a, both shear and bending deformations are in the elastic stages. In phase 1b, the shear deformation enters the post-elastic stage while the bending deformation is still elastic. In phase 1c, both shear and bending deformations are in the post-elastic stages. Phase 2 is the first post-loading phase in which the shear deformation will stop at the end, and the bending deformation continues. Phase 3 is the second post-loading phase in which the bending deformation terminates at the end.

If the shear-elastic stage ends in phase 1 but the bending-elastic stage ends in phase 2 for another example, the entire process can be categorized into a loading-elastic phase (phase 1a, $0<t<t_{se}$), a loading-bending-elastic phase (phase 1b, $t_{se}<t\leq t_d$), a post-loading-bending-elastic phase (phase 2a, $t_d<t\leq t_{me}$), a shear-terminating-post-elastic phase (phase 2b, $t_{me}<t\leq t_s$), and a bending-terminating-post-elastic phase

(phase 3, $t_s<t\leq t_f$). Phase 1a, phase 1b and phase 3 are the same as in the previous example, while phase 2 is divided into phase 2a and phase 2b. Phase 2a indicates the post-loading phase in which shear deformation is in the post-elastic stage, while the bending deformation is still in the elastic stage. Phase 2b is a post-loading phase in which both the shear and bending deformations are in post-elastic stages.

Any other possible combination can be derived in analogy to one of the aforementioned cases. It should be mentioned that a rectangular pulse load is considered in the present analysis. In the elastic stage, the system is simplified into an equivalent SDOF model to calculate its acceleration, velocity and displacement, while in the post-elastic stages, a bilinear plastic softening model for both the shear and bending deformation as shown in Fig. 7-2 is adopted.

7.3. Element resistance and failure criteria

In most of the reported research works in combining the shear and bending deformation effect, to simplify the derivation and calculation, the R-D relationship was assumed as either rigid-plastic (e.g. Ma *et al*. 2007) or bi-linear (e.g. Fallah and Louca 2007). Such simplification generally overestimates the resistance of an RC structural element. In the present study, the shear and bending deformations are analyzed based on the assumption of independent interactions between shear and bending resistance, which means the shear-bending yield surface is rectangular which is the same as that in Ma *et al*. (2007). The assumption used in the present study leads to the lower bound solution of the problem since the independent maximum bending and shear strength criteria used in the analysis circumscribe an interactive shear-bending yield surface. When elastic deformation is considered, it shall still be true since with the same impact energy, larger deformation will be resulted if a convex interactive shear-bending yield surface is adopted. When elastic deformation is included, the concept of bound solution is still valid since the independent maximum bending and shear strength criteria used in the analysis circumscribe an interactive shear-bending yield surface.

The stress-strain relationship of the steel reinforcement is remarkably different from the concrete which behaves very differently in compression and tension conditions

(Nawy 2003, McCormac 2006). When a structural element is made of RC, its shear and bending resistances are very complicated. The design code TM5-1300 (1990) gives out a guide on the permissible deformation of RC beam and slab in the design procedure. The element behaves linearly in the elastic phase and nonlinearly in the post-elastic phase. The support rotation is adopted as the definition of damage level. For civilian structures or structures without protective design, such damage definition is also suitable if certain modification is applied accordingly.

There are various criteria for assessing damage of structures. Some of them are based on strain energy definition at either the material level or the structure level. Some others combined the structural deformation and strain energy quantities for assessing structural damage. For example, the damage at the material level is better for damage assessment if the failure of reinforced concrete structure/element is spalling and penetration. Such definition of damage is much more accurate than deformation. However, for the sake of convenience, the maximum deformation occurred in a structure (beam, column and slab) has been widely used for assessing structural damage in practice. Therefore, the deformation in structure level is adopted as the damage criterion in the present study.

In the present study, the failure criteria of shear and bending remain the same as those in the previous chapters. The maximum bending deformation at the center of the beam element and the maximum shear deformation at the element supports can be expressed as Eqs. (3.49).

7.4. Failure modes and P-I equations

The pulse shape difference on P-I diagram has been discussed by Youngdahl (1970, 1971), and Li and Meng (2002b) that it can be eliminated by using the Yougdahl's correlation parameter method. For the convenience of the P-I equations derivation while not losing the generality of the solution, the rectangular pulse load with a magnitude of p_0 and a duration of t_d is again adopted in the present study.

The possible transverse velocity profiles which indicate the shear failure mode, the bending failure mode, and the combined failure mode are shown in Fig. 3-3 (Ma *et al*. 2007). The dimensionless strength ratio is also used, i.e.:

$$\nu = \frac{Q_e L}{2M_e} \tag{7.1}$$

where Q_e and M_e are the maximum elastic shear and bending resistance respectively; L is the half length of the beam element.

The Q_e and M_e in Eq. (7.1) are assumed to be independent from each other and obey the rectangular yield surface.

The general governing equation is expressed as:

$$\begin{cases} \dfrac{\partial Q}{\partial x} = -p_0 + m\ddot{y} & (loading) \\ \dfrac{\partial Q}{\partial x} = m\ddot{y} & (post-loading) \end{cases} \tag{7.2}$$

where Q is the transverse shear force; x is the abscissa on the element; p_0 is the constant pressure of the blast load; m is the mass per unit length; $\ddot{y}$ is the acceleration of a unit mass. The x-axis starts from the mid-span of the beam and only half of the beam is considered due to symmetry as shown in Fig. 7-3.

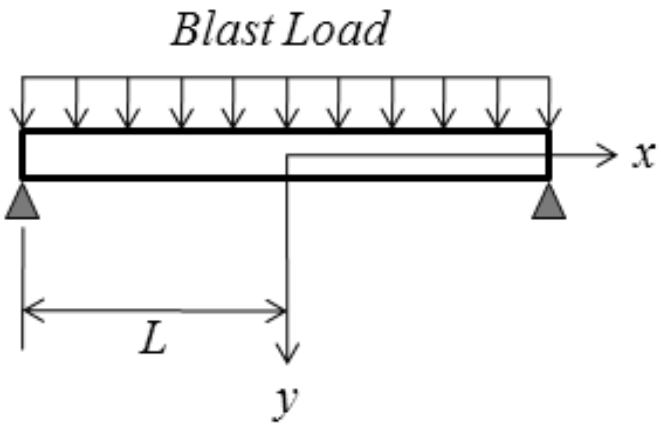

Fig. 7 - 3 Simply supported beam model

Table 7-1 shows the phase velocity profiles for different modes. Both the elastic and the post-elastic stages follow these profiles. Mode 1 contains the shear failure only.

Mode 2 indicates the bending failure which has a plastic hinge at the center of the element. Mode 3 can be considered as the combination of mode 1 and mode 2.

Table 7 - 1 Velocity profile

	Mode 1	Mode 2	Mode 3
Phase 1			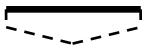
Phase 2			
Phase 3	N.A.	N.A.	

Details of derivation of the displacement time history for the three modes are given in the following context.

7.4.1. Mode 1 -shear failure mode

When $0 < \nu < 1$ and $p_0 \geq 2M_e\nu / L^2$, the shear failure mode will occur. The shear failure mode demonstrates that shear failure at the two supports which carry the maximum shear force, while the bending failure does not occur. In this mode, the dimensionless parameter υ is less than 1, which indicates a very low shear-to-bending resistance ratio.

The following context studies a case which includes two possible post-elastic stages. Derivation of the equations for other cases can be referred to this example.

There are totally three phases in this mode including loading-elastic phase (phase 1a, $0<t\leq t_{se}$), loading-post-elastic phase (phase 1b, $t_{se}<t\leq t_d$), and post-loading-post-elastic phase (phase 2, $t_d<t\leq t_f$) which end at t_{se}, t_d and t_f respectively.

In phase 1a, the SDOF system is adopted to present the elastic behavior of the RC element. Once the element enters the post-elastic phases (phase 1b and phase2), the mode approximation method used by Ma *et al*. (2007) is adopted.

Phase 1a is in the elastic stage with the blast loading action. The maximum acceleration, velocity, and displacement are calculated by the SDOF model as follows:

$$\ddot{y}_s = \frac{p_0}{m}, \quad \dot{y}_s = \frac{p_0 t}{m}, \quad y_s = \frac{p_0 t^2}{2m} \tag{7.3}$$

where $\ddot{y}$, $\dot{y}$, and y are the acceleration, velocity, and displacement variables respectively; the suffix s indicates the quantities by the shear force only; t is the time variable. The distribution patterns of these quantities can be deduced referring to the velocity profile.

At the end of this phase, the maximum velocity and displacement are denoted as $\dot{y}_s\left(t_{se}\right)$, and $y_s\left(t_{se}\right)$ respectively.

Phase 1b is in the post-elastic stage within the blast duration. The governing equation is:

$$\frac{\partial Q}{\partial x} = -p_0 + m\ddot{y}_s \tag{7.4}$$

The boundary conditions and initial conditions are:

$$\begin{cases} Q\left(x=0\right)=0, Q\left(x=L\right)=-Q_0\left(y_s\left(t\right)\right) \\ \dot{y}_s\left(T=0\right)=\dot{y}_s\left(t_{se}\right), y_s\left(T=0\right)=y_s\left(t_{se}\right) \end{cases} \tag{7.5}$$

where $Q_0(y)$ is the shear resistance of the beam element that deduced from the shear-resistance-displacement curve; T is the general time variable which equals to t-t_{se} in this phase.

Setting the iterative time step as $\Delta t = \frac{t_d - t_{se}}{n}$, where n is a pre-defined constant which satisfies the precision requirement of the integration. Then Eq. (7.4) is integrated with respect to time. In every integration step, the value of $Q_0(y)$ needs be updated due to the change of displacement.

The equations for integration are derived as:

$$\dot{y}_s\left(t_{i+1}\right)=\frac{\left[p_0L-Q_0\left(y_s\left(t_i\right)\right)\right]\cdot\Delta t}{mL}+\dot{y}_s\left(t_i\right) \tag{7.6}$$

$$y_s\left(t_{i+1}\right)=\frac{\left[p_0L-Q_0\left(y_s\left(t_i\right)\right)\right]\cdot\Delta t^2}{2mL}+\dot{y}_s(t_i)\cdot\Delta t+y_s(t_i) \tag{7.7}$$

At the end of phase 1b when $t=t_d$, the maximum velocity and displacement of the element are $\dot{y}_s\left(t_d\right)$ and $y_s\left(t_d\right)$ respectively.

Phase 2 is a post-loading-post-elastic phase, and the governing equation is:

$$\frac{\partial Q}{\partial x}=m\ddot{y}_s \tag{7.8}$$

The boundary conditions remain the same as for the previous phase, while the initial conditions change to:

$$\dot{y}_s\left(T=0\right)=\dot{y}_s\left(t_d\right), y_s\left(T=0\right)=y_s\left(t_d\right) \tag{7.9}$$

where T is equal to t-t_d.

The equations for integration are:

$$\dot{y}_s\left(t_{i+1}\right)=\frac{-Q_0\left(y_s\left(t_i\right)\right)\cdot\Delta t}{mL}+\dot{y}_s\left(t_i\right) \tag{7.10}$$

$$y_s\left(t_{i+1}\right)=\frac{-Q_0\left(y_s\left(t_i\right)\right)\cdot\Delta t^2}{2mL}+\dot{y}_s\left(t_i\right)\cdot\Delta t+y_s\left(t_i\right) \tag{7.11}$$

The iterative time step Δt is preliminarily estimated the same as that for the previous phase. Similarly, the final maximum displacement of the element can be yielded as $y_s\left(t_f\right)$ where t_f is the final time when the velocity of element reaches zero.

7.4.2. Mode 2 -bending failure mode

When $\nu\geq 1$ and $2M_e/L^2\leq p_0<2M_e\left(4\nu-3\right)/L^2$, in the bending failure mode, a plastic hinge forms at the mid-span of the element where the maximum bending moment occurs.

Similar to mode 1, the case with two post-elastic deformation phases is taken as an example. The derivation and integration procedures for mode 2 are similar to those for mode 1. Equations for other possible cases can refer to this example.

There are totally three phases in this mode including a loading-elastic phase (phase 1a, $0<t\leq t_{me}$), a loading-post-elastic phase (phase 1b, $t_{me}<t\leq t_d$), and a post-loading-post-elastic phase (phase 2, $t_d<t\leq t_f$) which ends at t_{me}, t_d and t_f respectively.

The same as mode 1, the SDOF system and the mode approximation method are adopted to represent the elastic and post-elastic stages.

Phase 1a is the elastic phase with the blast loading acting on the element. The maximum acceleration, velocity, and displacement can be derived as:

$$\ddot{y}_m = \frac{p_0}{m_e}, \quad \dot{y}_m = \frac{p_0 t}{m_e} \quad y_m = \frac{p_0 t^2}{2m_e} \tag{7.12}$$

where m_e is the effective mass used for the elastic phase in the bending failure mode; the suffix m indicates the relevant quantities are incurred by the bending moment.

At the end of this phase, the maximum velocity and displacement are expressed as $\dot{y}_m\left(t_{me}\right)$ and $y_m\left(t_{me}\right)$, respectively.

Phase 1b is the post-elastic phase within the blast loading duration. The governing equation is:

$$\frac{\partial Q}{\partial x} = -p_0 + m\ddot{y}_m\left(1-\frac{x}{L}\right) \tag{7.13}$$

The boundary conditions and initial conditions are:

$$\begin{cases} Q\left(x=0\right)=0, M\left(x=0\right)=M_0\left(y_m\left(t\right)\right) \\ \dot{y}_m\left(T=0\right)=\dot{y}_m\left(t_{me}\right), y_m\left(T=0\right)=y_m\left(t_{me}\right) \end{cases} \tag{7.14}$$

where $M_0(y)$ is the bending resistance of the beam element deduced from the bending-resistance-displacement curve; T is the response time.

Setting the iterative time step to $\Delta t = \frac{t_d - t_{me}}{n}$, Eq. (7.13) is then integrated with respect to time. In every integration step, the value of $M_0(y)$ should be updated since the displacement of element changes.

The equations for integration can be derived as:

$$\dot{y}_m\left(t_{i+1}\right) = \frac{\left[3p_0L^2 - 6M_0\left(y_m\left(t_i\right)\right)\right]\cdot\Delta t}{2mL^2} + \dot{y}_m\left(t_i\right) \tag{7.15}$$

$$y_m\left(t_{i+1}\right) = \frac{\left[3p_0L^2 - 6M_0\left(y_m\left(t_i\right)\right)\right]\cdot\Delta t^2}{4mL^2} + \dot{y}_m\left(t_i\right)\cdot\Delta t + y_m\left(t_i\right) \tag{7.16}$$

At the end of phase 1b when $t=t_d$, the maximum velocity and displacement of element are $\dot{y}_m\left(t_d\right)$ and $y_m\left(t_d\right)$ respectively.

Phase 2 is the unique post-loading-post-elastic phase, and the governing equation is written as:

$$\frac{\partial Q}{\partial x} = m\ddot{y}_m\left(1 - \frac{x}{L}\right) \tag{7.17}$$

The boundary conditions remain the same as for the previous phase, while the initial conditions change to:

$$\dot{y}_m\left(T=0\right) = \dot{y}_m\left(t_d\right), y_m\left(T=0\right) = y_m\left(t_d\right) \tag{7.18}$$

where T is equal to t-t_d.

The equations for integration are:

$$\dot{y}_m\left(t_{i+1}\right) = \frac{-3M_0\left(y_m\left(t_i\right)\right)\cdot\Delta t}{2mL^2} + \dot{y}_m\left(t_i\right) \tag{7.19}$$

$$y_s\left(t_{i+1}\right) = \frac{-3M_0\left(y_m\left(t_i\right)\right)\cdot\Delta t^2}{4mL^2} + \dot{y}_m\left(t_i\right)\cdot\Delta t + y_m\left(t_i\right) \tag{7.20}$$

where the time step Δt is set the same as that for the last phase.

The maximum displacement of the element is denoted as $y_m\left(t_f\right)$ when the velocity of element reaches zero.

7.4.3. Mode 3 -combined failure mode

Mode 3 is the combination of mode 1 and mode 2. Its sub-phases are much more than those for mode 1 or mode 2. The shear failure occurs at the two supports, while the bending failure induces a plastic hinge at the mid-span of the element.

One of the possible cases with the most post-elastic deformation phases is taken as an example. There are totally five sub-phases in this case including a loading-elastic phase (phase 1a, $0<t\leq t_{se}$), a loading-bending-elastic phase (phase 1b, $t_{se}<t\leq t_{me}$), a loading-post-elastic phase (phase 1c, $t_{me}<t\leq t_d$), a shear-terminating-post-elastic phase (phase 2, $t_d<t\leq t_s$), and a bending-terminating-post-elastic phase (phase 3, $t_s<t\leq t_f$). Equations for other cases can refer to the derivation for this example.

Again, the SDOF system and the mode approximation method are adopted for the elastic and post-elastic stages respectively.

Phase 1a is the first phase in which the blast load acts on the element and both shear and bending responses remain elastic. The maximum acceleration, velocity, and displacement due to shear and bending are the same as in Eqs. (7.3) and (7.12).

At the end of this phase, the maximum velocity and displacement are given as $\dot{y}_s\left(t_{se}\right)$, $y_s\left(t_{se}\right)$, $\dot{y}_m\left(t_{se}\right)$ and $y_m\left(t_{se}\right)$.

Phase 1b is the loading-bending-elastic phase within the blast loading duration when the shear deformation falls into the post-elastic stage while the bending response still remains elastic. The governing equation is the same as Eq. (7.4), and the boundary and initial conditions are the same as Eq. (7.5).

The equations for integration in this phase are as follows:

$$\dot{y}_s\left(t_{i+1}\right)=\frac{p_0\cdot\Delta t}{m}-\frac{4Q_0\left(y_s\left(t_i\right)\right)\cdot\Delta t}{mL}+\frac{6M_0\left(y_m\left(t_i\right)\right)\cdot\Delta t}{mL^2}+\dot{y}_s\left(t_i\right) \quad (7.21)$$

$$y_s\left(t_{i+1}\right)=\frac{p_0\cdot\Delta t^2}{2m}-\frac{2Q_0\left(y_s\left(t_i\right)\right)\cdot\Delta t^2}{mL}+\frac{3M_0\left(y_m\left(t_i\right)\right)\cdot\Delta t^2}{mL^2}+\dot{y}_s(t_i)\cdot\Delta t+y_s(t_i) \quad (7.22)$$

where the time step Δt equals to $\frac{t_{me}-t_{se}}{n}$.

By the same integration method as for mode 1, at the end of phase 1b, the maximum velocity and displacement are given as $\dot{y}_s\left(t_{me}\right)$, $y_s\left(t_{me}\right)$, $\dot{y}_m\left(t_{me}\right)$ and $y_m\left(t_{me}\right)$.

Phase 1c is the post-elastic phase for both shear and bending responses till the end of the blast duration. The governing equation for the combined deformations is given as:

$$\frac{\partial Q}{\partial x}=-p_0+m\ddot{y}_s+m\ddot{y}_m\left(1-\frac{x}{L}\right) \quad (7.23)$$

The boundary conditions and initial conditions are:

$$\begin{cases}Q\left(x=0\right)=0, Q\left(x=L\right)=-Q_0\left(y_s\left(t\right)\right)\\ M\left(x=0\right)=M_0\left(y_m\left(t\right)\right), M\left(x=L\right)=0\end{cases} \quad (7.24)$$

$$\begin{cases}\dot{y}_s\left(T=0\right)=\dot{y}_s\left(t_{me}\right), y_s\left(T=0\right)=y_s\left(t_{me}\right)\\ \dot{y}_m\left(T=0\right)=\dot{y}_m\left(t_{me}\right), y_m\left(T=0\right)=y_m\left(t_{me}\right)\end{cases} \quad (7.25)$$

where T equals to t-t_{me}.

The equations for the shear response integration are the same as Eqs. (7.21) and (7.22), while those for the bending response are given as follows:

$$\dot{y}_m\left(t_{i+1}\right)=\frac{p_0\cdot\Delta t}{m}+\frac{2Q_0\left(y_s\left(t_i\right)\right)\cdot\Delta t}{mL}-\frac{6M_0\left(y_m\left(t_i\right)\right)\cdot\Delta t}{mL^2}+\dot{y}_m\left(t_i\right) \quad (7.26)$$

$$y_m\left(t_{i+1}\right)=\frac{p_0\cdot\Delta t^2}{2m}+\frac{Q_0\left(y_s\left(t_i\right)\right)\cdot\Delta t^2}{mL}-\frac{3M_0\left(y_m\left(t_i\right)\right)\cdot\Delta t^2}{mL^2}+\dot{y}_m(t_i)\cdot\Delta t+y_m(t_i) \quad (7.27)$$

where the time step Δt equals to $\frac{t_d-t_{me}}{n}$.

At the end of this phase, the response quantities are $\dot{y}_s(t_d)$, $y_s(t_d)$, $\dot{y}_m(t_d)$ and $y_m(t_d)$.

Phase 2 is the post-loading-post-elastic phase, at the end of which, the shear response terminates. The governing equation for shear and bending is:

$$\frac{\partial Q}{\partial x} = m\ddot{y}_s + m\ddot{y}_m\left(1-\frac{x}{L}\right) \tag{7.28}$$

The boundary conditions are the same as in Eq. (7.24), and the initial conditions are updated as:

$$\begin{cases} \dot{y}_s(T=0) = \dot{y}_s(t_d), y_s(T=0) = y_s(t_d) \\ \dot{y}_m(T=0) = \dot{y}_m(t_d), y_m(T=0) = y_m(t_d) \end{cases} \tag{7.29}$$

where $T=t-t_d$.

The equations of integration for the shear and bending response are as follows:

$$\begin{cases} \dot{y}_s(t_{i+1}) = -\dfrac{4Q_0\left(y_s(t_i)\right)\cdot\Delta t}{mL} + \dfrac{6M_0\left(y_m(t_i)\right)\cdot\Delta t}{mL^2} + \dot{y}_s(t_i) \\ y_s(t_{i+1}) = -\dfrac{2Q_0\left(y_s(t_i)\right)\cdot\Delta t^2}{mL} + \dfrac{3M_0\left(y_m(t_i)\right)\cdot\Delta t^2}{mL^2} + \dot{y}_s(t_i)\cdot\Delta t + y_s(t_i) \end{cases} \tag{7.30}$$

$$\begin{cases} \dot{y}_m(t_{i+1}) = \dfrac{2Q_0\left(y_s(t_i)\right)\cdot\Delta t}{mL} - \dfrac{6M_0\left(y_m(t_i)\right)\cdot\Delta t}{mL^2} + \dot{y}_m(t_i) \\ y_m(t_{i+1}) = \dfrac{Q_0\left(y_s(t_i)\right)\cdot\Delta t^2}{mL} - \dfrac{3M_0\left(y_m(t_i)\right)\cdot\Delta t^2}{mL^2} + \dot{y}_m(t_i)\cdot\Delta t + y_m(t_i) \end{cases} \tag{7.31}$$

where the time step Δt is set to be $\dfrac{t_d - t_{me}}{n}$.

At the end of this phase when $t=t_s$, the velocity due to the shear force equals to zero, and the response quantities are $y_s(t_s)$, $\dot{y}_m(t_s)$ and $y_m(t_s)$.

Phase 3 is the last phase in which the total response of structural element will terminate. The governing equation is the same as in Eq. (7.17)and the boundary conditions are the same as in Eq. (7.24). The initial conditions are as follow:

$$\dot{y}_m\left(T=0\right)=\dot{y}_m\left(t_s\right), y_m\left(T=0\right)=y_m\left(t_s\right) \tag{7.32}$$

where T equals to t-t_s.

The equations of integration for the shear and bending response are as follows:

$$\dot{y}_m\left(t_{i+1}\right)=-\frac{3M_0\left(y_m\left(t_i\right)\right)\cdot\Delta t}{mL^2}+\dot{y}_m\left(t_i\right) \tag{7.33}$$

$$y_m\left(t_{i+1}\right)=-\frac{3M_0\left(y_m\left(t_i\right)\right)\cdot\Delta t^2}{2mL^2}+\dot{y}_m(t_i)\cdot\Delta t+y_m(t_i) \tag{7.34}$$

where the time step Δt is set as $\frac{t_d-t_{me}}{n}$.

At the end of this phase when t=t_f, the velocity due to the bending moment equals to zero, and the final responses is $y_m\left(t_f\right)$.

In all the above modes, the end time of the elastic phases (t_{se} and t_{me}) can be calculated as:

$$\begin{cases} t_{se}=\sqrt{\dfrac{2y_s\left(t_{se}\right)}{\ddot{y}_s\left(t_{se}\right)}} \\ t_{me}=\sqrt{\dfrac{2y_m\left(t_{me}\right)}{\ddot{y}_m\left(t_{me}\right)}} \end{cases} \tag{7.35}$$

7.5. P-I diagrams and discussions

Define dimensionless pressure P* and impulse I* for the blast load as:

$$P^*=\frac{p_0L}{Q_{0p}}=\frac{p_0L^2}{2\nu M_{0p}} \tag{7.36}$$

$$I^* = \frac{p_0 t_d}{\sqrt{2mQ_{0p}}} = \frac{p_0 t_d}{\sqrt{4mM_{0p} \cdot \nu / L}} \tag{7.37}$$

From the equations for the final displacements induced by the shear and bending failure, the P-I diagrams can be represented in unified forms as:

$$S\left(P^*, I^*\right) = \delta \cdot h \cdot \gamma_\nu = y_s \tag{7.38}$$

$$B\left(P^*, I^*\right) = L \cdot \beta_0 = y_m \tag{7.39}$$

where y_s is the maximum displacement due to shear that equals to $y_s(t_f)$ in the shear failure mode or $y_s(t_s)$ in the combined failure mode; y_m is the maximum displacement due to bending which equals to $y_m(t_f)$; $S(P^*,I^*)$ and $B(P^*,I^*)$ are implicit expressions with respect to the normalized pressure and impulse for shear and bending deformation modes according to the failure criteria.

7.5.1. Differentiation of failure modes

Differentiation of failure modes as given in Fig. 3-3 is determined in view of the motion initiation, i.e., the combination of p_0, t_d, and ν. For mode 1, the acceleration induced by the shear force at the supports should be larger than zero at the beginning of post-loading phase, and the maximum bending moment should be smaller than the bending strength of the element. Therefore, $p_0 \geq 2M_0\nu / L^2$ and $0 < \nu < 1$ should be satisfied. For mode 2, the initial acceleration due to bending should be positive at the beginning of post-loading phase, while the maximum shear force should be less than the shear strength. Therefore, $\nu \geq 1$ and $2M_0 / L^2 \leq p_0 < 2M_0\left(4\nu - 3\right) / L^2$ are required. For mode 3, combine the requirements of mode 1 and 2, $\nu \geq 1$ and $p_0 \geq 2M_0\left(4\nu - 3\right) / L^2$ become the boundary lines. The definition of the failure modes is similar to that by Ma *et al*. (2007).

The shear or bending failure are always and must be initiated within the loading phase since the differentiation of failure modes is decided by the initiation conditions of post-elastic structural response. In another word, if the blast load does

not satisfy the requirements of specified failure mode, the beam element will not response according to velocity profile of that mode. Under such situation, yielding will never occur after the loading phase in the present study. Such limitation can be eliminated when the differentiation method of failure modes is updated in future works.

7.5.2. Effect of resistance-deformation relationship

In the present study, the size of RC beam element in Barros and Dias' (2006) is adopted (1500mm×150mm×300m), and the parameters *K1*, *K2*, and *K3* for bending in the multi-linear R-D relationship are generated by curve fitting of Barros and Dias' (2006) results. Meanwhile, the above three *K* values for shear in the R-D relationship are generated from the results of Lee *et al*. (2008). In the present study, *K1*, *K2*, and *K3* for shear is calculated as 1.75, -1.47, and -0.012, while the values for bending are 1.53, -0.99, and -0.0059. M_{0p} is 1.53kN·m in all the following calculations and comparisons. Denoting Q^* and M^* as the normalized shear and bending resistances respectively and D^* for normalized displacement:

$$\begin{cases} Q^* = Q(y_s)/Q_0 \\ M^* = M(y_m)/M_0 \end{cases} \tag{7.40}$$

$$\begin{cases} D^* = y/y_{se} & shear \\ D^* = y/y_{me} & bending \end{cases} \tag{7.41}$$

Since the normalized shear and bending resistances Q^* and M^* are plotted with respect to normalized displacement D^*, the *K* values are dimensionless.

Fig. 7-4 shows the P-I diagrams for the rigid-plastic model, the elastic-rigid-plastic model, and multi-linear model suggested in the present analysis, with respect to the three failure modes. It is seen that the differences caused by the R-D relationship cannot be ignored. Fig. 7-5 shows the comparison of the results from the rigid-plastic, bi-linear, and multi-linear R-D relationships. As listed in Table 7-2, three loading scenarios, i.e., blast loads at far, middle, and close standoffs (load cases 1, 2, and 3, respectively), are assumed for each failure mode which conform to the initial conditions applied in the derivation for the three different modes.

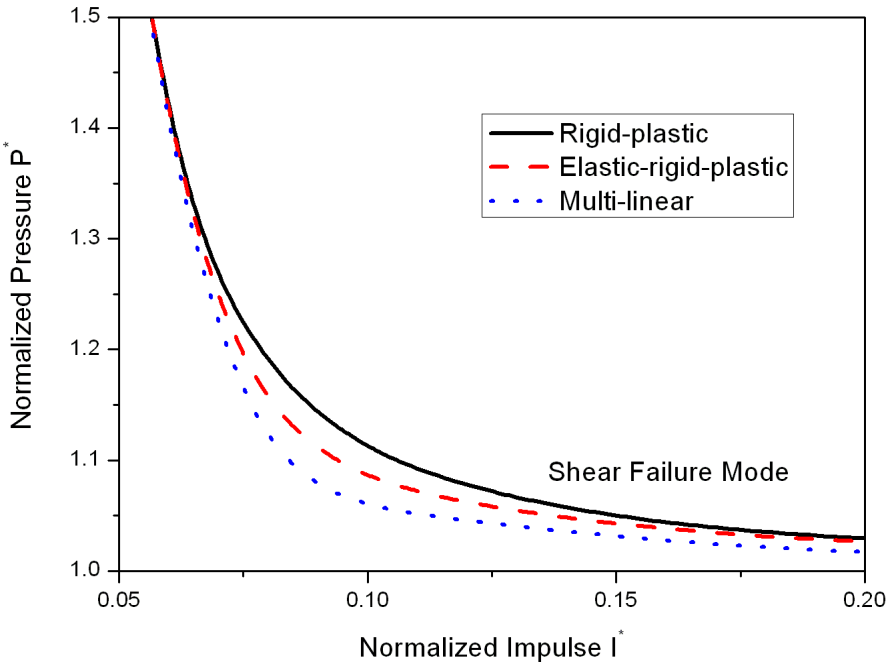

(a) Failure mode 1

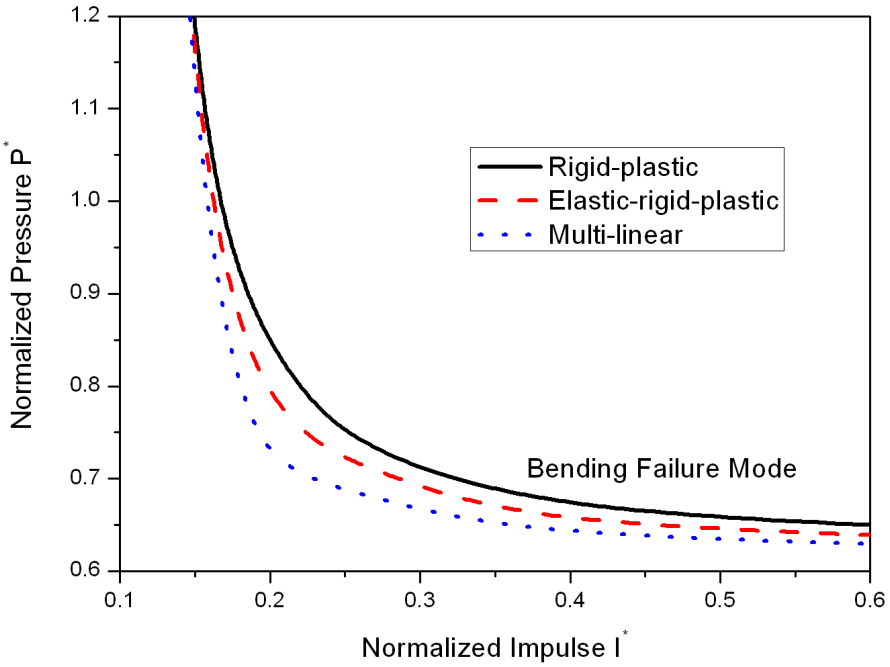

(b) Failure mode 2

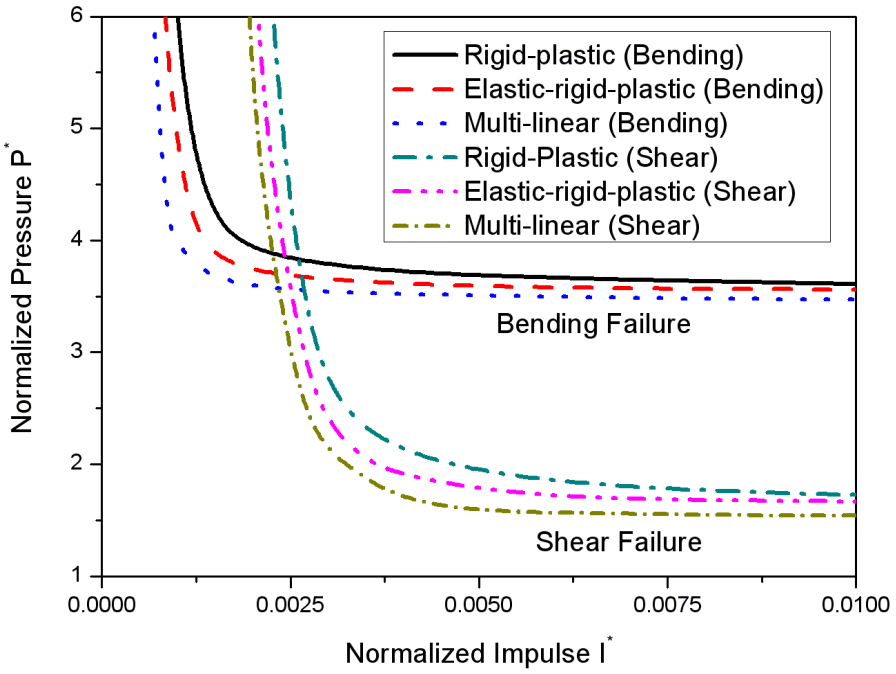

(c) Failure mode 3

Fig. 7 - 4 P-I diagrams of failure modes

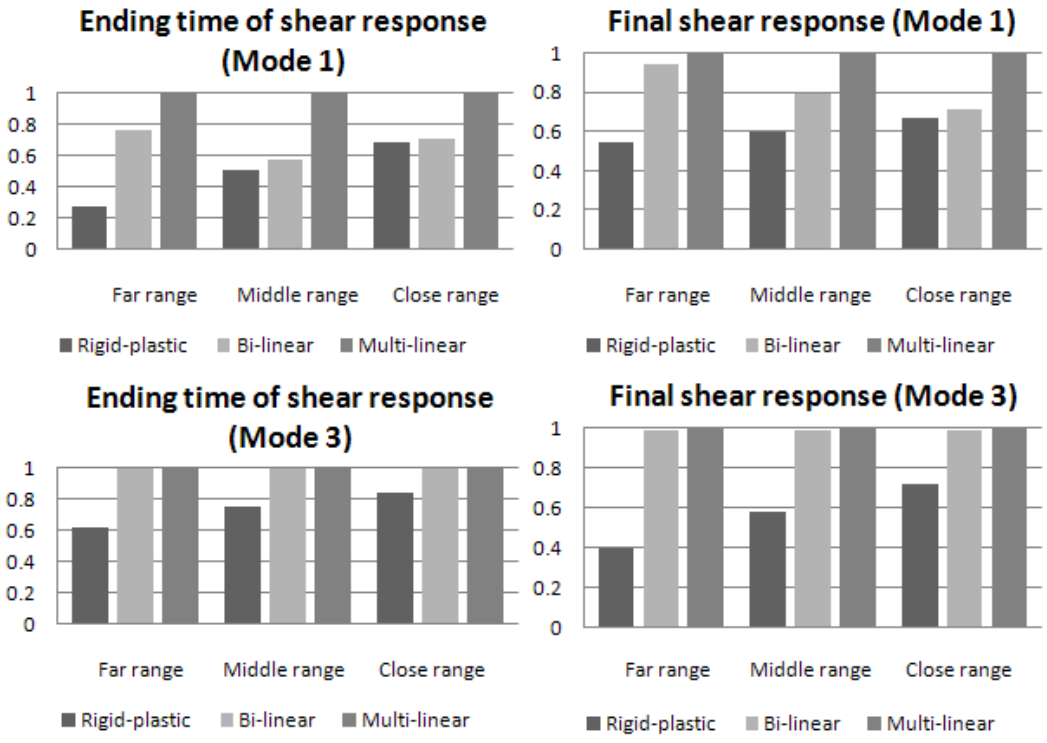

(a) Comparison of shear failure

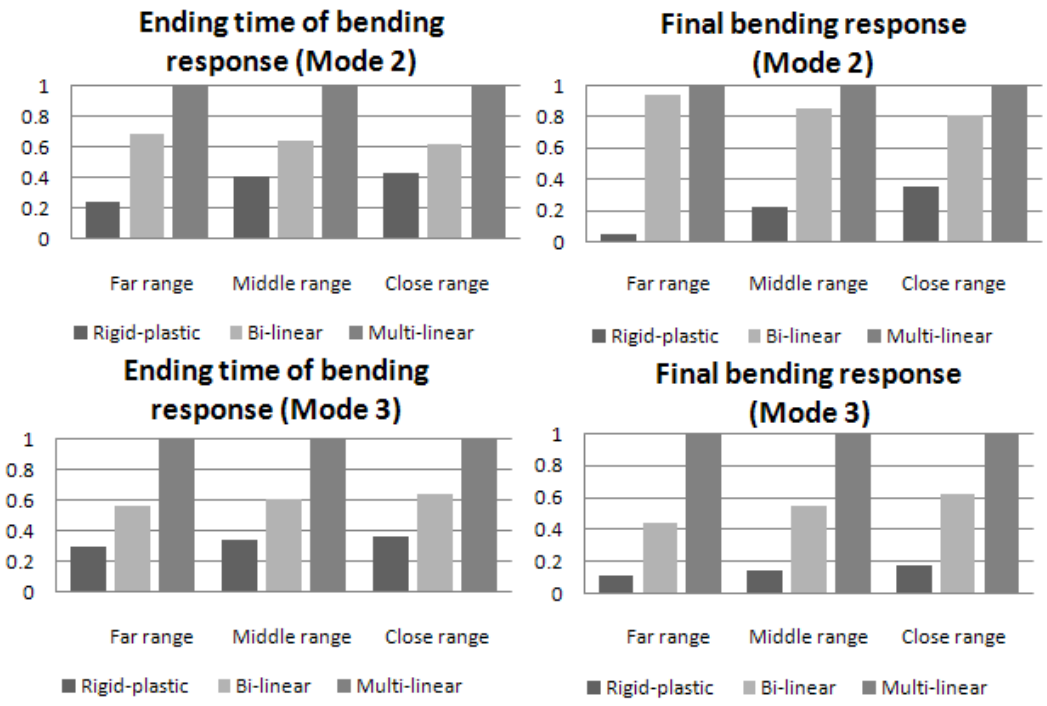

(b) Comparison of bending failure

Fig. 7 - 5 Normalized ending times and final responses

Table 7 - 2 Loads and parameters

Load case	Pressure p_0 (MPa)			Duration t_d (ms)		
	Mode 1	Mode 2	Mode 3	Mode 1	Mode 2	Mode 3
1	0.129	0.084	0.810	3.423	3.631	2.674
2	0.810	0.318	1.199	2.674	3.049	2.484
3	2.406	0.735	1.615	2.038	2.717	2.314

Based on the comparisons shown in Fig. 7-5, which take the results of the multi-linear model as a reference, the difference caused by the R-D relationship and loading scenarios can be stated as follows. The ending time and final displacement due to shear force are sensitive to the R-D relationship in all loading scenarios. The maximum difference in mode 1 can be 72.2% and 44.9% respectively. In mode 3, the above values change to 38.3% and 59.6%. The comparison also indicates that, the differences in both ending time and final displacement decrease with the increase of the shear-to-bending strength ratio υ. Such differences decrease as well

from the far range scenario to the close range scenario with the same failure mode. The ending time and final displacement due to the bending deformation have similar tendencies as those for the shear failure mode, but the maximum differences with regard to different R-D relationships are higher, especially for the final displacement. Generally, the difference between the results from the rigid-plastic and the bi-linear models is influenced by the elastic deformation, while the difference between the results from the bi-linear and multi-linear models is due to the softening behavior in the post-elastic phase. It can be stated that the present study demonstrates the remarkable effect of elastic deformation in damage analysis for RC structural elements, which, thus, cannot be ignored.

Adopting the rigid-plastic and the multi-linear R-D models respectively in the analysis of the failure mode 3, Fig. 7-6 shows the difference of the results for different damage levels. Generally, the effect is smaller in the light damage level, while it increases when the damage level increases. This tendency is true for both the shear and bending failure modes, while the bending failure mode is more sensitive to this effect. Such phenomenon can be explained by the effect of the post-elastic stages in the failure mode which has also been illustrated in Fig. 7-5.

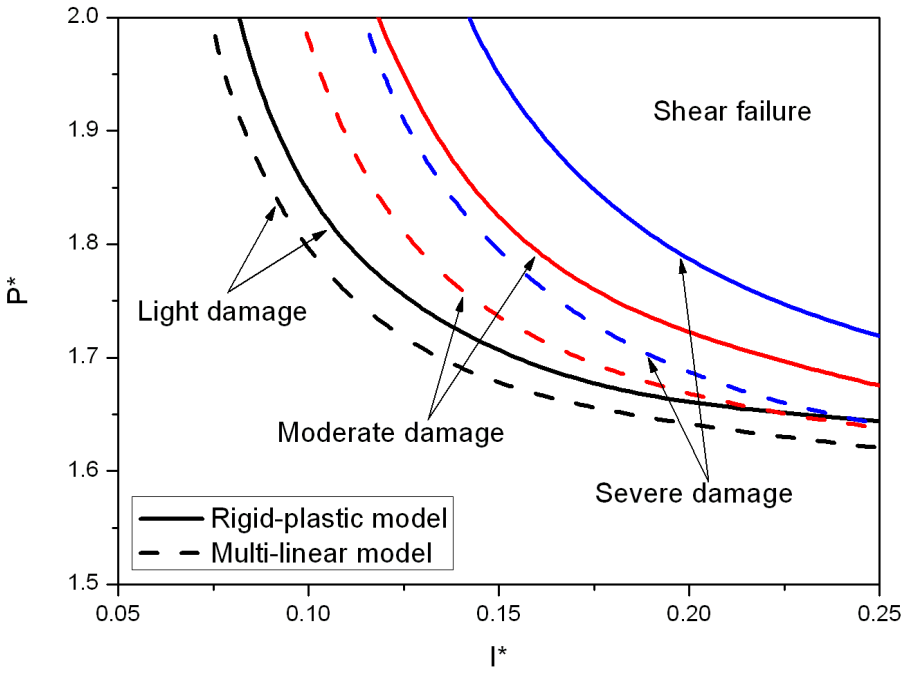

(a) Comparison of shear failure

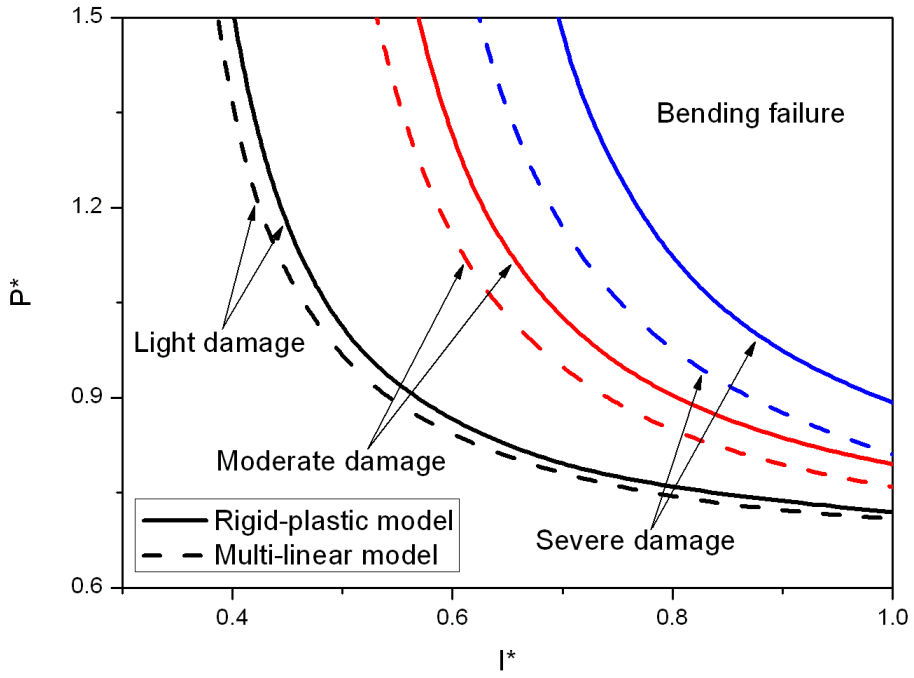

(b) Comparison of bending failure

Fig. 7 - 6 Model difference in damage levels

7.5.3. Parametric study

Since the bending and shear strength can be derived from experimental results, the relationship of the resistance versus displacement for both shear and bending failure can be in different profiles. The R-D curve as shown in Fig. 7-2 is applicable to different RC structural elements. According to the results reported by Polak (1997), Hadi (2005), Lee and Al-Mahaidi (2008), Rizzo and Lorenzis (2009), etc., the deformation property of reinforced concrete can be simplified as multi-linear.

The R-D relationship includes an ascending part, a descending part, and a relatively stable residual part with the slopes denoted as K_1, K_2, and K_3 respectively. K_1 is set equal to the elastic stiffness of the element and the resistance reaches the maximum at Q_1* or M_1*. K_2 is of a negative value and this part ends at Q_2* or M_2*. The value of K_3 is relatively small, which can be either negative or positive. Therefore, the resistance does not change a lot in the third part. The values of Q_1*, M_1*, Q_2*, and M_2* are based on the parameters in rigid-plastic model in previous comparison, and the K values for the shear and bending R-D relationships remain the same as those in the multi-linear model.

For failure mode 3 as an example, Fig. 7-7 shows the effect of K_2 and K_3. *C1* indicates the multi-linear model in the previous calculation, and the results are considered as references which are normalized as one. *C2* and *C3* stand for changing of K_3 and K_2 respectively. In this parametric study, the values of K_3 and K_2 for bending cases are determined by two kinds of curve fittings of the experiment result of Barros and Dias (2006), while K_3 and K_2 for shear cases are generated from the results of Lee *et al*. (2008) accordingly. And the increase rates based on values in *C1* are taken as 73.41% and 21.43% for K_3 and K_2 respectively. The ending time and final displacements in Fig. 7-7 are all normalized quantities.

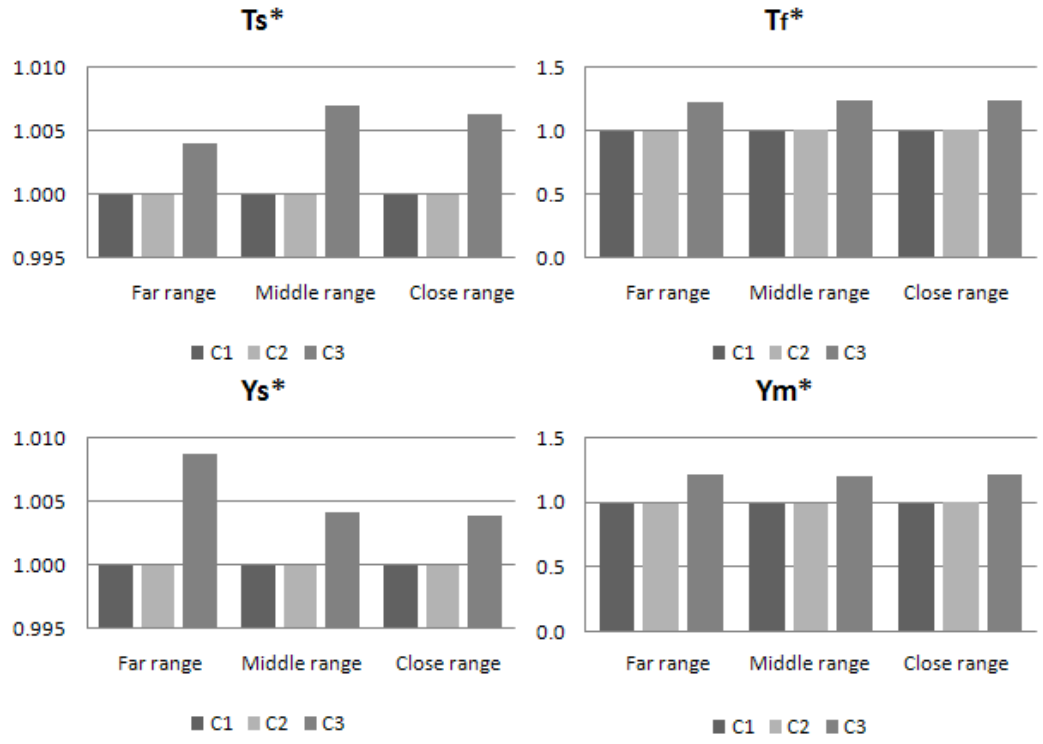

Fig. 7 - 7 Parametric study of K2 and K3

It can be seen that, the responses due to bending failure are more sensitive to the parameters K_2 than those due to shear failure. The differences for the ending time and final displacement due to the shear failure are only about 0.70% and 0.88% respectively, while those for the bending failure can be up to 24.10% and 21.79% respectively. The difference caused by varying K_3 is relatively small for both the ending time and the final displacement due to both shear and bending deformation,

while the varying K_2 affects the result evidently. The effect of varying K_3 and K_2 are roughly similar for all the three loading scenarios.

7.5.4. Applications in underground scenarios

Using the generalized integration method, even more complicated parameters can be considered in the calculation of underground structures under blast load. Taking failure mode 1 and mode 2 as examples, Fig. 7-8 and 7-9 show the P-I diagrams of underground RC structure against external and internal blast respectively. These P-I diagrams are based on the moderate damage level for both shear and bending, and the properties of different soils are the same as those in Chapter 6. The maximum damping coefficients (C_0) in non-constant SSI as expressed in Eq. (6.39) for dry sand and backfills, dense sands, and saturated sandy clay are C_0=*0.497* MPa s/m, C_0=*0.995* MPa s/m, and C_0=*2.941* MPa s/m respectively. The maximum spring coefficients (K_0) in non-constant SSI as shown in Eq. (6.40) for plastic beads-sand mixture, medium sands, and crushed rock are K_0=2.39 MN/m, K_0=3.83 MN/m, and K_0=4.83 MN/m respectively.

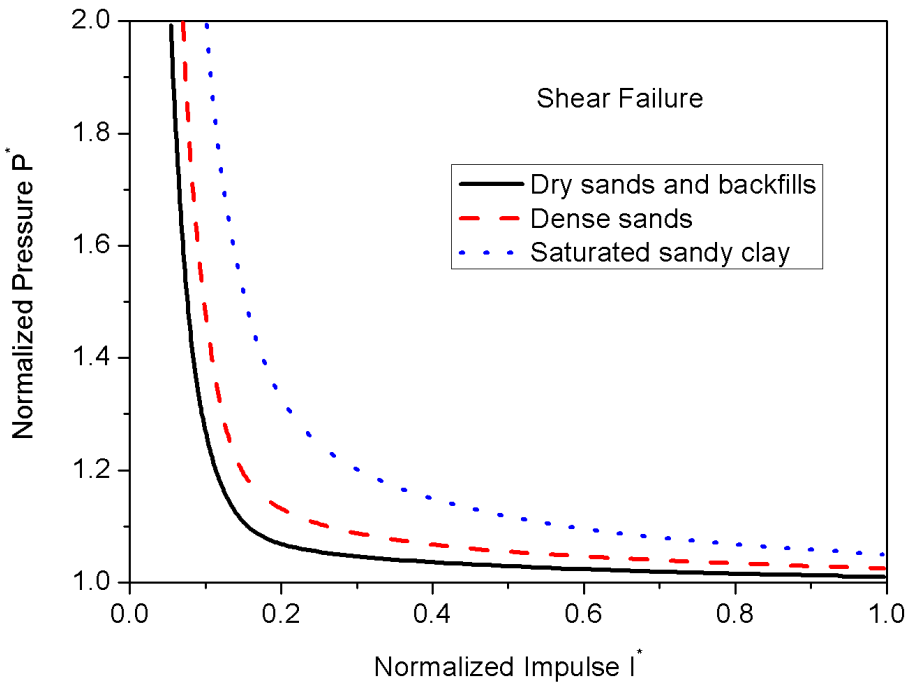

(a) Shear failure

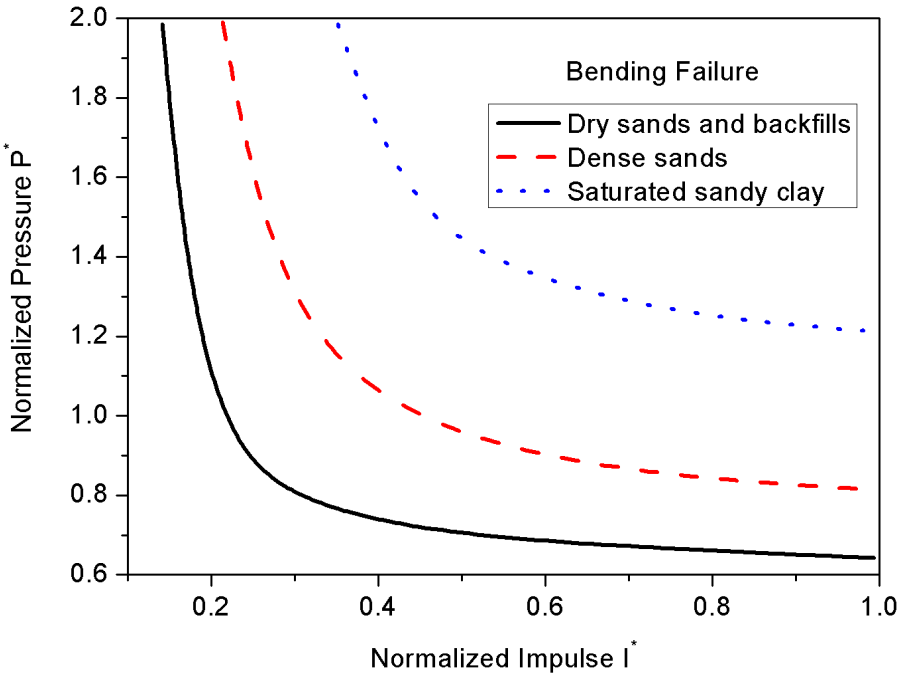

(b) Bending failure

Fig. 7 - 8 P-I diagrams of underground RC structure against external blast load

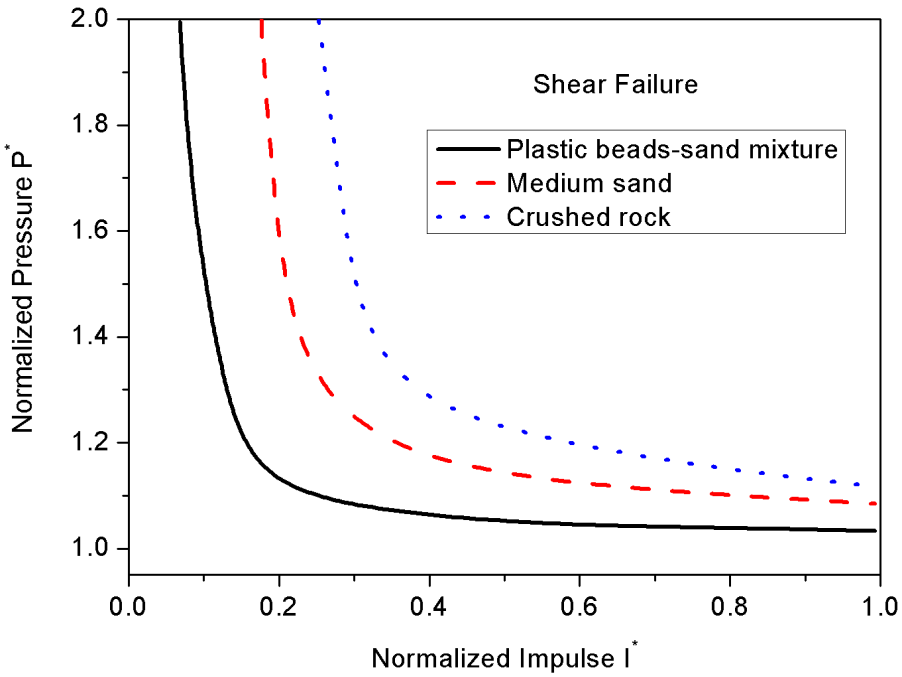

(a) Shear failure

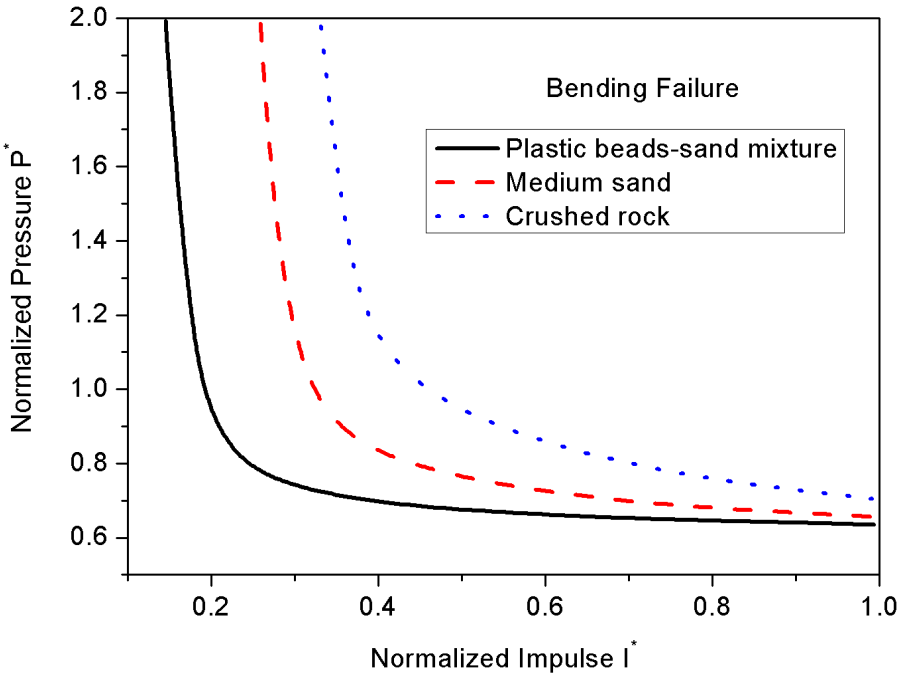

(b) Bending failure

Fig. 7 - 9 P-I diagrams of underground RC structure against internal blast load

7.6. Conclusions

The present study extends the MAM by adopting the generalized integration procedure and P-I diagrams were plotted for shear, bending, and combined failure modes by considering complex parameters. Besides the difference in failure modes, the parameters also include effect of elastic phase, nonlinearity of structural deformation, pulse shape difference, and effect of non-constant SSI for underground scenarios.

A multi-linear R-D relationship is adopted in the present study which is suitable to assess the damage of different RC structural elements with different designs. From the present study, the effect of different R-D relationships is remarkable.

The effect of the elastic phase cannot be ignored for far, middle, and close range loading scenarios. Generally in both shear and bending failures, the effect is more prominent when the damage level increases, and bending failure is more sensitive to this effect. Such phenomena can be explained by the effect of post-elastic or softening phases in the failure mode.

It was proved that using different deformation modes to satisfy the kinematic conditions of the beam has negligible effect on the maximum final deformation (Smith and Hetherington, 1994). But the result in the present study shows that, the elastic deformation has certain influence on the shear and bending plastic deformations, especially in the light damage level. In another word, the effect of the elastic stage increases with the decreasing of the plastic displacement.

The parametric study shows that the responses due to the bending failure are more sensitive to the post-elastic behavior than those due to the shear failure. The value of K_3 affects the ending time and the final displacement for shear and bending failure, and variation of K_2 affects the results more prominent. The effects of the variations of K_3 and K_2 are roughly similar for all the three loading scenarios. Therefore, it can be stated K_2 is the most critical parameter in the R-D relationship to affect the simulation results remarkably.

In the above calculations and analysis, the end time of elastic bending stage and elastic shear stage were calculated first, so that the differentiation of phases for each failure mode can be carried out. In the present study, the t_{se} is shorter than t_{me} occasionally that does not mean the shear-elastic stage always stops earlier than the bending-elastic stage.

The calculations of the multi-linear deformation model adopted in the present study are based on the SDOF system and the mode approximation method for elastic and post-elastic stages respectively. The calculations are carried out by a general integration procedure, that means the method proposed in the present study can be easily applied to any kind of deformation models without losing its accuracy.

CHAPTER 8

VERIFICATION OF MAM BASED P-I DIAGRAMS BY NUMERICAL SIMULATIONS

In the previous chapters, the P-I diagram method based on the MAM is successfully extended from surface structures to underground structures against external and internal blast load. Since the general integration procedure is adopted, complicated parameters can be considered in the derivation of P-I equations which include the more accurate blast load time history, the nonlinear structural deformational behavior, the pulse shape effect, the effect of the elastic phase, the non-constant SSI, and so on.

In this chapter, numerical simulations are carried out to validate the results in the previous chapters. The blast load is simulated in a 2-D model and remapped to a 3-D model of an RC wall. Three scenarios are simulated including surface structure against blast load, underground structure against external and internal blast load respectively. All the scenarios are simulated by the commercial code named ANSYS-AUTODYN. Results from the numerical simulations are compared with that from the analytical solutions in the form of P-I diagrams.

One strip from the center of the RC wall is taken as the beam element used in theoretical analysis. The MAM is adopted to generate P-I diagrams comparing with the results from numerical simulations.

For shear resistance:

$$Q_0 = 0.16 \times f'_{dc} \times b \times d \tag{8.1}$$

where f'_{dc} is the dynamic strength of concrete, b is the width of compression face, d is the distance from the extreme compression fiber to the centroid of the tension reinforcement.

In the present study, f'_{dc} equals to 35 MPa, b is 0.305 m for one strip of the wall for analysis, and d=0.105m. Therefore the shear resistance of wall strip is 183.95 KN.

For bending resistance:

$$M_0 = \left(A_s \times f_{ds} / b\right) \times \left[d - \left(a/2\right)\right] \tag{8.2}$$

where A_s is the area of tension reinforcement within the width b, f_{ds} is the dynamic design stress for reinforcement, a is the depth of equivalent rectangular stress block $a=A_s f_{ds}/(0.85\, b\, f'_{dc})$.

In the present study, A_s=0.000704 m^2, f_{ds}=414 MPa, so the bending resistance of the wall strip is 153.3 kN m.

Accordingly, the dimensionless strength ratio defined in Eq. 3.12 is v=1.2.

8.1. Simulation of blast load

The blast load will refer to different scaled distances. Several combinations of stand-off distance and equivalent TNT weight are listed in Table 8-1.

Table 8 - 1 Different charge weights

Distance	Charge weight (case number)		
11 m	172 kg (RC1)	423 kg (RC2)	629 kg (RC3)

It is a complex and tough task to study the dynamic response of an RC wall subjected to an explosion because the initiation of blast and the interaction between the wall and the blast wave are involved. In addition, computational cost is very high due to the simulation of the blast wave propagation. In order to reduce computational time and ensure the accuracy of results, the generation of blast loading in air is based on remapping technique provided by ANSYS-AUTODYN, which is an effective method to calculate the initiation of detonation and the blast wave propagation in air.

In the numerical simulation, the detonation is modeled using a wedge which is a common method used in ANSYS-AUTODYN. The information obtained from the wedge calculation is then written into a data file and subsequently remapped to a larger 3-D Euler air grid. The air grid loaded with blast pressure information is coupled to interact with the Lagrangian structural element, e.g. the RC wall model in the present analysis.

The first task of analysis is the simulation of explosion itself from the detonation instant and the propagation of the blast wave in air. The solution time is set to be very short referring to the arrival time when the blast wave impact on the RC wall. Just before the blast wave reaches the RC wall, the blast wave propagation simulation is stopped and the remapping file is generated based on the 2-D model. The second task is the input of previous remapping file and analysis of the impact effect and interaction with the wall of the blast wave. In this way, the results of 2-D analysis can be later mapped in the 3-D model representing the wall and the surrounded air volume drastically reducing the computational cost of numerical analysis.

The procedure of 2-D simulation is described as follows. The 2-D axial model is selected, and the basic units are mm, mg, and ms for length, mass, and time respectively. The air and TNT material models in ANSYS-AUTODYN's material library are adopted. The equation of state (EOS) for air is the ideal gas type which refers to Rogers and Mayhew (1994), while the EOS for TNT material is the JWL type which refers to Lee *et al*. (1973).

A wedge, as shown in Fig. 8-1, is built as the air part with the maximum radius the same as the distance from center of charge to the surface of the RC wall in different cases. The air part is divided as 10 mm for one cell in meshing and the initial energy for air is 2.68×105 J/kg. Later, the TNT material is filled at the center of the wedge as a circle, for example, with the radius of 318.36 mm which represents 110 kg of TNT since the shape of charge is assumed as a half-sphere. The number of cells across the radius is 1000 with grade zoning of 0.1 as the increment (*dx*). The single detonation point is located at the center of charge.

Fig. 8 - 1 2-D wedge model

After the part is built up, the solver of Euler 2-D multi-material is adopted to carry out the calculation. Fig. 8-2 shows one example of pressure contour at the end of calculation.

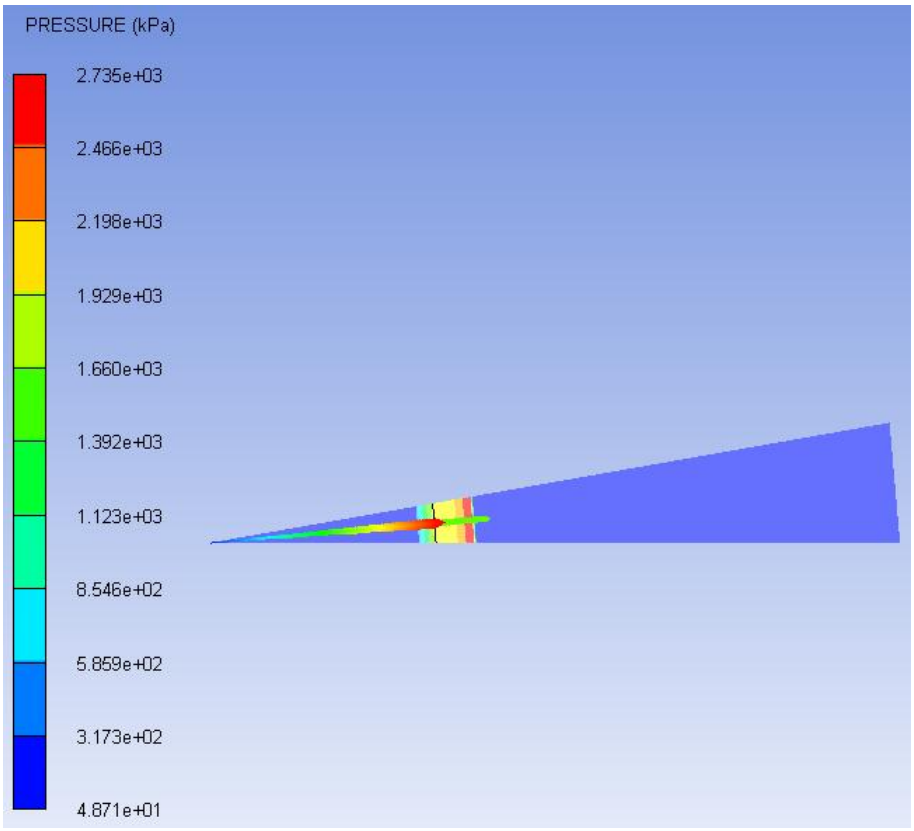

Fig. 8 - 2 Pressure contour of explosion

After the 2-D calculation is finished, the result is written in a data file which can be remapped to the 3-D simulation. Three scenarios will be shown in the following sections including surface structures against blast load, and underground structures against external and internal blast load respectively.

8.2. Simulation of surface RC wall against blast load

The numerical simulation of a surface RC wall model against blast load is carried out by the commercial code ANSYS-AUTODYN. Details of the simulation of the surface wall against blast load are as follows.

8.2.1. Geometry model

The section view of design drawing for the RC wall is shown in Fig. 8-3.

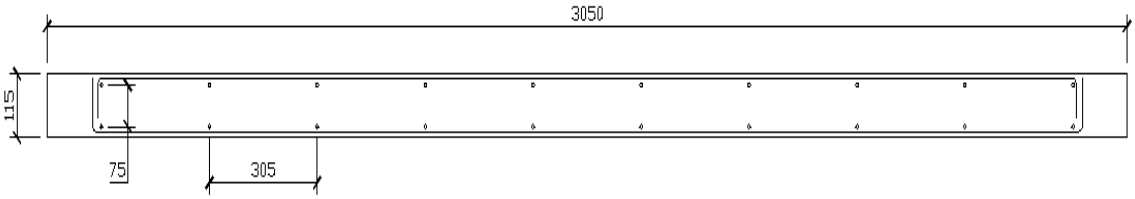

Fig. 8 - 3 Section view of RC wall

The Cartesian coordinate is defined as that in Fig. 8-4. The X-axis is from the bottom center of the RC wall along with the long edge; the Y-axis is from the bottom center of RC wall pointing to the top of RC wall; and the Z-axis is from the bottom center of RC wall pointing to the center of charge.

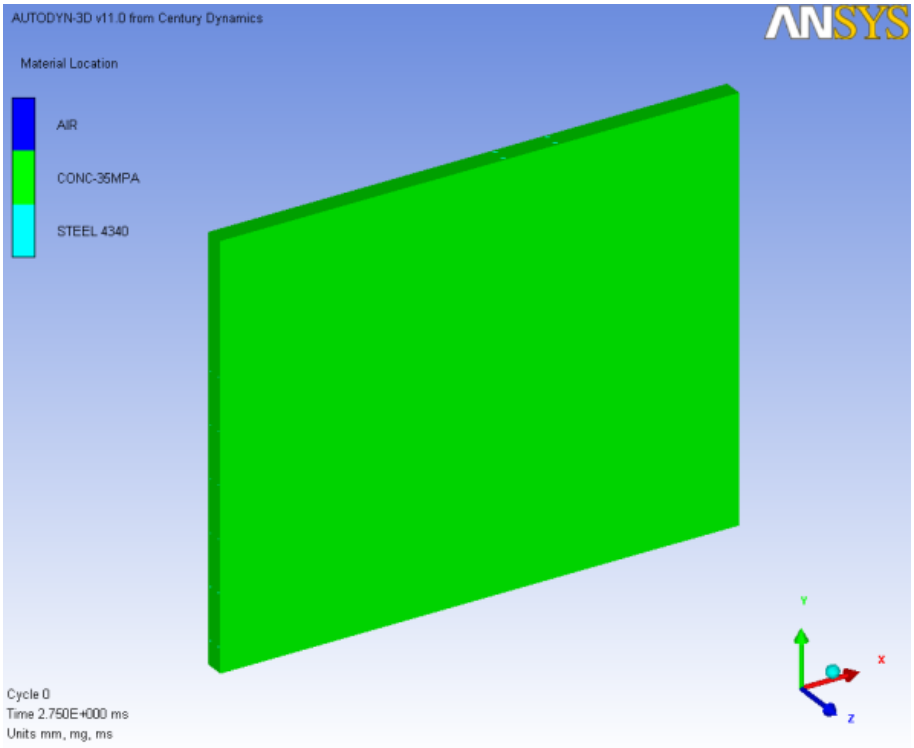

a) Full model

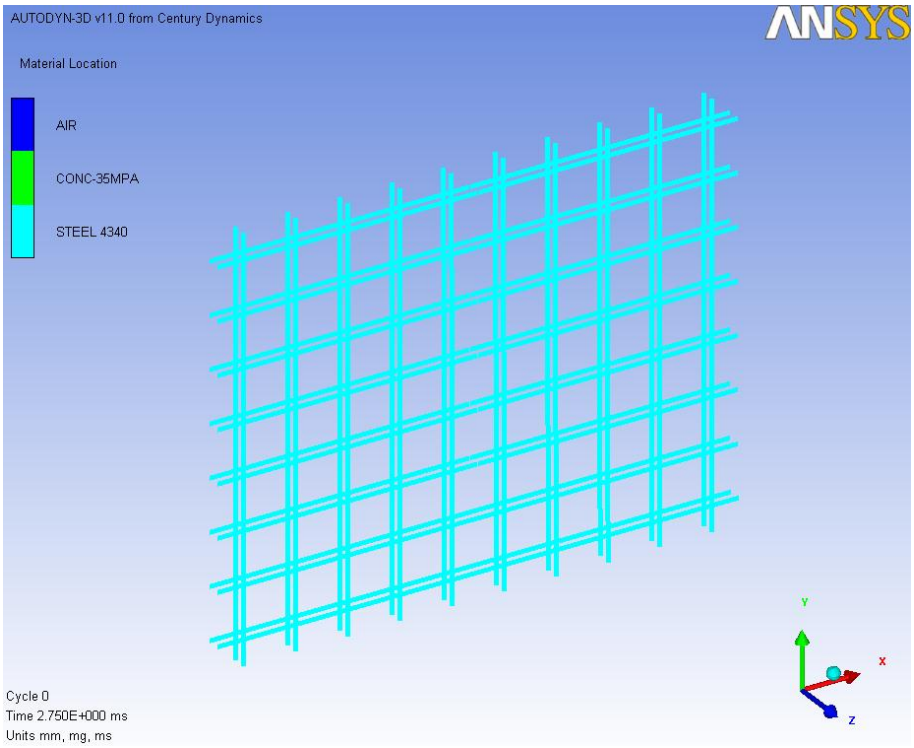

b) Rebars

Fig. 8 - 4 Geometry model of RC wall

The 3-D model, which included the RC structure and the surrounding air, and blast load are symmetrical to the YZ-plane in the Cartesian coordinate. To save the computational time, half models for both RC wall and air are built and the full models can be plotted by shown the mirror according to X-plane.

The geometrical model of RC wall as shown in Fig. 8-4 is the solid Largrange model, and the rebars are built up as beam model grouped to the RC nodes. In the present analysis, the total size of the RC wall model is 3050 mm(W) × 2440 mm(H) × 115 mm(T). The radius and span of the rebar are 10 mm and 305 mm respectively.

The solver for surrounding air is the Eular 3-D multi-material. The width and height of air are 4 m and 3 m respectively which fully covered the RC wall model. The length of the air model is 14 m from the center of charge, and the RC wall model is placed at 3 m from another end of the air model to the front surface of the RC wall. The mesh size of air and structure is defined as 0.1 m in three axial directions.

After the wall part and air part are built up, the data file from 2-D calculation can be filled. Both the air and TNT materials are remapped into the 3-D model, and the remapping is symmetrical to X-plane as well. Fig. 8-5 shows the vector contour of the blast load with the RC wall model.

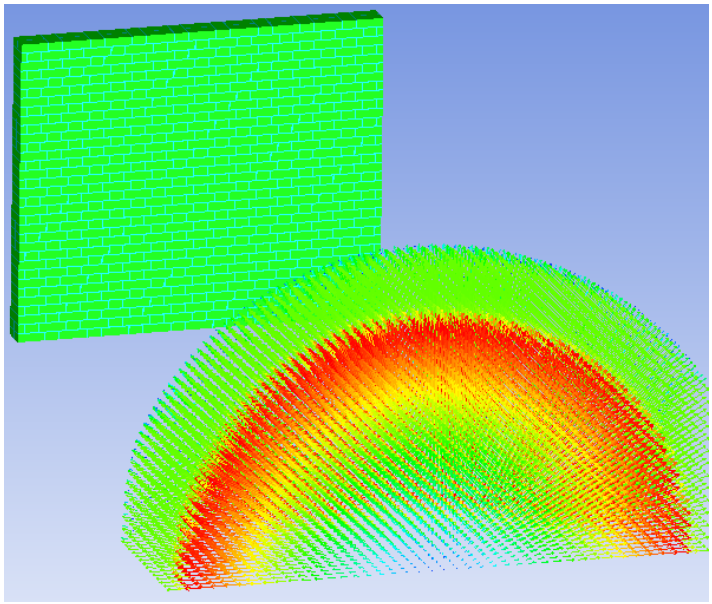

Fig. 8 - 5 Vector contour of blast load (with RC structure model)

In the solution control, the wrap-up criterion of energy friction is set to 0.5, and the starting time of calculation is set the same as the ending time of 2-D calculation so that the blast wave would keep on propagating in the 3-D model.

8.2.2. Material properties

The material properties of air, concrete, and rebar in the present study is modified from the original materials named air, conc-35_MPa, and steel_4340 in the ANSYS-AUTODYN material library respectively. The air material is the same as that used in 2D remapping calculation with the EOS of ideal gas.

The concrete material is modified based on the original conc-35_MPa material which refers to Riedel (2000). The P_alpha EOS is adopted; the strength and failure models are the RHT models; and the erosion criterion is based on the geometric strain.

The steel model is modified from the original steel_4340 model from Johnson and Cook (1985). The linear EOS equation and Johnson Cook strength model are adopted for the steel material. The failure criterion is based on the principal strain and the erosion criterion is again based on the geometric strain.

In the present analysis, the dynamic ultimate compressive strength of concrete is 35 MPa and the dynamic design stress for reinforcement is 410 MPa which are calculated according to the dynamic increase factor given in TM5-1300 (1990).

The computational time for each case is 100 ms, which is long enough to evaluate the final structural displacement after vibration. The numbers of elements for RC block, steel rebars, and air material are 5120, 1280, and 224000 respectively. The element types for RC, steel, and air are 3D solid element with RHT concrete model, 2D link element with Johnson Cook strength model, and 3D solid element with ideal gas EOS.

8.2.3. Erosion criterion

In the generalized integration procedure, the efficiency of calculation is affected by the time step and the quality of element which are decided by the shortest element

edge and the deformation of element in the present time step. The erosion is a technique adopted in numerical simulations to erode greatly distorted elements so that the problems associated with the mesh distortions caused by gross motions of a Lagrangian grid can be overcome. It should also be noticed that, the eroded elements will result in loss of internal energy, strength and mass, and they may affect the overall results. Therefore, the erosion criterion should be decided with discretion.

In general, the erosion criterion has to be selected according to loading conditions and objective in the work. In the present analysis, the RC structure is under high loading density (the blast load with certain distances). Under such condition, a large number of elements might reach the erosion criteria and would be eroded during computational process.

Normally the instantaneous geometric strain is set to be 150% as the erosion criterion in penetration simulations, and the erosion limit varies between 100% and 200%. In the present analysis, 100% geometric strain is set as the erosion criterion for both the concrete and steel materials. Such consideration is based on the general assumption in numerical simulation and the damage definition in the present study.

8.2.4. Boundary conditions

The RC wall model in the present analysis is simply supported on the long edges in the three axial directions as shown in Fig. 8-6.

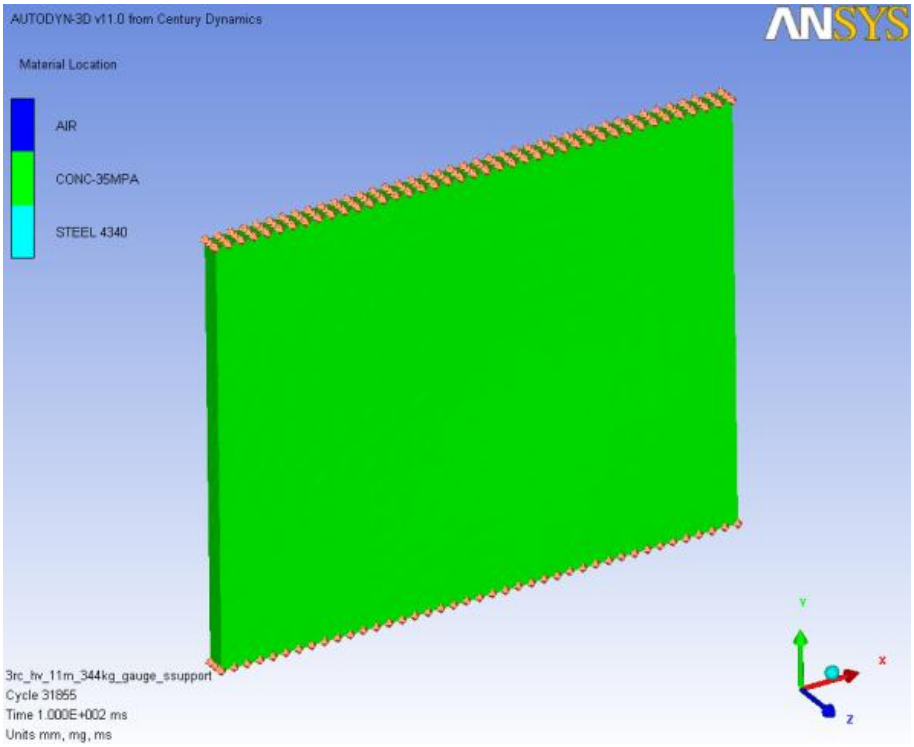

Fig. 8 - 6 Boundary conditions of RC wall

The flow-out boundary is added on the surrounding air but one surface is left unconstrained which indicates the ground to reflect blast wave. Fig. 8-7 shows half of the boundaries. In some cases (e.g., buried wall under external and internal blast load), the flow-out boundary is applied to all surfaces of the air model.

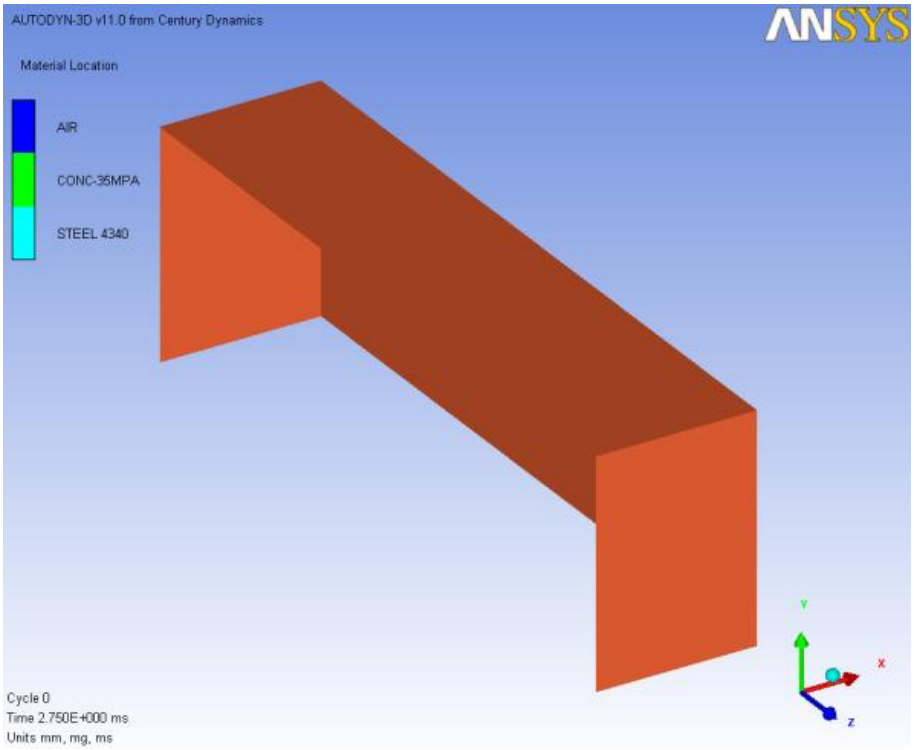

Fig. 8 - 7 Boundary conditions of air (half section at X-plane)

8.2.5. Results and discussion

The time histories of velocities and displacements of the RC wall before 100 ms after explosion under surface blast load are shown as Fig. 8-8 to 8-10 (as case RC1, RC2, and RC3). The velocities and displacements vibrate stably after the blast load is reflected by the RC wall.

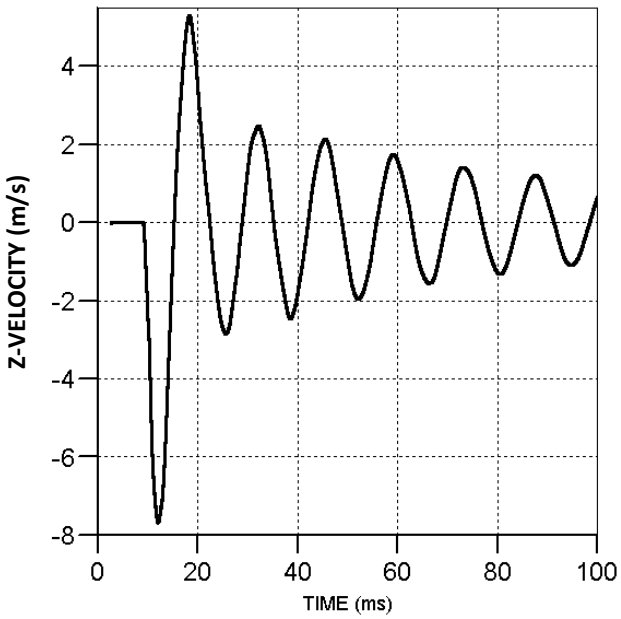

a) Time history of velocity

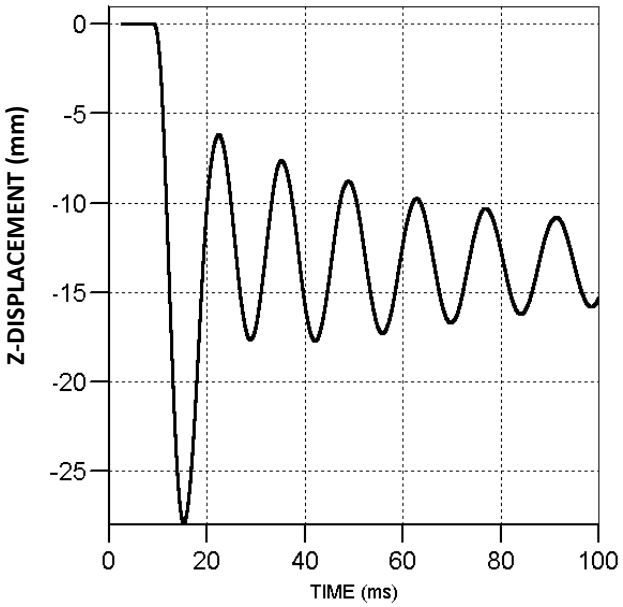

b) Time history of displacement

Fig. 8 - 8 Velocity and displacement for case RC1 (light bending damage)

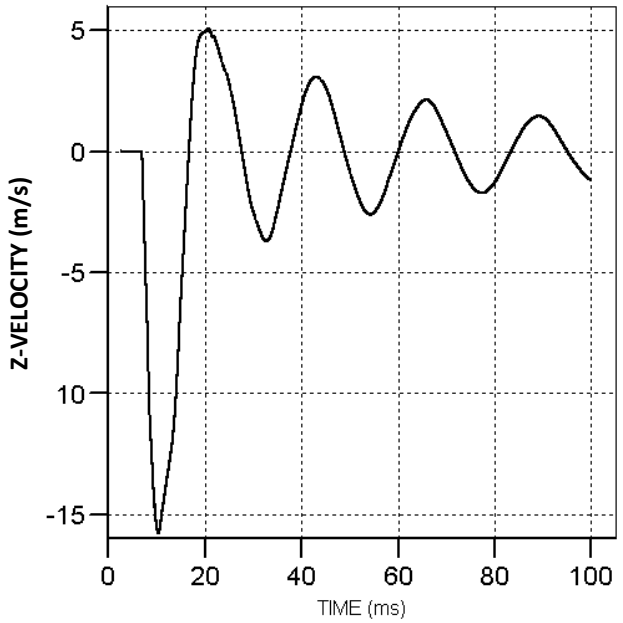

a) Time history of velocity

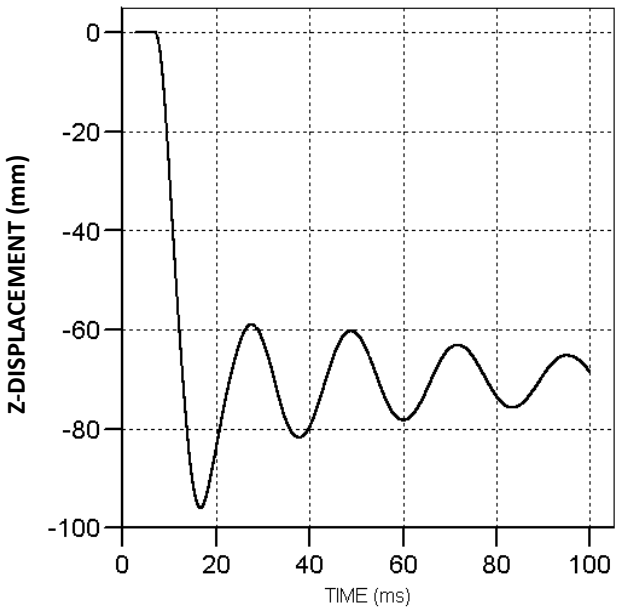

b) Time history of displacement

Fig. 8 - 9 Velocity and displacement for case RC2 (moderate bending damage)

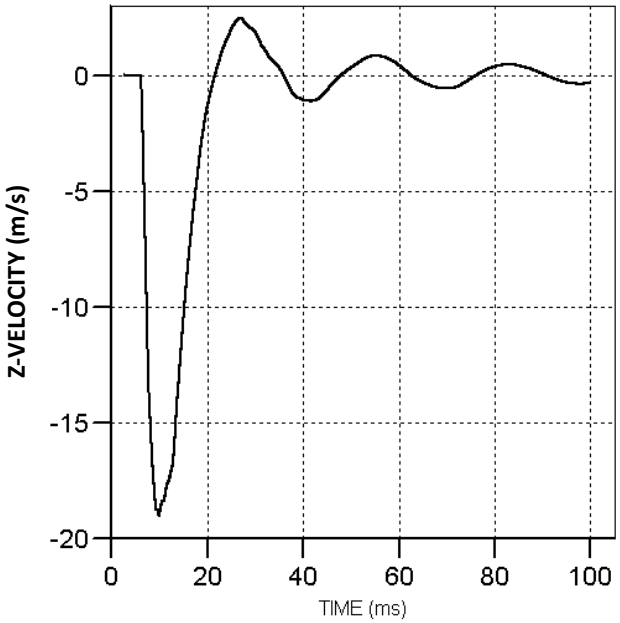

a) Time history of velocity

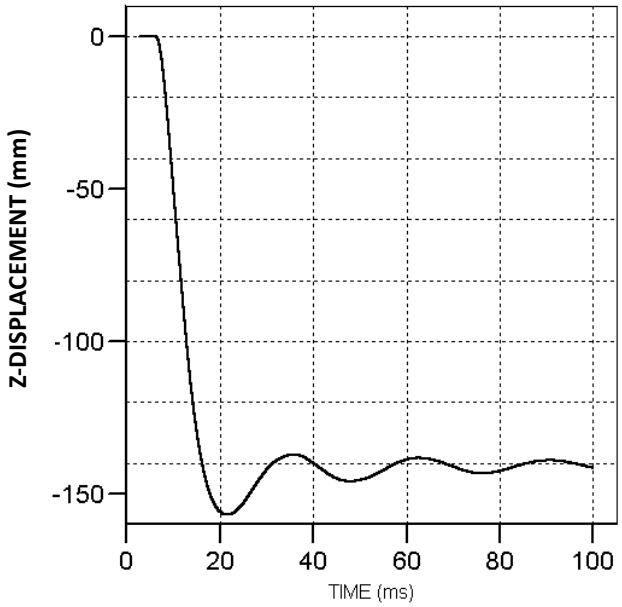

b) Time history of displacement

Fig. 8 - 10 Velocity and displacement for case RC3 (severe bending damage)

Results from the numerical simulation are compared with theoretical solutions. The P-I diagrams for numerical simulation are generated by curve fitting of result data. Fig. 8-11 shows the two results of surface RC structure under blast load. The charge (TNT) weights used in the numerical simulation are 172 kg, 423 kg, and 629 kg which present scaled distances of 1.978, 1.465, and 1.284 respectively. Such three loading cases are preliminarily designed that, the bending damage levels of the RC wall are light, moderate, and severe respectively. The shear deformations of RC wall are shown accordingly. Based on the ratio of shear to bending strength of the RC wall, failure mode 3, the combined failure mode with one plastic hinge at the center and direct shear failure near the supports is adopted in the comparison.

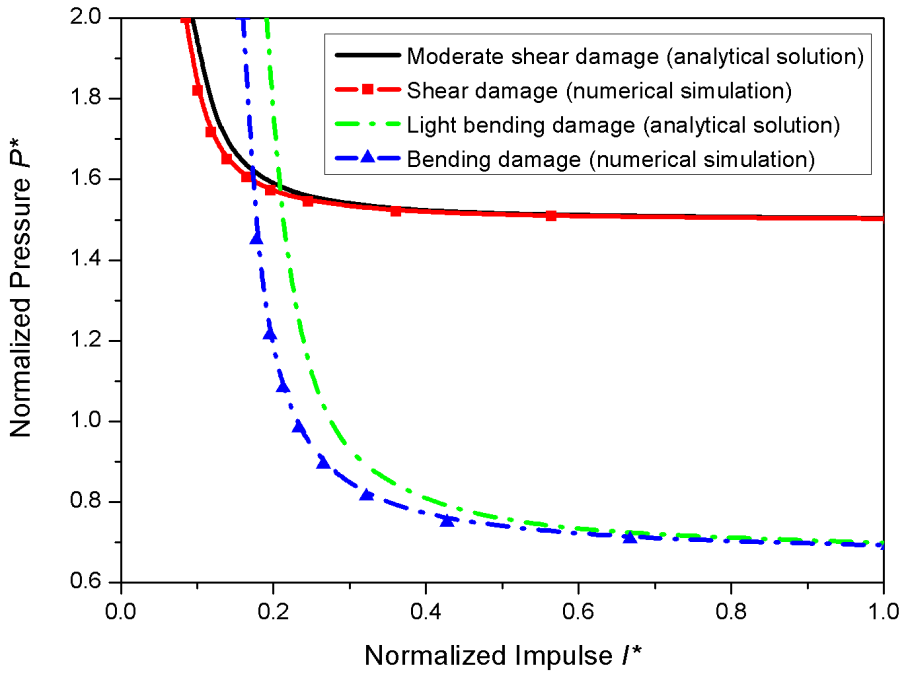

a) Light bending damage

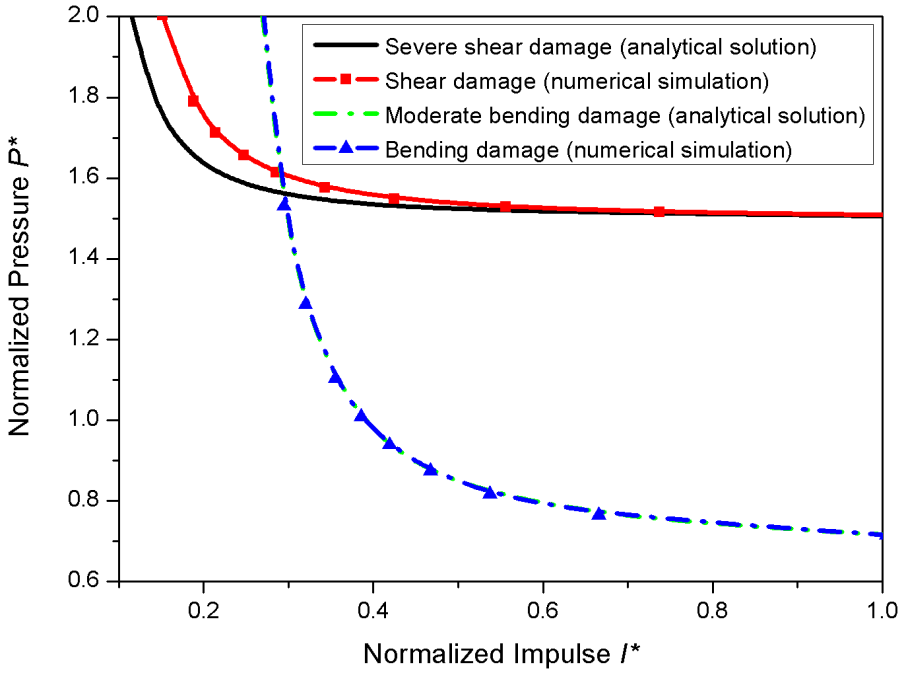

b) Moderate bending damage

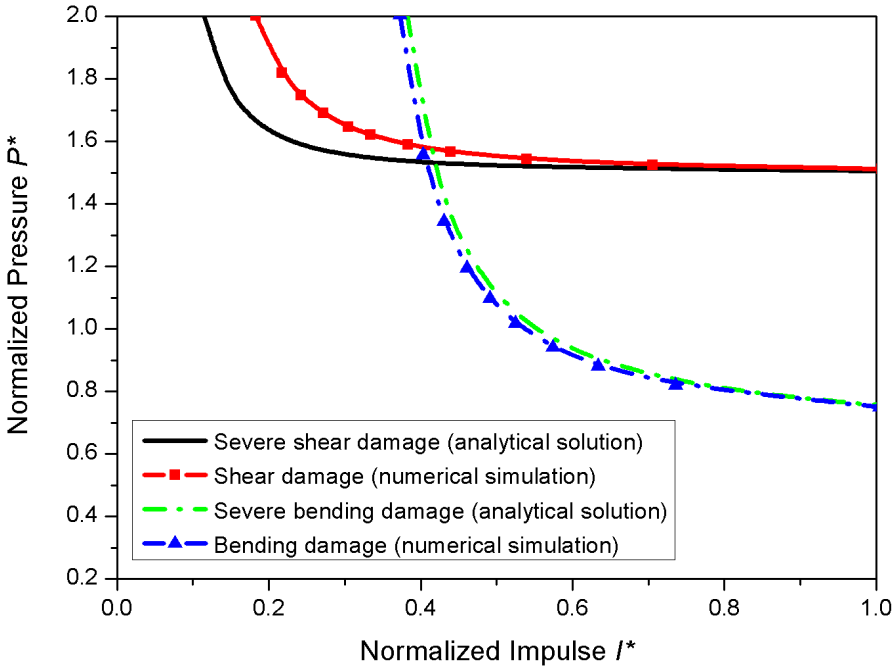

c) Severe bending damage

Fig. 8 - 11 Result comparison for surface blast cases

The P-I diagrams in Fig. 8-11 show that:

- The numerical simulations normally over-estimate the bending damage of surface RC structure under blast load. In the middle range from the center of explosion (moderate scaled distance, Fig. 8-11 b)), the bending damage generated from the theoretical solution and the numerical simulation are very close. The error in close-in range case (Fig. 8-11 c)) is acceptable, especially for the bending damage. The P-I diagrams with respect to severe shear damage have some discrepacies in the impulsive load region. The error of the bending damage in far range case (Fig. 8-11 a)) becomes considerable especially in the impulsive and dynamic regions of P-I diagram. However, the discrepacies with respect to moderate shear damage becomes minor based on Fig. 8-11 a). The errors of bending damage between the theoretical solutions and numerical simulations are 29.16%, 1.37%, and 4.58% for light, moderate, and severe bending damage level respectively.

- The shear damage in the above three cases falls in moderate or severe level. The shear damage is more severely presented than the bending damage. Such phenomena means that the RC wall is very vulnerable to shear damage and strengthening of the shear resistance of the RC wall by using stirrups is essential.

8.3. Simulation of underground RC wall against external blast load

Three load cases (RC-C1, RC-C2, and RC-C3) for the scenario of underground RC wall against external blast load are simulated. The geometric model, material properties, erosion criterion, and boundary conditions remain the same as those in section 8.2. The SSI is simplified as a damping ratio and is applied on all the elements of the RC part. According to general experience, the damping ratio is set to be 6% for simulating the SSI caused by dry sand and backfills used in Chapter 3. Although the blast wave propergation in soil is much different from that in air, for convenience of the simulation and comparison, the blast pressure and impulse on the RC wall remain the same as that in surface RC wall simulation. The difference of the blast wave propagation in different material is not in the scope of current study. The results of the RC wall response are shown in Fig. 8-12 to 8-14.

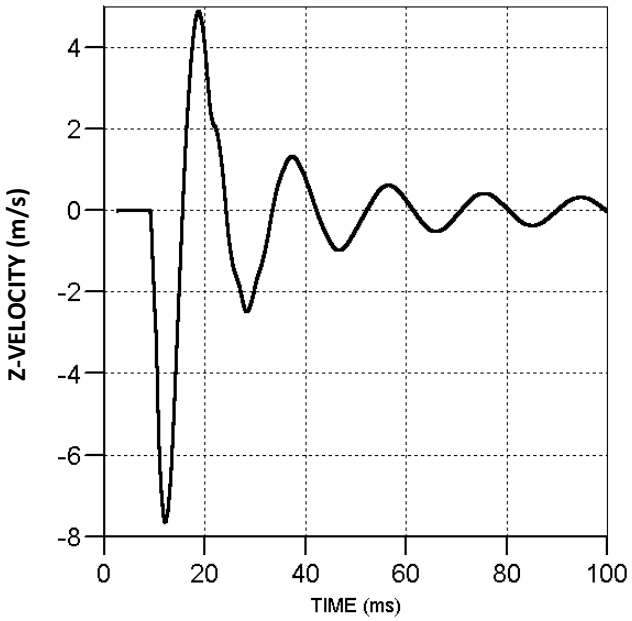

a) Time history of velocity

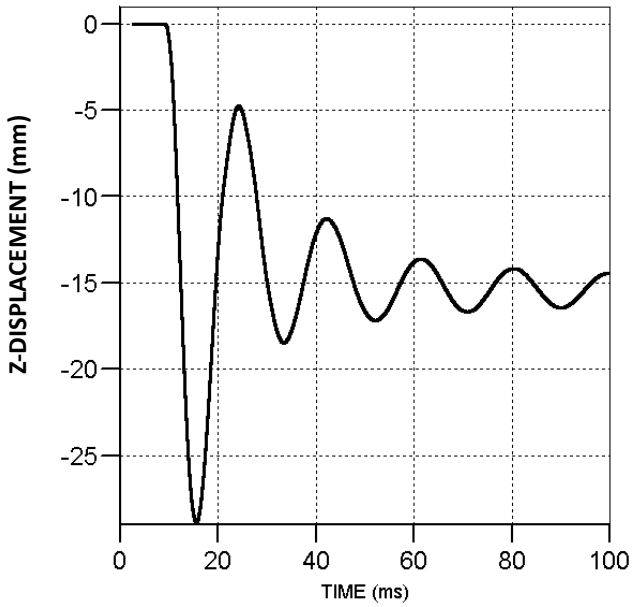

b) Time history of displacement

Fig. 8 - 12 Velocity and displacement for case RC-C1 (light bending damage)

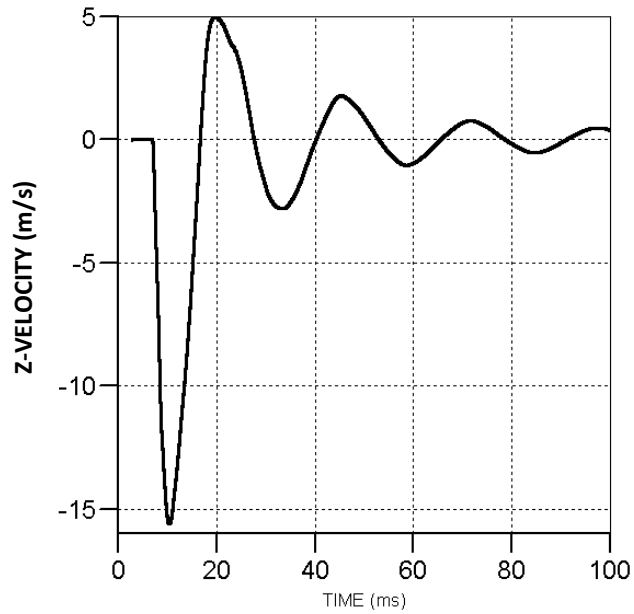

a) Time history of velocity

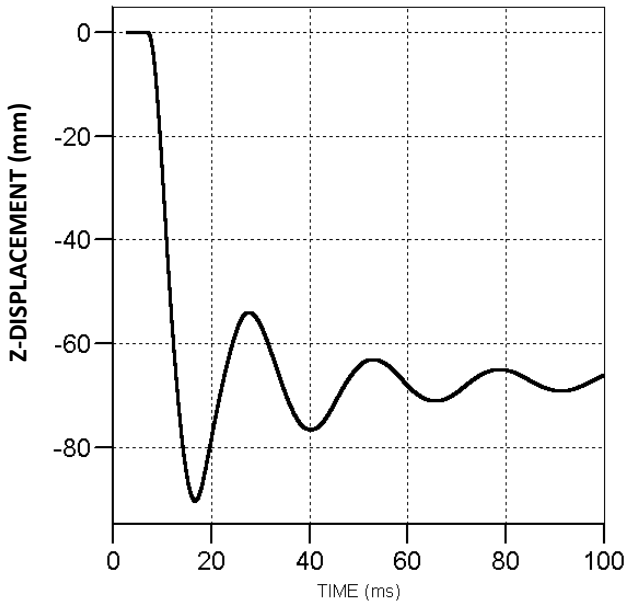

b) Time history of displacement

Fig. 8 - 13 Velocity and displacement for case RC-C2 (moderate bending damage)

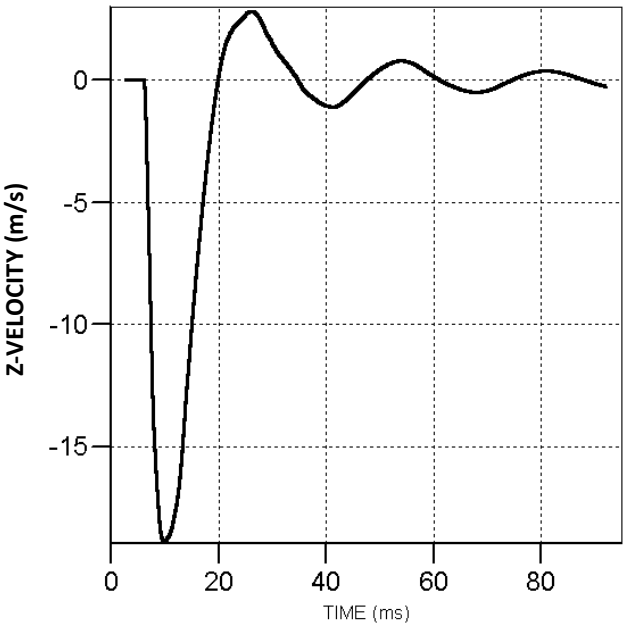

a) Time history of velocity

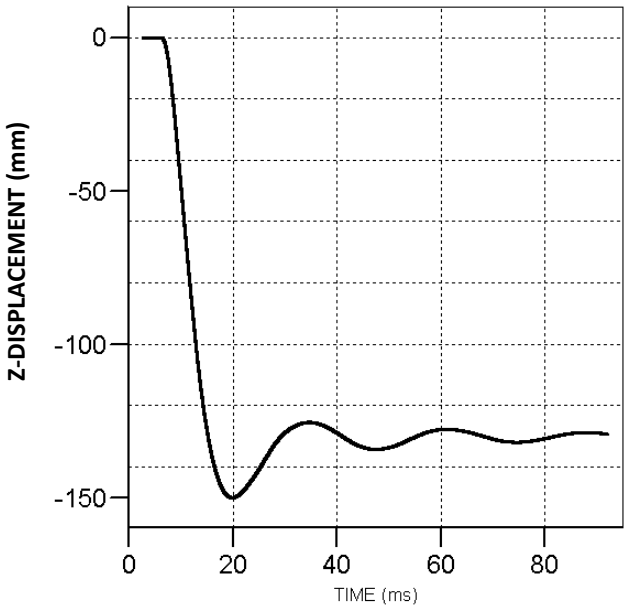

b) Time history of displacement

Fig. 8 - 14 Velocity and displacement for case RC-C3 (severe bending damage)

Comparison between the P-I diagrams of the underground RC wall against external blast load at different damage level is shown in Fig. 8-15.

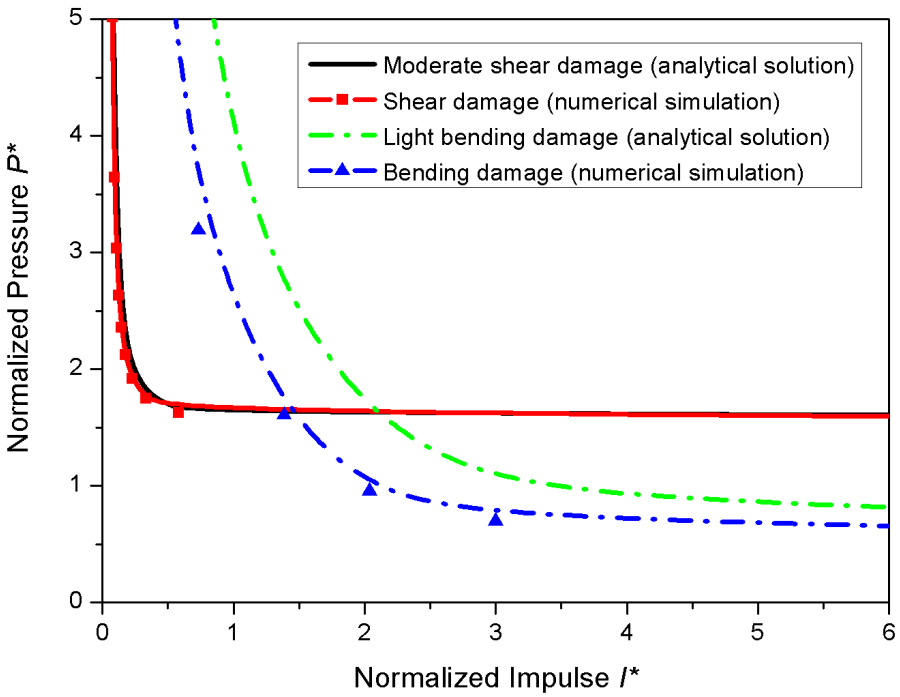

a) Light bending damage

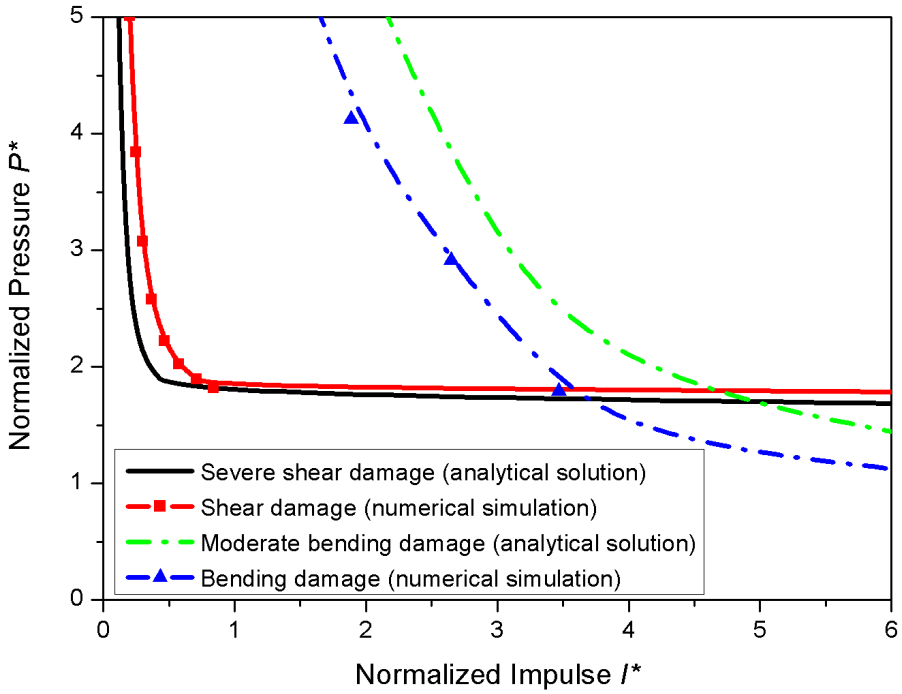

b) Moderate bending damage

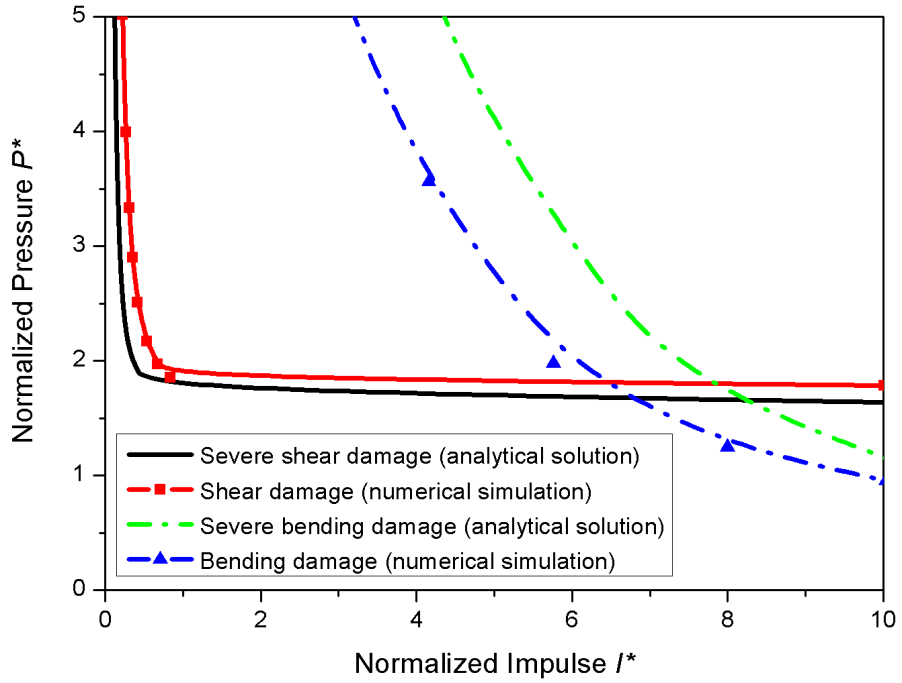

c) Severe bending damage

Fig. 8 - 15 Result comparison for underground external blast cases

The P-I diagrams for underground RC structure under external blast load show that:

- Because of the SSI (the damping effect for underground RC structure against external blast load), the bending damage is reduced in all damage levels. Such attenuation effect is much remarkable in the impulsive and dynamic regions of P-I diagrams. The attenuation percentages are 9.79%, 6.62%, and 22.58% for light, moderate, and severe bending damage respectively.
- The shear damage level is higher than bending damage level for different scaled distances. By comparing with the results of surface RC structure, the decrement of shear damage caused by the damping effect is 3.06%, 1.85%, and 23.19% in light, moderate, and severe bending damage cases respectively.

8.4. Simulation of underground RC wall against internal blast load

The soil material model used in numerical simulation is a simplified elastic-plastic model whose Young's modulus is defined according to Eq. (6.40). The interface of structure and soil is modeled as two contact faces, and the interaction is treated by the built-in solver of ANSYS-AUTODYN.

Three load cases (RC-K1, RC-K2, and RC-K3) of underground RC wall under internal blast load are simulated. The SSI is simulated as a block of soil attached to the rear face of RC wall as shown in Fig. 8-16. The blast wave on the RC wall remain the same as that in surface RC wall simulation since the blast wave propagates in air before hitting on the RC wall. The result is shown in Fig. 8-17 to 8-19.

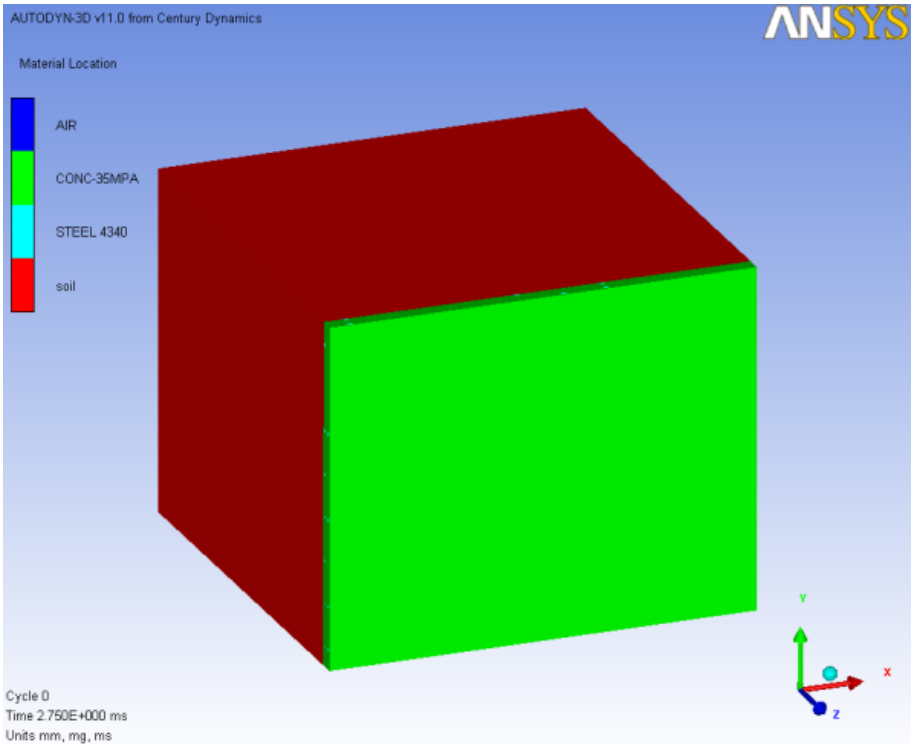

Fig. 8 - 16 Soil layer in RC-K cases

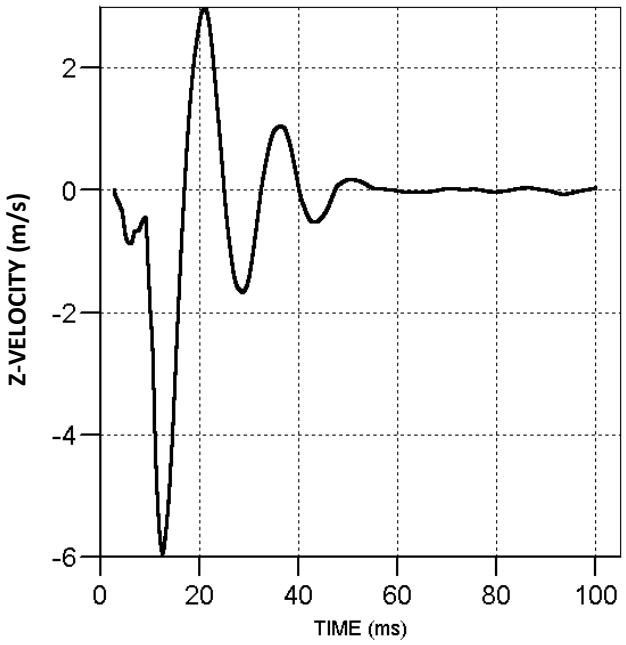

a) Time history of velocity

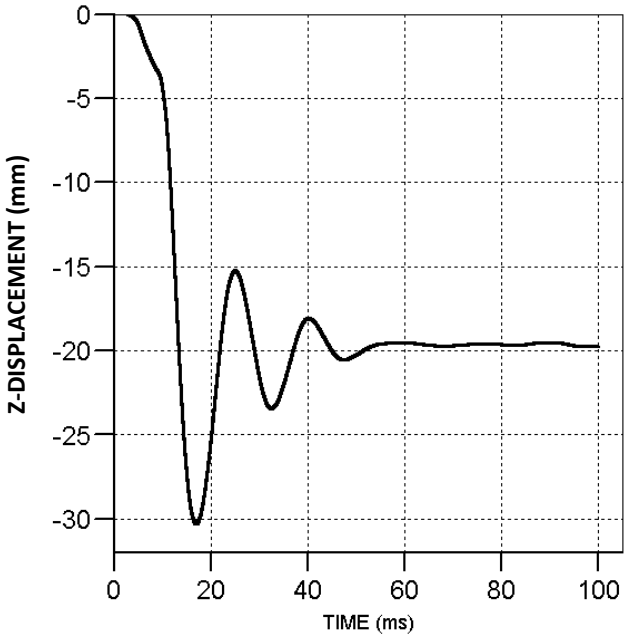

b) Time history of displacement

Fig. 8 - 17 Velocity and displacement for case RC-K1 (light bending damage)

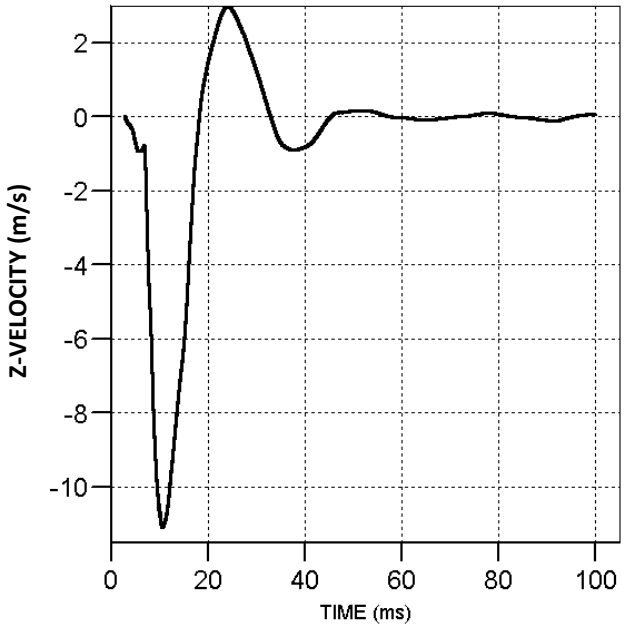

a) Time history of velocity

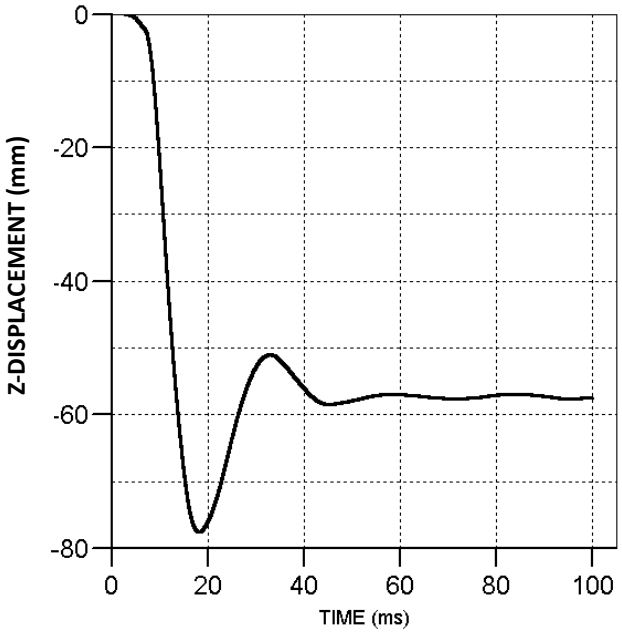

b) Time history of displacement

Fig. 8 - 18 Velocity and displacement for case RC-K2 (moderate bending damage)

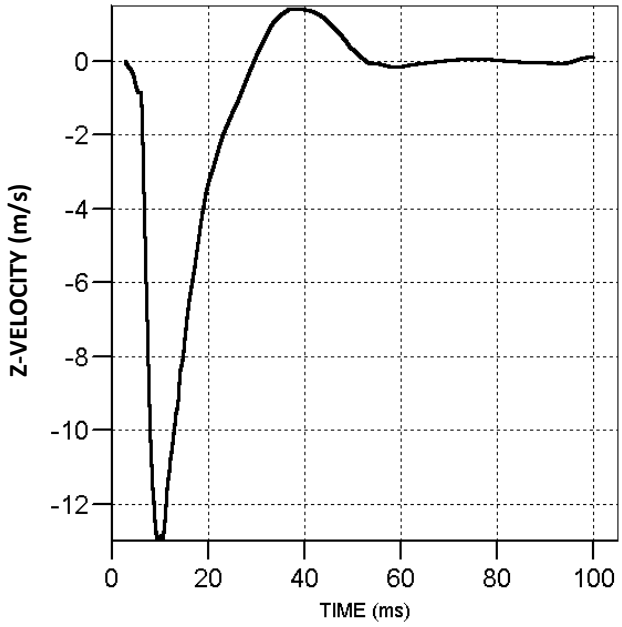

a) Time history of velocity

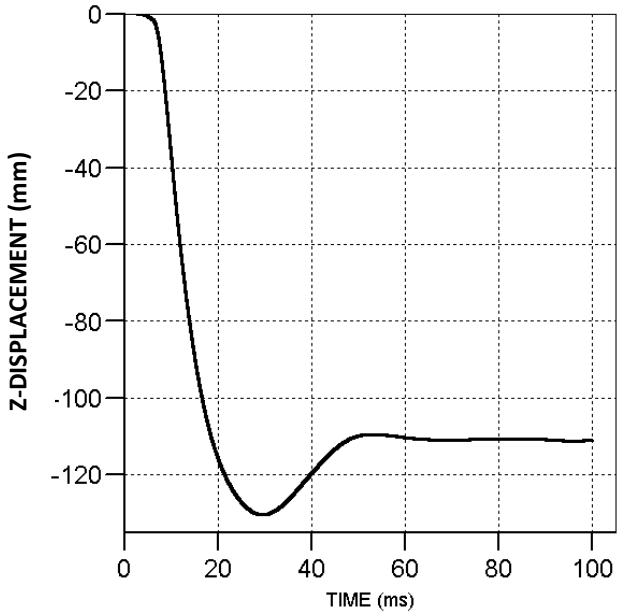

b) Time history of displacement

Fig. 8 - 19 Velocity and displacement for case RC-K3 (severe bending damage)

Comparison between P-I diagrams of underground RC wall against internal blast load at different damage level is shown in Fig. 8-20.

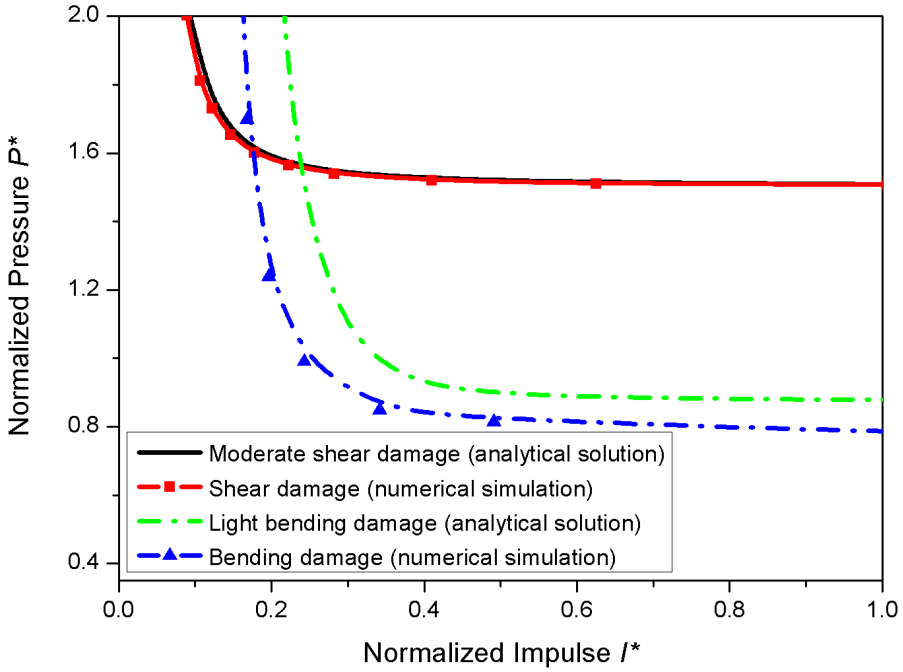

a) Light bending damage

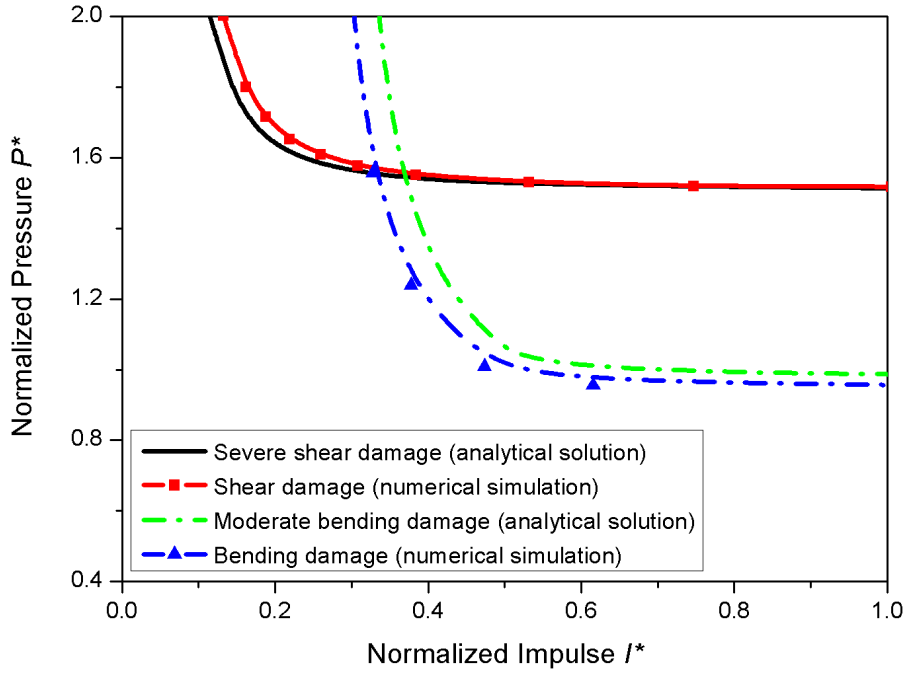

b) Moderate bending damage

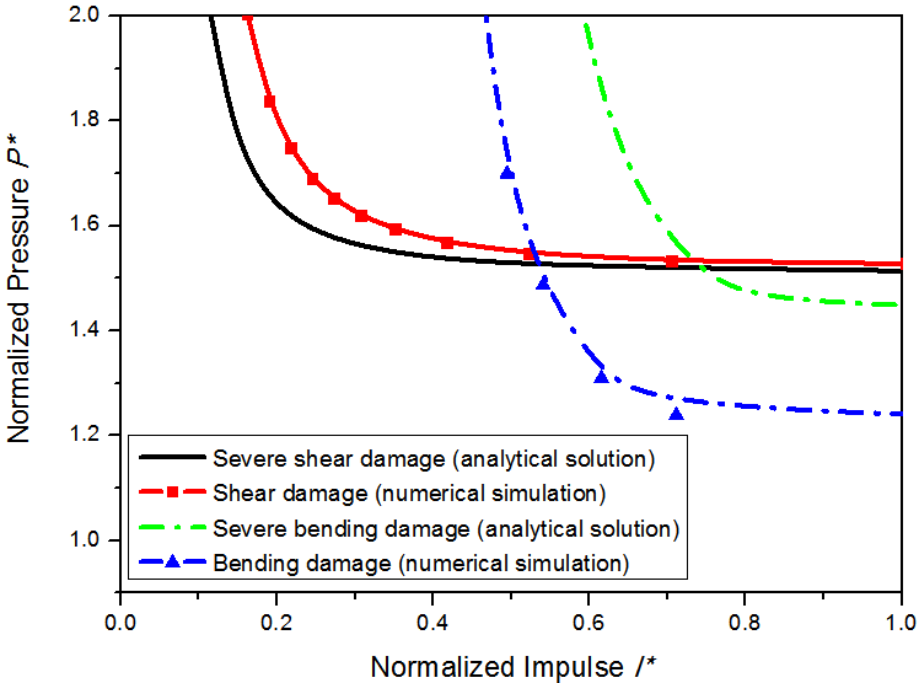

c) Severe bending damage

Fig. 8 - 20 Result comparison for underground internal blast cases

The P-I diagrams for underground RC structure under internal blast load show that:

- Due to the simplified SSI (the stiffness effect for underground RC structure under internal blast load), the bending damage is reduced in all damage levels, especially in severe bending damage level. The reduction percentages are 12.31%, 15.45%, and 19.59% for light, moderate, and severe bending damage respectively.
- The shear damage level is higher than the bending damage level for different scaled distances. By comparing with results of the surface RC structure, the decrement of shear damage caused by the stiffness effect is 9.77%, 24.93%, and 23.11% in light, moderate, and severe bending damage cases respectively.

8.5. Concluding remarks

Although the distribution of blast load is not uniform, the maximum displacement appears at the centroid of the RC wall. Such distribution may cause some error when using the P-I diagrams generated based on the MAM. Through comparing to the numerical results, it is observed that the discrepancies of the P-I curves are acceptable. Since the load used in the theoretical analysis is uniformly distributed, the results from numerical simulations are more conservative.

Based on the above comparison, it can be concluded that the the maximum displacement from the numerical simulations of a three-dimensional wall model is more conservative than that predicted by the two-dimensional beam model. Factors which cause such difference in result can be the distribution mode of the blast load, the accuracy of blast load calculated by ANSYS-AUTODYN and TM5-1300, difference in material properties, and so on.

In the underground RC structure against external blast load scenario, the SSI on bending damage at relatively large scaled distance is significant while it decreases with the increase of the scaled distance and the smallest error appear in the moderate bending damage cases. The SSI affects on the shear damage in the large scaled distance cases significantely, while it is not remarkable in the middle and small scaled distance cases.

In the scenario of underground RC structure against internal blast load, the SSI on bending damage at a large scaled distance is significant while it decreases with the increase of the scaled distance. The SSI on the shear damage affects in the moderate and large scaled distance cases, while the effect is minor in the small scaled distance cases.

Generally, results from numerical simulations agree favorably well with that from the theoretical solutions of beam model, especially at the moderate damage level. The P-I diagrams generated from the mode approximation method for surface and underground RC structure under different blast load cases are verified.

CHAPTER 9

CONCLUSIONS AND RECOMMENDATIONS

9.1. Conclusion and discussions on the present work

The present study develops a new progress in the damage assessment for reinforced concrete structures by using the P-I diagrams based on the mode approximation method. It can be concluded from the results that the mode approximation method is an effective way to generate P-I diagrams which can be used in damage assessment of surface and underground reinforced concrete structures again blast load. The generalized integration procedure makes it easy to involve nonlinear or non-constant parameters when generating the P-I equations. In addition, it is convenient to extend the P-I diagram method to other conditions such as other materials, load shape, and so on.

9.1.1. Damage assessment for underground structures against blast load

For the damage assessment of underground structures against external blast load, the SSI is simplified as a damping effect, and such effect only exists during the blast duration. The analysis is based on a rigid-plastic strength model to assess damage. The developed P-I diagrams consider decoupled SSI and can be applied conveniently to assess different failure modes of the underground structures. Comparison with the results of surface structures shows that the developed P-I diagram method based on the MAM is valid and it can be used to surface structures by setting the SSI coefficient small enough. The effect of soil cannot be ignored in estimating the blast load applied to the structure. With the increase of the acoustic impendence, interaction between the structure and the surrounding soil becomes more and more significant. The maximum shear displacement is more sensitive to the pressure applied than the maximum bending displacement, while the effect of the impulse to the maximum shear and bending displacements is similar.

For the damage assessment of underground structures subjected to internal blast load, the SSI is simplified as a spring effect which exists throughout the whole structural response time. A rigid-plastic beam model is applied in order to consider the combined effect of both shear and bending failure. Verification shows that the present analysis is a successful extension of the damage assessment of surface structures to underground structures. Results show that with the increase of the soil stiffness, the soil-structural interaction to the structural damage becomes very significant.

9.1.2. Generalized integration procedure as extension of mode approximation method

When the generalized integration procedure is adopted in the MAM, nonlinearities and non-constancy of parameters can be easily involved in the solution of the P-I equations.

The study of pulse shape effect shows that, in the analysis of surface structure, the error caused by pulse shape difference is limited in shear displacement, while the effect is distinct in bending displacement. Results from the triangular load and the rectangular load give higher estimation of the final displacements of both shear and bending.

In the analysis of underground structure under external blast load, the non-constancy of SSI is considered. It can be concluded that pulse shape effect still exists in such analysis. The constant damping coefficient may lead to a danger design and the non-constancy of SSI cannot be ignored.

The analysis of underground structure under internal blast load shows that, the result of triangular load is close to the rectangular load, and they both give higher estimation of the final displacements due to shear and bending. P-I diagrams are more sensitive to the non-constancy of SSI in the impulse and dynamic region.

The nonlinearity of the material shear and bending strengths are studied as well. The effect of different R-D relationships is significant. The effect of the elastic phase cannot be ignored in far, middle, and close range loading scenarios. Generally

in both shear and bending failures, the effect is more prominent when the damage level increases, and bending failure is more sensitive to this effect.

9.1.3. Validation by numerical simulation

The analytical results from chapter 3 to 7 are compared with numerical results obtained by using commercial code ANSYS-AUTODYN. The maximum displacement appears at the centroid of the RC wall. Based on the ratio of shear to bending strength of the RC wall, failure mode 3, the combined failure with one plastic hinge at the center and two shear sliding near the supports is adopted in the comparison.

In the scenario of surface RC wall against blast load, it can be concluded that the maximum displacement from the numerical simulations of a three-dimensional wall model is more conservative than that predicted by the two-dimensional beam model, and enhancement of the shear strength of RC wall is necessary.

In the underground RC structure under external blast load scenario, the SSI on bending damage at large scaled distance is considerable while it decreases with the increase of the scaled distance and the smallest error appear in the moderate bending damage cases. The SSI affects the shear damage at large scaled distance cases significantely, while it is minor in the middle and small scaled distance cases.

In the scenario of underground RC structure under internal blast load, the SSI on bending damage at large scaled distance is significant while it decreases with the increase of the scaled distance. The SSI affect the shear damage in the moderate and large scaled distance cases, while the effect is minor in the small scaled distance cases.

Generally, the results from numerical simulations agree well with that from the theoretical solutions of the beam model, especially at the moderate damage level. The P-I diagrams based on the MAM for surface and underground RC structure under different blast load cases are verified.

9.2. Recommendations on the future work

According to experience of the author, blast load in the close-in range is not accurate enough. Although a lot of researchers gave relative equations, results varies in a big range. Such uncertainty makes it hard to validate accuracy of the method used in the present study. Therefore, results of the present study are highly recommended for middle and far range explosion cases.

The present works can be improved and some recommendations are listed as below:

- In the present study, structures are simplified as two-dimensional beam element in the MAM although some generalized integration approach is adopted. There exists error when comparing with the numerical simulation results as shown. In the future study, the beam model can be replaced by a slab model so that more complex failure mode can be analyzed which is much more close to the real physical phenomenon. And more boundary conditions can be studied to show its effect when generating P-I diagrams.
- The failure due to shear force in the present study is direct shear and the bending failure is assumed as the plastic hinge, while in real cases other failure modes may appear, for example diagonal shear failure and more complicated bending failure. More analysis could be done on such failure modes.
- In the analysis of underground structure under external blast load, the SSI is simplified as a damping effect acting on the beam model, while in real cases, such interaction is more complicated since the soil material can be simulated in different models and the effect of SSI can be affected by factors such as soil type, water content, and so on. In another aspect, the external blast load will cause rigid body motion of the underground structure which reduces the maximum deformation of wall since such motion consumes some energy from blast wave. It is necessary to decouple the rigid body motion and local deformation of the wall.
- The generalized integration procedure used in the present study could combine more factors together to make the results closer to the experimental data. But such combination may cause accumulated error that cannot be

ignored since the error exists in every integration step. An improvement should be done by using a more powerful integration algorithm so that higher accuracy and faster convergence in each time step can be achieved.

REFERENCE

Abrahamson, G.R., and Lindberg, H.E. (1976). "Peak load impulse characterization of critical pulse loads in structural dynamics", *Nuclear Engineering Design*, **37**: 35-46.

Alves, M. and Jones, N. (2002). "Impact failure of beams using damage mechanics: Part I - Analytical model." *Int. J. Impact Eng*., **27**(8), 837-861.

Athanasopoulos, G.A., Pelekis, P.C., and Anagnostopoulos, G.A. (2000). "Effect of soil stiffness in the attenuation of Rayleigh-wave motions from field measurements", *Int. J. Soil. Dynam. Earthquake Eng.*, **19**, 277-288.

Barros, J.A.O. and Dias, S.J.E. (2006). "Near surface mounted CFRP laminates for shear strengthening of concrete beams", *Cement & Concrete Composites*, **28**(3), 276–292.

Biggs, J.M. (1964). *Introduction to Structural Dynamics.* McGraw-Hill, New York.

Bodner, S.R. and Symonds, P.S. (1979). "Experiments on viscoplastic response of circular plates to impulsive loading", *J. Mech. Phys. Solids* **27**,91-113.

Borgers, J.B.W. and Vantomme, J. (2006). "Towards a parametric model of a planar blast wave created with detonating cord", *19th International Conference of Military Aspects of Blast and Shock*, Canada.

Bleich, H.H. and Salvadori, M.G. (1955). "Impulsive motion of elasto-plastic beams", *Trans. A.S.C.E.*, **120**, 499.

Bulson, P.S. (1997). *Explosive Loading of Engineering Structures*, Taylor & Francis; 1st edition (September 1).

Campidelli, M. and Viola, E. (2007). "An analytical–numerical method to analyze single degree of freedom models under airblast loading", *J. Sound Vib.*, **302**, 260-286.

Chen, X.W., and Li, Q.M. (2003). "Shear plugging and perforation of ductile circular plates struck by a blunt projectile", *Int. J. Impact Eng.*, **28**, 513-536.

Chen, X.W., Li, Q.M., and Fan, S.C. (2005). "Initiation of adiabatic shear failure in a clamped circular plate struck by a blunt projectile", *Int. J. Impact Eng.*, **31**, 877-893.

Coombs, A. and Thornhill, C.K. (1960). Symposium uber wissenschaftliche Grundlagen des Schutzbaues am Ernst-Mach-Institut Freiburg i.Br.

de Oliveira, J.G. and Jones, N. (1978). "Some remarks on the influence of transverse shear on the plastic yielding of structures", *Int. J. Mech. Sci*. **20**, 759-765.

de Oliveira, J.G. amd Jones, N. (1979). "A numerical procedure for the dynamic plastic response of beams with rotator inertia and transverse shear effects", *J. Struct. Mech*., **7**(2), 193-230.

de Oliveira J.G. (1982). *"Beams under lateral projectile impact", Proc. ASCE, 108(EM1),* 51-71.

Dutta, S., Mandal, A. and Dutta, S.C. (2004). "Soil–structure interaction in dynamic behaviour of elevated tanks with alternate frame staging configurations", *J. Sound Vib.*, **277,** 825–853.

Fallah, A.S. and Louca, L.A. (2007). "Pressure–impulse diagrams for elastic-plastic-hardening and softening single-degree-of-freedom models subjected to blast loading", *Int. J. Impact Eng.*, **34**(4), 823–842.

Florek, J.R. and Benaroya, H. (2005). "Pulse–pressure loading effects on aviation and general engineering structures-review", *J. Sound Vib.*, **284**, 421–453.

Hadi, M.N.S. (2005). "Behaviour of high strength axially loaded concrete columns confined with helices", *J. Con. Build. Mat.*, **19**, 135-140.

Johnson, G.R. and Cook, W.H. (1985). "Fracture characteristics of three metals subjected to various strains, strain rates, temperatures and pressures", *J. Eng. Mech.*, **21**(1), 31-48.

Jones, N. (1968). "Finite deflections of a simply supported rigid-plastic annular plate loaded dynamically", *Int. J. Solids Structures* **4**(6), 593-603.

Jones, N. and de Oliveira, J.G. (1979). "The influence of rotator inertia and transverse shear on the dynamic plastic behavior of beams", *J. Appl. Mech.*, **46**(2), 303-310.

Jones, N. and Song, B. (1986). "Shear and bending response of a rigid plastic beam to partly distributed blast type loading", *Mechanics Based Design of Structures and Machines,* **14**(3), 275-320.

Jones, N. (1989). “On the dynamic inelastic failure of beams”, In: Wierzbicki, T. and Jones, N. editors, *Structural Failure*, New York: Wiley, 133-159.

Jones, N. (1997). “Structural impact, Paperback Ed. Cambridge”, *Cambridge University Press*..

Jones, N. and Jones, C. (2002). “Inelastic failure of fully clamped beams and circular plates under impact loading. Proceedings of the Institution of Mechanical Engineers. Part C”, *J. Mech. Eng. Sci.,* **216**(2), 133-149.

Jones, N. and Song, B. (1986). “Shear and bending response of a rigid plastic beam to partly distributed blast type loading”, *Mechanics Based Design of Structures and Machines*, **14(**3), 275-320.

Kalthoff, J.F. and Winkler, S. (1987). “Failure mode transition at high rates of loading”, In: Chiem, C.Y. *et al*., editors. *Proceedings of the International Conference on Impact Loading and Dynamic Behaviour of Materials*, Bremen, Deutsche Gesellschaft fur Metallkunde, DGM, 185-196.

Kalthoff, J.F. (1990). “Transition in the failure behavior of dynamically shear loaded cracks”, In: Chen, C.F., Kunze, H.D. and Meyer, L.W. editors. *Proceedings of the 11th US National Conference of Applied Mechanics*, Arizona: TUCSON, May, 5247-5250.

Kornhauser, M. (1954). “Prediction and Evaluation of Sensitivity to Transient Accelerations”, *Journal of Applied Mechanics*, **21**, 371-380.

Krauthammer, T. (1998). “Blast mitigation technologies: developments and numerical considerations for behavior assessment and design”, In: *Proceedings of international conference on structures under shock and impact*, SUSI, Melbourne, Australia 1998:1-10.

Krauthammer, T., Bazeos, N. and Holmquist, T.J. (1986). “Modified SDOF analysis of RC box-type structures”, *J. Struct. Eng*., **112(**4), 726-744.

Lee, C.H., Kim, J.W. and Song, J.G. (2008). “Punching shear strength and post-punching behavior of CFT column to RC flat plate connections”, *Journal of Constructional Steel Research*, **64** (4), 418–428.

Lee, E.L., Finger, M. and Collins, W. (1973). *JWL equation of state coefficients for high explosives.* Lawrence Livermore Laboratory, UCID-16189. Lawrence Livermore National Laboratory, Livermore, California, January 1973.

Lee, T.K. and Al-Mahaidi, R. (2008). "An experimental investigation on shear behaviour of RC T-beams strengthened with CFRP using photogrammetry", *J. Comp. Struct.*, **82(**2), 185-193.

Lellep, J. and Torn, K. (2004). "Plastic response of a circular cylindrical shell to dynamic loadings", *Int. J. Impact Eng.*, **30**, 555-576.

Lellep, J. and Torn, K. (2005). "Shear and bending response of a rigid-plastic beam subjected to impulsive loading", *Int. J. Impact Eng.*, **31**(9), 1081-1105.

Li, Q.M. and Jones, N. (1991). "The influence of boundary conditions on the dynamic plastic response of beams and circular plates", *In: Ponter ARS, Cocks ACF, editors. Applied Solid Mechanics-4. London: Elsevier Applied Science,* 52–71.

Li, Q.M. and Jones, N. (1994). "Blast loading of fully clamped circular plates with transverse shear effects*", Int. J. Solids Structures*, 31(14), 1861-1876.

Li, Q.M. and Jones, N. (1999). "Shear and adiabatic shear failures in an impulsively loaded fully clamped beam*", Int. J. Impact Eng.*, **22,** 589-607.

Li, Q.M. and Jones, N. (2000). "Formation of a shear localization in structural elements under transverse dynamic loads", *Int. J. Solids Structures*, **37**, 6683-6704.

Li, Q.M. and Jones, N. (2005a). "Initiation of adiabatic shear failure in a clamped circular plate struck by a blunt projectile", *Int. J. Impact Eng.*, **31**(7), 877-893.

Li, Q.M. and Jones, N. (2005b). "Foundation of correlation parameters for eliminating pulse shape differences on dynamic plastic response of structures", *J. App. Mech.-Trans.*, **72**(2), 172-176.

Li, Q.M. and Meng, H. (2002a). "Pressure-impulse diagram for blast loads based on dimensional analysis and single-degree-of-freedom model", *J. Eng. Mech.*, **128**(1), 87-92.

Li, Q.M. and Meng, H. (2002b). "Pulse loading shape effects on pressure–impulse diagram of an elastic–plastic, single-degree-of-freedom structural model", *Int. J. Mech. Sci*., **44**, 1985–1998.

Li, W. and Assimaki, D. (2010). "Simulating soil stiffness degradation in transient site response predictions", *Int. J. Soil. Dynam. Earthquake Eng.*, **30**, 299-309

Liu, J.H. and Jones, N. (1988). “Dynamic response of a rigid plastic clamped beam struck by a mass at any point on the span”, *Int. J. Solids Struct.,* **24,** 251-270.

Ma, G.W., Shi, H.J. and Shu, D.W. (2007). “P-I diagram method for combined failure modes of rigid-plastic beams”, *Int. J. Impact Eng*., **34**(6), 1081-1094.

MacGregor, J.G. and Wight, J.K. (2005). *Reinforced Concrete: Mechanics and Design (4th Edition),* Prentice Hall.

Marek, J., Joanna, S.-S. and Grzegorz, B. (2005). “The strength reserve due to restrained bending in brittle-matrix structures”, *J. Nuc. Eng. Des.,* **235**(17-19), 1837–1847.

Martin, J.B. and Symonds, P.S. (1966). “Mode approximation for impulsively loaded rigid plastic structures”, *J. Eng. Mech. Div*., **92**(EM5), 43-66.

McCormac, Jack C. (2006). *Design of reinforced concrete,* John Wiley.

McNeely, D.J. and Lash, S.D. (1963). “Tensile strength of concrete”, *Journal of the American Concrete Institute, Proceedings,* **60**(6), 751-761.

Menkes, S.B. and Opat, H.J. (1973). “Broken beams”, *Exp. Mech.,* **13,** 480-486.

Mortion, H.S. (1966). “Scaling the effects of air blast on typical targets”, The John Hopkins University, *Applied Physics Laboratory*; Technical Memorandum TG-733.

Nawy, E.G. (2003). *Reinforced concrete: a fundamental approach,* Prentice Hall.

Nonaka, T. (1977). “Shear and bending response of a rigid-plastic beam to blast-type loading”, *Ingenieur-Archiv* **46**, 35–52.

Polak, M.A. (1998). “Shear analysis of reinforced concrete shells using degenerate elements”, *J. Comp. Struct.,* **68**(1-3), 17-29.

Raphael, J.M. (1984). “Tensile strength of concrete”, *ACI Journal, Proceedings,* **81**(2), 158-165.

Richmond, D.R., Gaylord, C.S., Damon, E.G. and Taborelli, R. V. (1966). *DASA-AEC-LOVELACE foundation blast-simulation facility,* Technical progress report.

Riedel W. (2000). *Beton unter Dynamischen Lasten, meso- und makromechanische Modelle und ihre Parameter*. PhD thesis, vol. 5. University of the German Armed Forces Munich: Forschungsergebnisse der Kurzzeitdynamik;

Rizzo, A. and De Lorenzis, L. (2009). “Behavior and capacity of RC beams strengthened in shear with NSM FRP reinforcement”, *J. con. Build. Mat.*, **23**(4), 1555–1567.

Rogers G. F. C. and Mayhew Y. R. (1994). *Thermodynamic and Transport Properties of Fluids: S. I. Units*, Blackwell Publishers.

Sawangsuriya, A., Bosscher, P.J. and Edil, T.B. (1974). “Laboratory evaluation of the soil stiffness gauge (SSG)”, *Transportation research record ISSN 0361 - 1981 CODEN TRREDM*, 30-37.

Seiler, J.A., Cotter, B.A., and Symonds, P.S. (1956). “Impulsive loading of elastic-plastic beams”, *J. App. Mech.*, **23**,515.

Shen, W.Q. and Jones, N. (1993). “Dynamic response and failure of fully clamped curcular plates under impulsive loading”, *Int. J. Impact Engng.*, **13**(2),259-278.

Shi, Y.C., Hao, H. and Li, Z.X. (2008). “Numerical derivation of pressure-impulse diagrams for prediction of RC column damage to blast loads”, *Int. J. Impact Eng.*, **35**(11), 1213-1227.

Smith, P.D. and Hetherington, J.G. (1994). *Blast and ballistic loading of structures*, Oxford: Butterworth-Heinemann.

Stehmeyer, E.H. and Rizos, D.C. (2008). “Considering dynamic soil structure interaction (SSI) effects on seismic isolation retrofit efficiency and the importance of natural frequency ratio”, *Int. J. Soil. Dynam. Earthquake Eng.*, **28**, 468-479.

Symonds, P.S. (1968). *Plastic shear deformations in dynamic load problems*, Engineering plasticity. Cambridge: Cambridge University Press.

Symonds, P.S. and Chon, C.T. (1979). “Large visco plastic deflections of impulsively loaded plane frames”, *Int. J. Solids Struc.*, **15**(1), 15-31.

Teeling-Smith, R.G. and Nurick, G.N. (1991). “The deformation and tearing of thin circular plates subjected to impulsive loads”, *Int. J. Impact Engng.* **11**(1),77-91.

TM5-1300 (1990). *Structures to resist the effects of the accidental explosions*. US Department of Army, New Jersey.

TM5-855-1 (1986). *Fundamentals of Protective Design for Conventional Weapons*.

ülker-Kaustell, M., Karoumi, R., and Pacoste, C. (2010). “Simplified analysis of the dynamic soil-structure interaction of a portal frame railway bridge”, International Journal of Engineering Structures, **32**,3692-3698.

Weidlinger, P. and Hinman, E. (1988). “Analysis of underground protective structures”, *J. Struct. Eng.*, **114**, 1658-1673.

Wolf, J.P. (1985). *Dynamic soil-structure interaction*. Prentice-Hall, Englewood Cliffs, NJ.

Youngdahl, C.K. (1970). “Correlation parameters for eliminating the effect of pulse shape on dynamic plastic deformation”, *ASME J. Appl. Mech*., **37**, 744-752.

Youngdahl, C.K. (1971). “Influence of pulse shape on the final plastic deformation of a circular plate”, *Int. J. Solids Struct*,. **7**, 1127-1142.

Youngdahl, C.K. (1997). “A mode approximation method for the dynamic response of a strain-hardening cantilever”, *Int. J. Impact Engng*. **19**(1), 81-94.

Yu, J.L. and Jones, N. (1991). “Further experiment investigations on the failure of clamped beams under impact loads”, *Int. J. Solids Struct*., **27**, 1113-1137.

Yu, T.X. and Chen, F.L. (2000). “A further study of plastic shear failure of impulsively loaded clamped beams”, *Int. J. Impact Engng.* **24**(6-7), 613-629.

LIST OF PUBLICATIONS

X. Huang, L. He, G.W. Ma (2011), "Soil-structure interaction and pulse shape effect on structural element damage to blast load", *Journal of Performance of Constructed Facilities,* (accepted)

X. Huang, G.W. Ma, J.C. Li (2010), "Damage Assessment of Reinforced Concrete Structural Elements Subjected to Blast Load", *International Journal of Protective Structures*, **1**(1), 103-124

G.W. Ma, **X. Huang**, and J.C. Li (2010), "Simplified Damage Assessment Method for Buried Structures against External Blast Load", *ASCE Journal of Structural Engineering*, **136(**5), 603-612

J.C. Li, G.W. Ma, **X. Huang** (2009),"Analysis of Wave Propagation Through a Filled Rock Joint", *Rock Mechanics and Rock Engineering*, **43**(6), 789-798

G.W. Ma, **X. Huang**, and J.C. Li (2009), "Damage Assessment for Buried Structures against Internal Blast Load", *International Journal of Structural Engineering and Mechanics*, **32**(2), 301-320

X. Huang, J.C. Li, and G.W. Ma (2009), "Damage Analysis of RC Column/Beam Subject to Blast Load", *Proceedings of the 8th International conference on Shock and Impact Loads on Structures*, Adelaide, Australia 311-320

G.W. Ma, J.C. Li , **X. Huang** (2009), "Blasting response of steel shelter filled with recycled concrete", *Proceedings of the 8th International Conference on Shock & Impact Loads on Structures*, Adelaide, Australia 421-434

G.W. Ma, **X. Huang**, and J.C. Li (2008), "Damage Assessment for Buried Structures against Internal Blast Load", *Transactions of Tianjin University*, **14**(5), 353-357

J.C. Li, **X. Huang**, and G.W. Ma (2008). "Blasting Response of Steel Shelter Filled with Recycled Concrete", *Transactions of Tianjin University*, **14**(6), 426-429

APPENDIX

P-I DIAGRAM METHOD FOR COMBINED FAILURE MODES OF RIGID-PLASTIC BEAMS

The rigid-plastic beam model ignores the elastic response of the structure, while it can consider the transverse shear effects to the beam deformation (Jones, 1997). It is a special example in Li and Jones (1991).

The governing equation for the dominant shear effect is:

$$\frac{\partial Q}{\partial x} = -p + m\ddot{y} \tag{A.1}$$

where Q is the transverse shear force, x is the abscissa on the beam, p is the external uniformly distributed pressure, m is the mass per unit length, y is the transverse displacement of the beam and $\ddot{y}$ is the acceleration of the unit mass. Integrate the acceleration with time and consider the initial displacement and velocity, the final deformation of the beam can be derived. The transverse velocity profile of the beams changes significantly with the dimensionless parameter:

$$\nu = \frac{Q_0 L}{2M_0} \tag{A.2}$$

where Q_0 is the shearing strength, M_0 is the bending strength of the beam, and L is the beam half span.

Five possible transverse velocity profiles (Fig. A.1) are introduced and used for derivation of the beam motion under pulse loads. The deformation is induced by the pulse load and is terminated when the beam's kinetic energy is totally consumed by the shear and/or bending hinges.

In Fig. A-1, (a) is for the Mode 1 in which the shear hinges appear at the supports. (b) is for the Mode 3 that, the shear hinge appear at supports and the bending hinge appears at the mid-span. (c) is the Mode 2 that a stationary bending hinge exists at the mid-span of beam. (d) is for the Mode 5 with two shear hinges at the supports

and a dynamic bending hinge zone at the mid-span. (e) is for the Mode 4 with a dynamic bending hinge zone at the mid-span.

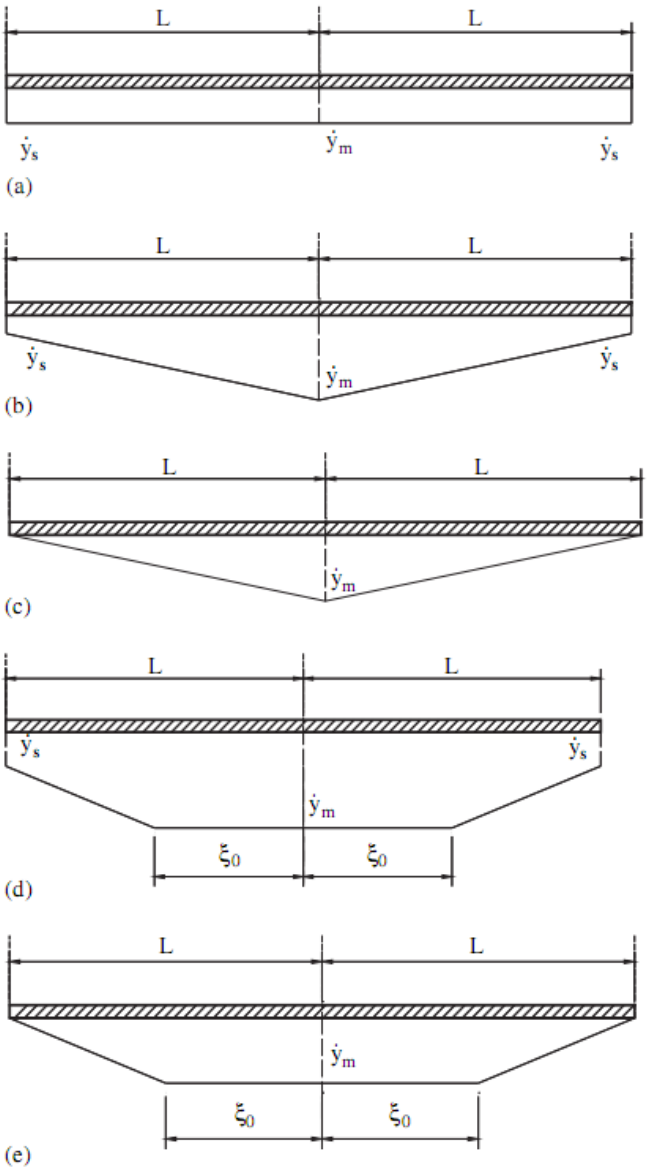

Fig. A - 1 Transverse velocity profiles

The rectangular pulse load can be expressed by:

$$p = \begin{cases} p_0, & t \le t_d \\ 0, & t > t_d \end{cases} \tag{A.3}$$

where t_d is the loading duration, p_0 is the constant pressure in the loading duration.

When $\nu \le 1$ and $p_0 \le \left(2M_0 / L^2\right)\nu$, or $\nu \ge 1$ and $p_0 \le \left(2M_0 / L^2\right)$, based on the rigid-plastic beam model, the beam will not deform because the shear and bending strengths are sufficient to sustain the applied load without plastic deformation.

Mode 1, when $\nu \le 1$ and $p_0 \ge \left(2M_0 / L^2\right)\nu$, shear failure.

The beam deforms as shown in Fig. A-1 (a). The motion has two phases, i.e. a loading phase and a post-loading phase. At the end of the loading phase, the beam reaches the maximum velocity. In the post-loading phase, the load is released and the beam decelerates till motion ceases.

(1) Phase 1, $0 < t \le t_d$

The governing equation for the dominant shear effect is:

$$\frac{\partial Q}{\partial x} = -p_0 + m\ddot{y}_s \tag{A.4}$$

where $\ddot{y}_s$ is the acceleration due to shear force.

The boundary and initial conditions are:

$$Q\left(x=0\right)=0, Q\left(x=L\right)=-Q_0 \tag{A.5}$$

$$\dot{y}_s\left(t=0\right)=0, y_s\left(t=0\right)=0 \tag{A.6}$$

where $\dot{y}_s$ and y_s are velocity and displacement due to shear force respectively.

By integrating Eq. (A.4) with respect to time, at the end of this phase when $t=t_d$:

$$\dot{y}_s = \frac{p_0 L - Q_0}{mL} t_d \tag{A.7}$$

$$y_s = \frac{p_0 L - Q_0}{2mL} t_d \tag{A.8}$$

(2) Phase 2, $t_d < t \le t_f$

After t_d, the load is removed, Eq. (A.4) turns into:

$$\frac{\partial Q}{\partial x} = m\ddot{y}_s \tag{A.9}$$

Using Eq. (A.5) as the boundary conditions and Eqs. (A.7)- (A.8) as the initial conditions to solve Eq. (A.9), at the end of phase 2, the final time t_f will be:

$$t_f = \frac{p_0 L}{Q_0} t_d \tag{A.10}$$

The final transverse displacement of beam due to shear force is:

$$y_s\left(t_f\right) = \frac{p_0\left(p_0 L - Q_0\right)}{2mQ_0} t_d^2 \tag{A.11}$$

Mode 2, when $1 \le \nu \le 1.5$ **and** $2M_0 / L^2 \le p_0 \le 2M_0\left(4\nu - 3\right) / L^2$ **, or** $\nu \ge 1.5$ **and** $2M_0 / L^2 \le p_0 \le 6M_0 / L^2$**, bending failure.**

The rotation of the stationary bending hinge at the beam mid-span absorbs all the kinetic energy in this case as shown in Fig. A.1 (c). Two phases exist during the whole deformation process, a loading phase and a post-loading phase.

(1) Phase 1, $0 < t \le t_d$

The governing equation is:

$$\frac{\partial Q}{\partial x} = -p_0 + m\ddot{y}_m\left(1 - \frac{x}{L}\right) \tag{A.12}$$

where $\ddot{y}_m$ is the acceleration due to bending moment.

The boundary and initial conditions are:

$$Q\left(x=0\right)=0, \quad Q\left(x=L\right)=-Q_0, \quad M\left(x=0\right)=M_0, \quad M\left(x=L\right)=0 \tag{A.13}$$

$$\dot{y}_m\left(t=0\right)=0, \quad y_m\left(t=0\right)=0 \tag{A.14}$$

where $\dot{y}_m$ and y_m are the velocity and displacement due to bending moment respectively.

Integrating Eq. (A.12), at the end of phase 1 when $t=t_d$, the maximum velocity and displacement of beam due to bending moment are:

$$\dot{y}_m = \left(\frac{3p_0}{2m} - \frac{3M_0}{mL^2}\right) t_d \tag{A.15}$$

$$y_m = \left(\frac{3p_0}{2m} - \frac{3M_0}{mL^2} \right) \frac{t_d^2}{2} \tag{A.16}$$

(2) Phase 2, $t_d < t \le t_f$

The governing equation changes to:

$$\frac{\partial Q}{\partial x} = m\ddot{y}_m \left(1 - \frac{x}{L} \right) \tag{A.17}$$

Using Eq. (A.13) as the boundary conditions and Eqs. (A.15)- (A.16) as the initial conditions, the final time t_f when $\dot{y}_m = 0$ is:

$$t_f = \frac{p_0 t_d L^2}{2M_0} \tag{A.18}$$

The final bending displacement of the beam is solved as:

$$y_m\left(t_f\right) = \frac{3p_0^2 t_d^2 L^2}{8mM_0} - \frac{3p_0 t_d^2}{4m} \tag{A.19}$$

Mode 3, $1 \le \nu \le 1.5$ **and** $p_0 > 2M_0(4\nu - 3)/L^2$ **, combined failure.**

The beam deforms as depicted in Fig. A.1 (b) and the motion can be divided into three phases, i.e. a loading phase ($t \le t_d$), a post-loading phase till the shear sliding ceases ($t_d \le t \le t_s$), and a post-loading phase from ceasing of the shear sliding to the motion termination ($t_s \le t \le t_f$). This failure mode can be considered as combination of mode 1 and mode 2.

(1) Phase 1, $0 < t \le t_d$

The governing equation is:

$$\frac{\partial Q}{\partial x} = -p_0 + m\ddot{y}_s + m\left(\ddot{y}_m - \ddot{y}_s\right)\left(1 - \frac{x}{L}\right) \tag{A.20}$$

With the same boundary and initial conditions given in Eqa. (A.13), (A.14) and (A.6), after integrating Eq. (A.20), at the end of phase 1 when $t=t_d$, the maximum displacement and velocity of the beam due to shear and bending are given respectively as follows:

$$\dot{y}_m\left(t_d\right)=\left[\frac{p_0}{m}+\frac{2M_0}{mL^2}\left(2\nu-3\right)\right]t_d \tag{A.21}$$

$$\dot{y}_s\left(t_d\right)=\left[\frac{p_0}{m}+\frac{2M_0}{mL^2}\left(3-4\nu\right)\right]t_d \tag{A.22}$$

$$y_m\left(t_d\right)=\left[\frac{p_0}{m}+\frac{2M_0}{mL^2}\left(2\nu-3\right)\right]\frac{t_d^2}{2} \tag{A.23}$$

$$y_s\left(t_d\right)=\left[\frac{p_0}{m}+\frac{2M_0}{mL^2}\left(3-4\nu\right)\right]\frac{t_d^2}{2} \tag{A.24}$$

(2) Phase 2, $t_d<t\le t_s$

The governing equation is:

$$\frac{\partial Q}{\partial x}=m\ddot{y}_s+m\left(\ddot{y}_m-\ddot{y}_s\right)\left(1-\frac{x}{L}\right) \tag{A.25}$$

The boundary conditions are still the same as those in the previous phase, while the initial conditions are Eqs. (A.21)- (A.24). After iterating the governing equation, when the velocity due to shear force equals to zero, the ceasing time of shear displacement, the maximum shear displacement , bending velocity and bending displacement are:

$$t_s=\frac{p_0t_dL^2}{2\left(4\nu-3\right)M_0} \tag{A.26}$$

$$y_s\left(t_s\right)=\frac{p_0t_dL^2}{4M_0m\left(4\nu-3\right)}-\frac{p_0t_d^2}{2m} \tag{A.27}$$

$$\dot{y}_m\left(t_s\right)=\frac{6p_0t_d}{m}\cdot\frac{\nu-1}{4\nu-3} \tag{A.28}$$

$$y_m\left(t_s\right)=\frac{\left(10\nu-9\right)p_0^2t_d^2L^2}{4M_0m\left(4\nu-3\right)^2}-\frac{p_0t_d^2}{2m} \tag{A.29}$$

(3) Phase 3, $t_s<t\le t_f$

The governing equation of this phase is the same as Eq. (A.17). Similarly, the motion termination time and the final displacement when $\dot{y}_m=0$ can be calculated as:

$$t_f = \frac{p_0 t_d L^2}{2M_0} \tag{A.30}$$

$$y_m\left(t_f\right) = \frac{\left(6\nu - 5\right) p_0^2 t_d^2 L^2}{4M_0 m\left(4\nu - 3\right)^2} - \frac{p_0 t_d^2}{2m} \tag{A.31}$$

Mode 4, $1.5 < \nu$ **and** $p_0 > 8M_0\nu^2 / 3L^2$**, complex bending failure.**

No shear sliding appears and there is a bending zone in the central portion of the beam (Fig. A.1 (e)). There exist three phases of the beam motion including a loading phase, one post-loading phase that the bending hinges moving towards the beam mid-span, and another post-loading phase that similar to phase 2 of mode 2.

(1) Phase 1, $0 < t \le t_d$

The transverse velocity field is like:

$$\dot{y} = \begin{cases} \dot{y}_m, & 0 \le x \le \xi_0 \\ \dot{y}_m \dfrac{L - x}{L - \xi_0}, & \xi_0 < x \le L \end{cases} \tag{A.32}$$

where ξ_0 is the half width of plastic zone.

When $0 \le x \le \xi_0$, $Q = 0$ and $M = M_0$, therefore $\ddot{y}_m = p_0 / m$.

At the $\xi_0 < x \le L$ portion, the governing equation is:

$$\frac{\partial Q}{\partial x} = -p_0 + m\ddot{y}_m \frac{L - x}{L - \xi_0} \tag{A.33}$$

Since the acceleration is continuous along the beam, the governing equation can be re-written as:

$$\frac{\partial Q}{\partial x} = -p_0 + p_0 \frac{L - x}{L - \xi_0} \tag{A.34}$$

Use Eq. (A.14) as initial conditions, the boundary conditions changes to:

$$Q\left(x = \xi_0\right) = 0, \quad Q\left(x = L\right) = -Q_0, \quad M\left(x = \xi_0\right) = M_0, \quad M\left(x = L\right) = 0 \tag{A.35}$$

After integration, the half width of plastic zone can be calculated as:

$$\xi_0 = L - \sqrt{\frac{6M_0}{p_0}} \tag{A.36}$$

Thus if $p_0 \geq 6M_0 / L^2$, the plastic zone due to bending moment can be initiated, otherwise it will be confined to only one bending hinge. At the end of this phase, the maximum velocity and displacement are:

$$\dot{y}_m(t_d) = \frac{p_0 t_d}{m} \tag{A.37}$$

$$y_m(t_d) = \frac{p_0 t_d^2}{2m} \tag{A.38}$$

(2) Phase 2, $t_d < t \leq t_1$

The governing equation is:

$$\frac{\partial Q}{\partial x} = m\ddot{y}_m \frac{L-x}{L-\xi} \tag{A.39}$$

where ξ is the distance between the plastic hinge and the mid-span of the beam.

ξ changes from ξ_0 to zero with time from t_d to t_1. And the boundary conditions are:

$$Q(x=\xi)=0, \quad Q(x=L)=-Q_0, \quad M(x=\xi)=M_0, \quad M(x=L)=0 \tag{A.40}$$

Solve the governing equation by using Eqs. (A.37)- (A.38) as the initial conditions, and the velocity of hinge moving is:

$$\dot{\xi} = \frac{-3M_0}{p_0 t_d (L-\xi)} \tag{A.41}$$

Since $\xi=\xi_0$ when $t=t_d$, ξ is solved as:

$$\xi = L - \sqrt{\frac{6tM_0}{p_0 t_d}} \tag{A.42}$$

When the plastic hinge moves to the mid-span of beam ($\xi=0$), the ending time of this phase is t_1 and the maximum velocity and displacement are:

$$t_1 = \frac{p_0 t_d L^2}{6M_0} \tag{A.43}$$

$$\dot{y}_m(t_1) = \frac{p_0 t_d}{m} \tag{A.44}$$

$$y_m(t_1) = \frac{p_0 t_d^2}{2m}\left(\frac{p_0 L^2}{3M_0} - 1\right) \tag{A.45}$$

(3) Phase 3, $t_1 < t \le t_f$

In this phase, the velocity profile is the same as that of phase 2 in mode 2. Therefore the governing equation and boundary conditions remain the same. By using Eqs. (A.44) and (A.45) as initial conditions, at the end of this phase ($\dot{y}_m = 0$), the final time and displacement are:

$$t_f = \frac{p_0 t_d L^2}{2M_0} \tag{A.46}$$

$$y_m(t_f) = \frac{p_0^2 t_d^2 L^2}{3mM_0} - \frac{p_0 t_d^2}{2m} \tag{A.47}$$

Mode 5, $\nu > 1.5$ **and** $6M_0 / L^2 \le p_0 \le 8M_0\nu^2 / 3L^2$ **, complex combined failure.**

Mode 5 is the most complicated mode as the combination of mode 1 and mode 4. There are four phases including one loading phase and three post-loading phases which end at t_d, t_s, t_1, and t_f respectively.

(1) Phase 1, $0 < t \le t_d$

The transverse velocity field is like:

$$\dot{y} = \begin{cases} \dot{y}_m, & 0 \le x \le \xi_0 \\ \dot{y}_s + (\dot{y}_m - \dot{y}_s)\dfrac{L-x}{L-\xi_0}, & \xi_0 < x \le L \end{cases} \tag{A.48}$$

When $0 \le x \le \xi_0$, $Q = 0$ and $M = M_0$, therefore $\ddot{y}_m = p_0 / m$.

At the $\xi_0 < x \le L$ portion, the governing equation is:

$$\frac{\partial Q}{\partial x} = -p_0 + m\ddot{y}_s + m(\ddot{y}_m - \ddot{y}_s)\frac{L-x}{L-\xi_0} \tag{A.49}$$

Using Eq. (A.14) as initial conditions, and Eq. (A.35) as the boundary conditions, after integration, the half width of plastic zone can be calculated as:

$$\xi_0 = \frac{2\nu - 3}{2\nu} L \tag{A.50}$$

At the end of this phase, the maximum velocity and displacement of bending are the same as Eqs. (A.37) and (A.38), while for shear are:

$$\dot{y}_s(t_d) = \left(\frac{p_0}{m} - \frac{8M_0\nu^2}{3mL^2} \right) t_d \tag{A.51}$$

$$y_s(t_d) = \left(\frac{p_0}{m} - \frac{8M_0\nu^2}{3mL^2} \right) \frac{t_d^2}{2} \tag{A.52}$$

(2) Phase 2, $t_d < t \le t_s$

When $0 \le x < \xi_0$, $Q = 0$ and $M = M_0$. Therefore $\ddot{y}_m = 0$.

When $\xi_0 \le x \le L$, the governing equation is:

$$\frac{\partial Q}{\partial x} = m\ddot{y}_s + m(\ddot{y}_m - \ddot{y}_s) \frac{L - x}{L - \xi_0} \tag{A.53}$$

Using Eq. (A.14) as initial conditions, and Eqs. (A.35) and (A.50) as the boundary conditions, after integration, the ending time of this phase and the velocity and displacement are:

$$t_s = \frac{3p_0 t_d L^2}{8M_0\nu^2} \tag{A.54}$$

$$y_s(t_s) = -\frac{p_0 t_d^2}{2m} + \frac{3p_0^2 t_d^2 L^2}{16M_0 m\nu^2} \tag{A.55}$$

$$\dot{y}_m(t_s) = \frac{p_0 t_d}{m} \tag{A.56}$$

$$y_m(t_d) = \frac{\left(8M_0\nu^2 - 3p_0L^2\right) \cdot p_0 t_d^2}{8M_0 m\nu^2} \tag{A.57}$$

(3) Phase 3, $t_s < t \le t_1$

When $0 \le x < \xi$, $\dot{y}_m = p_0 t_d / m$ and $y_m = p_0 t_d t / m - p_0 t_d^2 / 2m$.

When $\xi \le x \le L$, the governing equation, and boundary conditions are the same as those in phase 2 of mode 4, while the initial conditions are as Eq. (A.56) and (A.57). When $\xi = 0$, the maximum velocity does not change, and the ending time and the maximum bending displacement can be calculated as:

$$t_1 = \frac{p_0 t_d L^2}{6M_0} \tag{A.58}$$

$$y_m(t_1) = \frac{p_0 t_d^2}{2m}\left(\frac{p_0 L^2}{3M_0} - 1\right) \tag{A.59}$$

(4) Phase 4, $t_1 < t \le t_f$

The governing equation is Eq. (A.17). The boundary conditions are Eqs. (A.15)-(A.16). By using Eqs. (A.56) and (A.59) as initial conditions, at the end of this phase ($\dot{y}_m = 0$), the final time and displacement are:

$$t_f = \frac{p_0 t_d L^2}{2M_0} \tag{A.60}$$

$$y_m(t_f) = \frac{p_0^2 t_d^2 L^2}{3M_0 m} - \frac{p_0 t_d^2}{2m} \tag{A.61}$$